

Analysis of Beauty Quark Hadronization in Vacuum and Quark-Gluon Plasma with CMS

by

Zhaozhong Shi

B.A., University of California, Berkeley (2016)

Submitted to the Department of Physics
in partial fulfillment of the requirements for the degree of
Doctor of Philosophy in Physics

at the

MASSACHUSETTS INSTITUTE OF TECHNOLOGY

September 2021

© Massachusetts Institute of Technology 2021. All rights reserved.

Author
Department of Physics
August 27, 2021

Certified by
Yen-Jie Lee
Associate Professor of Physics
Thesis Supervisor

Accepted by
Deepto Chakrabarty
Associate Department Head of Physics

Analysis of Beauty Quark Hadronization in Vacuum and Quark-Gluon Plasma with CMS

by

Zhaozhong Shi

Submitted to the Department of Physics
on August 27, 2021, in partial fulfillment of the
requirements for the degree of
Doctor of Philosophy in Physics

Abstract

An analysis of fully reconstructed B_s^0 and B^+ mesons decay into J/ψ and strange hadrons using Compact Muon Solenoid (CMS) Experiment 2017 pp dataset and 2018 PbPb data at the center of mass energy per nucleon $\sqrt{s_{NN}} = 5.02$ TeV at the Large Hadron Collider (LHC) is presented. We apply machine learning techniques along with multivariate analysis to obtain significant B-meson signals and extend the kinematic regime of B-meson measurements with higher precision. In our analysis, B_s^0 signal of greater than 5σ significance is observed for the first time in heavy-ion collisions. The measured B_s^0/B^+ ratios as functions of transverse momentum and event centrality in PbPb collisions along with pp references are compared with theoretical model predictions. These results will help elucidate the beauty quark hadronization mechanisms in vacuum and quark-gluon plasma at the LHC energy. Significant B-meson signals have also been observed at low very p_T and high event multiplicity in pp collisions, which will allow us to study beauty quark hadrochemistry in small systems as well as energy loss mechanisms in the future.

Thesis Supervisor: Yen-Jie Lee
Title: Associate Professor of Physics

Acknowledgments

Today, sitting in front of my Macbook and writing up my PhD thesis, I am recalling the nice memory over the past 5 years of my academic and research journey at MIT. I have overcome countless challenges and seized every opportunity to accomplish my goals. I have absorbed plenty of knowledge like nutrients and lead a workaholic life. I used to work many hours, especially when deadlines are approaching. I am glad that I have overcome countless of deadlines and managed to finish most of my tasks on time during my graduate studies. Because of my hard work and achievements, during my graduate studies at MIT, I have been awarded the NSF-GRFP and DOE-SCGSR fellowships. While I am proud of my academic and research accomplishments, the more important things are love and friendship. I have been to many memorable places around the world and met many interesting people. They have taught me more than I can learn from papers, lectures, and experiments. I owed them a lot and am indebted to everyone for their influence on me. Without them, today, I will not be able to finish this work and grow up.

On the cloudy afternoon of February 12, 2016, I was anxiously waiting for my graduate admission decisions. At around 2 pm when I am returning home from Berkeley, I received my acceptance to MIT from the MIT Department of Physics Coordinator Catherine Modica. At that moment, I was still on my BART from UC Berkeley back to San Francisco. I was very excited and immediately called my family to share this great news. I understood that this would be the start of my exciting career as a PhD candidate in Nuclear Physics research. Without thinking too much, I quickly accepted the offer and got ready to join MIT.

During the MIT Open House, I met a lot of amazing people. I first visited the MIT Heavy Ion Group and then made friends with many of my peers. I would really like to thank Constantin Weisser for his generous accommodation during the Open House. I met my future PhD advisor Professor Yen-Jie Lee and LNS director Bolek Wyslouch. I also met my fellow students at LNS such as Lauren Yates, Sangbaek Lee, and Yi Jia. They are all very nice and kind. We have spent our first three semesters together

taking classes and discussing physics. I particularly want to mention Sangbaek since we used to discuss a lot about our life stories and future perspectives together. It was a quite memorable experience. I also frequently visited lattice QCD theorist Anthony Grebe. I still remembered the time we discussed physics questions, debated ideas, derive formulae at the Center for Theoretical Physics. He is a truly humble and kind person. I wish him to have a successful future career in theoretical particle physics.

As a resident of MIT Tang Hall, I met many interesting people. Here, I would like to thank Ali Fahimniya who also lived at Tang Hall for his first year. We often talked with each other during the cookies social in the Pappalardo Room. We shared our life experiences and future plans. It turns out that we defended our PhD just a day apart from each other.

Shortly after attending MIT, I decided to join the MIT Heavy Ion Group at LNS and pursued my scientific research career in Experimental High Energy Nuclear Physics. I would work on it as my PhD thesis topic for the next 5 years. Members of the MIT Heavy Ion Group have provided me with general supports and comprehensive guidance towards my PhD. Without them, I would not be able to overcome challenges and finish my thesis research projects.

At the graduate student's office, my desk is located in the northwest corner. Senior members of faculty in our group offered me excellent training and many opportunities to become an independent researcher and build up my international reputation in the field. I would especially like to thank Professor Yen-Jie Lee for his long and enduring support, both in research and life, for the past 5 years. He has provided me with many opportunities and ideas to carry out physics analysis and fought in the CMS collaboration to allow me to give talks at internationally recognized conferences. I am also deeply indebted to him for his care of my career development and letters of recommendation for fellowships and postdoctoral scholar positions. Thanks to his nurture, I have transformed from a student knowing almost nothing to become an independent researcher with big-picture visions. I am also grateful to the MIT Heavy Ion Group leader Professor Gunther Roland for his generous supports to allow me to work on sPHENIX and EIC projects. His letters of recommendation and grant

management advice have helped me a lot to get my first postdoctoral researcher position. I have also become more professional in developing leadership skills in academia. Both of them have provided me with opportunities to work at different places around the world such as MIT, Fermilab, BNL, and CERN. Aside from them, I appreciated the general research motivations, academic etiquette and soft skills from Professor Bolek Wyslouch and Professor Wit Busza.

My fellow senior graduate colleagues in my group have great impacts on me. First, the most senior graduate student Dragos Velicanu showed me around about our group and guided me through the Day-1 checklist. He also provided many remarks on my fellowship applications. Then, Alex Barberi used to sit next to my office desk. We have worked together and talked about funny stories. I also made acquaintances with Ta-Wei Wang. He created the skimmed files for me to play with and answered many technical questions in C++ programming and B mesons full reconstructions. As a newbie in the CMS analysis, I used to frequently bother Jing Wang with the analysis techniques and questions on codes. However, she still patiently helped and taught me until my confusions were gone. As the CMS spectra heavy flavor group leader, she also gave a lot of feedback and suggestions to validate my results and improve my analyses. Ran Bi, whose research was on photon and jet studies, was a bit reserved but still kindly helped me a lot with CMS software and technical concepts for data processing and analysis. Kaya Tatar was a very nice and resourceful guy. We used to discuss many physics and technical questions. Chris McGinn was one of my best friends at the MIT Heavy Ion Group. He provided me with a lot of technical assistance and saved me from the bugs of my codes. His help was very effective, which I really appreciated. We also debated many physics concepts and political issues. Austin Baty was one of my buddies at CERN who used to share his experience in life and academics with me.

Junior graduate students such as Michael Peters, Molly Taylor, and Gwang-Jun Kim were all very friendly and kind. I will never forget the time when Michael and I initiated the debate and insisted on our firm positions to try to convince each other. I also enjoyed working with Gwang-Jun and still remember the moments we stayed up

many days and nights fighting to advance the analysis from pre-approve to approval stage. I also would like to thank Molly for helping me look after my remaining items near my desks in the MIT office since I went to CERN and shared cat pictures with me when I was down.

Staff members of our group were very professional and resourceful. Dr. Gian Michele guided me through my analysis and gave me useful feedback for my first Quark Matter talk. I have learned a lot from him in the first two years of my PhD studies. Dr. Camellia Mironov has guided me through the CMS collaboration bureaucracy and went through the procedures to present and publish papers. Dr. George Stephans has provided me with many suggestions in MC simulations, technical questions, physics concepts, and computing knowledge. Dr. Christoph Roland has shared me with a lot of heavy-ion physics anecdotes, career development stories, detector hardware knowledge, software development skills, and analysis techniques. I would also like to thank Dr. Ivan Cali for his suggestions in windows codes programming, software development, and product design. Finally, I would like to thank the administrative assistant Anna Convertino for handling my travel and paperwork.

I would also like to thank my fellow students at the PPC group including Dr. Dylan Hsu, Dr. Brandon Allen, Dr. Sid Narayanan, Dr. Stephanie Brandt, and Jeff Krupa. They are all my good friends. We treated each other like brothers and made fun of each other. I could still remember that I visited the PPC office almost every day and shared how my day was with them. They used to say I would not be able to graduate in 6 years but I did manage to get my PhD within 5 years, which surprised them a lot. Jeff was also my buddy. We used to go out for lunch regularly and walked along the beach every semester. I missed them all very much!

Aside from that, many other professors at MIT have helped me a lot academically and professionally. I would particularly thank my academic advisor Professor Lindley Winslow. She is very kind, considerate, and helpful. She gave me very good advice on fellowship applications, courses selections, degree preparation, and postdoc tips. My graduate career has become much smoother and better planned thanks to her kind suggestions. In addition, I would like to thank Professor Iain Stewart, Richard Milner,

and Krishna Rajagopal for our occasional discussions. I would also like to thank Professor Barton Zwiebach for serving as the reader in my PhD thesis committee and provided me with some useful feedback about my defense and presentation.

Outside MIT, I have also met many senior sages who have given me a lot of wisdom. As a contributing member of sPHENIX calorimetry test beam crews at Fermilab, I met Dr. Craig Woody and worked with him during the first days in 2017. After that, he has been my mentor for the next 5 years and served as my laboratory scientist for the Electron-Ion Collider Electromagnetic Calorimeter project in my DOE SCGSR award. Moreover, he has written many letters for me and provided me with a lot of resources for career development. I am very thankful for his support. I also met Dr. Jin Huang and received many technical and analysis guidances for my sPHENIX EMCAL, heavy flavor physics simulation, and EIC EMCAL projects. I would also like to thank Dr. John Haggerty for his creative training and funny stories during my shifts at Fermilab in 2017 and 2018. At CERN, I felt very fortunate to work with Professor Mario Sitta on ALICE ITS project. He was my best friend during my stay in France and has kindly helped me move my personal items around with his car and debug my programs. Without him, my stay at CERN could be very miserable. I would also like to express my sincere gratitude to my collaborator Nuno Leonardo at LIP in Portugal. Collaborating on the B-meson analysis, he has provided me with many concrete solutions to improve the analysis, ideas to overcome the challenges from the CMS conveners, and workforce supports to complete part of the projects. He has saved this B-meson analysis many times. His efforts, along with my hard work, finally managed to make it possible and become part of my thesis. Without his support, my analysis would be stuck in many steps and may not be able to advance to the current ready for submission stage. His urgent emails and messages on Skype and Slack were truly unforgettable in my mind. I also met Ming Liu during the Fermilab test beam shifts and ALICE ITS commissioning at CERN. We worked together at that time. We will work together as a postdoc and a mentor for the next three years. Finally, I am very lucky to have a chance to have a nice lunch with Professor James Bjorken. I have really learned many stories in the great old days of

the Golden Age of particle physics and about the fun of physics with him. I also got to know his recent research interests and received some career advice from him. It was my great honor to chat with this great mind.

In addition to my mentors, colleagues, and friends, I would also like to thank my family. During the COVID-19 pandemic in the last year of my PhD studies, I stayed at home and received a lot of care from them. I was able to really focus on finishing my thesis research and became even more productive than the first 3 years of my graduate studies. I am really grateful for their unconditional love.

Finally, I would like to especially thank my significant other Zhixin Lai in this paragraph. Since I met her in February 2020, she has been my soulmate. We shared everything with each other in our life, worked together, and have learned a lot . When we experienced obstacles and failures, we cheered each other up. When we saw opportunities and success, we expressed our happiness with each other and celebrated our achievements on the phone. She has provided me with a lot of care and love in my life and helped me a lot in my career and gave me many helpful suggestions to improve the writing of my fellowship applications, job hunting, and PhD thesis. After almost a year and a half since we knew each other, the US-Canadian border finally opened. I finally had a chance to meet her in person. We sat together and prepared my thesis defense. Her company with me in my PhD thesis defense and my celebration dinner made it the most memorable day in my life. She has made me a more complete and mature person. I am indebted to her sincere love and really hope to experience more ups and downs together with her in the future.

I am sorry that I may not be able to exhaust the list of everyone here. But I really believe that I have really learned a lot from all of you. I am sincerely grateful for your friendships and mentorships on my growth as a scientist and a person.

Contents

1	Introduction	41
1.1	The Standard Model of Particle Physics	41
1.2	Quantum Chromodynamics	42
1.2.1	QCD Lagrangian	42
1.2.2	Asymptotic Freedom	43
1.2.3	Perturbative QCD	43
1.2.4	Non-perturbative QCD	45
1.2.5	QCD Factorization Theorem	45
1.2.6	Color Confinement	46
1.2.7	Hadronization	47
1.2.8	Initial State and Final Effect	47
1.3	Hot QCD	48
1.3.1	QCD in Finite Temperature	48
1.3.2	Temperature Dependence of QCD Static Potential	48
1.3.3	Color Deconfinement	49
1.3.4	QCD Phase Diagram	50
1.4	High Energy Nuclear Physics	52
1.4.1	Laboratories	53
1.4.2	Relativistic Heavy Ion Collider (RHIC)	53
1.4.3	Large Hadron Collider (LHC)	55
1.4.4	High Energy Physics Coordinates	57
1.4.5	Stages of Heavy-Ion Collisions	60

1.4.6	Global Event Observables	62
1.4.7	Glauber Model	64
1.5	Characterization of Quark-Gluon Plasma	68
1.5.1	Signatures	69
1.5.2	J/ψ and Υ suppression	69
1.5.3	Jet Quenching	71
1.5.4	Elliptic Flow	73
1.5.5	Strangeness Enhancement	79
1.5.6	Macroscopic Properties	81
1.5.7	Open Questions	82
1.6	Heavy Flavor Physics	82
1.6.1	Open Heavy Flavor Physics	82
1.6.2	Heavy Quarks	83
1.6.3	Heavy Flavor Physics in Vacuum	84
1.6.4	Heavy Quark Diffusion	90
1.6.5	Heavy Quark Energy Loss	93
1.6.6	Heavy Quark Hadronization	96
2	Review of Heavy Flavor Results	99
2.1	Elliptic Flow	99
2.2	Nuclear Modification Factor	101
2.3	Production Yield Ratio	104
2.4	Heavy Flavor Hadron-Jet Angular Correlations	108
2.5	Heavy Flavor Hadron-Hadron Correlations	110
2.6	Some Questions in Heavy Flavor Physics	111
2.7	Motivation of This Thesis	113
3	The CMS Detector	115
3.1	Overview	115
3.2	Triggers	117
3.2.1	L1 Trigger	117

3.2.2	MB Trigger	118
3.2.3	Centrality Efficiency with MB Trigger	120
3.2.4	HLT Trigger	121
3.2.5	DiMuon Trigger	122
3.3	Tracking System	123
3.3.1	Silicon Detectors	123
3.4	Muon System	124
3.5	Calorimeter System	127
3.5.1	ECAL	127
3.5.2	HCAL	128
3.5.3	HF	128
3.6	Relevant Detector Components	129
4	Reconstructed Objects	131
4.1	Events	131
4.2	Hits	133
4.3	Clusters	134
4.4	Tracks	135
4.4.1	Overview of Basic Principles	135
4.4.2	CMS Tracking Algorithm	138
4.5	Muons	144
4.6	Vertices	146
4.6.1	Primary Vertices	147
4.6.2	Secondary Vertices	148
5	Data Analysis	151
5.1	Analysis Tools	151
5.2	Analysis Strategies	152
5.2.1	Physics Goals	152
5.2.2	General Workflow	152
5.2.3	Technical Challenges	153

5.3	Analysis Samples	155
5.3.1	Dimuon Triggered Datasets	155
5.3.2	Monte Carlo Simulations Samples	156
5.3.3	\hat{p}_T Reweighting	157
5.3.4	RECO B-meson p_T Reweighting	159
5.3.5	Centrality Reweighting	159
5.3.6	PV _z Reweighting	160
5.4	Global Event Observables	161
5.4.1	Total Number of Events	162
5.4.2	Centrality Definition	163
5.4.3	$\langle N_{part} \rangle$, $\langle N_{coll} \rangle$, $\langle T_{AA} \rangle$ vs Centrality	163
5.4.4	Event Multiplicity	164
5.5	B-meson Reconstruction	165
5.5.1	Event Selections	166
5.5.2	Track Selections	167
5.5.3	Muon Selections	168
5.6	Cut Optimization	170
5.6.1	Topological Variables	171
5.6.2	Multivariate Analysis	172
5.6.3	Machine Learning Techniques	174
5.6.4	Terminologies	174
5.6.5	Boosted Decision Tree Algorithm	177
5.6.6	TMVA Training	178
5.6.7	Training Performance	179
5.6.8	Working Point Determination	181
5.6.9	Optimal Selection Performance	183
5.7	Background Studies	184
5.7.1	Overview	184
5.7.2	Individual Channel NP Background Studies	185
5.7.3	B-meson contribution of NP Background to B_s^0	186

5.7.4	B-meson Contribution of NP Background to B^+	189
5.8	Signal Extraction	191
5.8.1	Fitting Models	191
5.8.2	Raw Yield Extraction	193
5.8.3	Signal Significance Estimation	199
5.9	B-Meson Candidates MC-Data Comparison	201
5.9.1	Overview	201
5.9.2	Splot Techniques	201
5.9.3	Splot Variable Correlation Studies	203
5.9.4	Splot Results for Data-MC Comparison	203
5.10	Acceptance and Efficiency Correction	206
5.10.1	Overview	206
5.10.2	Tag & Probe Techniques	207
5.10.3	Traditional Efficiency Correction Results	209
5.10.4	Analysis Challenges	212
5.10.5	Fiducial Measurement	213
5.10.6	Finely Binned 2D Efficiency Map	214
5.10.7	Data-Drive Efficiency Correction	215
5.10.8	Results	216
5.11	Cross Section Measurement	217
5.12	Validation Tests	219
5.12.1	Mass Scraping Test	219
5.12.2	Raw Yield Closure	220
5.12.3	Efficiency Closure	222
5.12.4	<i>Splot</i> Closure on Efficiency	228
5.13	Statistical Uncertainties Determination	230
5.13.1	Data Bootstrapping	230
5.13.2	Statistical Uncertainties Interpretation	234
5.14	Systematic Uncertainties Estimation	235
5.14.1	Global Observables	236

5.14.2	Branching Ratios	236
5.14.3	Tracking Efficiency	236
5.14.4	Muon Efficiency	237
5.14.5	Selection Efficiency	239
5.14.6	Signal Extraction	246
5.14.7	Summary	252
5.15	Final Results	257
5.15.1	Overview	257
5.15.2	B_s^0 and B^+ Cross Sections	257
5.15.3	B_s^0/B^+ Ratios	261
6	Conclusions	267
6.1	pp References and Theoretical Models	267
6.2	Implications from the Experimental Data	269
6.3	Conclusions	270
6.4	Future Outlooks	272

List of Figures

1-1	The 17 elementary particles, including 6 leptons, 6 quarks, 4 gauge bosons, and the Higgs boson, and their basic properties, such as mass, electric charge, spin, in the Standard Model of Particles Physics are shown above.	42
1-2	The running of the strong coupling constant α_s in different experiments at different energy scales Q and the comparison with QCD calculations are shown above. Image from: [4]	44
1-3	The QCD factorization theorem applied to study charm hadron production in a pp collision event involving soft and hard processes is shown schematically above.	46
1-4	The fragmentation process of charms quarks hadronize into D^\pm (left) and the coalescence process of a beauty quark combining with a strange quark nearby to form a B_s^0 are shown above.	47
1-5	The QCD potential $V(r)$ from at zero and finite temperatures as a function of distance r is shown above. Here, the critical temperature $T_c = 192$ MeV. We can see that $V(r)$ saturates at a finite value at finite temperature.	49

1-6 The theoretical QCD phase diagram of different QCD matter, including hadron resonance gas, quark-gluon plasma, neutron star, and color superconductor, as a function of temperature and baryon chemical potential, is shown above. The solid line indicates the conjecture of first-order phase transition between quark-gluon plasma and hadron gas while the dashed line is a smooth crossover. Thermodynamically, a critical point must exist in the boundary of smooth crossover and first-order phase transition.	51
1-7 The reduced energy density ϵ/T^4 as a function of temperature T for different numbers of flavor scenarios from the lattice QCD calculations (data points) and the interpolation curves are shown above.	52
1-8 The view of RHIC at BNL from the sky is shown above. The actual locations of other facilities at BNL, including Linac, Booster, EBIS, NSRL, AGS, and the experiments at RHIC, such as STAR and PHENIX, are also labeled.	54
1-9 The acceleration of gold ions for RHIC is shown above.	55
1-10 The sky view of LHC at CERN is shown above. The actual locations of the experiments at the LHC: ATLAS, CMS, ALICE, and LHCb, as well as the French-Swiss border, are also displayed.	56
1-11 The schematic overview of the CERN accelerator complex with the accelerators labeled is shown above. Proton and lead ions are accelerated using these facilities and boost their energies to the TeV scale.	57
1-12 The cylindrical coordinate system in the position space (left) and the space-time diagram (right) for relativistic heavy-ion physics analysis are shown above.	58
1-13 A typical heavy-ion collision event with different stages as time evolves is shown above.	61

1-14 The space-time evolution diagram of heavy-ion collisions is shown above. It consists of five stages: initial state before the collisions, early stage of hard scattering processes, the hydrodynamic expansion of QGP, hadronization after QGP expands and cools down, and the freeze-out stage, first chemical freezeout when the particle species no longer change, and finally kinetic freezeout when the elastic scattering processes ceas.	61
1-15 The definitions of impact parameter b in heavy-ion collisions, the overlapping interaction region, and the break-up remnants of the two nuclei, called spectators, moving along the z -direction are shown above. An almond shape of the nuclear interaction region, which results in the azimuthally anisotropic emission of final state particles, is seen in heavy-ion collisions.	62
1-16 The plot showing a relationship among the number of charged particles, N_{ch} , related to the number of participants N_{part} , the differential cross section $\frac{d\sigma}{dN_{ch}}$, and the centrality, according to the Glauber Model calculations, is shown above.	65
1-17 Two gold ions collide head-on in the STAR detector. The event with reconstructed tracks of final state particles is displayed by STAR TPC shown above. Image from [61]	65
1-18 The A-B collision with the definition of the impact parameter vector \vec{b} and the distance of nucleon to the center of projectile B \vec{s} is shown above. The distance from the nucleon in B to the center of the target A is $\vec{s} - \vec{b}$ according to the vector subtraction rule. Here we assume both nuclei A and B are perfect spheres.	67
1-19 The N_{part} and N_{coll} as a function impact parameter calculated from the Glauber Model with optical approximation (lines) and from MC simulations (circles) are shown above. We can see they have an almost perfect agreement with each other.	69

1-24 The comparison of two-particle azimuthal distributions for central d + Au collisions to those seen in pp and central Au + Au collisions measured with the STAR experiment and the jet R_{AA} as a function p_T measured by the ALICE experiment at LHC (right). From the STAR results, in central Au + Au collisions, the back-to-back peak has disappeared due to the redistribution of jet energy to the slow expanding medium constituents. The jet R_{AA} from ALICE measurement is clearly below 1, suggesting that jets lose significant fractions of energy in AA collision compared to pp	74
1-25 The figure above shows the ellipsoid of the overlapping nuclear reaction region of two nuclei in heavy-ion collisions. The reaction plane, which is the x - z plane shown above, is constructed by the beam direction and the impact parameter vector. The emission of particles is azimuthally anisotropic in the x - y plane due to the almond shape geometry.	75
1-26 The elliptic flow v_2 of charged particles as a function of p_T in Au + Au collision measured by the STAR experiments at RHIC (left) and in PbPb collisions by the ALICE experiments at LHC (right) are shown above. Clearly, $v_2 > 0$ is observed in both experiments.	79
1-27 The yield ratios of ϕ/π as a function N_{part} in $p+p$, $p+Au$, and $Au+Au$ from the STAR experiment at RHIC are shown above.	80
1-28 The yield ratios of strange hadrons $K_s^0, \Lambda^+, \Xi^0, \Omega^-$ as a function of $\langle dN_{ch}/d\eta \rangle$ from the ALICE experiment at LHC are shown above.	80
1-29 The four lowest order tree-level Feynman diagrams of heavy quark pair production are shown above.	83
1-30 The schematic demonstrations of heavy quark production and hadronization in vacuum (left) and QGP (right) are shown above.	84
1-31 The charm quark (left) and beauty quark (right) differential cross section $\frac{d\sigma}{dp_T}$ as a function transverse momentum p_T at $ y < 1$ from FONLL calculations, are shown above.	85

1-32 The charm quark (left) and beauty quark (right) p_T spectra and the ratio with FONLL and GM-VFNS pQCD theoretical calculations are shown above.	86
1-33 Single-inclusive hadron production process, where fragmentation function are involved, in (a) electron-positron annihilation, (b) deep-inelastic lepton-nucleon scattering, (c) proton-proton scattering, are shown above.	86
1-34 The comparison between the Peterson fragmentation function (green) and the delta function (blue) is shown above.	88
1-35 R , the corrected yield ratio of B_s^0/B^+ , as a function of the pp collision energy \sqrt{s} (top), the f_s/f_d ratio as a function p_T (middle), and the f_s/f_d ratio as a function η_B (bottom) from the LHCb experiment, are shown above.	91
1-36 The charm quark fragmentation fraction to different charm hadrons species in e^+e^- , ep , and pp collisions are presented above. From the ALICE experiment, we can clearly see that the fragmentation fraction of D^0 has dropped by about 40% while the Λ_c^+ has enhanced by about a factor of 4. Therefore, the hadronization universality is clearly broken at the LHC energy in the charm sector.	92
1-37 The schematic demonstration of the pQCD picture: collisional energy loss (left) and radiative energy loss (right) of heavy quarks in the QGP medium.	94
1-38 The schematic demonstration of ADS/CFT picture: a quark loses energy in the QGP medium holographically due AdS/CFT drag force.	94
1-39 The schematic demonstration of a charm quark radiation is shown above. A suppression in small angles due to the dead cone effect in the QGP medium is highlighted.	95
1-40 The ladder diagram used by the TAMU model to describe heavy quark diffusion in the QGP medium is shown schematically above.	97

2-1	The NCQ scaled $D^0 v_2/n_q$ vs K_T/n_q and the comparison of light hardons measured by the STAR experiment at RHIC (left) and the CMS experiment at LHC (right) are shown above.	100
2-2	The v_2 of electrons from b-hadron decays as a function of electron p_T measured by the ALICE experiment (left) and the v_2 of muons from b-hadron decays as a function of muon v_2 measured by the ATLAS experiment (right) are shown above.	100
2-3	The R_{pA} as a function of p_T of prompt D mesons measured by the ALICE experiment is shown above.	101
2-4	The R_{pA} as a function of p_T of B^+ , B^0 , and B_s^0 mesons measured by the CMS experiment is shown above.	102
2-5	The fully reconstructed $D^0 R_{AA}$ vs p_T with the STAR experiment in 0 - 10%, 10 - 40%, and 40 - 80% centrality at RHIC and D^0 , B^+ , non-prompt J/ψ , and charged hadrons R_{AA} vs p_T at 0 - 100% centrality with the CMS experiment at LHC are shown above.	102
2-6	The R_{AA} of prompt D mesons vs p_T down to $p_T = 0$ (left) and non-prompt D mesons down to $p_T = 1$ GeV/c (right) are shown above. . .	103
2-7	The fully reconstructed D_s^+/D^0 ratios in Au + Au measured by the STAR experiment at RHIC (left) and in PbPb the ALICE experiment at LHC (right) as functions of p_T are shown above.	104
2-8	The fully reconstructed Λ_c^+/D^0 ratio in pp and heavy-ion collisions measured by the STAR experiment at RHIC (left) and the CMS experiment at LHC (right) are shown above.	105
2-9	The fully reconstructed D_s^+/D^0 (top) and Λ_c^+/D^0 ratios (bottom) as a function of event multiplicity $\langle dN_{ch}/d\eta \rangle$ within $ \eta < 0.5$ in p_T from 2 - 4, 4 - 6, 6 - 8, 8 - 12, and 12 - 24 GeV/c in pp , pPb, and PbPb collisions measured by the ALICE experiment are shown above. . . .	106
2-10	The fully reconstructed B_s^0 and B^+ R_{AA} (left) and B_s^0/B^+ R_{AA} ratio (right) as a function of p_T using the 2015 CMS pp and PbPb datasets are shown above.	107

2-11 The fully reconstructed Λ_b^0/B^+ R_{pA} ratios as a function p_T (left) and y (right) in pp , pPb, and Pbpb collisions measured by the LHCb experiment are shown above.	108
2-12 Distributions of fully reconstructed D^0 mesons in jets, as a function of the distance from the jet axis (r) for jets of $p_T^{jet} > 60$ GeV/c and $ \eta^{jet} < 1.6$ measured in pp and PbPb collisions at $\sqrt{s_{NN}} = 5.02$ TeV, for $4 < p_T^D < 20$ GeV/c and $p_T^D > 20$ GeV/c, are shown above. The jet radius is defined as $r = \sqrt{(\Delta\phi_{jD})^2 + (\Delta\eta_{jD})^2}$ where ϕ_{jD} and η_{jD} are the η and ϕ of the D^0 meson with respect to the jet axis.	109
2-13 The ALICE D-hadron angular correlation in both pp (blue) and pPb (red) collision (left) and the comparison of pp data with PYTHIA calculations (right) are shown above.	110
2-14 The 2D $\Delta\eta \times \Delta\phi$ distributions of D^0 mesons and associated hadrons in Au + Au centrality 0 - 20%, 20 - 50%, and 50 - 80% at $\sqrt{s_{NN}} = 200$ GeV measured by the STAR experiment are shown above.	111
3-1 The front view of the CMS detector at the underground collision hall is shown above.	116
3-2 The schematic view of the CMS detector with brief descriptions of all its components is shown above. Image from [157]	116
3-3 The figure above demonstrates how the CMS L1 hardware trigger function schematically.	118
3-4 In the CMS 2018 PbPb Run 326791, the ZB data (red), Empty Bunches (blue), and MB data (green) ADC distributions (left) and the HF energy according to the charges collected as a function of ADC (right) are shown above. We can see that the HF energy has conversion factor about (0.5 - 1) to the ADC.	119

3-5 In the CMS 2018 PbPb Run 326791, the ZB data (red), Empty Bunches (blue), and MB data (green) maximum ADC distributions (left) and the efficiencies of MB OR (blue) and MB AND (red) as a function ADC threshold (right) are shown above.	119
3-6 The figure above shows the total number of 20 PbPb MB events from and corresponding luminosity how the as a function Run ID from November 15 to December 2, 2018.	120
3-7 The efficiency vs centrality with $\text{ADC} > 16$ for MB OR (blue) and MB AND (green) are shown above.	121
3-8 The dimuon invariant mass spectrum $m_{\mu\mu}$ reconstructed by CMS HLT trigger in the 2018 pp dataset is shown above. We can identify the neutral vector boson resonances above.	122
3-9 The schematic view of the CMS tracking system is shown above.	123
3-10 The schematic plot explaining how a silicon tracker detects charged particles is shown above.	124
3-11 The particle flow of long-life particles, such as electrons, muons, photons, charged hadrons: π, K, p , and neutral hadrons: neutrons, in the CMS detector are shown above.	125
3-12 A visualization of Townsend Avalanche (top) and schematic plot of the CMS drift tube detecting a muon (bottom) are shown above.	126
3-13 The schematic view of the CMS forward region including HF, CASTOR, and ZDC (left) and the physical view of the HF (right) are shown above.	128
3-14 The distribution of the sum of HF energy using MB Trigger and Jet Trigger with the classification of centrality binning is shown above. As we can see, the energy of the HF increase as the collision events become more central, which is within our expectation.	129
3-15 The picture of the CASTOR (left) at the CMS underground collision hall and ZDC (right) at 140 m away from the CMS beam interacting point are shown above.	130

4-1	The photo of an Ω^- baryon reconstructed from an event: $K^- p \rightarrow K^0 K^+ \Omega^- \rightarrow \Xi^0 \pi^- \rightarrow \Lambda^0 \gamma\gamma \rightarrow \pi^- p$ taken from the bubble chamber of the group led by Nicholas Samios at BNL is shown above.	132
4-2	The schematic plot of a CMS silicon chip with pixel sensors is shown above.	133
4-3	The schematic views of a charged particle (blue line) entering the silicon pixel layer (black) at a normal angle (left) and a small tilting angle (right) with the pixels fired (red) are shown above. The left cluster has 1 hit and the right cluster has 4 hits.	134
4-4	The helix motion of a charged particle under a constant and uniform magnetic field \vec{B} pointing in the $+z$ direction (left) and the fit to 3 points to determine the center and the radius of a circle (right) are shown above.	136
4-5	A track (blue) initiated from the beam spot (orange) passing through 3 layers of pixel detectors (black) leaving 3 clusters (red) is shown on the left and the circular fit to the 3 clusters with the definition of R , L , and θ is shown on the right.	137
4-6	The transverse momentum resolution $\frac{\sigma_{p_T}}{p_T}$ of a track as a function of transverse momentum p_T is shown above.	138
4-7	The Data (blue) and MC (red) of the number of primary vertex distribution (left) and event multiplicity (right) in 2017 pp dataset are shown above. We can see that an event could have more than one vertex with more than 100 tracks, which makes it very challenging to perform tracking.	139
4-8	The schematic block diagram of CMS tracking workflow is shown above.	140
4-9	The four steps of CMS track finding workflow (left) and the schematic demonstration of each step (right) are shown above.	141
4-10	The four schematic plots demonstrating each of the four steps for track finding are shown respectfully above.	142

4-11 The schematic demonstration Kalman Filter along with Rugga-Katta propagator to improve the tracks fitting is shown above.	143
4-12 The CMS tracking efficiency (left) and fake rate (right) as a function of p_T from simulations of $t\bar{t}$ events at 13 TeV with different pileup conditions are shown above.	144
4-13 The schematic block diagram of muon reconstruction in the CMS muon system is shown above.	145
4-14 The relationship between different reconstructed muon in CMS is shown above	146
4-15 A pp collision event display of the CMS detector with reconstructed tracks (green curves) and primary vertices (yellow dots) is shown above.	148
4-16 The decay of $D^0 \rightarrow K^-\pi^+$ with the definition of the secondary vertex is shown above	149
5-1 The block diagram of the workflow with major steps for B-meson cross section measurements is shown above.	153
5-2 The strategies to fully reconstruct B_s^0 and B^+ in the selected exclusive decay modes are shown above.	154
5-3 J/ψ generated p_T distribution before (upper left) and after (upper right) \hat{p}_T reweighing, B^+ generated p_T distribution before (middle left) and after (middle right) \hat{p}_T reweighing, and B_s^0 generated Gp_T distribution before (lower left) and after (lower right) \hat{p}_T reweighing are shown above.	158
5-4 $B_s^0 p_T$ normalized raw yields obtained in PbPb MC and Data are shown above on the top left panel. The data/MC ratio and different fitting functions: Linear (Red), Quadratic(Green), Linear + Inverse (Blue), Linear + Square Root (Purple), and Linear + Log (Cyan) and their χ^2 are shown above on the top right panel. The bottom plots are the data/MC reweighed yields with different functions from the fit on the top right panel.	159

5-5	The normalized B^+ raw yield in MC (green) and Data (red) as a function RECO B^+ p_T (left) and the fourth-order polynomial fits to their ratio (right) are shown above.	160
5-6	The comparison between N_{coll} and Data vs hiBin (left), centrality distribution of MC (red) and data (blue) in PbPb collisions in the centrality interval 0-100% without N_{coll} weight (middle), and with N_{coll} weight (right) are shown above.	161
5-7	The PV_z distributions fitted with Gaussian functions in MC (left) and data (middle), and reweighed with MC to data with the ratio (right) are shown above. The PV_z distributions are well described by the Gaussian functions and the reweighing PV_z reduces the MC-data discrepancy. .	162
5-8	The nominal (black) and uncertainties band (green) hiHF vs hiBin for CMS 2018 PbPb dataset are shown above.	164
5-9	The schematic block diagram of the full reconstruction workflows for B_s^0 via the decay channel of $B_s^0 \rightarrow J/\psi\phi \rightarrow \mu^+\mu^-K^+K^-$ in the <i>Bfinder</i> is shown above.	166
5-10	The schematic block diagram of the full reconstruction workflows for B^+ via the decay channel of $B^+ \rightarrow J/\psi K^+ \rightarrow \mu^+\mu^-K^+$ in the <i>Bfinder</i> is shown above.	167
5-11	The number of reconstructed B-meson candidates per event distributions in the dimuon PbPb dataset for B_s^0 (left) and B^+ (right) are shown above. Multiple B-meson candidates are reconstructed in one event.	168
5-12	The total efficiency, including reconstruction, identification, and trigger, of a single muon in 2018 PbPb (left) and 2017 pp (right) are shown above. The black curve is the 2015 PbPb and pp 90% muon efficiency boundary while the green curve is the 2017 pp and 2018 PbPb 90% muon efficiency boundary. The green boundary is translated to numerical values in Table 5.4	169

5-13 The invariant mass distributions of fully reconstructed B_s^0 (left) and B^+ (right) after preselection are shown above.	171
5-14 The definitions of topological variables in the decay of $B_s^0 \rightarrow J/\psi\phi \rightarrow \mu^+\mu^-K^+K^-$ (left) are schematically shown above.	173
5-15 The definitions of topological variables in the decay of $B^+ \rightarrow J/\psi K^+ \rightarrow \mu^+\mu^-K^+$ are schematically shown above.	174
5-16 The performance of traditional rectangular selection with a range of x and y (left) compared to the MVA method of a curve as a function of X and Y (right) are shown above. Here, we have the total signal S = 215 and the background B = 1000.	175
5-17 The solutions to classification, regression, and clustering problems with supervised and unsupervised machine learning approaches are shown schematically above.	176
5-18 The definitions of signal (red band) and background region (blue band) in the fully reconstructed B-meson invariant mass distribution for B_s^0 (left) and B^+ (right) are shown above.	176
5-19 The schematic illustration of boosting procedures in machine learning is shown above.	178
5-20 The schematic block diagram of a binary decision tree with NTree = 4 to separate signal and background in a training sample.	179
5-21 The correlation matrices of B_s^0 (left) and B^+ (right) in data at $10 < p_T < 15$ GeV/c are shown above.	180
5-22 The B_s^0 ROC curves of CutsSA, CutsGA, BDT, MLP, and MLPBNN2 algorithms are shown above.	181
5-23 The Kolmogorov-Smirnov overtraining tests on the signal (blue) and background (red) in B_s^0 (left) and B^+ (right) at $10 < p_T < 15$ GeV/c are shown on the right. These plots suggest that they both pass the tests.	181

5-24 The significance: $Sig = \frac{S}{\sqrt{S+B}}$ as a function of BDT in B_s^0 from $10 < p_T < 15$ GeV/c are shown above. We can see that B_s^0 BDT peaks near 0.32 while B^+ peaks near 0.09.	183
5-25 The J/ψ (left) and ϕ (right) meson mass distributions after applying $BDT > 0$ for MC (top) and data (bottom) in B_s^0 analysis are shown above.	185
5-26 The B_s^0 (left) and B^+ (right) invariant mass distributions after applying optimal BDT selections from $10 < p_T < 50$ GeV/c in data are shown above.	186
5-27 Individual NP background contributions with respect to the total background components from 10 to 15 GeV (top left), 15 to 20 GeV (top right), 20 to 50 GeV (bottom left), and 10 to 50 GeV (bottom right) in B_s^0 invariant mass distributions. The non-prompt background from all channels listed above is negligible compared to the inclusive background. Also, no peak near the B_s^0 resonance is observed when the $B^0 \rightarrow J/\psi K^{*0}$ and $B_s \rightarrow J/\psi K^+ K^-$ components subtract from inclusive background.	187
5-28 Individual Non-prompt background contributions with respect to the total background components and the signal channel from 10 to 15 GeV (top left), 15 to 20 GeV (top right), 20 to 50 GeV (bottom left), and 10 to 50 GeV (bottom right). We can see that the inclusive background is small compared to the signal in our studies.	188
5-29 B^+ , B_s^0 , B^0 channels make nearly equal contribution in the signal region for all p_T bins 10 - 15 GeV/c, 15 - 20 GeV/c, 20 - 50 GeV/c, and 10 - 50 GeV/c.	189
5-30 B^+ invariant mass distributions obtained from inclusive B-meson MC production after vetoing the contribution of genuine B^+ signal candidates is shown above.	191
5-31 Peaking background contribution from $B^+ \rightarrow J/\psi \pi$ and from $K^{*0}(892)$ and $K^{*+}(892)$ resonant decay channels of B^0 and B^+ are shown above.	192

5-32 The signal B_s^0 (left) and B^+ (right) invariant mass widths as a function of p_T are shown above. We could see a rather large variation of the B-meson mass width from low to high p_T	193
5-33 The B_s^0 invariant mass distributions as well as the fits to extract the signal raw yield N_S in different p_T bins are shown above.	194
5-34 The B_s^0 invariant mass distributions as well as the fits to extract the signal raw yield N_S in centrality bins 0 - 30%, 30 - 90%, and 0 - 90% are shown above.	195
5-35 The B^+ invariant mass distributions as well as the fits to extract the signal raw yield N_S in different p_T bins are shown above.	196
5-36 The B^+ invariant mass distributions as well as the fits to extract the signal raw yield N_S in centrality bins 0 - 30%, 30 - 90%, and 0 - 90% are shown above.	197
5-37 The significance vs signal yield for p_T bins from 7 – 10, 10 – 15, 15 – 20, and 20 – 50 GeV/c for 0 - 90% centrality are shown above	199
5-38 The significance vs signal yield for centrality bins in 0 - 30%, 30% - 90% 0 - 90% for p_T from 10 - 50 GeV/c are shown above	200
5-39 The illustration of <i>Splot</i> techniques via an unbinned fit to B^+ invariant mass distribution using our fitting model to extract the <i>Splot</i> weights w_S and w_B is shown above.	202
5-40 The correlation matrices in data (left) and MC (right) of B_s^0	203
5-41 The correlation matrices in data (left) and MC (right) of B^+	204
5-42 Comparison of B_s^0 BDT distributions in data (red) and MC (green) using the <i>Splot</i> method.	204
5-43 Comparison of B^+ BDT distributions in data (red) and MC (green) using the <i>Splot</i> method.	205
5-44 The workflow to obtain L2 and L3 muons in order to apply the tag-&-probe method is shown above.	208

5-45 The B_s^0 acceptance (top), selection efficiency (middle), and efficiency (bottom) as a function of p_T (left) and event centrality (right) are shown respectfully above. We should note that there is no significant centrality dependence on the B_s^0 acceptance, which makes sense.	210
5-46 The B^+ acceptance (top), selection efficiency (middle), and efficiency (bottom) as a function of p_T (left) and event centrality (right) are shown respectfully above. We should note that there is no significant centrality dependence on the B^+ acceptance, which makes sense.	211
5-47 The finely binned 2D B-meson candidates distribution vs p_T and $ y $ for data (left) and MC (right) in centrality 0 - 90% are shown respectfully above.	213
5-48 The workflow for the efficiency correction including the data-driven tag-&-probe approach in B-meson analysis is shown above.	214
5-49 The finely binned 2D $\frac{1}{\alpha \times \epsilon}$ vs $B_s^0 p_T$ and B $ y $ in centrality 0 - 90% (top), 0 - 30% (middle), and 30% - 90% (bottom) are shown respectfully above.	215
5-50 The finely binned 2D $\frac{1}{\alpha \times \epsilon}$ vs $B^+ p_T$ and B $ y $ in centrality 0 - 90% (top), 0 - 30% (middle), and 30% - 90% (bottom) are shown respectfully above.	215
5-51 The B_s^0 efficiency correction factor $\langle \frac{1}{\alpha \times \epsilon} \rangle$ vs p_T (left) and 0 - 30 % and 30 - 90% centrality (middle) and the inclusive 0 - 90% centrality (right) are shown above.	216
5-52 The B^+ efficiency correction factor $\langle \frac{1}{\alpha \times \epsilon} \rangle$ vs p_T (left) and 0 - 30 % and 30 - 90% centrality (middle) and the inclusive 0 - 90% centrality (right) are shown above.	217
5-53 The B_s^0 pull distributions and the Gaussian fits for 0 - 90% from p_T 7 - 10, 10 - 15, 15 - 20, 20 - 50 GeV/c are shown respectfully above.	221
5-54 The B_s^0 pull distributions and the Gaussian fits in 0 - 30%, 30 - 90%, and 0 - 90% event centrality are shown respectfully above.	222
5-55 The B^+ pull distributions and the Gaussian fits for 0 - 90% at p_T 7 - 10, 10 - 15, 15 - 20, 20 - 50 GeV/c are shown respectfully above.	223

5-56 The B^+ pull distributions and the Gaussian fits for 0 - 30%, 30 - 90%, and 0 - 90% event centrality are shown respectfully above.	224
5-57 The percent deviation distributions of $B_s^0 \langle \frac{1}{\alpha \times \epsilon} \rangle$ to RECO/GEN for the data-like randomly constructed MC samples in centrality 0 - 90% from 7 - 10, 10 - 15, 15 - 20, and 20 - 50 GeV/c as well as 0 - 90%, 0 - 30%, and 30 - 90% event centrality from 10 - 50 GeV/c are shown respectfully above.	226
5-58 The percent deviation distributions of $B^+ \langle \frac{1}{\alpha \times \epsilon} \rangle$ to RECO/GEN for the data-like randomly constructed MC samples in centrality 0 - 90% from 7 - 10, 10 - 15, 15 - 20, and 20 - 50 GeV/c as well as 0 - 90%, 0 - 30%, and 30 - 90% event centrality from 10 - 50 GeV/c are shown respectfully above.	227
5-59 The sPlot weight distributions for B_s^0 (left) and B^+ (right) candidates are shown above.	229
5-60 The B_s^0 corrected yield distributions of the 1000 data-like randomly resampled datasets for centrality in 0 - 90% in the p_T range of 7 - 10, 10 - 15, 15 - 20, and 20 - 50 GeV/c as well as 0 - 90%, 0 - 30%, and 30 - 90% in the p_T range of 10 - 50 GeV/c are shown above.	232
5-61 The B^+ corrected yield distributions of the 1000 data-like randomly resampled datasets for centrality in 0 - 90% in the p_T range of 7 - 10, 10 - 15, 15 - 20, and 20 - 50 GeV/c as well as 0 - 90%, 0 - 30%, and 30 - 90% in the p_T range of 10 - 50 GeV/c are shown above.	233
5-62 The schematic block diagrams demonstrating the calculations of the uncertainties on tag-&-probe scale factors (left) and the asymmetric systematic uncertainties due to muon efficiency on the efficiency correction factor (right) are shown above.	237
5-63 The distributions of $B_s^0 \langle \frac{1}{\alpha \times \epsilon} \rangle$ for centrality in 0 - 90% in the p_T range of 7 - 10, 10 - 15, 15 - 20, and 20 - 50 GeV/c as well as 0 - 90%, 0 - 30%, and 30 - 90% in the p_T range of 10 - 50 GeV/c are shown above. The red dash lines are our nominal values for efficiency correction. . .	242

5-64 The distributions of $B^+ \langle \frac{1}{\alpha \times \epsilon} \rangle$ for centrality in 0 - 90% in the p_T range of 7 - 10, 10 - 15, 15 - 20, and 20 - 50 GeV/c as well as 0 - 90%, 0 - 30%, and 30 - 90% in the p_T range of 10 - 50 GeV/c are shown above. The red dash lines are our nominal values for efficiency correction.	243
5-65 The fits of B_s^0 invariant mass distributions for p_T from 20 - 50 GeV/c and centrality from 0 - 90% are shown above. The signal PDFs are gaussian (with widths and relative proportions fixed from MC), double gaussian with all the parameters fixed (including the mean), increased width ($a=1.1$), and decreased width ($a=0.9$) from top left to bottom right.	248
5-66 The fit of B_s^0 invariant mass distributions for p_T from 20 - 50 GeV/c and centrality from 0 - 90% are shown above. The signal PDFs are gaussian (with widths and relative proportions fixed from MC), double gaussian with all the parameters fixed (including the mean), increased width ($a=1.1$), and decreased width ($a=0.9$) from top left to bottom right.	249
5-67 The Invariant mass fits to B_s^0 candidates for $B_s^0 p_T$ from 20 - 50 GeV/c and centrality from 0 to 90% in 5.02 TeV PbPb. The background PDFs from left to right are first-, second-, and third-order polynomials.	251
5-68 The Invariant mass fits to B^+ candidates for $B^+ p_T$ from 20 - 50 GeV/c and centrality from 0 to 90% in 5.02 TeV PbPb. The background PDFs from left to right are first-, second-, and third-order polynomials.	251
5-69 The summary of B_s^0 systematic uncertainties plotted as a function of p_T (left), centrality in 0 - 30% and 30 - 90% (middle), and the inclusive centrality bin 0 - 90% (right) are shown above.	256
5-70 The summary of B^+ systematic uncertainties plotted as a function of p_T (left), centrality in 0 - 30% and 30 - 90% (middle), and the inclusive centrality bin 0 - 90% (right) are shown above.	256

5-71 The measurement of B_s^0 and B^+ p_T differential cross section $\frac{1}{T_{AA}} \frac{dN}{dp_T}$ as a function of B-meson p_T within 0 - 90% centrality is shown above. It should be pointed out that the cross section results are plotted in the unit of pb c/GeV since T_{AA} is in the unit of pb $^{-1}$ while the p_T is in the unit of GeV/c. The open markers from 7 - 10 GeV/c stand for the fiducial measurements in the B-meson rapidity of $1.5 < y < 2.4$	258
5-72 The measurement of B_s^0 and B^+ cross section $\frac{1}{T_{AA}} N$ as a function of $\langle N_{part} \rangle$ in different PbPb collision centralities within B-meson p_T from 10 - 50 GeV/c is shown above.	260
5-73 The measurement of B_s^0/B^+ as a function of p_T is shown above. The open markers from 7 - 10 GeV/c stand for the fiducial measurements in B-meson rapidity of $1.5 < y < 2.4$	262
5-74 The measurement of B_s^0/B^+ as a function of p_T is shown above.	263
5-75 The comparison of B_s^0/B^+ as a function of p_T between the CMS 2018 PbPb datasets in centrality 0 - 90% (red) and the 2015 PbPb dataset in centrality 0 - 100% (green) is shown above.	264
6-1 The fully reconstructed B_s^0/B^+ ratio (right) as a function of p_T (left) and PbPb event centrality (right) using the 2018 CMS dimuon PbPb dataset are shown above. Both plots include the ATLAS (magenta) and LHCb (blue) 7 TeV pp references. The TAMU model (orange) has only p_T dependent predictions shown on the left figure while the Cao, Sun, Ko model (green) has both p_T and centrality predictions plotted on both figures.	268
6-2 The fully reconstructed B^+ via the decay channel of $B^+ \rightarrow J/\psi K^+ \rightarrow \mu^+ \mu^- K^+$ in the p_T range of 0 - 1 GeV/c using the full CMS 2017 pp dataset is shown above. The statistical significance is about 6. The selection is optimized with the BDT algorithm using a subset of topological variables in PbPb B^+ studies.	272

List of Tables

5.1	List of PbPb HLT datasets and triggers with the corresponding integrated luminosities used in the analysis.	155
5.2	Summary table of the total number of MB events and their uncertainties in different centralities	163
5.3	A summary table of the total number of MB events vs centrality is shown below. The uncertainties are represented in terms of percentage in the parenthesis.	164
5.4	Summary table of the muon acceptance selection for muon: $ \eta^\mu $ as a function p_T^μ	169
5.5	The numerical values of the comparison between the traditional rectangular selections and MVA.	173
5.6	The summary table of signal and background estimation of B_s^0 in each p_T and centrality bin in the analysis.	182
5.7	The summary of optimal BDT selection maximizing the B_s^0 statistical significance.	183
5.8	The summary of optimal BDT selection maximizing the B^+ statistical significance.	184
5.9	The summary table of B_s^0 fits results of Gaussian mean, signal raw yield, and background raw yield as well as their uncertainties.	198
5.10	The summary table of B^+ fits results of Gaussian mean, signal raw yield, and background raw yield as well as their uncertainties.	198
5.11	The summary table of B_s^0 likelihood significance for each p_T and centrality bin.	201

5.12 The summary table of B_s^0 efficiency correction factor $\langle \frac{1}{\alpha \times \epsilon} \rangle$ for each p_T and centrality bin.	217
5.13 The summary table of B^+ efficiency correction factor $\frac{1}{\langle \alpha \times \epsilon \rangle}$ for each p_T and centrality bin.	218
5.14 The summary table of BDT vs mass dependence systematics on the background yields from the fits in different p_T and centrality bins are shown below.	220
5.15 The results of B_s^0 efficiency factors $\langle \frac{1}{\alpha \times \epsilon} \rangle$ and $\frac{1}{\langle \alpha \times \epsilon \rangle}$ and their percent deviations are shown above.	225
5.16 The results of B^+ efficiency factors $\langle \frac{1}{\alpha \times \epsilon} \rangle$ and $\frac{1}{\langle \alpha \times \epsilon \rangle}$ and their percent deviations are shown above.	225
5.17 The percent deviation of B_s^0 efficiency factors from the expected value in the statistics similar to the data analysis is shown above.	228
5.18 The percent deviation of B^+ efficiency factors from the expected value in the statistics similar to the data analysis is shown above.	228
5.19 The B_s^0 <i>Splot</i> weighted efficiency correct factor $\langle \frac{1}{\alpha \times \epsilon} \rangle'$, nominal unweighed $\langle \frac{1}{\alpha \times \epsilon} \rangle$, and their percent deviation for each p_T and centrality bin are summarized below.	229
5.20 The B^+ <i>Splot</i> weighted efficiency correct factor $\langle \frac{1}{\alpha \times \epsilon} \rangle'$, nominal unweighed $\langle \frac{1}{\alpha \times \epsilon} \rangle$, and their percent deviation for each p_T and centrality bin are summarized below.	230
5.21 The B_s^0 RMS/Mean and their asymmetric up and down statistical uncertainties of the corrected yield distributions are summarized below.	235
5.22 The B^+ RMS/Mean and their asymmetric up and down statistical uncertainties of the corrected yield distributions are summarized below.	235
5.23 The B_s^0 systematic uncertainties due to muon efficiency for each p_T and centrality bin are summarized below.	238
5.24 The B^+ systematic uncertainties due to muon efficiency for each p_T and centrality bin are summarized below.	238

5.25 The B_s^0 systematic uncertainties due to data-MC discrepancy for each p_T and centrality bin are summarized below.	240
5.26 The B^+ systematic uncertainties due to data-MC discrepancy for each p_T and centrality bin are summarized below.	240
5.27 The B_s^0 systematic uncertainties due to limited MC sample statistics for each p_T and centrality bin are summarized below.	244
5.28 The B^+ systematic uncertainties due to MC sample statistics for each p_T and centrality bin are summarized below.	244
5.29 The B_s^0 systematic uncertainties due to unknown B-meson p_T shape in PbPb collisions for each p_T and centrality bin are summarized below.	245
5.30 The B^+ systematic uncertainties due to unknown B-meson p_T shape in PbPb collisions for each p_T and centrality bin are summarized below.	246
5.31 The B_s^0 selection efficiency uncertainties are summarized below.	246
5.32 The B^+ selection efficiency uncertainties are summarized below.	247
5.33 The B_s^0 systematic uncertainties due to signal PDF variation in p_T and centrality bin are summarized below.	250
5.34 The B^+ systematic uncertainties due to signal PDF variation in p_T and centrality bin are summarized below.	250
5.35 The B_s^0 systematic uncertainties due to background PDF variation in p_T and centrality bin are summarized below.	252
5.36 The B^+ systematic uncertainties due to background PDF variation in p_T and centrality bin are summarized below.	252
5.37 The B_s^0 signal extraction systematic uncertainties due to PDF variation in p_T and centrality bin are summarized below.	253
5.38 The B^+ signal extraction systematic uncertainties due to PDF variation in p_T and centrality bin are summarized below.	253
5.39 Summary of systematic uncertainties in each B_s^0 p_T bin. All the values are reported in percentage.	253
5.40 Summary of systematic uncertainties in each B_s^0 centrality bin. All the values are reported in percentage.	254

5.41	Summary of systematic uncertainties in each B^+ p_T bin. All the values are reported in percentage.	254
5.42	Summary of systematic uncertainties in each B^+ centrality bin. All the values are reported in percentage.	255
5.43	The numerical values and uncertainties of the B_s^0 cross section as a function of p_T are summarized below.	257
5.44	The numerical values and uncertainties of the B^+ cross section as a function of p_T are summarized below.	259
5.45	The numerical values and uncertainties of B_s^0 cross section as a function of centrality are summarized below.	259
5.46	The numerical values and uncertainties of B^+ cross section as a func- tion of centrality are summarized below.	259
5.47	The numerical values and uncertainties of B_s^0/B^+ cross section ratio as a function of p_T are summarized below.	261
5.48	The numerical values and uncertainties of B_s^0/B^+ cross section ratio as a function of centrality are summarized below.	263

Chapter 1

Introduction

1.1 The Standard Model of Particle Physics

There are four known fundamental forces in nature: gravitational force, electromagnetic force, strong force, and weak force. The gravitation force describes the interaction between two massive objects. The electromagnetic force describes the interaction between electrically charged objects. The strong force describes the interaction between nucleons. The weak force describes the radioactive decay of particles. The Standard Model (SM) of Particle Physics, first proposed and named by physicist Steven Weinberg in the 1960s [1], is based on theoretical frame of relativistic quantum field theory with a gauge symmetry of $SU(3) \times SU(2) \times U(1)$ [2]. It unifies the electromagnetic and weak interactions and includes the strong interaction into a theory and describes all particles participating in these interactions. The ingredients of the standard model are leptons, quarks, gauge bosons, and the Higgs boson shown in Figure 1-1.

There are 19 parameters in the Standard Model: 6 quark masses, 3 lepton masses, 3 coupling strengths, 4 angles in the Cabibbo-Kobayashi-Maskawa Matrix, Higgs mass, vacuum expectation value, and QCD vacuum angle. These parameters are determined from the experiments. Physicists perform calculations based on the Standard Model and predict the cross sections of different processes in high-energy physics experiments. Since it is proposed in the 1970s, the Standard Model has been tested

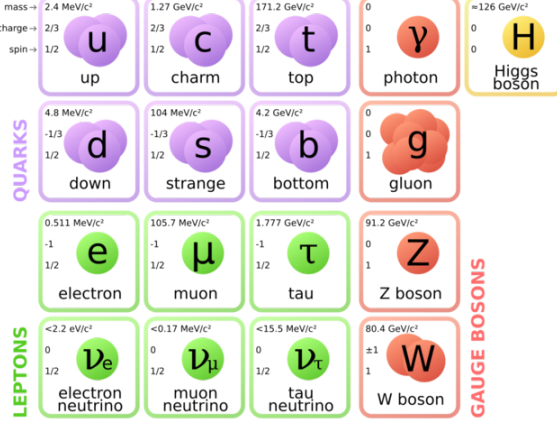


Figure 1-1: The 17 elementary particles, including 6 leptons, 6 quarks, 4 gauge bosons, and the Higgs boson, and their basic properties, such as mass, electric charge, spin, in the Standard Model of Particles Physics are shown above.

extensively in countless high-energy physics experiments. Its prediction holds for all of them with very few exceptions. The Standard Model consists of two sectors: the Electroweak theory (EW) and Quantum Chromodynamics (QCD). The Lagrangian of the Standard Model can be written as the sum of EW and QCD: $\mathcal{L}_{SM} = \mathcal{L}_{EW} + \mathcal{L}_{QCD}$

1.2 Quantum Chromodynamics

1.2.1 QCD Lagrangian

QCD, a non-abelian gauge theory with $SU(3)$ symmetry, is the theory for the strong interaction between quarks and gluons. The QCD Lagrangian is shown as follows:

$$\mathcal{L}_{QCD} = \bar{\Psi}^i i(\not{D})_{ij} \Psi^j - m \bar{\Psi}^i \Psi_i - \frac{1}{16\pi^2} G_a^{\mu\nu} G_{\mu\nu}^a \quad (1.1)$$

Where

$$\not{D} = \gamma^\mu \partial_\mu - ig_s \frac{\lambda}{2} \gamma^\mu A_\mu \quad (1.2)$$

$$G_a^{\mu\nu} = \partial^\mu A_a^\nu - \partial_\nu A_a^\mu + g_s f_{abc} A_b^\mu A_c^\nu \quad (1.3)$$

Here, λ are the Gell-Mann Matrices. f_{abc} is the structure of constant of $SU(3)$. A^μ is the eight gluon field. g_s is the strong coupling constant. The color indices i and j run from 1 to 3, which stands for 3 colors: red, blue, and green. The gluon field indices a , b , and c run from 1 to 8, standing for the 8 gluon state (Gluon octet as the combination of 3 colors and 3 anticolors: $3 \times \bar{3} = 1 \oplus 8$) living in the adjoint representation of $SU(3)$ of color.

1.2.2 Asymptotic Freedom

The running of the strong coupling constant $\alpha_s = \frac{g_s^2}{4\pi}$ according to the 1-loop calculations in the renormalization theory [3] is shown as follows

$$\alpha_s(Q^2) = \frac{12\pi}{(11N_c - 2N_f) \ln(\frac{Q^2}{\Lambda_{QCD}^2})} \quad (1.4)$$

We can see that as the energy scale increases, the coupling strength of the strong interaction decreases. This is in contrast to QED where the electromagnetic coupling strength increases as the energy scale increases. In the ultra-violate limit $Q^2 \rightarrow \infty$ and $\alpha_s \rightarrow 0$, quarks and gluons behave like free particles. This feature in QCD is called Asymptotic Freedom [5]. Meanwhile, in the infrared limit, the strong coupling constant increases. Near the $\Lambda_{QCD} \simeq 100$ MeV, the strong coupling is greater than 1, and the perturbative expansion of QCD breaks down. Experimentally, physicists measure the strong coupling constant at different energy scales from different experiments at different colliders. Figure 1-2 [4] shows the running of the strong coupling constant in experiments and comparison with the theoretical calculations

An excellent agreement between theoretical predictions and experimental results of the strong coupling constant is observed in Figure 1-2.

1.2.3 Perturbative QCD

So far, there is not any closed-form expression yet for the partition function $Z[J(x)]$ of the Standard Model Lagrangian under the Quantum Field Theory framework.

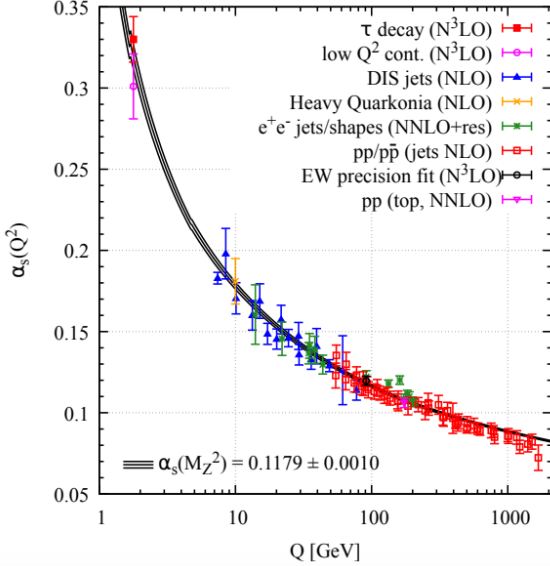


Figure 1-2: The running of the strong coupling constant α_s in different experiments at different energy scales Q and the comparison with QCD calculations are shown above. Image from: [4]

$$Z[J(x)] = \int \mathcal{D}[\phi(x)] e^{iS + \int d^4x J(x)\phi(x)} \quad (1.5)$$

Therefore, physicists develop perturbation theory in Quantum Field Theory and apply it to the Standard Model. Physicists perform asymptotic expansions to obtain power series of the coupling constants and approximately calculate the expectation values of the observables to predict experimental results.

Perturbation theory is applicable to QCD in high energy and hard scattering processes since the coupling constant is much less than 1. Feynman rules and diagrams are applied to calculate the matrix element and predict the cross section of hard parton-parton scattering. Perturbative QCD (pQCD) calculations have been extensively tested with various experiments such as electron-positron annihilations, deep inelastic electron-proton scatterings, and high-energy proton-proton collisions.

1.2.4 Non-perturbative QCD

For soft scattering processes at low energy, the strong coupling constant is greater than 1. Perturbation theory of QCD breaks down. Many low-energy QCD processes such as hadronization and hadron-hadron interactions are non-perturbative. Historically, physicists developed the lattice gauge theory where the spacetime is discretized into lattices with finite sizes to evaluate the path integrals in the partition function $Z[J(x)]$. Lattice QCD can be applied to calculate the mass of the proton [6]. Aside from lattice gauge theories, effective theories are also developed to study non-perturbative QCD. For example, Chiral Perturbation Theory, where a low-energy effective Lagrangian in the degree of freedom of hadrons is constructed by exploiting the approximate chiral symmetry while preserving other symmetries such as parity and charge conjugation, has achieved some success to study pion-nucleon scattering [7]. Non-perturbative QCD has achieved many successes in hadronic physics. Currently, some novel developments applying non-perturbative QCD to understand the nuclear structure and nucleon spin structure are being carried in the community. For instance, Chiral Perturbation Theory has been applied to study light nuclei structure such as 3_3Li and $^{10}_5B$ [8] and Lattice is employed to investigate nucleon spin structure [9].

1.2.5 QCD Factorization Theorem

The QCD factorization theorem states that in events with hadrons as incoming particle involving both hard and soft QCD processes, hard and soft processes are mathematically factorized in the cross section computation shown schematically below [10]:

$$\sigma = PDF \otimes Diagrams \otimes FF \quad (1.6)$$

The hard processes are encoded in the factor of partonic cross sections while the soft processes are measured in experiments. Physicists employ parton distribution function (PDF), defined as the probability of finding a particle with a certain longitudinal momentum fraction x at resolution scale of μ^2 , to describe the initial

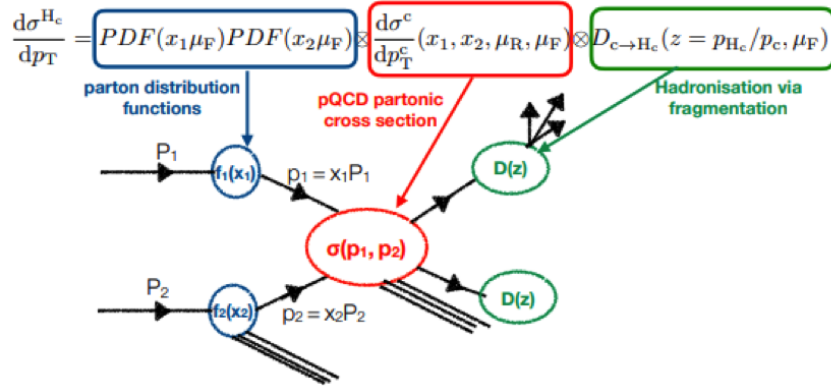


Figure 1-3: The QCD factorization theorem applied to study charm hadron production in a pp collision event involving soft and hard processes is shown schematically above.

kinematic of partons inside hadrons [11] and fragmentation function (FF), defined as the probability of a parton turning into a hadron $D_i^h(z)$ for a given energy fraction of the parton z at resolution scale of μ^2 , to describe the hadronization process of partons [12].

In addition to PDF, we could also define nuclear PDF (nPDF) for [13] to describe the parton kinematics inside the nucleus. nPDF could be understood as the PDF of nucleons modified by the nuclear environment. Both parton distribution function and fragmentation function are extracted in experiments.

Physicists apply the QCD factorization theorem to perform pQCD calculations and compare them with hadron spectra in electron-positron (e^+e^-), electron-proton (ep), and proton-proton (pp) collisions.

1.2.6 Color Confinement

Another feature of QCD as a non-abelian gauge theory is color confinement. The strong force carrier gluon itself is also color charged. Color charged partons, namely quarks and gluons, are never detected in isolation. In experiments, only color-neutral hadrons are detected. Currently, the analytic explanation of color confinement is still not yet rigorously proven. The theoretical explanation of color confinement in QCD

remains one of the unsolved problems in physics.

1.2.7 Hadronization

The formation process of hadrons from partons is called hadronization. Because in experiments we can only measure final state hadrons, in order to study the interactions and dynamics of quarks and gluons during the partonic stage from hadron spectra, we also need to understand hadronization mechanisms. However, hadronization is in general non-perturbative and cannot yet be described by first principle QCD calculations. Therefore, physicists make phenomenological models such as the Statistical Hadronization Model [14], Lund String Model [15], Cluster Hadronization Model [16], Quark Coalescence Model [17] to study hadronization. Figure 1-4 schematically shows the hadronization of heavy quarks via fragmentation [18] and recombination mechanism [19].

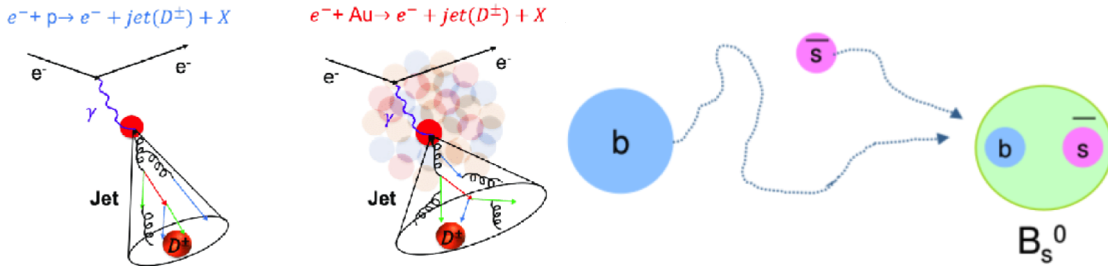


Figure 1-4: The fragmentation process of charms quarks hadronize into D^\pm (left) and the coalescence process of a beauty quark combining with a strange quark nearby to form a B_s^0 are shown above.

1.2.8 Initial State and Final Effect

In high-energy proton-nucleus (pA) collisions, protons scatter off nucleons inside nuclei. Assuming QCD factorization still holds, nPDF could be applied to calculate the cross section of particle production. The initial state effects of nuclei including event-by-event geometry fluctuations due to nuclear dynamics [20], nuclear shadowing effect [21], EMC effect [22] will modify the PDFs of nucleons in nuclei compared

to PDFs of nucleons in vacuum.

In the final state, the struck parton will lose energy from the interactions with the nuclear fragments, which modifies the final state hadron spectra. Because the parton-hadron interaction is generally non-perturbative, to retain the formula of QCD factorization theorem, the parton FF is also modified [23]. These initial stage and final stage effects in pA collision are called cold nuclear matter effects.

1.3 Hot QCD

1.3.1 QCD in Finite Temperature

In a system of dense and energetic quarks and gluons confined in a given size of volume, they scatter with each other and exchange momenta via the strong interaction. Many-body dynamics between quarks and gluons becomes relevant. In the limit of a large number of quarks and gluons, after a sufficiently long period of time, the system eventually converges to a thermal equilibrium state via strong interaction [26–28] regardless of its initial states. Therefore, a description based on thermodynamics can be formulated to study many-body QCD systems [29]. We call the thermalized many-body system of quarks and gluons to be QCD matter. Therefore, a thermodynamic variable temperature (T) can be introduced to characterize these many-body QCD systems. The study of many-body QCD in finite temperature is called hot QCD.

1.3.2 Temperature Dependence of QCD Static Potential

If we consider two color charged quarks in the limit of infinite mass and are essentially at rest in the lab frame, we can define a QCD static potential between these two quarks due to the strong interaction. In vacuum, such potential is called “Cornell Potential” [30]. The potential as a function of the distance between two quarks is shown as follows:

$$V(r) = -\frac{\alpha_{eff}}{r} + \sigma r \quad (1.7)$$

Here, α_{eff} is the effective strong coupling between the two quarks and $\sigma \simeq 0.184$ GeV/c is the string coupling constant [31].

Now if we consider a thermalized system in finite temperature T , the potential becomes:

$$V(r) = -\frac{\alpha_{eff}}{r} e^{-m_D r} + \frac{\sigma}{m_D} (1 - e^{-m_D r}) \quad (1.8)$$

Here, $m_D \sim g_s T$ is the Debye mass due to the Debye color screening effect [32], which essentially modifies the gluon propagator by inserting a finite mass term: $-i \frac{g^{\mu\nu}}{q^2} \rightarrow -i \frac{g^{\mu\nu}}{q^2 - m_D^2}$. We have observed that as $V(\infty) = \frac{\sigma}{g_s T}$, which is finite for $T > 0$. In fact, Equation (2) reduces to the Cornell potential when $T = 0$. The QCD static potential is shown below in Figure 1-5 [33]

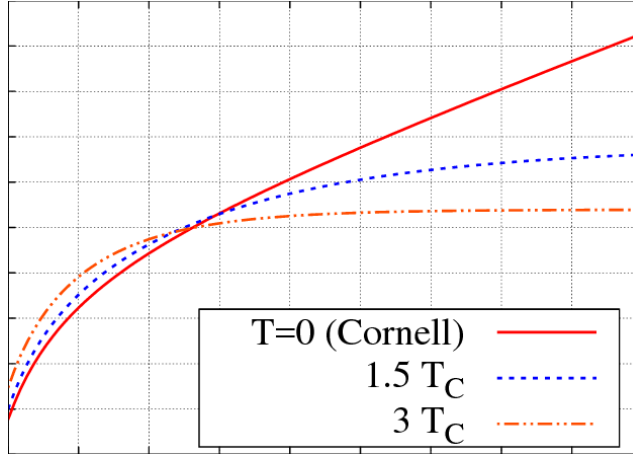


Figure 1-5: The QCD potential $V(r)$ from at zero and finite temperatures as a function of distance r is shown above. Here, the critical temperature $T_c = 192$ MeV. We can see that $V(r)$ saturates at a finite value at finite temperature.

1.3.3 Color Deconfinement

As mentioned in the sections above, at finite temperature, the QCD static potential is screened and the color degree of freedom becomes relevant in the system. As

the temperature of the system increases, quarks and gluons confined in color-neutral hadrons will have more available phase space and start to deconfine [34]. At some critical temperature T_c , hadrons will melt and form a new state of color deconfined QCD matter, which is called Quark-Gluon Plasma (QGP). A typical temperature of QGP is in the order of a few hundred MeV or about 10^{12} K, which is about hundreds of thousands times hotter than the core of the Sun. It is believed that QGP existed in the early universe several microseconds after the Big Bang [35]. Cosmologically, the research on QGP will help us envision the quark epoch and study the quark-hadron phase transition to understand the early history of the universe [36].

1.3.4 QCD Phase Diagram

Our everyday matter such as metal, water, wood, glass, and plastic, which is formed by electromagnetic interaction, could be described macroscopically by equations of states that are parameterized by thermodynamic variables. Similarly, QCD matter formed via the strong interaction between many quarks and gluons can also be described by the equations of states parameterized by thermodynamical variables, for instance, temperature (T) and baryon chemical potential (μ_B). Like our everyday matter, which has gas, liquid, and solid phases at different pressure and temperature, QCD matter also has different phases at different temperatures and baryon chemical potentials. QCD matter can be characterized by QCD phase diagrams. Figure 1-7 shows the QCD phase diagram at different temperatures and baryon chemical potentials:

Considering a system of free up and down quarks, antiquarks, and gluons in temperature T and baryon chemical potential μ_B , according to the MIT Bag Model [37], its equation of state is given by

$$\epsilon(T, \mu_B) = \frac{37\pi^2}{30}T^4 + \frac{\mu_B^2}{3}T^2 + \frac{\mu_B^4}{54\pi^2} - \mathcal{B} \quad (1.9)$$

Here p is the pressure and \mathcal{B} is the bag constant, which can be understood as the pressure of the vacuum on the quarks and gluons pointing inward to make them form

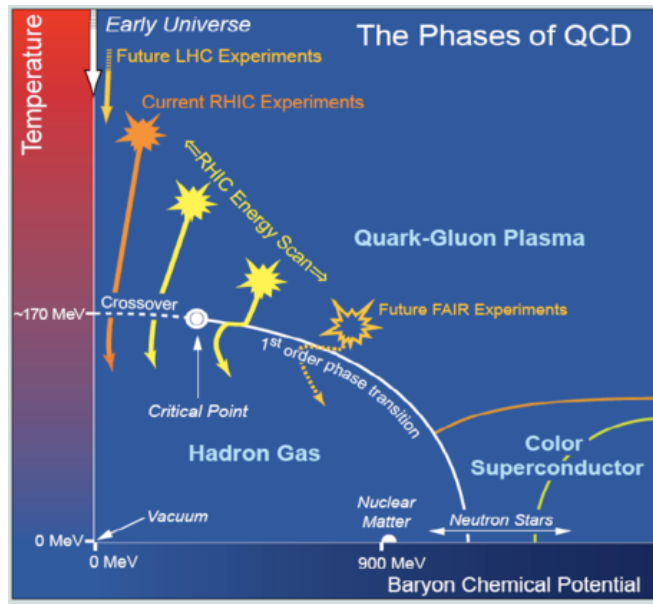


Figure 1-6: The theoretical QCD phase diagram of different QCD matter, including hadron resonance gas, quark-gluon plasma, neutron star, and color superconductor, as a function of temperature and baryon chemical potential, is shown above. The solid line indicates the conjecture of first-order phase transition between quark-gluon plasma and hadron gas while the dashed line is a smooth crossover. Thermodynamically, a critical point must exist in the boundary of smooth crossover and first-order phase transition.

hadrons with finite volume.

In a system of interacting quarks and gluons at $\mu_B = 0$, based on lattice QCD calculations [38], the reduced energy density ϵ/T^4 as a function of the temperature T is shown below

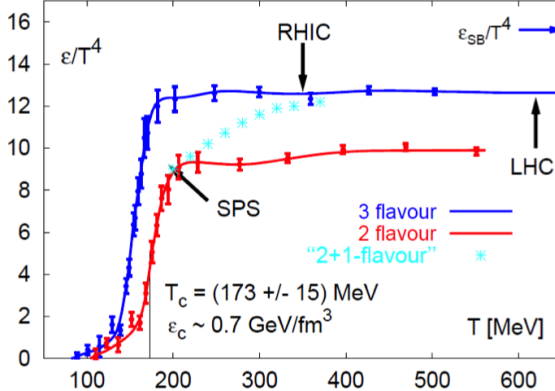


Figure 1-7: The reduced energy density ϵ/T^4 as a function of temperature T for different numbers of flavor scenarios from the lattice QCD calculations (data points) and the interpolation curves are shown above.

A steep increase of the ϵ/T^4 near the critical temperature at around $T_c = 173$ MeV is observed, which signals the transition from hadron gas to the QGP [39]. Experimentally, the critical point is estimated to be around $T_c = 175^{+1}_{-7}$ MeV near $\mu_B = (22 \pm 4.5)$ MeV [40] .

1.4 High Energy Nuclear Physics

Nuclear Physics is the study of atomic nuclei and their constituents and interactions. The typical energy scales of nuclear physics range from MeV to GeV. High Energy Nuclear Physics is a subfield of Nuclear Physics at an energy scale of GeV. Its main goal is to understand the physics of QCD matter from various approaches such as collider experiments, astrophysical observations, physics simulations, and theoretical modelings. In this thesis, I will focus on the research of QGP from the experimental approach using high-energy heavy-ion colliders.

1.4.1 Laboratories

In laboratories, high-energy nuclear physicists accelerate and collide heavy ions ($A > 56$) at the center of mass high energy per nucleon at greater than 1 GeV to create extremely hot and dense conditions and study QGP. Relativistic heavy-ion collision is also known as “The Little Bang” compared to “The Big Bang” in cosmology [41]. Historically, many colliders, such as the Alternating Gradient Synchrotron (AGS) at Brookhaven National Laboratory (BNL), in Upton, Long Island, New York, Super Proton Synchrotron (SPS) at European Center for Nuclear Research (CERN) in Meyrin, Switzerland, and GSI at Helmholtz Centre for Heavy Ion Research with both proton-proton and relativistic heavy-ion collision capabilities, have been built and established high-energy nuclear physics research programs. Today, two active colliders facilities, the Relativistic Heavy Ion Collider (RHIC) at BNL and the Large Hadron Collider (LHC) at CERN, are running at a wide range of energies with various nuclei species and different impact parameters. In the future, another collider, called Facility for Antiproton and Ion Research (FAIR) running at relatively low energies, is being constructed at Darmstadt, Germany to map the location of the critical point in the QCD Phase Diagram.

In addition to collider facilities, the QGP might also be studied from astrophysical observations. For instance, strange stars, a quark star made of strange quark matter, may come from stable strangelets according to Bodmer–Witten conjecture [42] or exist in the core of neutron stars under extreme pressure and temperature. It is believed that there are several potential strange stars candidates based on the telescope observations and gamma-ray burst analyses [43–45].

1.4.2 Relativistic Heavy Ion Collider (RHIC)

Located at BNL in Upton, Long Island, New York, the United States of America, RHIC is one of the major high-energy accelerator facilities and currently the highest energy collider in America. It is a circular collider with a circumference of 3.843 kilometers and can provide proton energy up to 500 GeV and gold ion energy up to 200

GeV [46]. It was built in 2000 in order to search for a strongly interacting hot and dense state of nuclear matter created under ultra-relativistic heavy-ion collisions, currently known as QGP, with hints from the measurements at AGS and SPS. Moreover, RHIC provides physicists with a wide range of energies and a variety of ion species from proton to deuteron and copper to uranium to create systems of different sizes at different temperatures and baryon densities. In addition, taking the advantage of its highly polarized beam with high luminosity, RHIC also has great machine capabilities for cold QCD physics. Figure 1-8 below shows a sky view of RHIC at BNL:

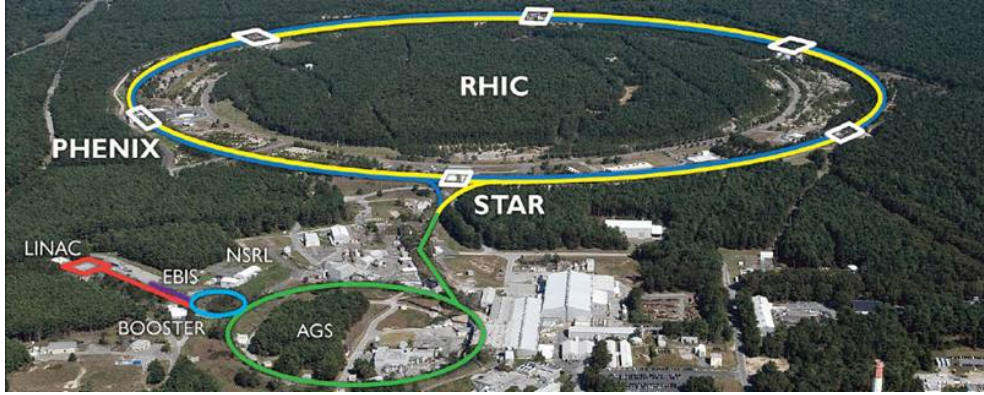


Figure 1-8: The view of RHIC at BNL from the sky is shown above. The actual locations of other facilities at BNL, including Linac, Booster, EBIS, NSRL, AGS, and the experiments at RHIC, such as STAR and PHENIX, are also labeled.

Here is how RHIC accelerates charged particle beams to the energy scale of GeV per nucleon through multiple electron stripping and acceleration stages. For instance, if we consider the acceleration of a typical ion source gold ($^{197}_{79} \text{Au}$) ion [47], we first use a cesium sputter ion source operated in the pulsed beam mode and point it to the gold metal to produce the Au^- ion [48]. Then, the Au^- will undergo a series of electron stripping processes to reach the Au^{79+} ion [49]. First, 13 electrons are stripped by the carbon foil in the Terminal Stripping (S1) after the acceleration of the tandem Van der Graaf generator to turn Au^- into Au^{12+} . Then, the Au^{12+} ion will go through the Object Foil (S2) at the second stripping stage and becomes Au^{31+} . Next, the Au^{31+} will go through the third stripping station BTA foil (S3) made of aluminum and vitreous carbon between the Booster Synchrotron and AGS and becomes Au^{77+} .

Finally, two more electrons of the gold ion Au^{77+} are removed at the fourth stripping station ATF foil (S4) made of thin tungsten, located in between the AGS and RHIC. The fully stripped gold ions Au^{79+} will then be injected into the blue and yellow rings at RHIC. For polarized protons, H^- pass a single stripping stage called located in the Booster Synchrotron. The stripping station is called the Linac-to-Booster (LTB) stripper made of carbon foils with special geometry and converts polarized H^- to H^+ . Figure 1-9 schematically shows the accelerating process of gold ions at RHIC [50]

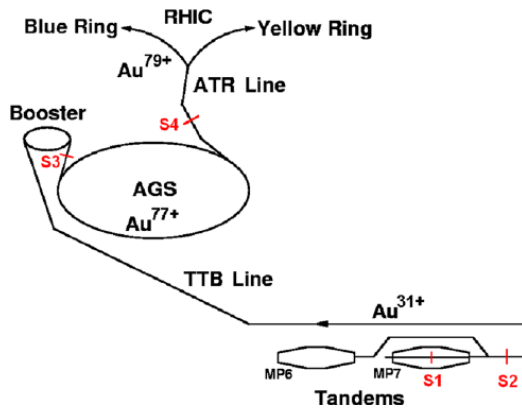


Figure 1-9: The acceleration of gold ions for RHIC is shown above.

At RHIC, we will accelerate the Au^{79+} ions in the superconducting Radio Frequency (RF) cavity under perpendicular electric and magnetic fields until they reach energies up to about 100 GeV/c per nucleon. Subsequently, we collider them via bunch crossing at the interaction points of the experiments to perform relativistic heavy-ion collisions and study high-energy nuclear physics. RHIC usually operates in the first six months of a calendar year. At RHIC, the center of mass energy can also decrease where the ion beams collide with ions at a lower energy in the laboratory frame. The STAR experiment at RHIC has already finished the beam energy scan and is currently taking data in the fixed target program.

1.4.3 Large Hadron Collider (LHC)

Located at the border between Switzerland and France, LHC is one of the major high-energy accelerator facilities in Europe and currently the highest energy collider

in the world. It is a circular collider with a circumference of 26.7 kilometers and can provide proton energy up to 14.0 TeV and lead ion energy up to 5.02 TeV [51]. It was built in 2008 with the main purpose to discover the Higgs Boson, perform precision measurements on SM, and search for Physics beyond SM. Due to its high-energy ion capabilities, high-energy nuclear physicists also use the existing general-purpose detectors designed for high-energy particle experiments at the LHC to conduct research on relativistic heavy-ion physics. LHC ion physics runs usually start at the end of the year and lasts for about a month. The photo taken from the sky to picture LHC is shown in Figure 1-10:

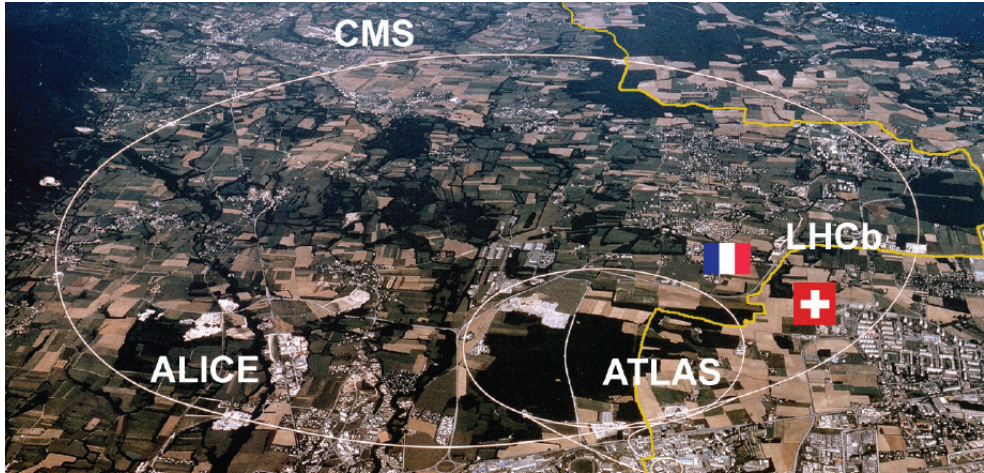


Figure 1-10: The sky view of LHC at CERN is shown above. The actual locations of the experiments at the LHC: ATLAS, CMS, ALICE, and LHCb, as well as the French-Swiss border, are also displayed.

CERN usually uses lead ions ($^{208}_{82}Pb$), which are stable and approximately spherical. In the 2017 ion physics run, it also used xenon ions ($^{131}_{52}Xe$). Currently, there are also discussions of potential future usage of lighter ions such as oxygen $^{32}_{16}O$ to study smaller systems [52]. Similar to RHIC, the lead ions at the LHC also undergo a series of stripping processes using stripping foils in order to become partially ionized Pb^{81+} [53]. Also, the lead ions pass a series of energy boosting before reaching the desired energies at the LHC. Lead ions start from a source of vaporized lead and enter Linac 3 before being collected and accelerated in the Low Energy Ion Ring (LEIR) at an energy from 4.2 MeV to 72 MeV. Then, the lead ions will be injected into Proton

Synchrotron (PS) to boost their energies. Next, they are sent to the Super Proton Synchrotron (SPS). Finally, the lead ions are injected into the LHC and increase their energies to TeV scale in two LHC rings with the RF cavity [51]. Finally, the energetic lead ion beams from two LHC rings will collide with a small crossing angle at the interaction points of the LHC experiments. The CERN accelerator complex is shown schematically in 1-11

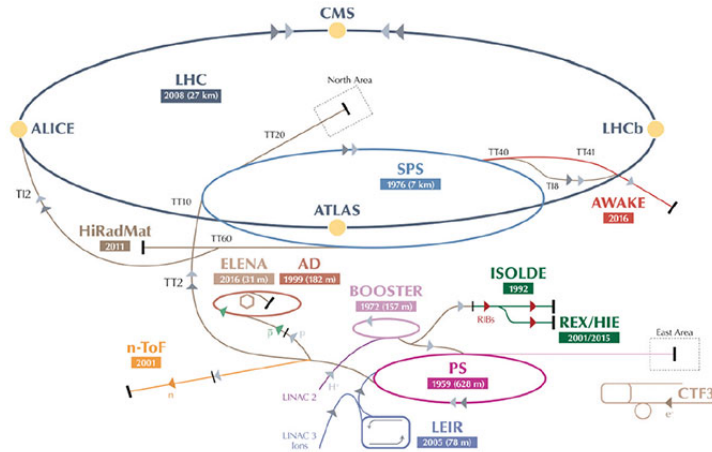


Figure 1-11: The schematic overview of the CERN accelerator complex with the accelerators labeled is shown above. Proton and lead ions are accelerated using these facilities and boost their energies to the TeV scale.

After Run III, LHC will be upgraded to high-luminosity (HL) LHC and allows physicists to collect huge datasets, which is crucial for precision measurements in the heavy-ion physics program. Because the beam energy at the LHC is higher than RHIC, the QGP created at the LHC has a higher temperature and a smaller baryon chemical potential than the one created at RHIC.

1.4.4 High Energy Physics Coordinates

As mentioned in the previous section, the heavy-ion beams are in general highly relativistic. Therefore, Lorentz transformation will be relevant in our studies. In Cartesian coordinates $x^\mu = (t, x, y, z)$, under Lorentz transformation, if we boost the system by a speed β in the $+z$ direction. The Lorentz gamma factor will be given by

$\gamma = \frac{1}{\sqrt{1-\beta^2}}$. The four vector $x^\mu \rightarrow x'^\mu$ transforms as follows

$$\begin{bmatrix} t' \\ x' \\ y' \\ z' \end{bmatrix} = \begin{bmatrix} \gamma & 0 & 0 & -\gamma\beta \\ 0 & 1 & 0 & 0 \\ 0 & 0 & 1 & 0 \\ -\gamma\beta & 0 & 0 & \gamma \end{bmatrix} \begin{bmatrix} t \\ x \\ y \\ z \end{bmatrix} \quad (1.10)$$

The equation above is called the Lorentz Transformation. It is an orthogonal transformation preserving the Minkowski metric tensor $diag(1, -1, -1, -1)$ using the conventions in particle physics.

Nowadays, heavy-ion detectors usually have 2π angular coverages in the transverse direction with some finite longitudinal acceptance along the beamline. They are essentially cylindrically symmetric. Hence, it is convenient and sensible to choose a cylindrical coordinate system and use Lorentz invariant kinematic variables. In general, we define the beam direction to be the z -direction of the coordinate system. For the standard cylindrical coordinates in the position space, the Lorentz four-vector is $(t, x, y, z) \rightarrow (t, r, \phi, z)$.

The relativistic coordinate system for our analysis is shown below in Figure 1-12.

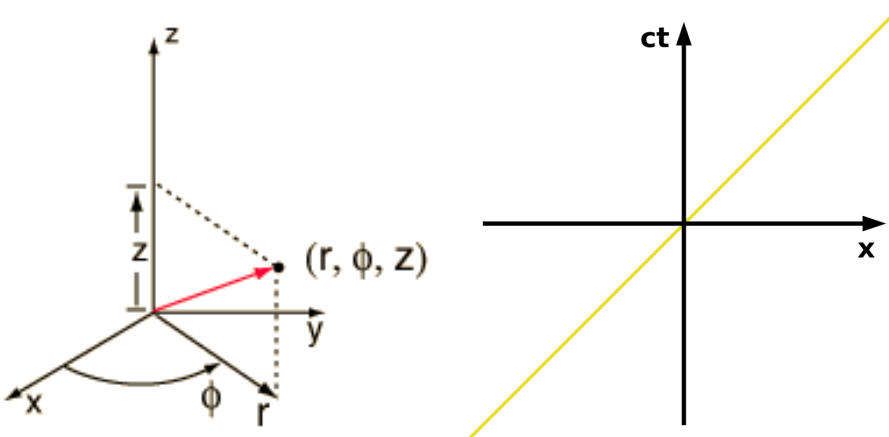


Figure 1-12: The cylindrical coordinate system in the position space (left) and the space-time diagram (right) for relativistic heavy-ion physics analysis are shown above.

Thus, in the momentum space, we can use $p^\mu = (E, p_x, p_y, p_z) \rightarrow (E, p_T, \phi, p_z)$

$$p_T = \sqrt{p_x^2 + p_y^2} \quad (1.11)$$

$$\phi = \arctan\left(\frac{p_y}{p_x}\right) \quad (1.12)$$

We also define rapidity y , a relativistic version of velocity that can be convenient added to the boost:

$$y = \frac{1}{2} \ln \frac{E + p_z}{E - p_z} \quad (1.13)$$

Experimentally, we also use pseudo-rapidity η , which is more directly connected to the detector measurements assuming ultra-relativistic limit kinematics ($E \rightarrow p$). The definition of pseudo-rapidity η is shown as follows:

$$\eta = -\ln \tan\left(\frac{\theta}{2}\right) \quad (1.14)$$

Here θ is the angle labeled in the left of Figure 1-12. Particularly, $y = 0$ and $\eta = 0$ when $p_z = 0$. In addition, boosting by a speed β in the longitudinal z -direction, we found that the rapidity simply shifts by a const number $y' = y + \tanh \beta$. We should note that the cylindrical coordinates (p_T, ϕ, p_z) are perfectly orthogonal while (p_T, ϕ, y) or (p_T, ϕ, η) are not.

In general collider experiments, two particles are moving toward each other with four-momenta p_1^μ and p_2^μ and interact with each other. It is also very convenient to use the Mandelstam variables s, t, u in our studies. They are defined as follows

$$s \equiv (p_1 + p_2)^2 \quad (1.15)$$

$$t \equiv (p_1 - p_2)^2 \quad (1.16)$$

$$u \equiv (p_1 - p_3)^2 \quad (1.17)$$

In the center of mass frame, it follows $\vec{p}_1 = -\vec{p}_2 = \vec{p}$. Therefore, $p_1^\mu = (E, \vec{p})$ and $p_2^\mu = (E, -\vec{p})$. Hence, $s \equiv (p_1 + p_2)^2 = 4E^2 = E_{CM}^2$. Hence, the center of mass energy of the collision system could be represented by the Mandelstam variable \sqrt{s} : $E_{CM} = \sqrt{s}$.

1.4.5 Stages of Heavy-Ion Collisions

In high-energy heavy-ion collisions, both Electroweak and QCD processes occur in each event and contribute to the total cross section. We classify the events with elastic and inelastic reaction processes. For elastic processes, two nuclei scatter mainly electromagnetically with each via photon exchange without breaking themselves up or losing energy. For inelastic scattering, we classify diffractive and non-diffractive disassociation processes. In diffractive dissociation processes, the two nuclei may be slightly excited and lose relatively small fractions of their energies, and produce a relatively small number of particles. On the other hand, in non-diffractive dissociation processes, the nuclei lose substantial fractions of their energies and produce a large number of particles [54].

Therefore, in events with significant contribution from non-diffractive dissociation, the interaction between two nuclei has multiple stages including both perturbative and non-perturbative QCD processes. We can define the stages of heavy collisions and study the details of each stage. There are five stages: the initial state of two highly Lorentz contracted nuclei before the collisions, the very early pre-equilibrium stage when hard scatterings between partons inside nuclei begin, the rapid expansion of the fireball when the thermally and chemically equilibrated QGP is created, the hadronization stage after QGP expands and cools down, and the freeze-out stage when the inelastic scattering processes cease.

Theoretically, many phenomenological models such as Ultra-Relativistic Quantum Molecular Dynamics (UrQMD) and A Multi-Phase Transport Model (AMPT) are

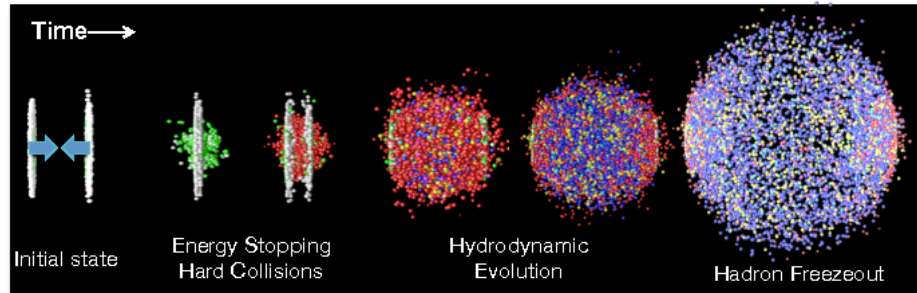


Figure 1-13: A typical heavy-ion collision event with different stages as time evolves is shown above.

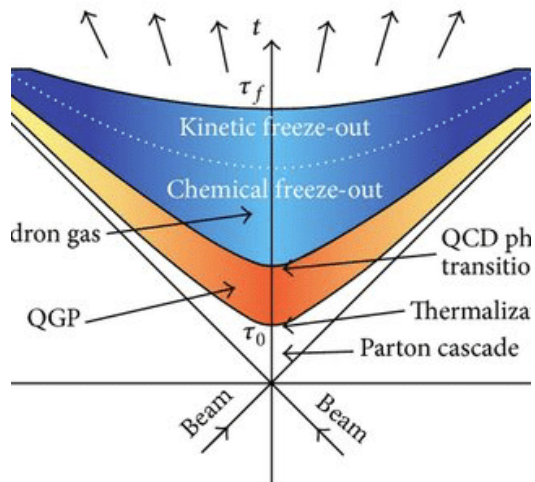


Figure 1-14: The space-time evolution diagram of heavy-ion collisions is shown above. It consists of five stages: initial state before the collisions, early stage of hard scattering processes, the hydrodynamic expansion of QGP, hadronization after QGP expands and cools down, and the freeze-out stage, first chemical freezeout when the particle species no longer change, and finally kinetic freezeout when the elastic scattering processes ceas.

developed to describe relativistic heavy-ion collisions.

1.4.6 Global Event Observables

Globally, we can define some physical quantities in heavy-ion collisions to generally characterize each event. Heavy-ion physicists define the impact parameter, centrality, number of participants, number of binary nucleon-nucleon collisions, and event multiplicity. We will discuss all of them below.

Impact Parameter: Prior to heavy-ion collisions, similar to other collider experiments, each event is prepared with the same unpolarized incoming particles with the same center of mass energy. Therefore, the incoming state $|i\rangle$ is used for each event. However, different from e^+e^- and pp collisions, in heavy-ion physics, we introduce another parameter called the impact parameter denoted b to the transverse distance between center of two nuclei to classify the events. Therefore, the incoming state can be rewritten as $|i(b)\rangle$. Figure 1-15 graphically shows the definition of impact parameter in heavy-ion collisions [55].

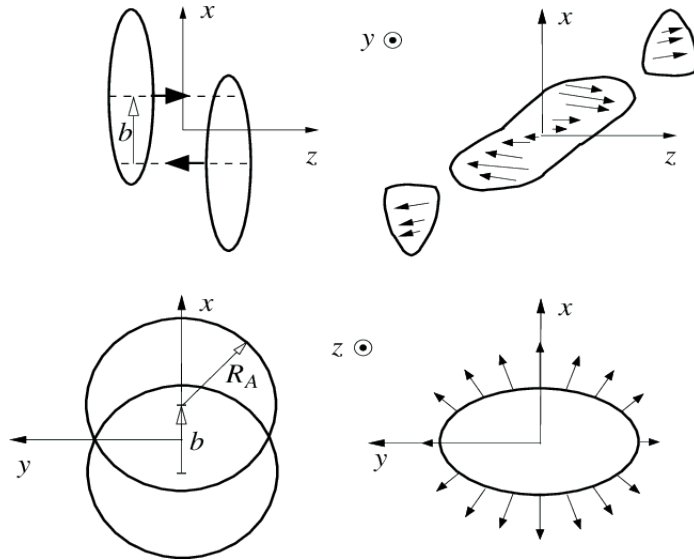


Figure 1-15: The definitions of impact parameter b in heavy-ion collisions, the overlapping interaction region, and the break-up remnants of the two nuclei, called spectators, moving along the z -direction are shown above. An almond shape of the nuclear interaction region, which results in the azimuthally anisotropic emission of final state particles, is seen in heavy-ion collisions.

Number of Participants: Right at the end of heavy-ion collisions after two nuclei pass through each other, we can define the number of participants denoted as N_{part} . The number of participants is essentially equivalent to the number of participating nucleons. The smaller the impact parameter, the more overlap volume between two nuclei, leading to a larger number of participating nucleons in the collision. The nuclear interaction system size is determined by the number of participants. However, because of the event-by-event nuclei geometry fluctuations caused by the motion of nucleons inside nuclei [20], it is more proper to say that the average number of participants $\langle N_{part} \rangle$ is related to the impact parameter.

Number of Binary Nucleon-Nucleon Collisions: In addition to N_{part} , we can also define another quantity that characterizes the detailed interactions in the events at rather hard scales. The number of binary nucleon-nucleon collisions, denoted as N_{coll} , is also related to the impact parameter. In higher energy nuclei collisions, nucleons inside nuclei become the relevant degrees of freedom to describe the cross section. We could treat the collisions of two nuclei as the superposition of the collisions between nucleons inside the nuclei. Since binary nucleon-nucleon collision has a rather small cross section, it dominates the total nucleon-nucleon cross section according to the binomial principle. Higher-order effects, such as ternary nucleon-nucleon collisions, are negligible. the Glauber Model [56] has been developed to study the relationship between b , N_{part} , and N_{coll} in nuclei collisions and will be discussed in the following subsection.

Centrality: Experimentally, it is difficult to directly measure the impact parameter of each collision. Therefore, we define another physical quantity called centrality to characterize the impact parameter. The centrality (C) is defined as the fraction of the total nuclear interaction cross section: $C = \int_0^b \frac{d\sigma}{dx} dx$. Centrality is expressed in terms of percentage [57]. It is related to the quantity: $\frac{\pi b^2}{4\pi R_A^2}$ where R_A is the radius of nuclei defined above in Figure 1-15. When the impact parameter between two nuclei is 0, the centrality is at 0%. When the impact parameter between two nuclei is $2R_A$, the centrality is 100%. There is also a relationship between the centrality and the average number of participants. Heavy-ion experimental measurements are

in general presented in terms of centrality or the average number of participants. Experimentally, we look at the number of tracks and cluster energies of calorimeters at the forward direction, for instance, the forward hardonic calorimeters, to estimate the centrality [58–60].

Virtuality: Similar to deep inelastic scattering, we can also define the virtuality Q^2 , which is the momentum transfer between the two particles in nucleon-nucleon collisions. To generate nucleon-nucleon collision events in Monte Carlo (MC) simulations, we use \hat{p}_T , defined as the transverse momentum of the hard subprocess, which is a quantity related to Q^2 . One of these MC simulations is called PYTHIA. It is developed by the high-energy theory group of Lund University.

Event Multiplicity: We can also define the event multiplicity by counting the number of final state charged particles to quantify the event activity. Event multiplicity could be denoted as N_{trk} , the number of tracks in the event, which is approximately proportional to the number of charged particles denoted as N_{ch} . Figure 1-16 shows the correlation between the number of participants, its corresponding cross section, and the impact parameter in heavy-ion collisions, defining the centrality classes [56].

The initial global parameters such as the collisions energy, impact parameter, collision nuclei species, and polarization can be treated as knobs for high-energy nuclear physicists to play with in order to study relativistic heavy-ion collisions and create strongly interacting systems with different sizes, chemical potentials, and temperatures in the QCD phase diagram. Figure 1-17 shows an event display of thousands of tracks from a central Au + Au collision event at 200 GeV recorded by the Time Projection Chamber (TPC) of the STAR experiment at RHIC.

1.4.7 Glauber Model

The Glauber Model, named after physicist Roy Glauber [62], was originally developed to address high energy scattering problems with composite particles in the optical limit where optical theorem is applicable [63, 64]. It is a model describing two composite objects collider inelastically with each other and decompose the total cross section to the cross section of collision between two point objects. the Glauber Model

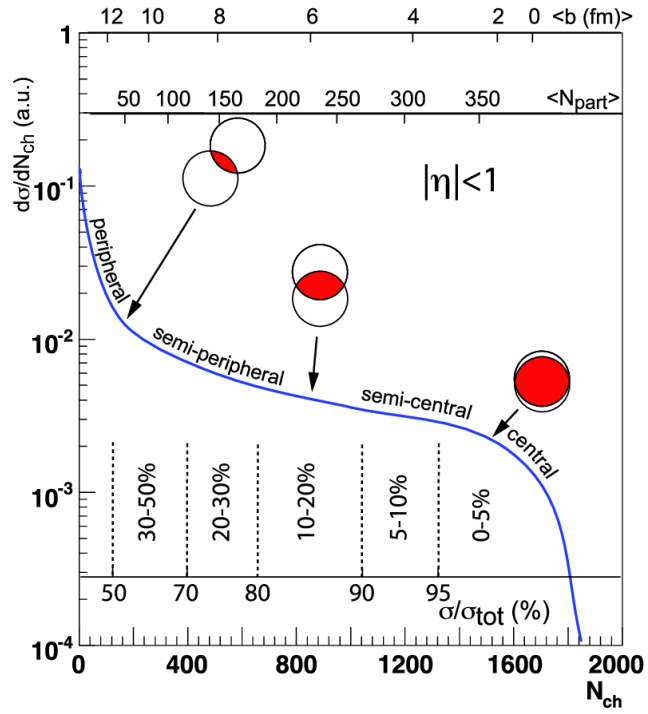


Figure 1-16: The plot showing a relationship among the number of charged particles, N_{ch} , related to the number of participants N_{part} , the differential cross section $\frac{d\sigma}{dN_{ch}}$, and the centrality, according to the Glauber Model calculations, is shown above.

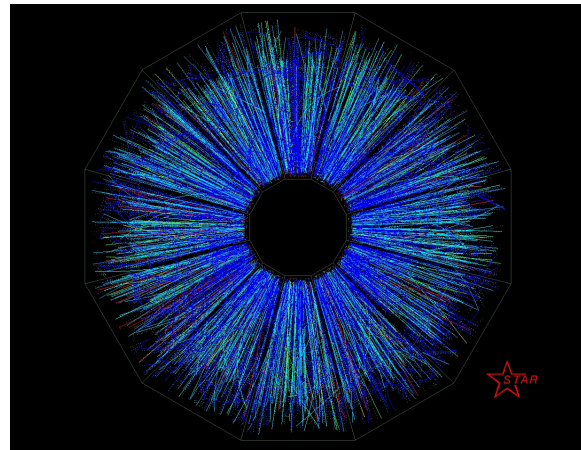


Figure 1-17: Two gold ions collide head-on in the STAR detector. The event with reconstructed tracks of final state particles is displayed by STAR TPC shown above. Image from [61]

can be applied to study nucleon-nucleus (N-A) and nucleus-nucleus (A-B) collisions with nucleon-nucleon (N-N) collisions and determine the relationship between the global observables mentioned in the previous subsection.

If we consider a spherically symmetric nucleus, the nuclear charge density $\rho(r)$ can be described by the Fermi distribution with three parameters below

$$\rho(r) = \rho_0 \frac{1 + w(r/R)^2}{1 + \exp(\frac{r-R}{a})} \quad (1.18)$$

The equation above is called the Wood-Saxon density formula. According to the Glauber Model [62], the N-N inelastic cross section is denoted as σ_{in}^{NN} and the effective thickness function of a nucleon is defined as a function of impact parameter in the transverse direction: $T(\vec{b})$. It is defined as follows

$$T(\vec{b}) = \int \rho(\vec{b}, z) dz \quad (1.19)$$

It is normalized to unity: $\int_0^{R_A} T(\vec{b}) d^2 b = 1$. $T(\vec{b})$ essentially depends on the density of the nucleus $r(b)$. Therefore, the probability that a nucleon collides with a nucleon inside the nucleus is given by $\sigma_{in}^{NN} T(\vec{b})$. Therefore, the probability of n nucleon collisions is given by

$$P_n = \binom{A}{n} \sigma_{in}^{NN} T(\vec{b})^n [1 - \sigma_{in} T(\vec{b})]^{A-n} \quad (1.20)$$

Hence, if we consider a constant fraction of μ ($0 \leq \mu \leq 1$) of particle produced after each collision, we can calculate the average event multiplicity $\langle N(\mu) \rangle$:

$$\langle N(\mu) \rangle = \sum_n P_n \sum_0^{n-1} \mu^m = \sum_{n-1} P_n \frac{1 - \mu^n}{1 - \mu} = \frac{1}{1 - \mu} \{1 - [1 - (1 - \mu) \sigma_{in} T(\vec{b})]^A\} \quad (1.21)$$

It turns out that we have the following relationship between N_{part} and N_{coll} with $\langle N(\mu) \rangle$ [62]

$$N_{part} = \langle N(\mu = 0) \rangle \quad (1.22)$$

$$N_{coll} = \frac{1}{2} \langle N(\mu = 1) \rangle = AT(\vec{b})\sigma_{in}^{NN} \quad (1.23)$$

In a more generalized case: A-B collisions, Figure 1-18 shows side view and beam-line view of heavy-ion collision of projectile B on target A

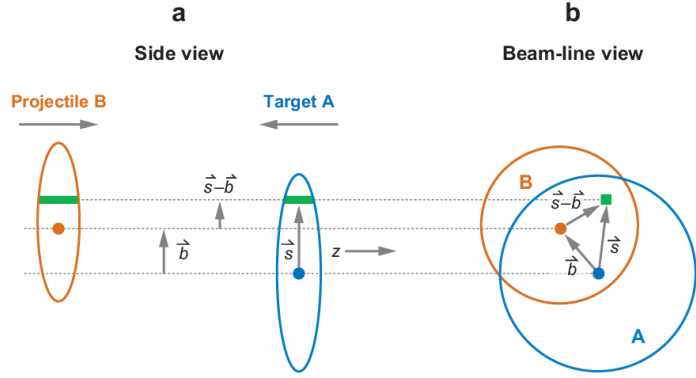


Figure 1-18: The A-B collision with the definition of the impact parameter vector \vec{b} and the distance of nucleon to the center of projectile B \vec{s} is shown above. The distance from the nucleon in B to the center of the target A is $\vec{s} - \vec{b}$ according to the vector subtraction rule. Here we assume both nuclei A and B are perfect spheres.

Using similar ideas [56], we could first calculate the effective thickness function T_{AB} as follows:

$$T_{AB}(\vec{b}) = \int T_A(\vec{s})T_B(\vec{b} - \vec{s})d^2s \quad (1.24)$$

Now replacing $T(\vec{b})$ in N-A by $T_{AB}(\vec{b})$ in A-B, we can obtain

$$\begin{aligned} \langle N(\mu) \rangle &= \frac{A}{1-\mu} \int_0^b T_A(\vec{s}) \{1 - [1 - (1-\mu)T_B(\vec{b} - \vec{s})\sigma_{in}^{NN}]\}^A d^2s \\ &\quad + \frac{B}{1-\mu} \int_0^b T_B(\vec{s}) \{1 - [1 - (1-\mu)T_A(\vec{b} - \vec{s})\sigma_{in}^{NN}]\}^B d^2s \end{aligned} \quad (1.25)$$

To obtain N_{part} , evaluating at $\mu = 0$, we get

$$N_{part} = A \int_0^b T_A(\vec{s}) \{1 - [1 - T_B(\vec{b} - \vec{s})\sigma_{in}^{NN}]^A\} d^2 s + B \int_0^b T_B(\vec{s}) \{1 - [1 - T_A(\vec{b} - \vec{s})\sigma_{in}^{NN}]^B\} d^2 s \quad (1.26)$$

To obtain N_{coll} , evaluating at $\mu = 1$, we get

$$N_{coll} = AB T_{AB}(\vec{b}) \sigma_{in}^{NN} \quad (1.27)$$

In a very special case, assume the nuclei are simply perfectly rigid spheres with the same radii and collide with zero impact parameter $b = 0$. That is $T_A \sigma_{in}^{NN} = T_B \sigma_{in}^{NN} = T_{AB} \sigma_{in}^{NN} = 1$, we get

$$N_{part} = A + B \quad (1.28)$$

$$N_{coll} = AB \quad (1.29)$$

The results above of N_{part} and N_{coll} agree to our expectations.

The comparison of N_{part} and N_{coll} as a function of impact parameter b between the Glauber Model calculations and simulations is shown in Figure 1-19 from the [56]

Therefore, we can apply the Glauber Model to determine N_{part} and N_{coll} for a given centrality range of AA collision ($T_{AB} \rightarrow T_{AA}$), which will be used in our analysis to obtain the corrected yield. It has been reported that the productions of light hadrons, such as pions and kaons, are scaled as N_{part} [65] while Electroweak bosons, such as W and Z bosons, are scaled as N_{coll} [66].

1.5 Characterization of Quark-Gluon Plasma

Equipped with the knowledge and collider technologies of heavy-ion collisions, we are ready to apply them to conduct scientific research on QGP in laboratories. The following subsections will describe the characterization of QGP from its predicted signatures to open questions today, which leads to my thesis research.

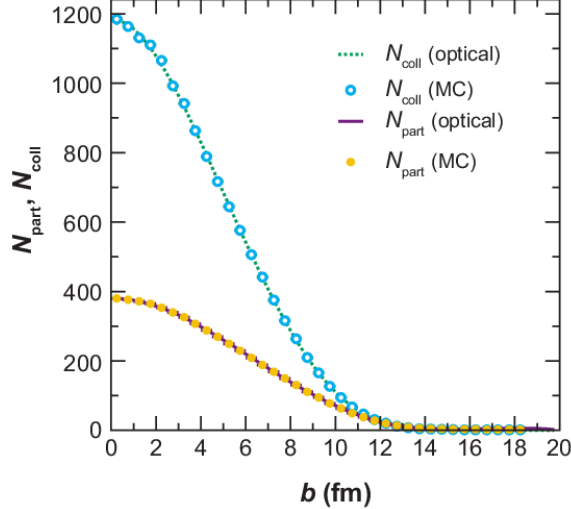


Figure 1-19: The N_{part} and N_{coll} as a function impact parameter calculated from the Glauber Model with optical approximation (lines) and from MC simulations (circles) are shown above. We can see they have an almost perfect agreement with each other.

1.5.1 Signatures

QGP has been hypothesized long before its discovery as a color deconfined phase of quark matter named “quark gluon plasma” [67] and will demonstrate some specific benchmarks in experiments to provide evidence of its creation [68]. Here, four classic signatures of QGP will be discussed: J/ψ and Υ suppressions, jet quenching, elliptic flow, strangeness enhancement.

1.5.2 J/ψ and Υ suppression

J/ψ meson, as a type of heavy quarkonium, is a bound state of a charm quark and an anti-charm quark ($c\bar{c}$). It has a mass greater than the Λ_{QCD} . Therefore, we could approximately treat the interaction between charm and the anti-charm quark with a Cornell potential $V(r)$ in the non-relativistic quantum mechanical hamiltonian system [69]:

$$\hat{H} = \hat{T} + \hat{V} \quad (1.30)$$

$$\hat{H} |\psi\rangle = i \frac{\partial}{\partial t} |\psi\rangle \quad (1.31)$$

and solve the Schrödinger equation to describe the J/ψ mesons in vacuum. As we have seen in Section 1.3.2, with the presence of the QGP medium, at a finite temperature T , the potential is modified due to the color screening effect [70]. The distance between two charm quarks $V(r) \rightarrow \frac{\sigma}{m_D}$, which does not diverge, as $r \rightarrow \infty$. Therefore, the $c\bar{c}$ system could be unbounded if they have sufficiently high energy. In the field theory picture, this could be understood as the color string breaking between charm and anti-charm quark [71], also known as quarkonia melting [72]. Hence, with the influence of QGP at $T > 0$, the production cross section of J/ψ will decrease compared to the vacuum at $T = 0$. Experimentally, we define an observable to quantify the modification of particle production cross section in AA collision compared to the reference pp collisions normalized by the number of binary nucleon-nucleon collisions N_{coll} , which is explained in the previous subsection. This observable is called nuclear modification factor, denoted as R_{AA} . Mathematically, R_{AA} is defined as follows:

$$R_{AA} = \frac{1}{N_{coll}} \frac{\frac{d^2 N_{AA}}{dp_T dy}}{\frac{d^2 N_{pp}}{dp_T dy}} = \frac{1}{T_{AA}} \frac{\frac{d^2 N_{AA}}{dp_T dy}}{\frac{d^2 \sigma_{pp}}{dp_T dy}} \quad (1.32)$$

Therefore, $R_{AA} < 1$ means suppression. $R_{AA} = 1$ means no modification. $R_{AA} > 1$ means enhancement. Hence, in experiments, we expect to observe the $R_{AA} < 1$ due to the suppression of J/ψ production with the presence of the QGP medium. Figure 1-20 shows the measurements of fully reconstructed J/ψ at RHIC and LHC [73]

In fact, we could see that $R_{AA} < 1$ for every data point, which indicates a clear suppression of J/ψ production from experiments at both RHIC and the LHC. However, we should note that the larger J/ψ R_{AA} observed at the LHC compared to RHIC could be explained by the regeneration mechanism [74].

Similarly, we expect to see this in Υ , which is made of $b\bar{b}$. Indeed, they expect to have a sequential suppression since three Υ states: $\Upsilon(1S)$, $\Upsilon(2S)$, and $\Upsilon(3S)$, could be observed in experiments. Because the total energy of the $b\bar{b}$ system or

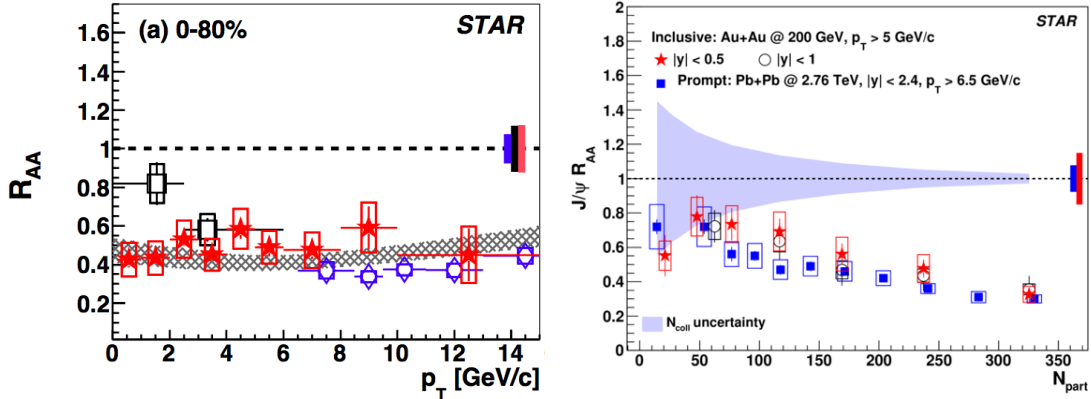


Figure 1-20: The nuclear modifications factor R_{AA} of fully reconstructed J/ψ as a function of p_T (left) and N_{part} (right) measured by the STAR experiment (red data points) at RHIC and the CMS (blue diamond data points) and ALICE (blue circle data points) experiments at the LHC are shown above. We can see that the $J/\psi R_{AA}$ is below 1 for both p_T and N_{part} . There is no significant p_T dependence of $J/\psi R_{AA}$. The $J/\psi R_{AA}$ decreases as N_{part} increases, consistent with the increasing creation probability of QGP with larger N_{part} .

equivalently the rest mass: $m_{\Upsilon(3S)} > m_{\Upsilon(2S)} > m_{\Upsilon(1S)}$, a sequential suppression: $R_{AA}^{\Upsilon(1S)} > R_{AA}^{\Upsilon(2S)} > R_{AA}^{\Upsilon(3S)}$ should be observed if QGP is created. Figure 1-21 shows the measurements of fully reconstructed Υ states at RHIC and LHC [75, 76]

1.5.3 Jet Quenching

Experimentally, due to color confinement, it is impossible to directly detect and track the energetic partons. Therefore, physicists define a jet as a spray of collimated hadrons within a narrow cone initiated from color charged partons. In nuclear and particle physics, jets are used to study the dynamics of partons before hadronization [77] and understand the properties of QGP. A schematic view of a di-jet production from di-quark event in electron-positron collider $e^+e^- \rightarrow q\bar{q}$ is shown below in Figure 1-22

Since we know that QGP is a color deconfined state of matter, an energetic parton carrying color charge traveling through the QGP medium is expected to lose a substantial amount of its energy to the medium. This is similar to the effect that an electron beam losing energy in the electron-ion plasma via electromagnetic inter-

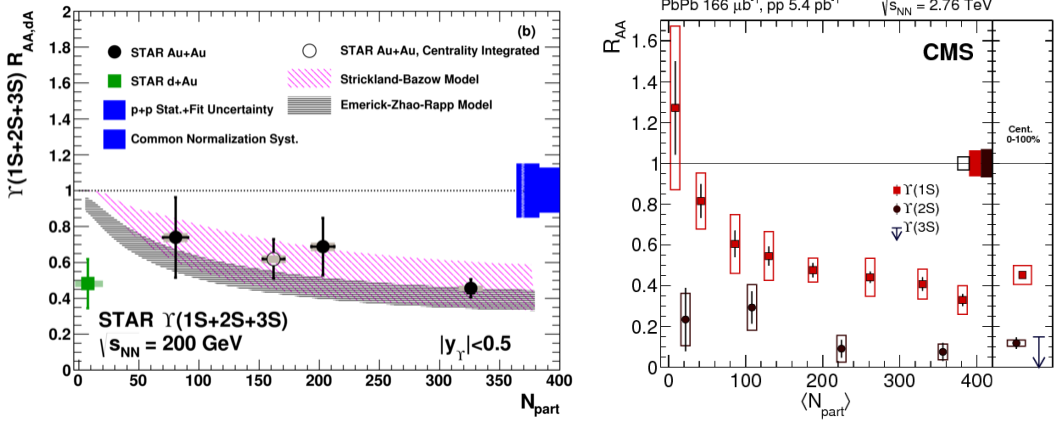


Figure 1-21: The nuclear modifications factor R_{AA} of fully reconstructed Υ as a function of N_{part} measured by the STAR experiment (left) at RHIC and CMS experiment (right) at the LHC are shown above. We can see that the R_{AA} of the three Υ states are below 1 when $N_{part} > 3$. The ΥR_{AA} decreases as N_{part} increases, consistent with the increasing creation probability of QGP with larger N_{part} . In addition, a sequential suppression of ΥR_{AA} is observed by the CMS experiment: $R_{AA}^{\Upsilon(1S)} > R_{AA}^{\Upsilon(2S)} > R_{AA}^{\Upsilon(3S)}$, which agrees with the expectation of QGP color screening effect.

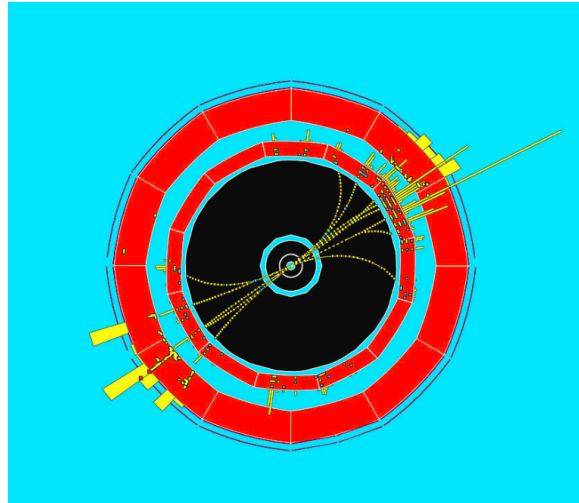


Figure 1-22: The schematic display of a di-jet event from the ALEPH (a particle detector at the Large Electron-Positron collider) Experiment at the Large Electron-Positron Collider (LEP) is shown above. We can see two sprays of back-to-back particles within a narrow cone, representing a di-jet event.

action [78]. We call this effect as jet quenching. Figure 1-23 shows jet quenching in QGP in AA collisions compared to pp collisions

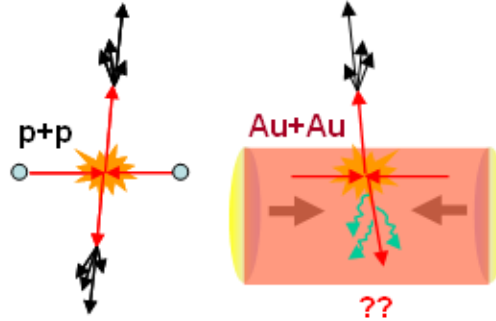


Figure 1-23: The schematic picture explaining jet quenching is shown above. Hard scatterings in pp collisions produce back-to-back "jets" of particles, but in $Au + Au$ collisions, the presence of QGP modifies the jets' properties.

Experimentally, compared to pp collisions where the QGP is not expected to be created, the jet spectra are modified by the QGP medium in AA collisions. The angular distributions would be broadened due to interaction between the jet and the medium. The p_T spectra will be shifted to the left due to energy loss. This can be quantified by the jet nuclear modification factor R_{AA} similar to the R_{AA} for quarkonium suppression mentioned previously. Figure 1-24 shows the measurements of hadron angular correlation with the STAR experiment at RHIC and jet R_{AA} as a function of p_T with the ALICE experiments at LHC [79,80]:

The jet R_{AA} are all below 1 at RHIC and LHC [80,81], which suggests jet quenching in AA collisions, supporting the existence of QGP.

1.5.4 Elliptic Flow

The reaction region in heavy-ion collisions, where the two nuclei overlap with each other, is an almond shape, which is azimuthally asymmetric. If the color deconfined matter QGP is created, particles emitted from the almond shape fireballs are expected to be azimuthally anisotropic due to differences of the pressure gradients and their path length through QGP in the x and y directions. Experimentally, physicists Dr.

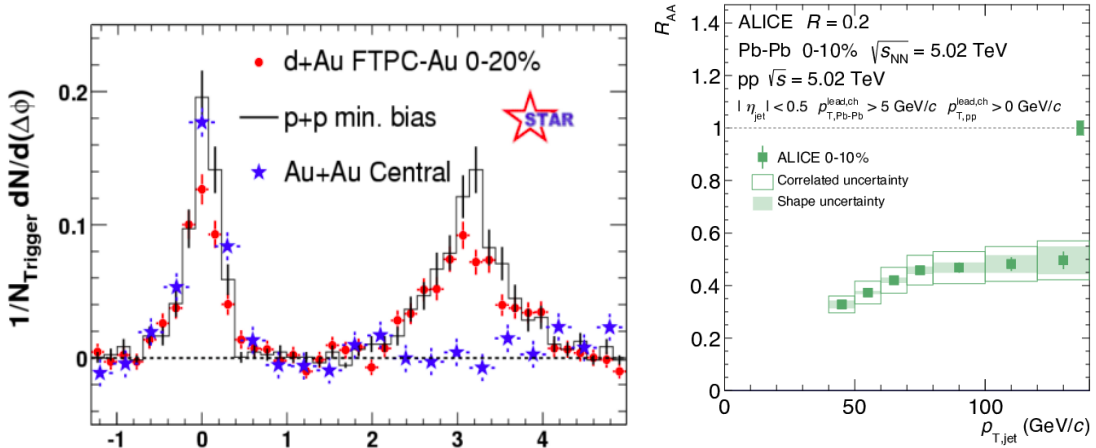


Figure 1-24: The comparison of two-particle azimuthal distributions for central $d + \text{Au}$ collisions to those seen in pp and central $\text{Au} + \text{Au}$ collisions measured with the STAR experiment and the jet R_{AA} as a function p_T measured by the ALICE experiment at LHC (right). From the STAR results, in central $\text{Au} + \text{Au}$ collisions, the back-to-back peak has disappeared due to the redistribution of jet energy to the slow expanding medium constituents. The jet R_{AA} from ALICE measurement is clearly below 1, suggesting that jets lose significant fractions of energy in AA collision compared to pp .

Arthur Poskanzer (who sadly just passed away on June 30 2021) and Dr. Sergey Voloshin developed the event plane method to analyze the azimuthal anisotropy of particle emission in heavy-ion collisions [82]. The reaction plane is spanned by the impact parameter and the x -axis. Figure 1-25 schematically shows the definition of the reaction plane in heavy-ion collisions.

The particle spectra in heavy-ion collisions can be factorized as

$$E \frac{d^3 N}{d^3 p} = E \frac{1}{2\pi p_T} \frac{d^3 N}{dp_T dy d\phi} = E \frac{1}{2\pi p_T} \frac{d^2 N_1}{dp_T dy} \frac{dN_2}{d\phi} \quad (1.33)$$

Since the particle emission is azimuthally anisotropic, we can expand the $F(p_T, \phi, y) = \frac{dN_2}{d\phi}$ into a Fourier series [82]:

$$F(p_T, \phi, y) = \frac{x_0(p_T, y)}{2\pi} + \sum_{n=1}^{\infty} [x_n(p_T, y) \cos(n\phi) + y_n(p_T, y) \sin(n\phi)] \quad (1.34)$$

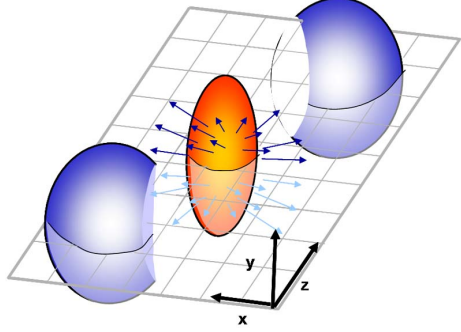


Figure 1-25: The figure above shows the ellipsoid of the overlapping nuclear reaction region of two nuclei in heavy-ion collisions. The reaction plane, which is the x - z plane shown above, is constructed by the beam direction and the impact parameter vector. The emission of particles is azimuthally anisotropic in the x - y plane due to the almond shape geometry.

According to trigonometry, we get

$$F(p_T, \phi, y) = \frac{x_0(p_T, y)}{2\pi} + \sum_{n=1}^{\infty} 2v_n(p_T, y) \cos[n(\phi - \Psi_n)] \quad (1.35)$$

Here, $v_n = \frac{1}{2}\sqrt{x_n^2 + y_n^2}$ and $\Psi_n = \frac{1}{n} \arctan\left(\frac{y_n}{x_n}\right)$.

To find the Fourier coefficients v_n , we can apply the Fourier tricks to find x_n and y_n .

Theoretically, because the function $\frac{dN_2(\phi)}{d\phi}$ is continuously analytical, we can use integral to find the Fourier coefficients [18]

$$x_n = 2 \int_0^{2\pi} \frac{dN_2(\phi)}{d\phi} \cos(n\phi) d\phi \quad (1.36)$$

$$y_n = 2 \int_0^{2\pi} \frac{dN_2(\phi)}{d\phi} \sin(n\phi) d\phi \quad (1.37)$$

Experimentally, because our data only take on discrete values, we can convert the integral into a sum

$$x_n = \frac{2}{N} \sum_{i=1}^N \cos(n\phi^i) = 2\langle \cos n\phi \rangle \quad (1.38)$$

$$y_n = \frac{2}{N} \sum_{i=1}^N \sin(n\phi^i) = 2\langle \sin n\phi \rangle \quad (1.39)$$

Here, we sum up all tracks in the experiment to get the x_n and y_n . Then, we will be able to find

$$v_n = \frac{1}{2} \sqrt{x_n^2 + y_n^2} = \sqrt{(\langle \cos n\phi \rangle)^2 + (\langle \sin n\phi \rangle)^2}. \quad (1.40)$$

In heavy-ion physics, the first-order Fourier coefficient v_1 is called the directed flow.

$$v_1 = \sqrt{(\langle \cos \phi \rangle)^2 + (\langle \sin \phi \rangle)^2}. \quad (1.41)$$

It can be connected to the initial tilting source of the colliding nuclei [83] and can be used to study Chiral Magnetic Effect [84].

The second-order Fourier coefficient v_2 is called the elliptic flow.

$$v_2 = \sqrt{(\langle \cos 2\phi \rangle)^2 + (\langle \sin 2\phi \rangle)^2} = \sqrt{(\langle \cos^2 \phi \rangle - \langle \sin^2 \phi \rangle)^2 + (2\langle \sin \phi \rangle \langle \cos \phi \rangle)^2}. \quad (1.42)$$

Assuming in the initial stage before the collisions, the sum of the momentum of two colliding nuclei \vec{p}_1 and \vec{p}_2 is exactly 0 without any fluctuation. That is

$$\vec{p}_1 + \vec{p}_2 = 0 \quad (1.43)$$

According to momentum conservation, for the final state particles, we have

$$\sum_i^N p_x^i = 0 \quad (1.44)$$

$$\sum_i^N p_y^i = 0 \quad (1.45)$$

Therefore, we have

$$\langle p_T \cos \phi \rangle = \langle p_x \rangle = \frac{1}{N} \sum_i^N p_x^i = 0 \quad (1.46)$$

$$\langle p_T \sin \phi \rangle = \langle p_y \rangle = \frac{1}{N} \sum_i^N p_y^i = 0 \quad (1.47)$$

But since the p_T and ϕ are completely orthogonal, the random variable p_T is uncorrected to ϕ . Therefore, we have

$$\langle p_T \cos \phi \rangle = \langle p_T \rangle \langle \cos \phi \rangle = 0 \quad (1.48)$$

$$\langle p_T \sin \phi \rangle = \langle p_T \rangle \langle \sin \phi \rangle = 0 \quad (1.49)$$

Finally, we know that $p_T > 0$, thus

$$\langle p_T \rangle > 0 \quad (1.50)$$

Hence,

$$\langle \cos \phi \rangle = 0 \quad (1.51)$$

$$\langle \sin \phi \rangle = 0 \quad (1.52)$$

Therefore, we have

$$v_2 = \sqrt{(\langle \cos^2 \phi \rangle - \langle \sin^2 \phi \rangle)^2 + (2\langle \sin \phi \rangle \langle \cos \phi \rangle)^2} = \langle \cos^2 \phi \rangle - \langle \sin^2 \phi \rangle. \quad (1.53)$$

In terms of momentum p_x and p_y , we can rewrite v_2 as

$$v_2 = \langle \cos^2 \phi \rangle - \langle \sin^2 \phi \rangle = \left\langle \frac{p_x^2}{p_T^2} \right\rangle - \left\langle \frac{p_y^2}{p_T^2} \right\rangle = \left\langle \frac{p_x^2 - p_y^2}{p_T^2} \right\rangle = \left\langle \frac{p_x^2 - p_y^2}{p_x^2 + p_y^2} \right\rangle. \quad (1.54)$$

Classically, we know that the momentum is proportional to the pressure gradient. Schematically, we could write

$$p_x \simeq \frac{m\tau}{\rho} \frac{\partial P}{\partial x} \simeq \frac{m\tau}{\rho} \frac{P}{L_x} \quad (1.55)$$

Where m is the mass of the particle, τ is the lifetime of the QGP, ρ is the density of the QGP, and L_x is the minor axis of the ellipse in the x direction according to the geometry of Figure 1-25.

Likewise, we have the same relation for p_y

$$p_y \simeq \frac{m\tau}{\rho} \frac{\partial P}{\partial y} \simeq \frac{m\tau}{\rho} \frac{P}{L_y} \quad (1.56)$$

Here, L_y is the major axis of the ellipse in the y direction according to the geometry of Figure 1-25. Apparently, $L_y > L_x$.

Hence, we can write v_2 as

$$v_2 = \left\langle \frac{p_x^2 - p_y^2}{p_x^2 + p_y^2} \right\rangle = \frac{\frac{1}{L_x^2} - \frac{1}{L_y^2}}{\frac{1}{L_x^2} + \frac{1}{L_y^2}} = \frac{L_y^2 - L_x^2}{L_x^2 + L_y^2} > 0 \quad (1.57)$$

In heavy-ion collisions, we define the eccentricity ϵ_s of an ellipse is defined as [85]

$$\epsilon_s \equiv \frac{L_y^2 - L_x^2}{L_x^2 + L_y^2} \quad (1.58)$$

Hence, we have

$$v_2 \simeq \epsilon_s \quad (1.59)$$

Therefore, we can see that v_2 is essentially proportional to the eccentricity simply based on the ellipse geometry of the reaction region. Historically, v_2 has been extensively studied experimentally and theoretically. It turns out light hadrons demonstrate collectivity. Their elliptic flow v_2 could be calculated using relativistic viscous hydrodynamics [86]. If QGP is created, we expect v_2 of the light flavor hadrons to be positive as derived above. Figure 1-26 show the v_2 as a function of p_T of charged light flavor hadrons in heavy-ion collisions at mid-rapidity measured by RHIC and LHC experiment [87,88]

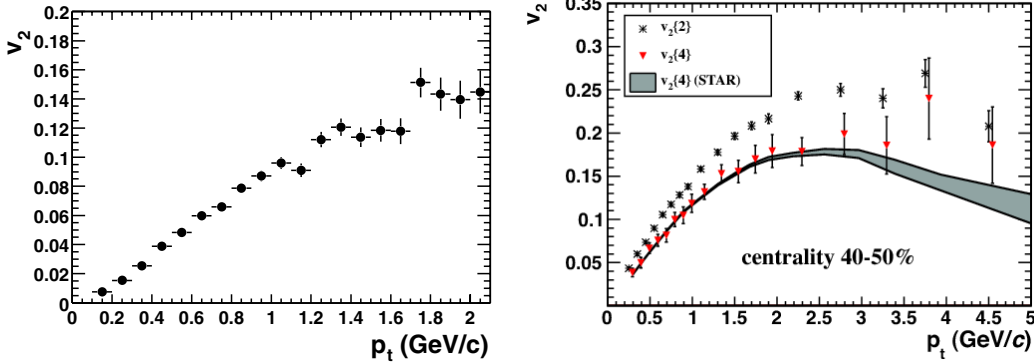


Figure 1-26: The elliptic flow v_2 of charged particles as a function of p_T in Au + Au collision measured by the STAR experiments at RHIC (left) and in PbPb collisions by the ALICE experiments at LHC (right) are shown above. Clearly, $v_2 > 0$ is observed in both experiments.

We can clearly see positive v_2 of charged particles at both RHIC and LHC, which also supports the creation of QGP in high-energy heavy-ion collisions.

1.5.5 Strangeness Enhancement

As described in Section 1.4.6, the temperature of QGP is well above 100 MeV, which is much larger than the strange quark mass (about 95 MeV). Therefore, since $T_{QGP} > m_s$, in the thermally and chemically equilibrated QGP, strange quarks could be produced thermally via the pair production processes: $u\bar{u} \rightarrow s\bar{s}$, $d\bar{d} \rightarrow s\bar{s}$, and $gg \rightarrow s\bar{s}$, establishing the chemical abundance equilibrium [89]. Therefore, the strangeness content in the QGP is enhanced, which could be experimentally observed from the enhancement of strange particle yields in AA collisions compared to pp collisions. A direct experimental observable is the ratio of strange hadron-to-pion yield in AA and pp collisions scaled by N_{part} . Figure 1-27 and Figure 1-28 show the measurements on strange mesons and baryons to pion ratios in AA and pp collisions at RHIC [90] and LHC [91].

We can see that ϕ/π ratio increases as N_{part} and $\sqrt{s_{NN}}$ increases, which indicates strangeness enhancement in AA collisions compared to pp collisions. This again could be served as a piece of evidence for the formation of QGP in heavy-ion collisions at

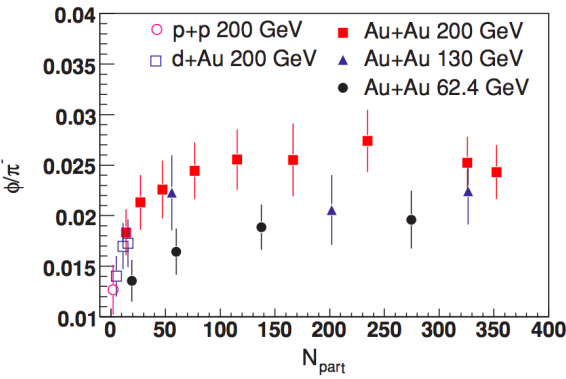


Figure 1-27: The yield ratios of ϕ/π as a function N_{part} in $p+p$, $p+Au$, and $Au+Au$ from the STAR experiment at RHIC are shown above.

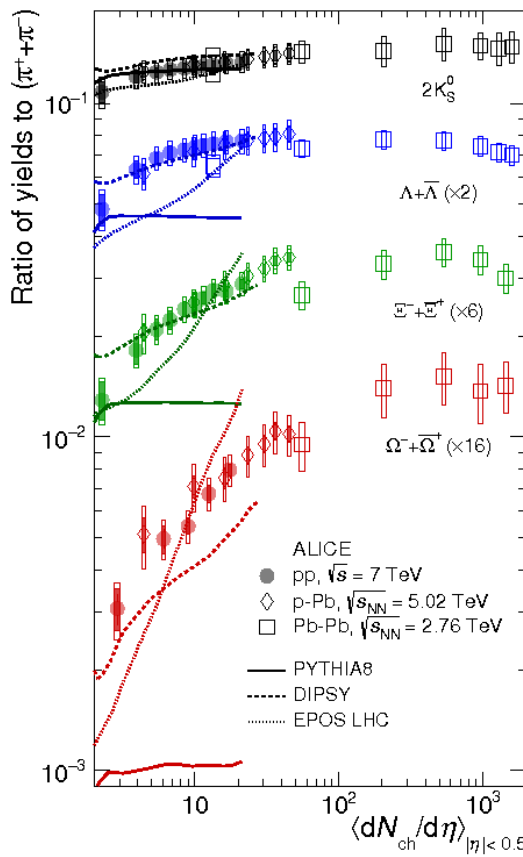


Figure 1-28: The yield ratios of strange hadrons $K_s^0, \Lambda^+, \Xi^0, \Omega^-$ as a function of $\langle dN_{ch}/d\eta \rangle$ from the ALICE experiment at LHC are shown above.

RHIC and LHC.

1.5.6 Macroscopic Properties

Physicists have conducted extensive studies to understand the macroscopic properties of QGP. Below are some of the interesting properties of QGP observed in experiments:

Transient Lifetime: According to the experimental results at RHIC and LHC, QGP has a very short lifetime. It is on the order of 10 fm/c [92]. It is generally assumed that QGP reaches thermal [93] and near chemical equilibrium [94] via strong interaction. However, so far, there is still not sufficient experimental evidence to directly support this assumption.

Strongly Interacting System: Moreover, QGP, as a deconfined state of matter, demonstrates strongly interacting behaviors, which contradicts the prediction of weak coupling according to the asymptotic freedom of quarks and gluons in QCD [5]. At $T \sim 1 - 3 T_c$, the coupling strength of QGP is still strong: $g_s \sim O(1)$ [95]. Therefore, the strong interaction between the QGP constituents is in general non-perturbative. The equation of state of the strongly interacting QGP, as input for hydrodynamic calculations, can be calculated by the MIT Bag Model [37] or lattice QCD [96].

Perfect Liquid Behavior: Finally, QGP demonstrates nearly perfect liquid properties. The expansion of QGP in the fireball stage is approximately isentropic and could be well described by hydrodynamics [97]. More specifically, due to the relativistic nature of the strongly coupled near-perfect liquid system, assuming QGP reaches thermal [93] and near chemical equilibrium [94], relativistic viscous hydrodynamics [86] is the correct theoretical formalism to describe the dynamics of QGP. As an almost perfect liquid, the shear viscosity to entropy density ratio of the QGP is very small: $\frac{\eta}{s} \sim (1 - 2.5) \frac{1}{4\pi}$ [98], approaching the quantum limit $\frac{\eta}{s} = \frac{1}{4\pi}$ predicted by the strongly coupled $N=4$ supersymmetric Yang-Mills plasma in Anti-de-Sitter Space/Conformal Field Theory (AdS/CFT) correspondence [99] from the holographic principle in string theory.

Color Opaque Plasma: It is also interesting that QGP is a color opaque plasma [100]. This means that gluons propagating through the QGP will be absorbed by the

plasma medium. Experimentally, the suppression of hadrons is a measure of the color opacity of the QGP [100]. Physicists have found that QGP is indeed highly color opaque [101].

1.5.7 Open Questions

However, although extensive studies have been carried out for past decades, today there are still many open questions, most of which are derived from the mysterious macroscopic behaviors of the QGP. Below is the list of selected open questions that are currently under active investigation by the heavy-ion physics community [102]:

- 1) **Thermalization of QGP:** How can QGP reach thermal equilibrium within such a short time, which is on the order $1 \text{ fm}/c$, from the non-equilibrium stage?
- 2) **Inner Workings of QGP:** What is the correct degree of freedom to describe the QGP? The inner workings of QGP, as a deconfined phase of matter, must lay between asymptotically free quarks and gluons and color-neutral hadrons. That is also why the sPHENIX experiment at RHIC, as the next generation DOE flagship Heavy Ion Physics program in the U.S., is going to be built at BNL and collect data to probe the inner workings of QGP by resolving its properties at shorter and shorter length scales.
- 3) **Smallest Droplet of QGP:** What is the smallest droplet of QGP that can be created? Can QGP be created in pPb , pp , or even e^+e^- collision systems? What are the limits of the applicability of hydrodynamics?

1.6 Heavy Flavor Physics

1.6.1 Open Heavy Flavor Physics

My graduate research focuses on answering the second question through the data analysis of fully reconstructed heavy flavor hadrons with the CMS experiment to understand the transport properties and probe the microscopic structure of the QGP. In this section, we will focus on discussing open heavy flavor physics where only one

heavy quark Q is in a hadron. Open heavy flavor hadrons have ± 1 heavy flavor quantum numbers. Quarkonia states $Q\bar{Q}$ are considered as hidden heavy flavor with a zero net heavy flavor quantum number. Their properties are very different from open heavy flavor hadrons. We will not discuss them in this thesis and focus only on open heavy flavor physics.

1.6.2 Heavy Quarks

Heavy quarks, such as charm and beauty quarks, whose masses are on the order of GeV, lie in a scale above both Λ_{QCD} and T_{QGP} . Therefore, they are predominantly produced in the early stage of heavy-ion collisions where hard scattering processes occur. Their production could be calculated by perturbation QCD. Figure 1-29 shows the lowest order Feynman diagrams of heavy quark pair production in QCD.

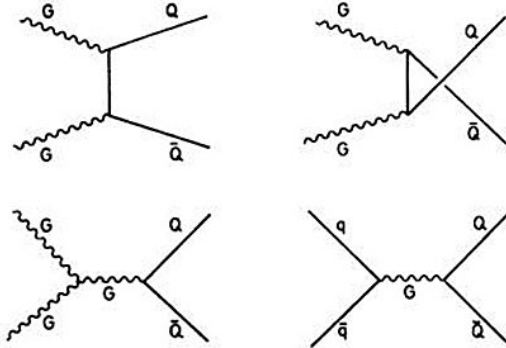


Figure 1-29: The four lowest order tree-level Feynman diagrams of heavy quark pair production are shown above.

In general, due to their relatively small momentum transfer to the QGP medium constituents compared to their large masses [103], they should not reach complete thermalization via multiple scattering as they traverse through the QGP. In addition, since their lifetimes are much longer than the QGP lifetime, they retain their identities and record the evolution of the QGP, which makes them excellent probes. Then, they travel through the medium, hadronize into heavy flavor hadrons, and decay weakly. Their decay products are detected and identified by particles detectors.

Experimentally, from the final stage decay products, we can fully reconstruct

heavy flavor hadrons where the dynamics of heavy quarks is encoded. In different transverse momenta, we can study their diffusion coefficients, hadronization mechanism, and energy loss. We can probe the microscopic structure of QGP via their scattering patterns with the QGP constituents at different wavelengths. Figure 1-30 below shows respectfully an event of beauty quark production and hadronization in vacuum and QGP.

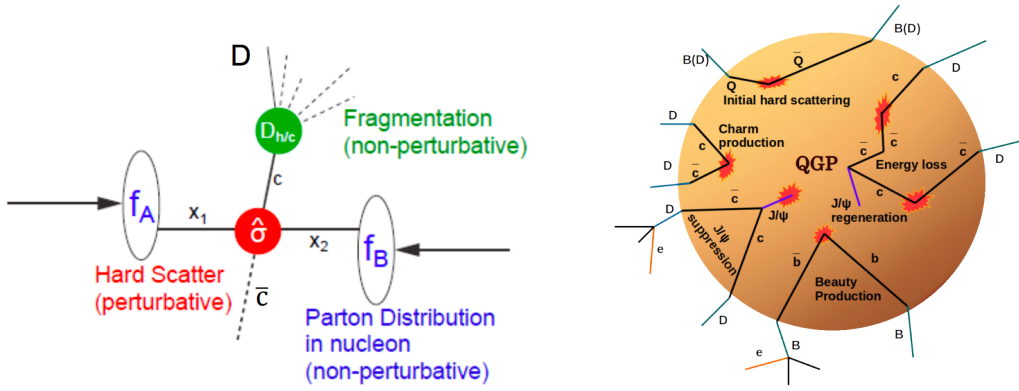


Figure 1-30: The schematic demonstrations of heavy quark production and hadronization in vacuum (left) and QGP (right) are shown above.

1.6.3 Heavy Flavor Physics in Vacuum

To use heavy quark to probe the QGP created in heavy-ion collisions, we first need to understand heavy quark physics in vacuum from pp collisions. In the process $pp \rightarrow Q\bar{Q}$, QCD factorization theorem could be applied. High precision pQCD calculations, including next-to-leading order (NLO), Fixed-to-Next-to-the-Leading (FONLL) [104, 105], A Variable-Flavour Number Scheme for NNLO (GM-VFNS) [106], and POWHEG [107], have been developed to describe heavy quark production in pp collisions. Here, we will show the FONLL calculations of charm and beauty quarks spectra, schematically denoted as: $\frac{d^2\sigma^Q}{p_T dp_T dy}$, in $pp \rightarrow Q\bar{Q}$ at different energies [108]. Figure 1-34 shows the FONLL calculations of charm and beauty quarks spectra for pp collisions at the LHC energy $\sqrt{s} = 5.02$ TeV.

The comparison between different pQCD theoretical calculations and charm [109]

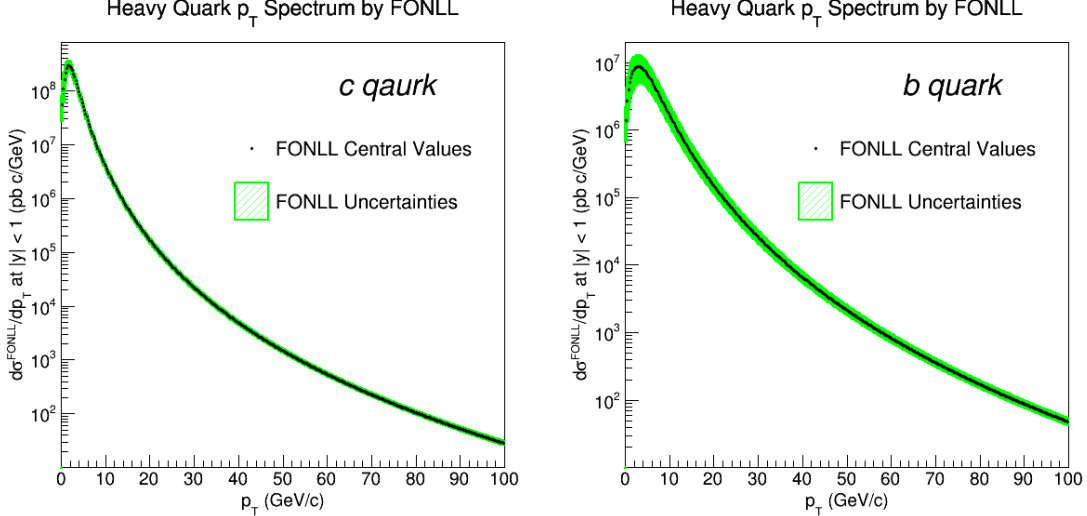


Figure 1-31: The charm quark (left) and beauty quark (right) differential cross section $\frac{d\sigma}{dp_T}$ as a function transverse momentum p_T at $|y| < 1$ from FONLL calculations, are shown above.

and beauty [110] hadrons production in pp collisions with the CMS experiment at the LHC is shown below in Figure 1-32

At higher p_T , reasonably good agreement between FONLL and GM-VFNS with the pp data for both D^0 and B^+ p_T spectra. However, at lower p_T , FONLL tends to underpredict the data while GM-VFNS tends to overshoot the data. Both of the calculations have large theoretical uncertainties at low p_T as the applicability of pQCD starts breaking down in softer collisions.

In vacuum, heavy quarks fragment into heavy flavor hadrons $Q \rightarrow H_Q$. We can define the parton fragmentation function $D_i^{H_Q}(z, \mu^2)$ which is the probability for a quark q with energy E fragment into a hadron with energy zE ($0 < z < 1$) at the factorization scale of μ^2 [12]. According to pQCD, $D_i^{H_Q}(z, \mu^2)$ is universal in vacuum for e^+e^- , ep , and pp collisions. Figure 1-33 shows the scattering processes in which fragmentation fraction is involved:

Next, we are ready to define heavy quark fragmentation fraction $f(Q \rightarrow H_Q)$. First, we know, the energy

$$E = \sqrt{m^2 + p_T^2 \cosh^2 y} \quad (1.60)$$

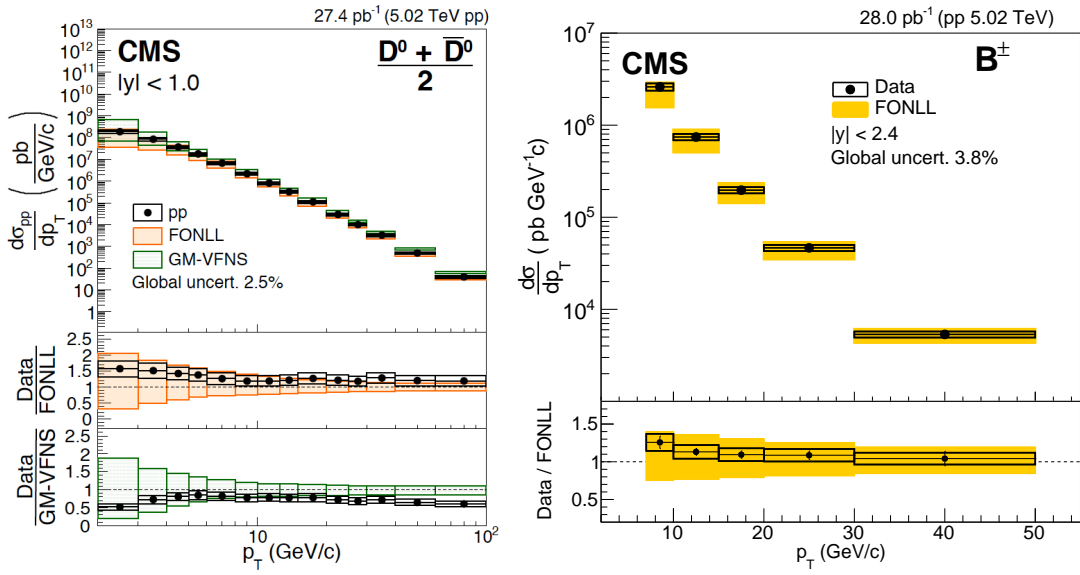


Figure 1-32: The charm quark (left) and beauty quark (right) p_T spectra and the ratio with FONLL and GM-VFNS pQCD theoretical calculations are shown above.

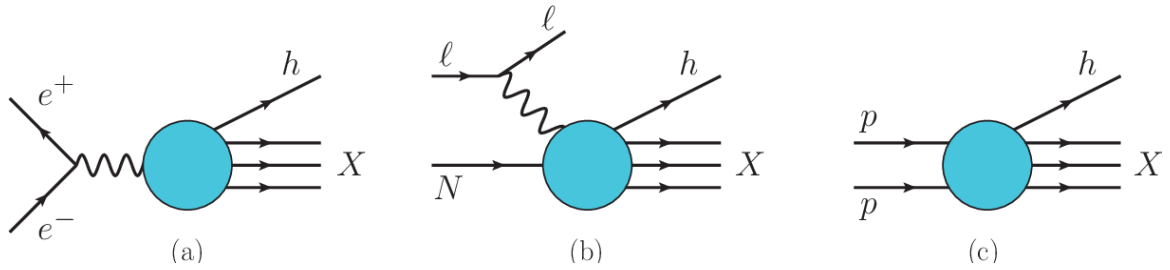


Figure 1-33: Single-inclusive hadron production process, where fragmentation function are involved, in (a) electron-positron annihilation, (b) deep-inelastic lepton-nucleon scattering, (c) proton-proton scattering, are shown above.

Ignoring the mass, we have

$$E \simeq p_T \cosh y \quad (1.61)$$

So the energy of the hadron E^h where the quark with E^Q fragments into will be

$$E^h = z E^Q \quad (1.62)$$

So we have the transverse momentum of the hadron p_T^h

$$p_T^{H_Q} = z p_T^Q \quad (1.63)$$

With heavy quark spectra $\frac{d^2\sigma^Q}{p_T dp_T dy}$ and parton fragmentation function $D_i^{H_Q}(z, \mu^2)$, we let

$$\frac{d^2\sigma^Q}{p_T dp_T dy} = F^Q(p_T, y) \quad (1.64)$$

Hence, for a hadron with p_T , the heavy quark will have p_T/z with the probability $D_i^{H_Q}(z)$ to fragment into this hadron. Therefore, the heavy flavor hadron spectra is given by:

$$\frac{d^2\sigma^{H_Q}}{p_T dp_T dy} = \int_{x_T}^1 F^Q(p_T/z, y) D_i^{H_Q}(z, \mu^2) dz \quad (1.65)$$

Here $x_T = \frac{2p_T}{\sqrt{s}}$ [111].

Now if we consider a factorization scale near the heavy quark mass $\mu^2 \rightarrow m_Q^2$, according to PDG reference [4], solving the leading evolution equation, the heavy quark fragmentation function $D_Q^{H_Q}(z)$ is in a form of a delta function and light quarks q and gluons g ($i = g, q$) will not contribute to producing heavy flavor hadrons. Hence, we could write

$$D_{q,g}^{H_Q}(z, \mu^2)|_{\mu^2=m_Q^2} = 0 \quad (1.66)$$

In fact, the Peterson fragmentation function of heavy quarks $D_Q^{H_Q}(z, \epsilon_Q)$ is given

by [112]

$$D_Q^{H_Q}(z, \epsilon_Q) = \frac{N}{z[1 - 1/z - \epsilon_Q/(1-z)]^2} \quad (1.67)$$

Here, N is the normalization constant such that $\int_0^1 D_Q^{H_Q}(z, \epsilon_Q) dz = 1$. $\epsilon_c = 0.03$ and $\epsilon_b = 0.005$. The comparison between the Peterson fragmentation function of beauty quarks and the delta function is shown below

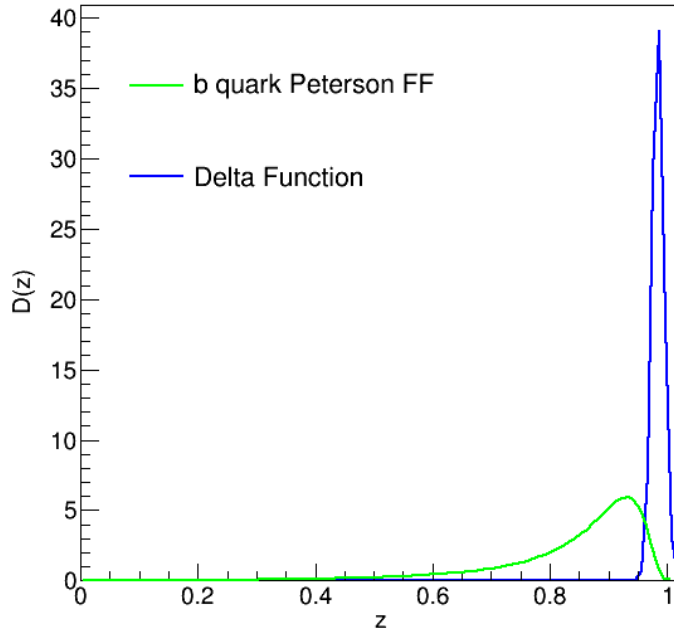


Figure 1-34: The comparison between the Peterson fragmentation function (green) and the delta function (blue) is shown above.

Graphically, we find that the Peterson fragmentation function can be roughly approximated by a delta function. In fact, when $\epsilon_Q = 0$, the Peterson fragmentation function is essentially a delta function $D_Q^{H_Q}(z, \epsilon_Q = 0) \simeq \delta(1 - z)$. Hence, we can define

$$D_Q^{H_Q}(z, \mu^2) |_{\mu^2 = m_Q^2} = f(Q \rightarrow H_Q) \delta(1 - z) \quad (1.68)$$

Here $f(Q \rightarrow H_Q)$ is the heavy quark fragmentation fraction and stands for the

probability of a heavy quark Q hadronize into an open heavy flavor hadron H_Q . Indeed, according to the momentum sum rule that constrains the parton fragmentation function [12]

$$\sum_{H_Q} \int_0^1 z D_Q^{H_Q}(z, \mu^2) dz = 1 \quad (1.69)$$

$$\sum_{H_Q} \int_0^1 z f(Q \rightarrow H_Q) \delta(1 - z) dz = 1 \quad (1.70)$$

$$\sum_{H_Q} f(Q \rightarrow H_Q) = 1 \quad (1.71)$$

This verifies that the sum of heavy quark fragmentation fraction over all heavy flavor hadrons is equal to unity. Next, we have

$$\frac{d^2\sigma^{H_Q}}{p_T dp_T dy} = \int_{x_T}^1 F^Q(p_T/z, y) D_i^{H_Q}(z, \mu^2) dz = \int_{x_T}^1 F^Q(p_T/z, y) D_Q^{H_Q}(z, m_Q^2) dz \quad (1.72)$$

Thus,

$$\frac{d^2\sigma^{H_Q}}{p_T dp_T dy} = \int_{x_T}^1 F^Q(p_T/z, y) f(Q \rightarrow H_Q) \delta(1 - z) dz = f(Q \rightarrow H_Q) F^Q(p_T, y) \quad (1.73)$$

Hence, we have

$$\frac{d^2\sigma^{H_Q}}{p_T dp_T dy} = f(Q \rightarrow H_Q) \frac{d^2\sigma^Q}{p_T dp_T dy} \quad (1.74)$$

This means that the open heavy flavor hadron spectra $\frac{d^2\sigma^{H_Q}}{p_T dp_T dy}$ is essentially proportional to the heavy quark spectra $\frac{d^2\sigma^Q}{p_T dp_T dy}$ with heavy quark fragmentation fraction $f(Q \rightarrow H_Q)$ as the coefficient of proportionality. Experimentally, charm and beauty fragmentation fractions have been measured at LEP, HERA, and LHC and documented in PDG [4]. The fragmentation fraction is often treated roughly a constant,

independent to p_T , y , and \sqrt{s} , and is assumed to be universal in e^+e^- , ep , and pp collisions systems [4].

In terms of being a constant, according to LHCb pp results [113], it appears that the fragmentation fraction has significant \sqrt{s} and p_T dependences while no significant y_B (or η_B) dependence is observed. Figure 1-35 shows the beauty quark fragmentation fraction: $f_u = f(b \rightarrow B^+)$, $f_d = f(b \rightarrow B^0)$, and $f_s = f(b \rightarrow B_s^0)$

In terms of universality, according to Strangeness Quark Matter Conference (SQM) in 2021, a hadronization universality breaking is recently observed from the ALICE experiment at the LHC [114]. Figure 1-36 shows the hadronization universality breaking reported by the ALICE experiment in SQM 2021

Further investigations of these results are currently ongoing. However, we will not expand the discussions here. Now, equipped with the understanding of heavy flavor physics in vacuum from pp collisions as a reference, we are ready to use heavy quarks to study QGP created in heavy-ion collisions.

1.6.4 Heavy Quark Diffusion

In the limit of low p_T or equivalently long wavelength, for heavy quarks inside the QGP medium, the elastic collision cross section dominates. In the elastic $Qq \rightarrow Qq$ process in the thermally equilibrated QGP medium, heavy quarks have relatively small momentum transfers on the order of the temperature compared to the masses of heavy quarks: $m_Q > |k| \simeq T$. If we consider mean free time of heavy quarks in the QGP medium to be about $\tau \sim 0.44 fm/c$ [115], the number of scattering of heavy quarks in the QGP medium will be about $n \sim \frac{\tau_{QGP}}{\tau_{HQ}} \simeq 23 \sim O(10)$.

Now, we can consider a simple binomial process to model the diffusion of the heavy quark in the QGP medium. Assuming the momentum of the heavy quark at $t = 0$ is p , after the time τ_{HQ} , one scattering happens. The momentum of the heavy quark at $t = \tau_{HQ}$ either $p + k$ or $p - k$. Each has $1/2$ probability. Next, after another τ_{HQ} , another scattering happens. The momentum of the heavy quark at $t = 2\tau_{HQ}$ either $p + 2k$, p or $p - 2k$ with $1/4$, $1/2$, and $1/2$ probability respectfully. Therefore, the standard deviation of binomial process $\sigma_p = \frac{\sqrt{n}}{2}k$. If we take $n = 25$,

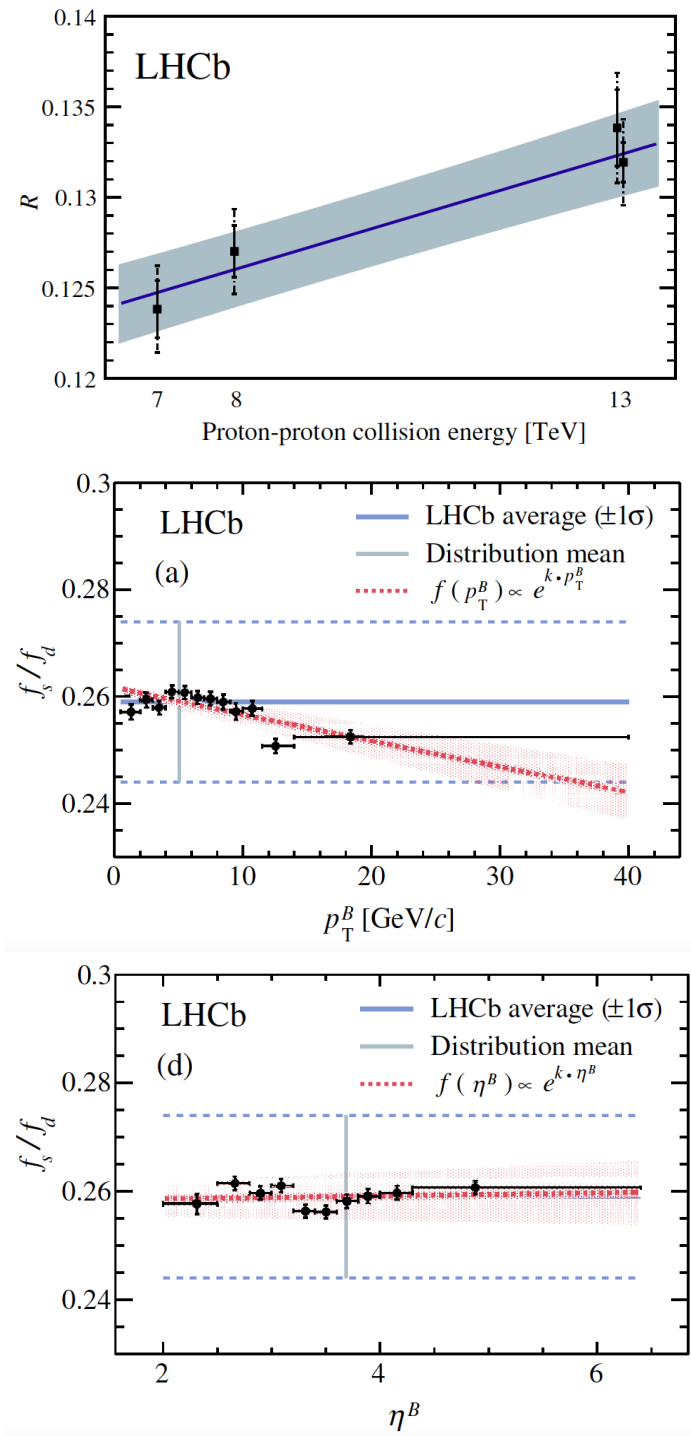


Figure 1-35: R , the corrected yield ratio of B_s^0/B^+ , as a function of the pp collision energy \sqrt{s} (top), the f_s/f_d ratio as a function p_T (middle), and the f_s/f_d ratio as a function η_B (bottom) from the LHCb experiment, are shown above.

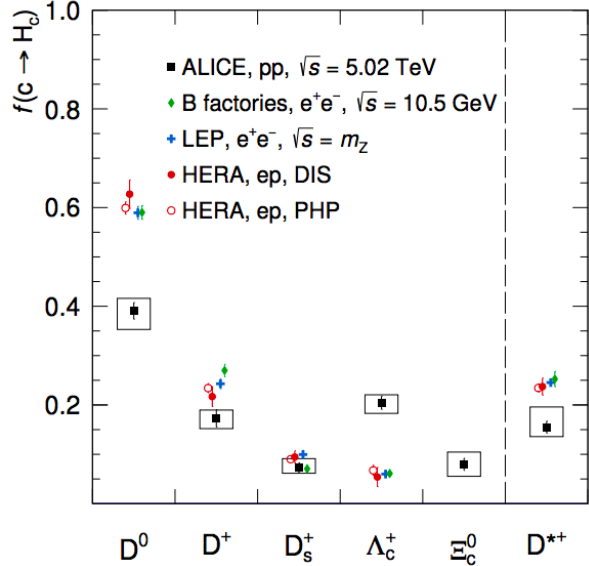


Figure 1-36: The charm quark fragmentation fraction to different charm hadrons species in e^+e^- , ep , and pp collisions are presented above. From the ALICE experiment, we can clearly see that the fragmentation fraction of D^0 has dropped by about 40% while the Λ_c^+ has enhanced by about a factor of 4. Therefore, the hadronization universality is clearly broken at the LHC energy in the charm sector.

$\sigma_p = 2.5k \simeq 2.5T_{QGP} = 0.4$ GeV. Experimentally, we consider a heavy quark with a momentum of about $p > 1.5$ GeV/c $>>$ σ_p . According to Figure 1-34, we could see that the heavy quark transverse momentum is well above 1 GeV/c. Hence, the heavy quark should still retain a lot of memory about its initial conditions even after multiple small scatterings with QGP medium. Hence, in these conditions, heavy quark undergoes Brownian-like motion in the QGP medium [103]. Its motion in the QGP medium could be characterized by the Planck-Fokker Equation, which could be schematically written as follows [116]:

$$\frac{\partial}{\partial t} f_q(t, \vec{p}) = \frac{\partial}{\partial p_i} \{ A_i(\vec{p}) f_q(t, \vec{p}) + \frac{\partial}{\partial p_j} [B_{ij}(\vec{p}) f_q(t, \vec{p})] \} \quad (1.75)$$

Here, $f_q(t, \vec{p})$ is the heavy quark phase-space distribution function. If we ignore the modification of cold nuclear matter effects on the heavy quark initial production spectra, then in heavy-ion collisions:

$$F^Q(t = 0, p_T) \propto \frac{d\sigma_{FONLL}}{p_T dp_T} \quad (1.76)$$

$A_i(\vec{p})$ and $B_{ij}(\vec{p})$ are transport parameters.

$$A_i(\vec{p}) = A(\vec{p})p_i \quad (1.77)$$

The transport parameter $A_i(\vec{p})$ is related to the thermal relaxation rate and $B_{ij}(\vec{p})$ is related to the momentum diffusion of heavy quarks [103]. The heavy quark spatial diffusion coefficient D_s is related to the transport parameter as follows:

$$D_s = \frac{T}{m_Q A(p = 0)} \quad (1.78)$$

D_s characterizes the fundamental property of the QGP $\frac{\eta}{s}$ via the relationship

$$2\pi T D_s \simeq \frac{\eta}{s} \quad (1.79)$$

More detailed studies have been carried out to examine the coupling strength of heavy quarks and quantify the information that heavy quarks carry as they traverse through the QGP medium [117].

1.6.5 Heavy Quark Energy Loss

In the limit of high p_T or equivalently short wavelength, the inelastic cross section starts to dominate [103]. Heavy quarks lose a substantial amount of energy as they travel fast through the QGP medium [118]. In a simplified schematization, there are two different pictures that describe the energy loss mechanism of heavy quarks in the QGP medium. In the pQCD picture, the coupling of the constituents of the QGP is assumed to be weak. Therefore, the QGP is made of weakly coupled quasiparticles. Heavy quarks scatter off the constituents incoherently when propagating through the QGP medium. There are two energy loss mechanisms: collisional energy loss and radiative energy loss [116]. The collisional energy loss is given by $-\frac{dE}{dx} = \kappa_{coll} T^2$ and the radiative energy loss is given by $-\frac{dE}{dx} = \kappa_{rad} T^3 x$ [119, 120]. Figure 1-37 shows

schematically heavy quark energy loss mechanism in the QGP medium

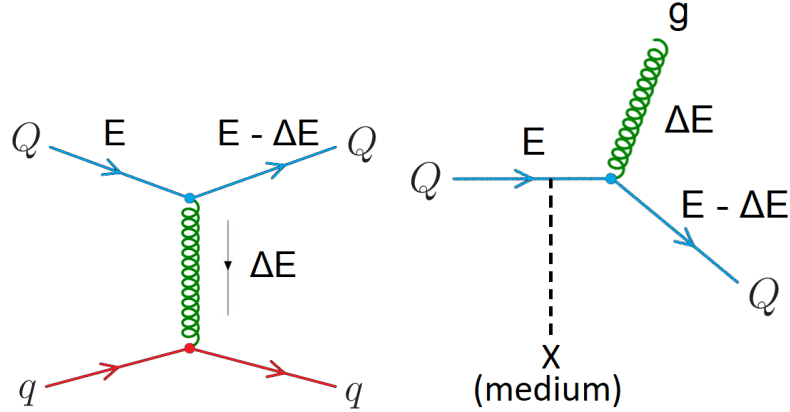


Figure 1-37: The schematic demonstration of the pQCD picture: collisional energy loss (left) and radiative energy loss (right) of heavy quarks in the QGP medium.

The other picture, AdS/CFT, takes the strong coupling limit. In this picture, QGP behaves like a liquid and heavy quarks scatter off the constituents coherently in the QGP medium. The AdS/CFT model applies holographic drag force [121] to calculate the energy loss of heavy quark [122] in the QGP medium

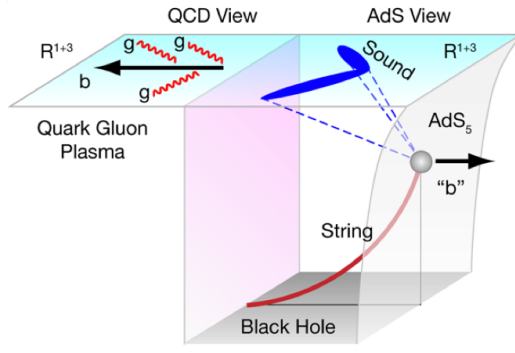


Figure 1-38: The schematic demonstration of ADS/CFT picture: a quark loses energy in the QGP medium holographically due AdS/CFT drag force.

In the pQCD picture, as $p_T \rightarrow \infty$, similar to electron Bremsstrahlung via QED radiation in the matter [123], for a heavy quark traveling through the QGP medium, its radiative energy loss via soft gluon radiation will dominate. The soft gluon radiation spectrum by a parton in the QGP medium is given by [124]

$$dP = \frac{\alpha_S C_F}{\pi} \frac{d\omega}{\omega} \frac{k_\perp^2 dk_\perp^2}{(k_\perp^2 + \omega^2 \theta_0^2)^2} \quad (1.80)$$

Where

$$\theta_0 \equiv \frac{m}{E} \quad (1.81)$$

Here, ω is the energy of the gluon and k_\perp is the transverse momentum of the gluon, C_F is the color factor (Casimir) which is 3 for gluons with one color and one anti-color charges and $4/3$ for quarks with one color charge. From Equation 1.80 above, a suppression of radiation at a small angle $0 < \theta < \theta_0$ is expected. This effect is known as the dead cone phenomenon [124]. In Equation 1.81, that as m increases, the dead cone angle $\theta_0 = \frac{m}{E}$ will decrease as the parton mass increases. Figure 1-39 schematically shows a charm quark radiating gluons in the medium with a dead cone in the small angles:

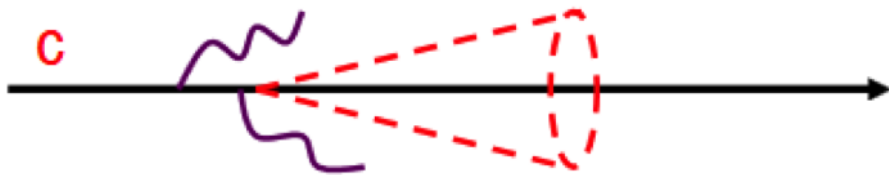


Figure 1-39: The schematic demonstration of a charm quark radiation is shown above. A suppression in small angles due to the dead cone effect in the QGP medium is highlighted.

Since we have the following mass hierarchy for quarks and gluons:

$$m_g < m_q < m_c < m_b \quad (1.82)$$

We should expect the energy loss to follow

$$\Delta E_g > \Delta E_q > \Delta E_c > \Delta E_b \quad (1.83)$$

We call the inequality above to be the flavor dependence of energy loss, which is an important feature of the heavy quark energy loss mechanism in the QGP medium. The studies of the heavy quark energy loss mechanism in QGP will help us determine the fundamental jet transport coefficient \hat{q} that characterizes the scattering power of the medium [103], which relates to the mean free path and the momentum diffusion coefficient of heavy quarks [125]. The determination of \hat{q} will be crucial for us to decipher the inner workings of the QGP [126].

1.6.6 Heavy Quark Hadronization

After heavy quarks traverse through the medium, it will hadronize into heavy flavor hadrons, which could be fully reconstructed from their final state decay products in experiments. As described in Section 1.2.7, in general, hadronization is non-perturbative. Considering heavy quark dynamics and applying hadronization models, physicists develop theoretical models to describe heavy quark hadrochemistry. Below, I will present three model candidates, the Texas A&M University (TAMU) Model [127], the model developed from Cao et. al. (Cao, Sun, Ko) [128], and the Equal Velocity Recombination (EVR) Model [129], to describe beauty quark production and hadronization in vacuum:

TAMU Model

The TAMU Model uses a thermodynamic T-matrix formalism in terms of “ladder diagrams” to compute the in-medium scattering amplitude between heavy quarks and light quarks and determine the non-perturbative transport parameters A_i and B_{ij} in the Planck-Fokker equation shown in Eq 1.75 [127]. Figure 1-40 shows schematically the “ladder diagram” describing the dynamic evolution of a heavy quark in the QGP medium.

The input of T-matrix is a lattice QCD potential [130] corrected with relativistic effects to model the non-perturbative interactions between heavy quarks and partons in the medium, which makes it consistent with heavy flavor spectroscopy in vac-

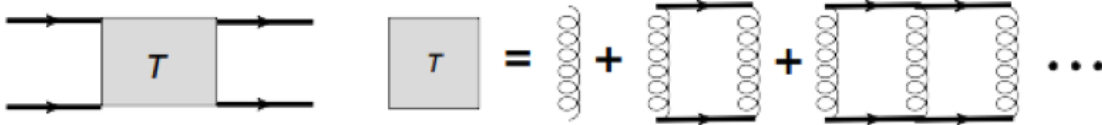


Figure 1-40: The ladder diagram used by the TAMU model to describe heavy quark diffusion in the QGP medium is shown schematically above.

uum to determine the thermal relaxation rate coefficient $A_i(p, T)$. Only elastic collisional energy loss is included in the calculations. Resonance recombination model of heavy quarks with light quarks nearby is applied to describe heavy quark hadronization [131]. A FONLL fragmentation hadronization treatment is implemented for the partons that do not coalesce. Finally, effective hadronic scattering amplitudes are used to model heavy flavor hadronic rescattering with other hadrons before the kinetic freeze-out stage. The background parton composition and kinematics are modeled by the standard hydrodynamic simulations of the bulk medium in nuclear collisions.

Cao, Sun, Ko Model

The Cao, Sun, Ko Model employs an advanced Langevin-hydrodynamics approach [133, 134] incorporating both elastic and inelastic energy loss of heavy quarks inside the dynamical QGP medium. Below shows schematically the relativistic Langevin equations to simulate the dynamics of heavy quarks in the QGP medium

$$\Delta \vec{p} = -\gamma \frac{T^2}{M} \vec{p} \Delta t + \vec{\xi}(t) \quad (1.84)$$

And

$$\Delta \vec{x} = -\frac{\vec{p}}{E} \Delta t \quad (1.85)$$

The noise is modeled by the Gaussian diffusion function

$$P(\vec{\xi}) \propto \exp\left[\frac{\vec{\xi}^2}{2D_p \Delta t}\right] \quad (1.86)$$

The dimensionless γ factor is defined as

$$\gamma = \frac{M}{\tau_{HQ} T^2} \quad (1.87)$$

The Cao, Sun, Ko Model uses a comprehensive coalescence model with strict energy-momentum conservation and PYTHIA fragmentation simulation [132] with the default Peterson fragmentation function. The coalescence probability is determined from the resonant scattering rate of heavy quarks in the QGP according to the resonant recombination model [131, 135]. In this model, if heavy quarks do not coalesce, they will hadronize via fragmentation mechanism. The hadron interactions in the freeze-out stage are model with UrQMD developed by the Duke theory group.

EVR Model

In this model, the transverse momentum distribution of the initially produced heavy quark is calculated by FONLL [129]. The jet quenching effect in heavy-ion collisions is considered according to the R_{AA} measurement of B^+ . The transverse momentum distributions of light-flavor quarks are obtained from data of light hadrons in the model. The EVR Model is particular designed to study low p_T and mid-rapidity charm quarks produced at the LHC energy. It considers the equal-velocity combination of bottom quark with light-flavor anti-quarks to form B mesons, a framework based on of co-moving quark recombination model (QCM).

In addition to TAMU, Cao, Sun, Ko, and EVR Models, many other theoretical models attempt to describe heavy quark hadrochemistry in heavy-ion collisions. A complete list of heavy quark hadrochemistry models is compiled in the heavy flavor review paper [116]. Nevertheless, the large discrepancies among different hadronization models significant limits our abilities to interpret heavy flavor data. Therefore, heavy-ion experimentalists precisely measure heavy flavor physics observables with different hadron species over broad kinematic ranges and provide constraints for models to reduce the theoretical uncertainties in hadronization.

Chapter 2

Review of Heavy Flavor Results

In the previous section, we have introduced relativistic heavy-ion physics and heavy flavor physics in vacuum and QGP. Physicists propose many experimental observables to study open heavy flavor physics and test theoretical models in heavy-ion collisions. Traditionally, heavy flavor hadron observables, such as v_2 , R_{AA} , and production yield ratio, have been extensively studied. In this section, we will review selected experimental results and their comparisons with theoretical models and discuss the physics messages from the measurements.

2.1 Elliptic Flow

In the QGP medium, heavy quarks are diffused by the color force and multiple scatter with medium constituents, which could generate sizable azimuthal anisotropy v_2 [103]. In addition, due to the azimuthal anisotropic geometry of the medium, heavy quarks will have different path lengths in different directions, which will also contribute to building up v_2 . Experimentally, we scale the v_2 and the hadron kinetic energy $KE_T = \sqrt{m^2 + p_T^2} - m$ of heavy quarks by $1/n_q$ according to the Number of Constituent Quark (NCQ) Scaling in quark coalescence model [136]. Figure 2-1 shows the comparison of the v_2/n_q as a function of K_T/n_q of D^0 ($c\bar{u}$) meson with light flavor hadrons with STAR experiments at RHIC [137] and the CMS experiment at LHC [138].

We could see a reasonably good NCQ scaling behavior of D^0 meson with other

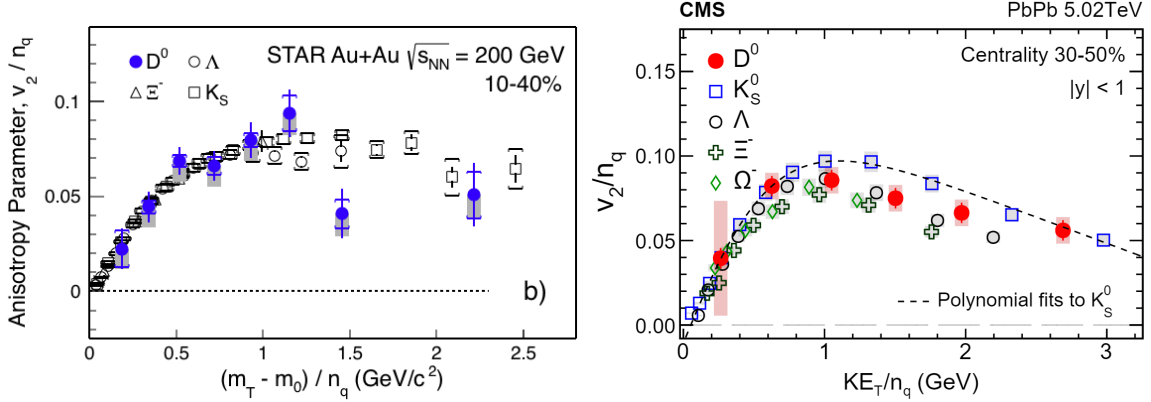


Figure 2-1: The NCQ scaled D^0 v_2/n_q vs K_T/n_q and the comparison of light hadrons measured by the STAR experiment at RHIC (left) and the CMS experiment at LHC (right) are shown above.

light flavor hadrons, which suggests sizable collectivity of charm quarks in the QGP medium.

To study beauty quarks v_2 , an indirect approach is employed. Figure 2-2 shows the elliptic flow of electrons from beauty hadron decays $b(\rightarrow c) \rightarrow e$ measured by the ALICE experiment [139] and muons from beauty hadron decays $b \rightarrow \mu$ measured by the ATLAS experiment [140]:

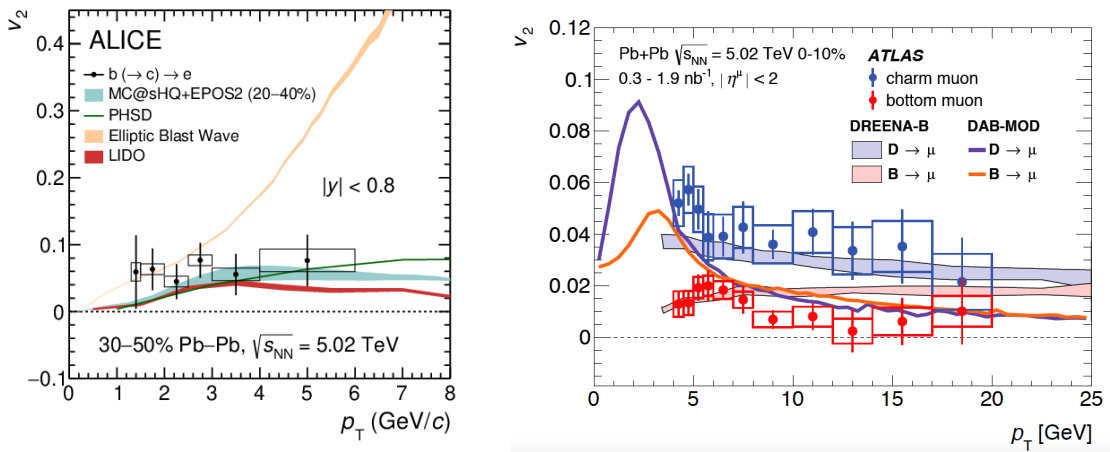


Figure 2-2: The v_2 of electrons from b-hadron decays as a function of electron p_T measured by the ALICE experiment (left) and the v_2 of muons from b-hadron decays as a function of muon v_2 measured by the ATLAS experiment (right) are shown above.

Comparing Figure 2-2 with Figure 2-1, we can see that beauty quarks do not demonstrate as much anisotropy as charm quarks in heavy-ion collisions. However, so far, fully reconstructed B-meson v_2 has not been measured by any experiment.

2.2 Nuclear Modification Factor

As mentioned previously, the nuclear modification factor R_{AA} can describe the modification of hadron spectra in AA collisions with respect to the pp collisions. To study the medium modification to heavy quarks, we first would like to investigate the cold nuclear matter effect in pA collisions. Figure 2-3 and Figure 2-4 show the prompt D mesons and B mesons nuclear modification factors R_{pA} in pPb collisions measured by the ALICE experiment [141] and the CMS experiment [142] respectively

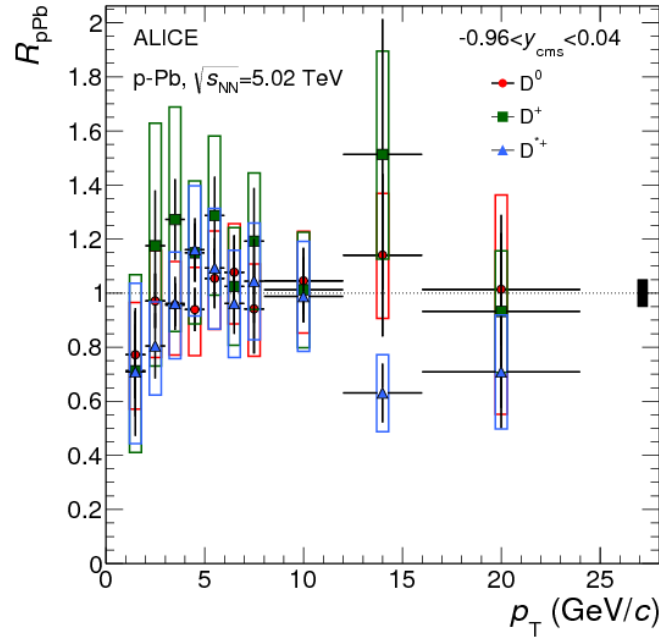


Figure 2-3: The R_{pA} as a function of p_T of prompt D mesons measured by the ALICE experiment is shown above.

There is no significant modification of the charm quarks due to cold nuclear matter effects since the R_{pA} of D^0 are overall unity within experimental uncertainties. Hence, any modification of D and B mesons observed in the AA collisions should come from

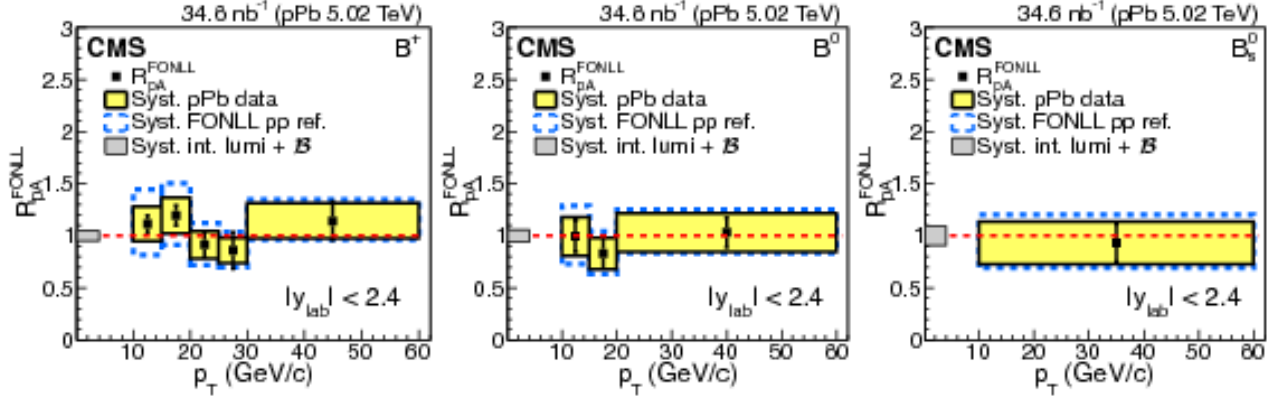


Figure 2-4: The R_{pA} as a function of p_T of B^+ , B^0 , and B_s^0 mesons measured by the CMS experiment is shown above.

the final state QGP effect instead of the initial state effects due to the nPDF of Pb ions.

Next, we investigate B mesons R_{AA} in the AA collisions. Figure 2-5 shows R_{AA} heavy flavor hadrons measured with experiments at RHIC and LHC.

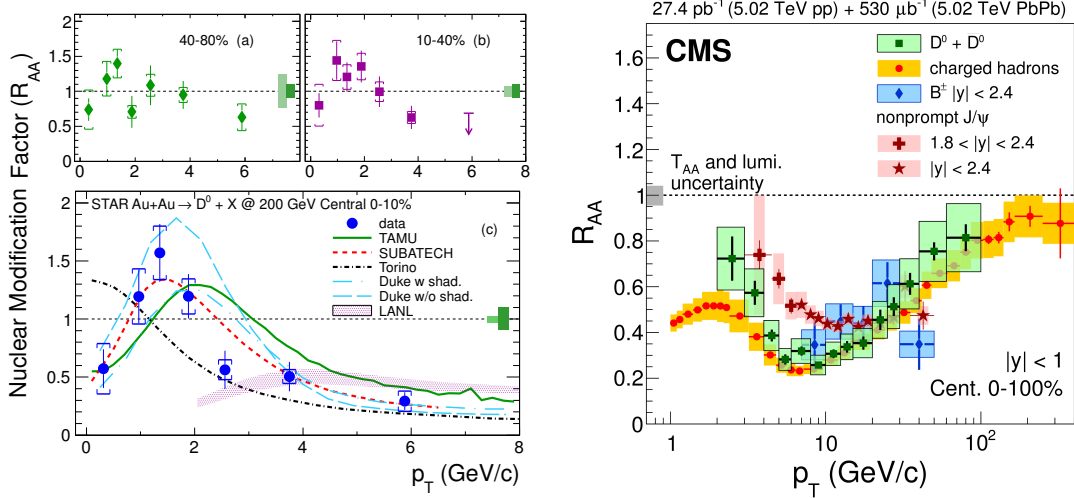


Figure 2-5: The fully reconstructed D^0 R_{AA} vs p_T with the STAR experiment in 0 - 10%, 10 - 40%, and 40 - 80% centrality at RHIC and D^0 , B^+ , non-prompt J/ψ , and charged hadrons R_{AA} vs p_T at 0 - 100% centrality with the CMS experiment at LHC are shown above.

We could see that the R_{AA} of D^0 and B^+ are both below 1, which suggests charm and beauty quarks lose a significant fraction of energy to the QGP medium. As p_T

increases, the R_{AA} of light and heavy flavor hadrons converge to the same values and approach unity where Lorentz γ factor comes into play and the mass of the hadron becomes irrelevant. In addition, the CMS results above indirectly agree with the expectation of the flavor dependence of energy loss: $R_{AA}^h < R_{AA}^D < R_{AA}^B < 1$. Most theoretical model calculations are in reasonable agreement with the R_{AA} data.

To better constrain theoretical model calculations and understand the energy loss mechanism of heavy quarks in the QGP medium, we need to perform more precise measurements of B- and D-mesons R_{AA} and v_2 down to lower p_T where the mass of heavy quarks becomes important and models diverge from each other. The ALICE experiment has performed the first measurement of prompt and non-prompt D^0 R_{AA} down to $p_T = 0$ shown in Figure 2-6 below

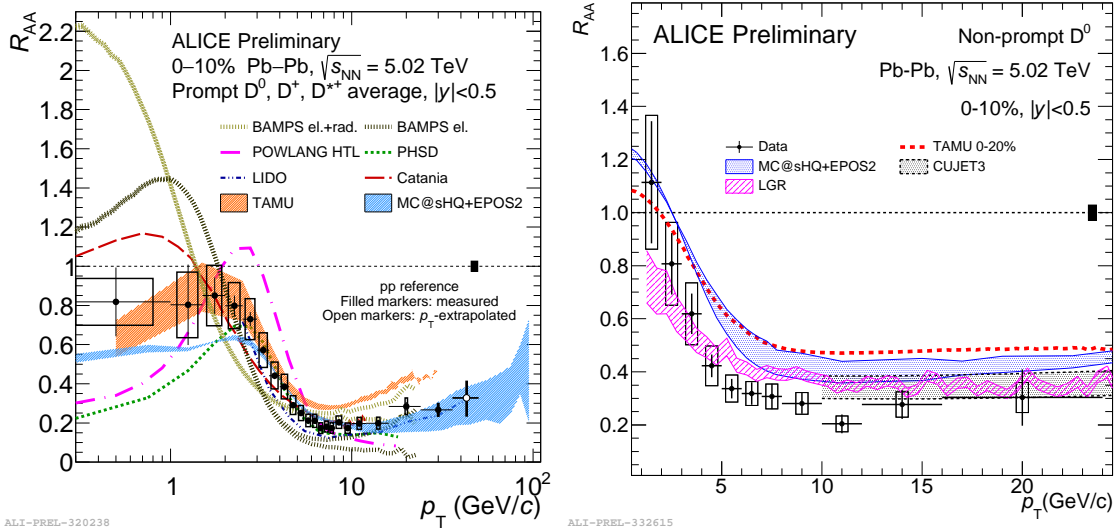


Figure 2-6: The R_{AA} of prompt D mesons vs p_T down to $p_T = 0$ (left) and non-prompt D mesons down to $p_T = 1$ GeV/c (right) are shown above.

From the ALICE measurement of prompt and non-prompt D mesons R_{AA} down to very low p_T , we could see that very few models are able to simultaneously describe D^0 R_{AA} at both low and high p_T . Nonetheless, the fully reconstructed B-meson R_{AA} measurement from exclusive b decay down to very low p_T is still missing. We should try to perform B-meson R_{AA} measurement down to very low p_T to provide a complete picture to constrain the jet transport coefficient \hat{q} and heavy-quark diffusion

coefficient. Also, fully reconstructing B mesons down to $p_T = 0$ will allow us to measure inclusive beauty production cross section in pp collisions and test pQCD calculations.

2.3 Production Yield Ratio

According to the theoretical reviews of heavy-quark hadrochemistry in heavy-ion collisions [144, 145], the strange-to-non-strange meson (H_s/H^0) and baryon-to-meson (Λ_Q/H^0) ratios are excellent observables to test hadronization models. Both RHIC and LHC have carried out extensive measurements of fully reconstructed charm hadron yield ratios. Figure 2-8 shows the fully reconstructed prompt D_s^+/D^0 ratios measured by the STAR [146] and ALICE [147] experiments

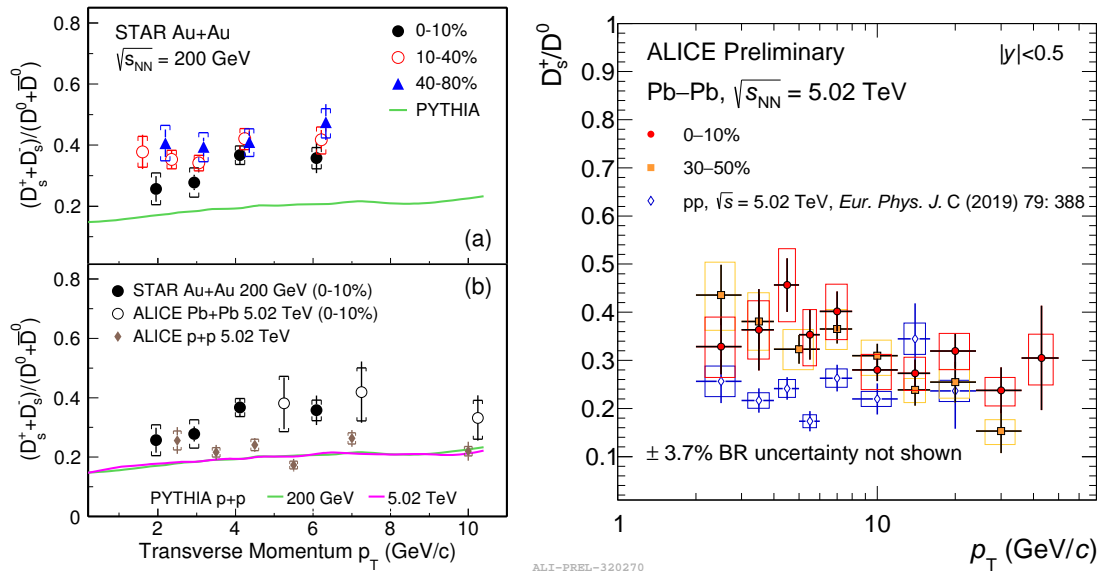


Figure 2-7: The fully reconstructed D_s^+/D^0 ratios in Au + Au measured by the STAR experiment at RHIC (left) and in PbPb the ALICE experiment at LHC (right) as functions of p_T are shown above.

We can see that in general, both D_s^+/D^0 ratios in heavy-ion collisions lie above pp collisions.

Figure 2-8 shows the fully reconstructed Λ_c^+/D^0 ratios measured by the STAR [149] and ALICE [150] experiments

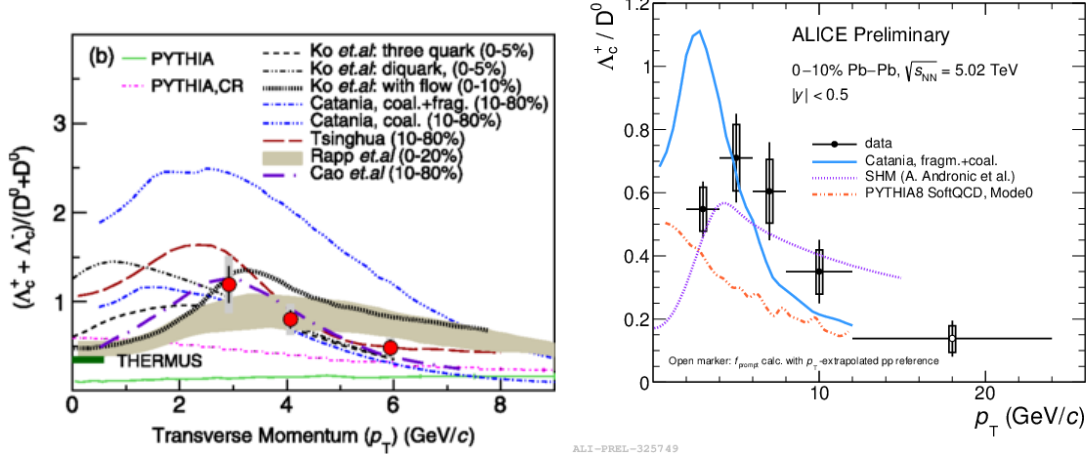


Figure 2-8: The fully reconstructed Λ_c^+/D^0 ratio in pp and heavy-ion collisions measured by the STAR experiment at RHIC (left) and the CMS experiment at LHC (right) are shown above.

Many different theoretical predictions agree reasonably well with the experiments due to their large uncertainties. However, these large discrepancies among hadronization models significantly limit our ability to interpret heavy flavor experimental data.

The ALICE experiment also performs a comprehensive study on charm quark hadronization in pp , pPb , and $PbPb$. Figure 2-9 shows the D_s^+/D^0 and Λ_c^+/D^0 ratios as functions of event multiplicity from small to large collision systems.

In the multiplicity studies, overall increasing trends of both D_s^+/D^0 and Λ_c^+/D^0 ratios in higher multiplicity are observed. Moreover, this is only in the charm sector. Similar fully reconstructed b-hadron measurements to study beauty hydrochemistry are still missing.

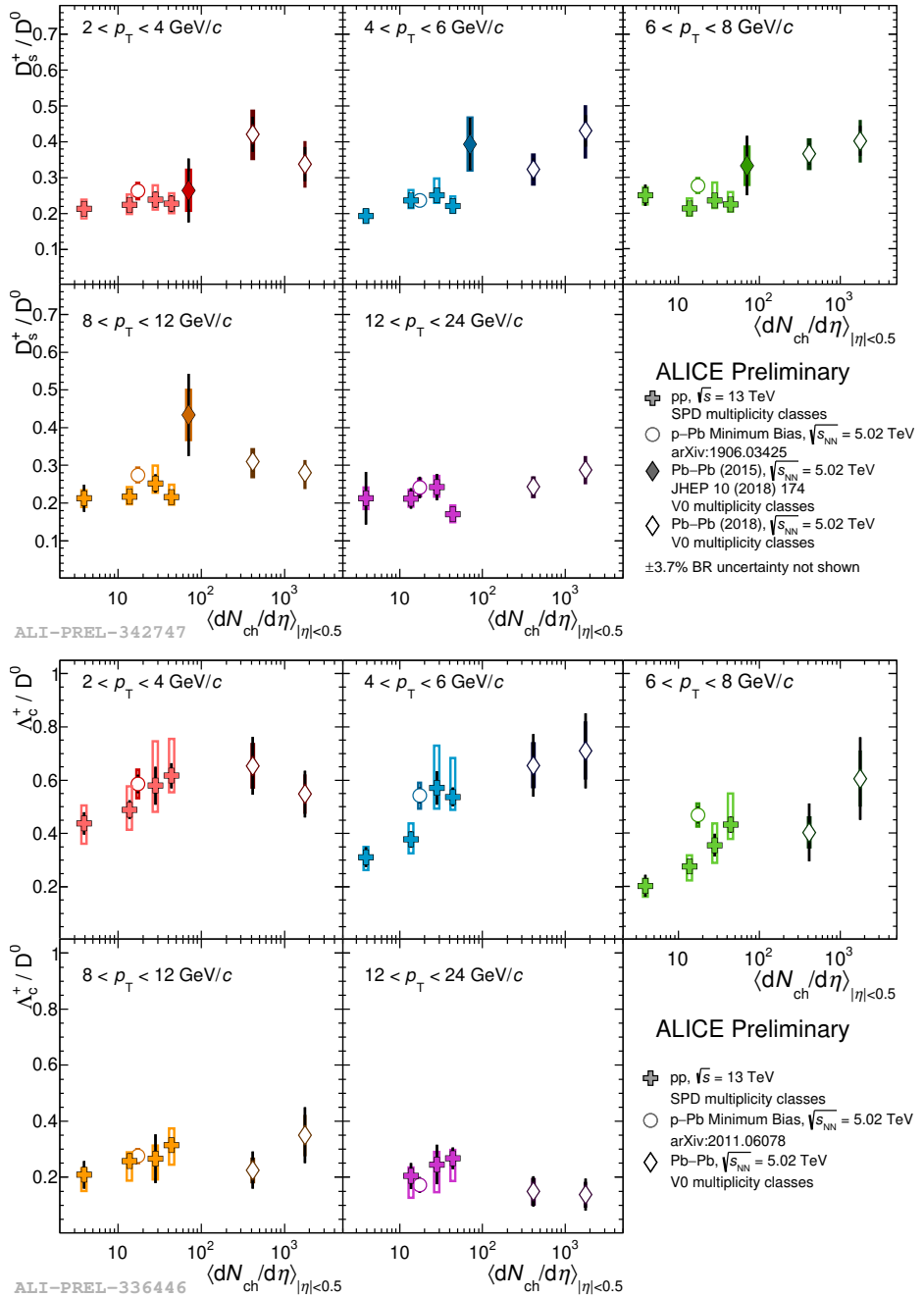


Figure 2-9: The fully reconstructed D_s^+/D^0 (top) and Λ_c^+/D^0 ratios (bottom) as a function of event multiplicity $\langle dN_{ch}/d\eta \rangle$ within $|\eta| < 0.5$ in p_T from 2 - 4, 4 - 6, 6 - 8, 8 - 12, and 12 - 24 GeV/c in pp , pPb, and PbPb collisions measured by the ALICE experiment are shown above.

Therefore, it is crucial to have more precise measurements over a wide range of p_T and multiplicity in both beauty and charm sectors to constrain theoretical models. Currently, the only published fully reconstructed b-hadron measurements in heavy-ion collision are the B_s^0 and B^+ based on CMS 2015 PbPb datasets [148]. Figure 2-10 shows the B_s^0 B^+ R_{AA} R_{AA} and their ratios in pp and PbPb collisions

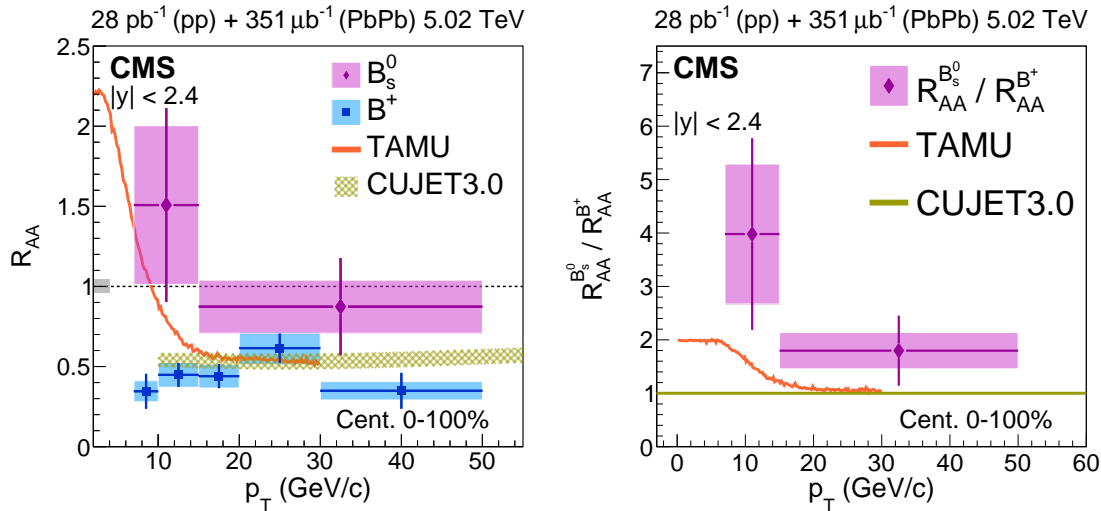


Figure 2-10: The fully reconstructed B_s^0 and B^+ R_{AA} (left) and B_s^0/B^+ R_{AA} ratio (right) as a function of p_T using the 2015 CMS pp and PbPb datasets are shown above.

These first fully reconstructed B-meson measurements in heavy-ion collisions are good. Nonetheless, the B_s^0 measurement has relatively large uncertainties due to the very limited statistics. The B_s^0 significance is still below 5σ . In order to better constrain hadronization model calculations and better interpret our data, we should perform more differential measurements in the beauty sector with enhanced precision.

In the baryon-to-meson ratio studies, LHCb has conducted fully reconstructed Λ_b^0/B^+ ratio in pp and pPb collision [151] shown below in Figure 2-11

The Λ_b^0/B^0 double ratios in pPb to pp in the forward region are near unity according to the LHCb measurement. No significant p_T or y dependence is observed. It would be interesting to conduct similar measurements in mid-rapidity region in pp and pPb collisions. However, so far no fully reconstructed Λ_b^0 measurement has been carried out in heavy-ion collisions due to the limited statistics and large combinatorial

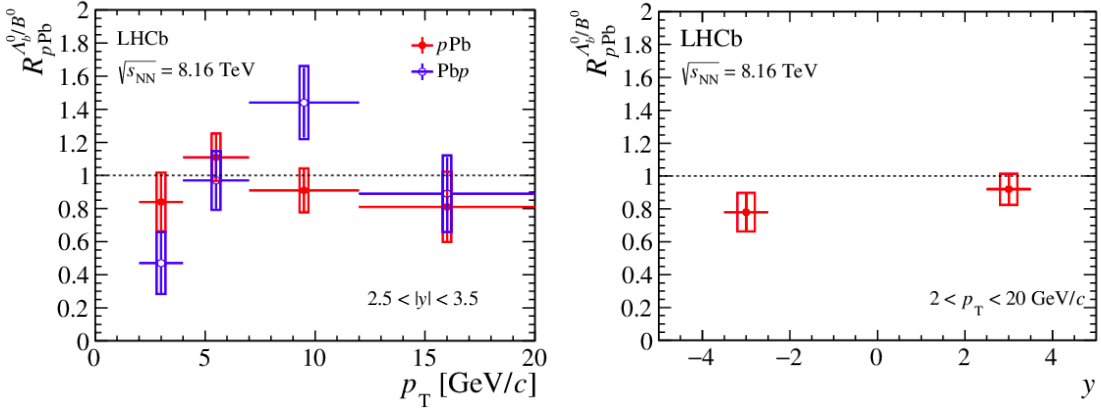


Figure 2-11: The fully reconstructed Λ_b^0/B^+ R_{pA} ratios as a function p_T (left) and y (right) in pp , pPb , and Pbp collisions measured by the LHCb experiment are shown above.

background of Λ_b^0 .

2.4 Heavy Flavor Hadron-Jet Angular Correlations

Aside from the traditional heavy flavor observables: R_{AA} , v_2 , and production yield ratio, modern observables, such as heavy flavor hadron-hadron and heavy flavor hadron-jet angular correlations, have better differentiation to provide more insight for the understanding of the dynamics and interaction mechanism of heavy quarks in the QGP medium.

The measurements of angular correlations between heavy flavor hadrons and jets can be used to constrain parton energy loss mechanisms and to better understand heavy-quark diffusion in the medium. From the D-jet angular correlation studies, the quantitative studies of the medium modification to the radial profile of charm quarks could shed light on the interaction mechanism of charm quarks with the medium. Figure 2-12 shows the measurement of D-jet angular correlation in $PbPb$ and pp collisions with the CMS experiment [152]

At low p_T , the D^0 mesons are pushed radially outward in $PbPb$ collisions compared to pp , which shows effects of charm-quark diffusion with the presence of the QGP medium. At high p_T , the shape is approximately consistent with unity. While the

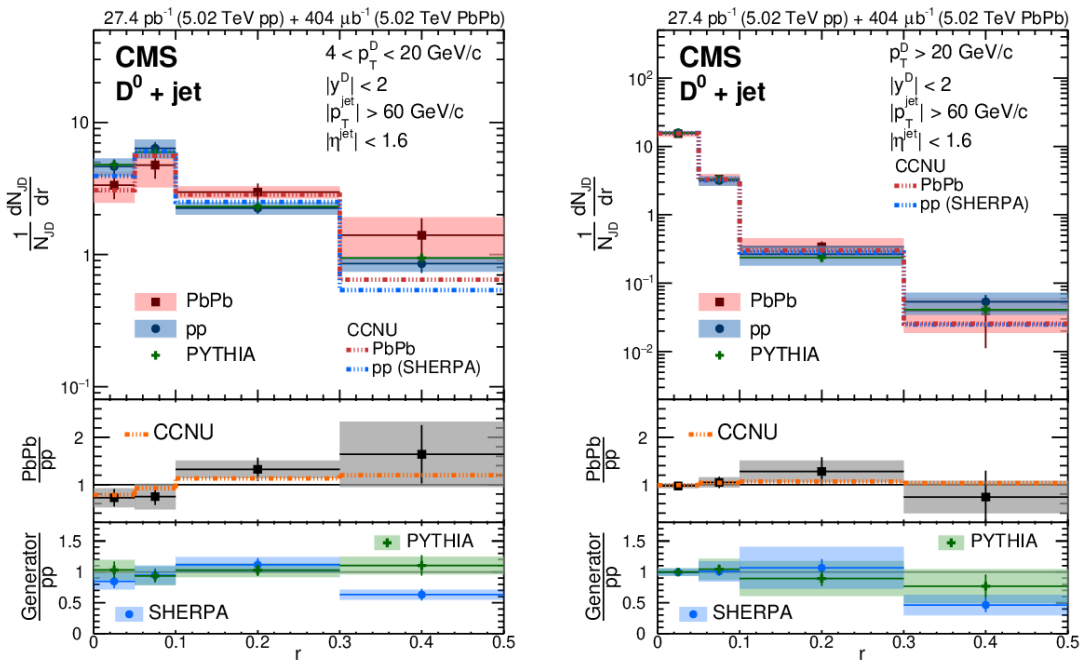


Figure 2-12: Distributions of fully reconstructed D^0 mesons in jets, as a function of the distance from the jet axis (r) for jets of $p_T^{jet} > 60$ GeV/c and $|\eta^{jet}| < 1.6$ measured in pp and $PbPb$ collisions at $\sqrt{s_{NN}} = 5.02$ TeV, for $4 < p_T^D < 20$ GeV/c and $p_T^D > 20$ GeV/c, are shown above. The jet radius is defined as $r = \sqrt{(\Delta\phi_{jD})^2 + (\Delta\eta_{jD})^2}$ where ϕ_{jD} and η_{jD} are the η and ϕ of the D^0 meson with respect to the jet axis.

CCNU model is in reasonably good agreement with the PbPb/ pp ratio, its predictions are lower compared to the measurements of $\frac{1}{N_{jD}} \frac{dN_{jD}}{dr}$ in individual pp and PbPb collisions.

2.5 Heavy Flavor Hadron-Hadron Correlations

Another observable is heavy flavor hadron-hadron correlation, which is even better to tag the heavy quark $Q\bar{Q}$ pair the produced back-to-back in the early stage of hard scattering processes and understand the modification effects as they propagate through vacuum and medium. Experimentally, the observable is a fully reconstructed open heavy flavor hadron correlates with associated hadrons produced within the same event and subtracts the background in mixed events. In the analysis, $\Delta\eta$ and $\Delta\phi$ distributions of the heavy flavor hadrons from associated hadrons are used to quantify the correlation. Figure 2-13 shows the D meson-hadron angular correlation measured with the ALICE experiment [153]

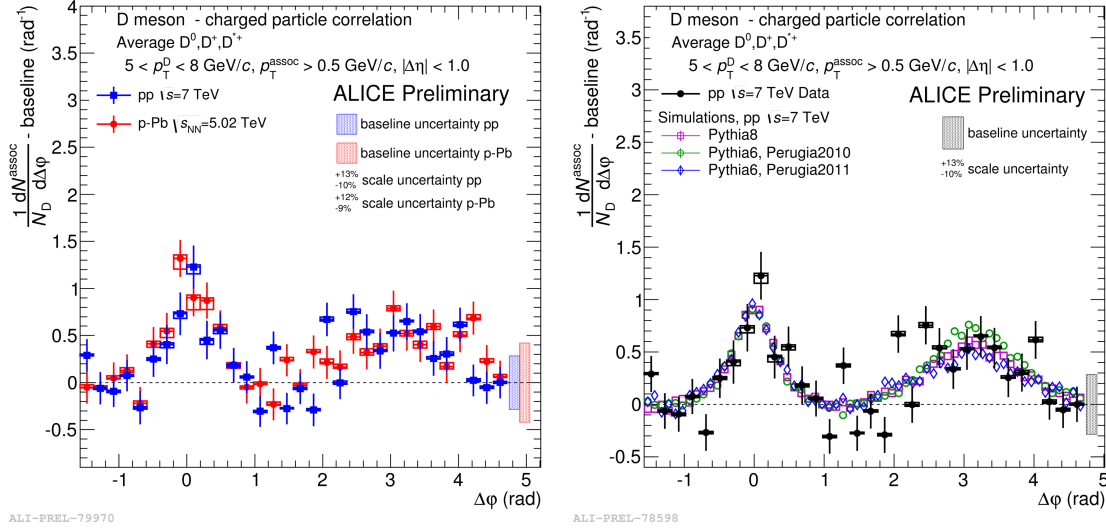


Figure 2-13: The ALICE D-hadron angular correlation in both pp (blue) and pPb (red) collision (left) and the comparison of pp data with PYTHIA calculations (right) are shown above.

In the D-hadron correlation, there are two peaks at $\Delta\phi = 0$ and π . At $\Delta\phi = 0$, hadrons are produced along with the charm quarks via fragmentation mechanism. At

$\Delta\phi = \pi$, the hadrons are produced from back-to-back jets to maintain momentum conservation. The pp measurements are overall consistent with PYTHIA calculations. From the comparison between the results in the pp and pPb, the D-hadron angular correlation distributions are compatible with each other within uncertainties. Consequently, no evident effects on the charm fragmentation and hadronization due to cold nuclear matter can be claimed [153].

STAR has also performed the 2D $\Delta\eta \times \Delta\phi$ measurement of fully reconstructed D^0 -hadron correlation in Au + Au collisions [154] shown in Figure 2-14

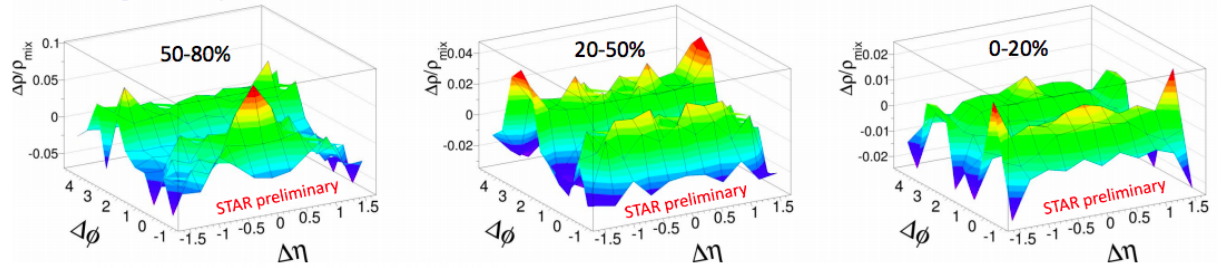


Figure 2-14: The 2D $\Delta\eta \times \Delta\phi$ distributions of D^0 mesons and associated hadrons in Au + Au centrality 0 - 20%, 20 - 50%, and 50 - 80% at $\sqrt{s_{NN}} = 200$ GeV measured by the STAR experiment are shown above.

As expected, the D^0 -hadron angular correlation get broadened and the peak near $\Delta\eta = 0$ and $\Delta\phi = 0$ disappear in more central Au + Au collisions where QGP is more likely to be created and redistribute the energy among particles. In the beauty sector, so far, no such measurement has been carried out in heavy-ion collisions. The B-hadron correlation measurement, along with the D-hadron correlation measurement, will be crucial to provide deeper insights to study heavy quark diffusion and energy loss in the QGP medium.

2.6 Some Questions in Heavy Flavor Physics

As seen in Section 2.1 - 2.5, extensive studies on fully reconstructed charm hadrons have been performed at RHIC and LHC. Furthermore, many measurements of fully reconstructed b-hadrons produced in pp and pPb collisions have been carried out

by the LHCb experiment. In heavy-ion collisions, only one measurement of fully reconstructed b-hadron has also been published with the CMS experiment. Hence, to have a more comprehensive understanding of heavy flavor physics, we should perform more precise and differential measurements on fully reconstructed b hadrons.

As seen above, Figure 2-1 and Figure 2-6 show that charm hadrons not only have sizable v_2 but also have much less than unity R_{AA} in heavy-ion collisions. Such results could be interpreted as a hint of thermalization of charm quarks in the QGP medium [155], which could make charm quark not an ideal probe to the QGP medium.

However, results from Figure 2-2 and Figure 2-10 show that beauty quarks have a much smaller probability of being thermalized in the QGP medium compared to charm quarks because they are heavier. Hence, beauty quarks are more desired probes for QGP. However, so far, due to their relatively small production cross section, lower reconstruction efficiency, and larger combinatorial background level in the decay chain, the fully reconstructed b-hadron measurements from exclusive production in heavy-ion collisions are challenging.

Finally, in terms of hadronization studies, extensive measurements in the charm sections have been carried out. Theoretically, it has been argued that the enhancement effect of strange-to-non-strange and baryon-to-meson ratios are more prominent in the beauty sector because beauty quarks are heavier [145]. Therefore, the precise and differential measurement of Λ_b^0/B^+ and B_s^0/B^+ as functions of p_T and event multiplicity in pp and AA collisions will be crucial to test hadronization models, understand beauty quark hadronization mechanisms in vacuum and QGP, and allow us to better interpret our heavy flavor measurements.

These all leave us with some questions related to beauty hydrochemistry. They are listed as follows:

- Can we confirm the observation of fully reconstructed B_s^0 production in nucleus-nucleus collisions?
- Can more differential and precise measurements be carried out to study beauty energy loss mechanism in QGP?

- Do our measurements have enough precision to constrain theoretical model predictions?
- Can our measurements provide enough information to understand beauty quark hadronization mechanisms from vacuum to QGP?
- Does strangeness enhancement also occur in b-hadron production in PbPb collisions?
- How much information about heavy-quark diffusion coefficients can we provide?
- Does hadronization universality breaking also occur in the beauty sector?

2.7 Motivation of This Thesis

To answer these questions, we propose to perform fully reconstructed B_s^0 and B^+ measurements of R_{AA} and B_s^0/B^+ ratios using the 2018 CMS PbPb at $\sqrt{s_{NN}} = 5.02$ TeV dataset, which has about 3 times as many statistics as the 2015 PbPb dataset, and the 2017 pp at $\sqrt{s_{NN}} = 5.02$ TeV dataset, which has more than 10 times statistics than the 2015 pp dataset. Our goal is to perform better measurements than the published results using the 2015 datasets [148]. In order to improve our measurements and achieve our goals, machine learning techniques along with a multivariate analysis approach will be applied in the B-meson analysis. Our measurements will help elucidate the questions above and shed light on beauty quark hadronization mechanisms in vacuum and QGP.

Chapter 3

The CMS Detector

3.1 Overview

The Compact Muon Solenoid (CMS) Detector is a general-purpose high-energy physics detector located 100 meters underground in the French side of the LHC [156]. Overall, the complete detector is 21 m long, 15 m wide, and 15 m high with a weight of 14 kilotons, heavier than the Eiffel Tower in Paris. It functions as a giant, high-speed camera, taking 3D “photographs” of particle collisions from all directions up to 40 million times each second. Figure 3-1 shows the photo taken for the CMS detector at the underground collision hall.

The CMS detector consists of many sub-detectors including silicon strip and pixel trackers, the pre-shower made of silicon strips, the crystal electromagnetic calorimeter (ECAL), the superconducting solenoid with 3.8 T of magnetic field strength, the inner hadronic calorimeter (HCAL), the steel returning yoke to enhance the magnetic field strength, the outer hadronic calorimeter, the muon chambers, and the forward hadronic calorimeter [156]. Figure 3-2 shows a schematic view of the CMS detector

The CMS detector is built, operated, and maintained by the CMS Collaboration. The CMS Collaboration consists of over 4000 members including scientists, engineers, technicians, students, and administrative assistants from 200 institutes and universities in 40 countries around the world. Physicists take data from the CMS detector and share data with each other with the CERN online system, which actually led to

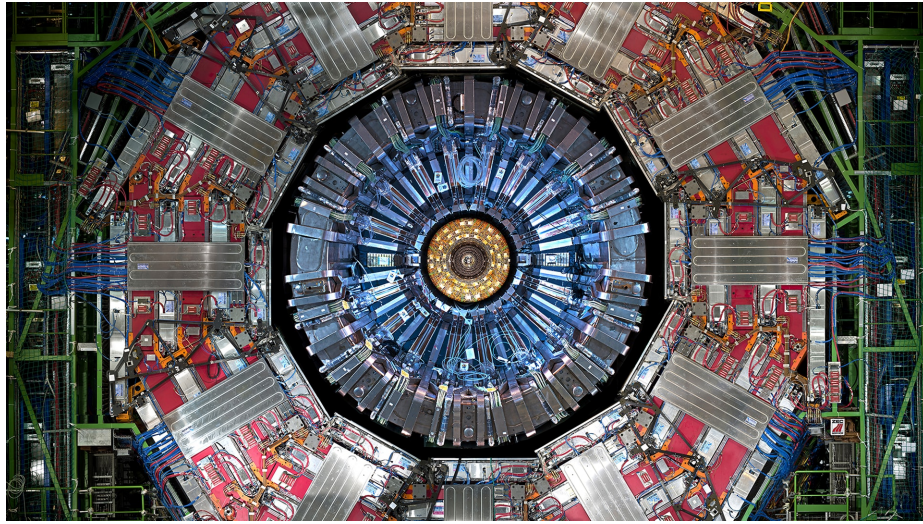


Figure 3-1: The front view of the CMS detector at the underground collision hall is shown above.

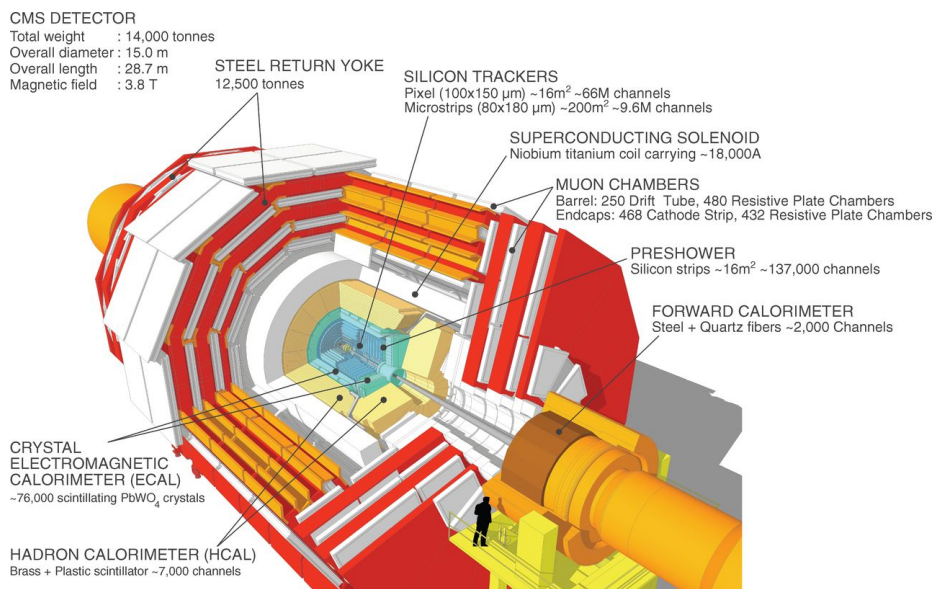


Figure 3-2: The schematic view of the CMS detector with brief descriptions of all its components is shown above. Image from [157]

the discovery of World Wide Web. The data are stored in tapes and kept at different institutions. Members of the CMS experiment collaborate with each other on detector studies and data analysis to produce important scientific results and have published in more than 1000 papers in internationally recognized journals.

In the following sections, I will describe the CMS experiment including the trigger system for data acquisition, the tracking system to track charged particles, the muon system for muon detection, identification, and reconstruction, and the calorimeter system to measure the energies of the particles.

3.2 Triggers

The CMS experiment develops triggers to acquire experimental data [158]. Its main purpose is to select events of potential physics interests from the particles collisions rate of approximately one billion events per second at the LHC. The CMS trigger system consists of two levels of triggers: hardware level 1 (L1) trigger and the software high-level trigger (HLT). Different triggers encoded in the L1 and HLT are designed and fire to collect datasets for specific physics studies.

3.2.1 L1 Trigger

In the CMS experiment, an event is defined as a snapshot of one collision at the LHC. In the L1 trigger, physicists develop algorithms according to detector electronics response to decide if an event is accepted or rejected within the L1 trigger latency time. Figure 3-3 shows the schematic overview of the L1 trigger making its decision online to select events based on the information from the calorimeter and muon systems.

In the interest of heavy-ion studies, physicists develop a set of dedicated triggers algorithms in the L1 trigger to build datasets. The minimum biased (MB) trigger is designed to collect MB data for elliptic flow, D^0 mesons, and charged-particle multiplicity analyses while the single muon trigger is designed to select muons events for heavy flavor and electroweak physics analyses. Here, we will explain the MB trigger since we will need to use it to determine the number of MB events in our

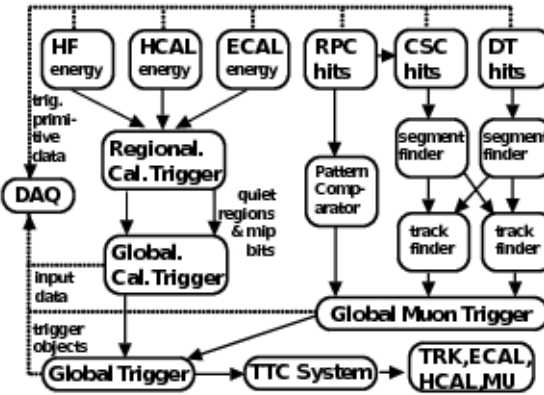


Figure 3-3: The figure above demonstrates how the CMS L1 hardware trigger function schematically.

analysis.

3.2.2 MB Trigger

By definition, an MB event corresponds to a non-single diffractive inelastic interaction [159]. A totally inclusive trigger, or called zero bias (ZB) trigger, corresponds to a randomly readout from the detector whenever a collision is possible. MB trigger is an algorithm to determine interesting MB events based on the response from forward HCAL located at $3 < |\eta| < 5$. It puts a fixed analog to digital converter (ADC) threshold in the HCAL response to reject background noise and collect MB events from the ZB trigger. There is also an essentially linear relationship between the maximum ADC with the actual energy response of the forward HCAL. Figure 3-4 shows the ADC distribution and HF energy as a function of ADC in the 2018 PbPb run.

The MB trigger consists of “MB OR”, which requires the ADC thresholds on either one of the forward HCAL (HF) out of both forward ECAL in both positive and negative sides, and “MB AND”, which requires the ADC thresholds on both of HFs out of both forward ECAL in both positive and negative sides. Figure 3-5 shows the L1 MB trigger analysis of Run 326791 in the 2018 CMS PbPb data taking

In the 2018 CMS PbPb data taking, to reject the noisy background, the max ADC

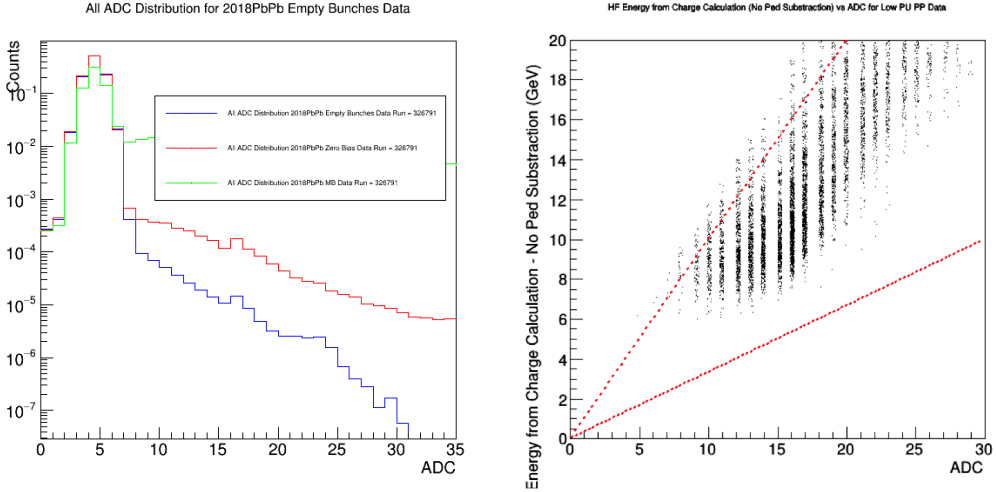


Figure 3-4: In the CMS 2018 PbPb Run 326791, the ZB data (red), Empty Bunches (blue), and MB data (green) ADC distributions (left) and the HF energy according to the charges collected as a function of ADC (right) are shown above. We can see that the HF energy has conversion factor about (0.5 - 1) to the ADC.

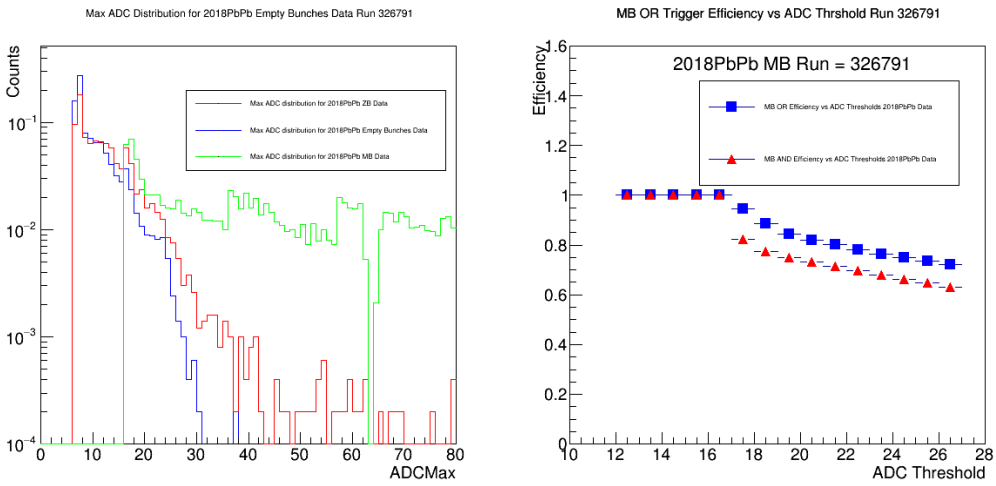


Figure 3-5: In the CMS 2018 PbPb Run 326791, the ZB data (red), Empty Bunches (blue), and MB data (green) maximum ADC distributions (left) and the efficiencies of MB OR (blue) and MB AND (red) as a function ADC threshold (right) are shown above.

of each event is required to be greater than 15 with MB AND along with the HLT trigger. In addition, at least 1 pixel track are applied to select MB events, as seen above from Figure 3-5 in the max ADC distribution of MB events in green. A total number of about 2.4 billion MB events corresponding to a luminosity of about 1.7 nb^{-1} have been collected by CMS during the 2018 LHC PbPb run from November to December 2018. Figure 3-6 shows the MB events and corresponding luminosity as a function of Runs ID throughout the 2018 CMS PbPb data-taking period

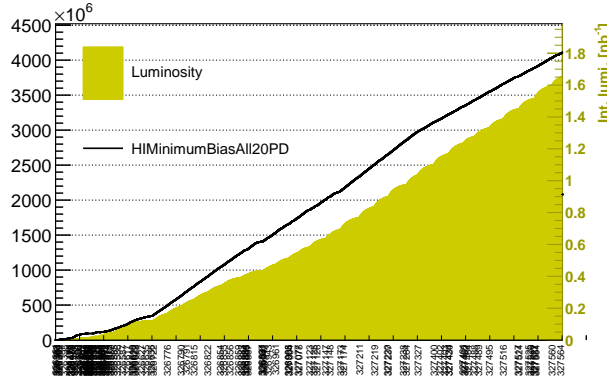


Figure 3-6: The figure above shows the total number of 20 PbPb MB events from and corresponding luminosity how the as a function Run ID from November 15 to December 2, 2018.

3.2.3 Centrality Efficiency with MB Trigger

In addition to overall efficiency vs the ADC with the MB trigger, we also study the centrality efficiency with different ADC thresholds. Figure 3-7 shows the centrality as a function of efficiency using MB OR and MB AND with different thresholds

Because other physics triggers are mainly based on the MB datasets, in the physics analyses using 2018 CMS PbPb datasets, it is recommended to remove the very peripheral centrality range from 90 - 100%, which is not fully efficient (efficiency < 100%). Therefore, most of the CMS heavy-ion physics results using the 2018 PbPb dataset will be reported in the centrality range of 0 - 90%.

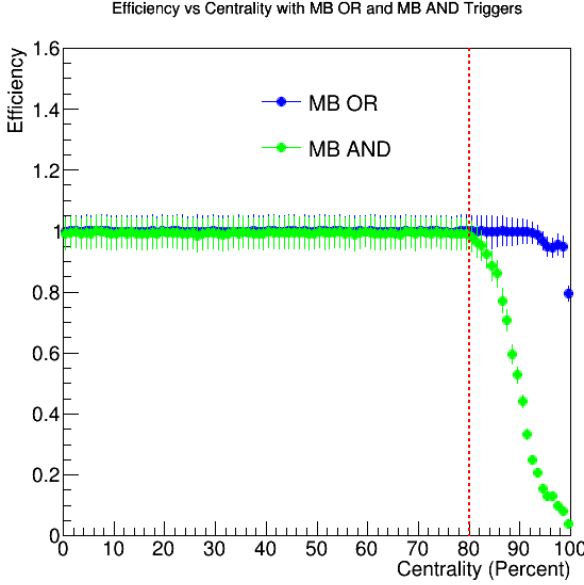


Figure 3-7: The efficiency vs centrality with $\text{ADC} > 16$ for MB OR (blue) and MB AND (green) are shown above.

3.2.4 HLT Trigger

The HLT software trigger is an array of commercially available computers running high-level physics algorithms [158]. Unlike the online L1 hardware trigger which runs on-the-go during the data-taking process, HLT is an offline software trigger that runs after the data are acquired. In the HLT trigger, more sophisticated analyses are performed to determine if the event is kept or not for a specific dataset. The event data are stored locally on disks and eventually transferred to downstream systems, the CMS Tier-0 computing center, for offline HLT processing and permanent storage [158]. Many trigger paths in the HLT, such as the high multiplicity trigger to specifically collect events with many tracks, the D-meson trigger to select high p_T D mesons, and the dimuon trigger to enrich Drell-Yen events, are designed and encoded in the HLT trigger. In the following, we will describe the dimuon trigger in detail because the dimuon dataset will be used to fully reconstruct B mesons in this thesis.

3.2.5 DiMuon Trigger

The dimuon trigger, as it is named, is a trigger based on the information of two muons tracks. The HLT is able to quickly reconstruct the invariant mass of two oppositely charged muons $m_{\mu\mu}$. Figure 3-8 shows the $m_{\mu\mu}$ reconstructed by the CMS HLT with the 2018 pp dataset.

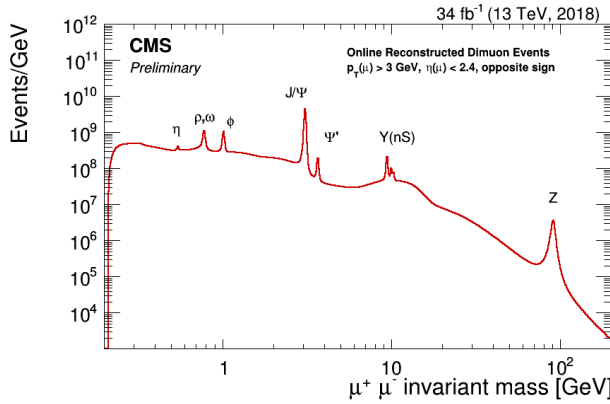


Figure 3-8: The dimuon invariant mass spectrum $m_{\mu\mu}$ reconstructed by CMS HLT trigger in the 2018 pp dataset is shown above. We can identify the neutral vector boson resonances above.

In the 2018 PbPb run, the dimuon trigger requires the presence of two muon candidates, with no explicit momentum threshold and with the HLT reconstructed dimuon invariant mass of $1.0 \text{ GeV}/c^2 < m_{\mu\mu} < 5.0 \text{ GeV}/c^2$, near the J/ψ PDG mass $m_{J/\psi} = 3.0969 \text{ GeV}/c^2$ [4], in coincidence with lead bunches crossing at the interaction point. Moreover, one of the trigger-level muons is reconstructed using information both from the muon detectors and the inner tracker with the requirement of more than or equal to 10 hits (named as L3 muon), while the other one muon only requires information from the muon detectors (named as L2 muon) [160].

3.3 Tracking System

3.3.1 Silicon Detectors

The CMS tracking system applies solid-state semiconductor technologies. It consists of the 3 layers of silicon pixel tracker and 10 layers of silicon strip detector including 4 inner barrel layers and 6 outer barrel layers [161]. It has a $\phi = 2\pi$ and $|\eta| < 2.4$ acceptance coverage. Figure 3-9 shows the CMS tracking system schematically

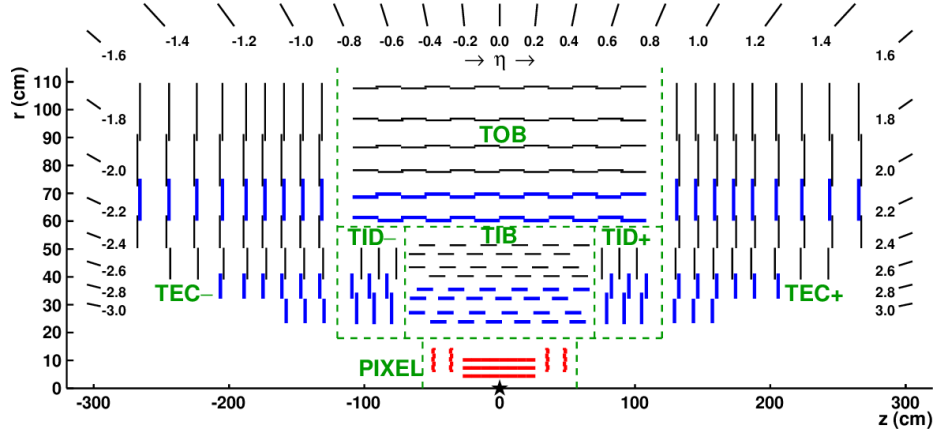


Figure 3-9: The schematic view of the CMS tracking system is shown above.

In nuclear and particle physics, a tracker is a detector that measures the trajectories of charged particles via ionization. In general, it does not destroy or significantly change the energy of the particle. With the external magnetic field, the tracker can measure the momentum, the charge, and the mass of the particle by studying the electric charges collected from electron avalanches or electron-hole pairs. The CMS tracking systems provide physicists with excellent tracking capabilities. The CMS silicon tracker is a solid-state detector employing semiconductor technologies. The silicon tracker is operated at a reserve bias mode with a depletion voltage of about 600V. A high energy charged particle passing through the silicon tracker have an energy loss of $dE/dx \simeq 0.5$ keV/ μ m [4]. Therefore, for a $320\ \mu$ m thick silicon sensor, the charged particle will lose about 160 keV. The electron-hole pair in silicon is about 3 eV per pair. Therefore, the charged particle will produce roughly on the order of 10^4 electrons. The hit resolution in $r\phi$ direction of the silicon strip is about 10 – 40

μm [162]. Figure 3-10 shows schematically how a high-energy charged particle ionizes an electron-hole pair in the depletion region of a silicon P-N junction diode operated at a reverse-bias mode

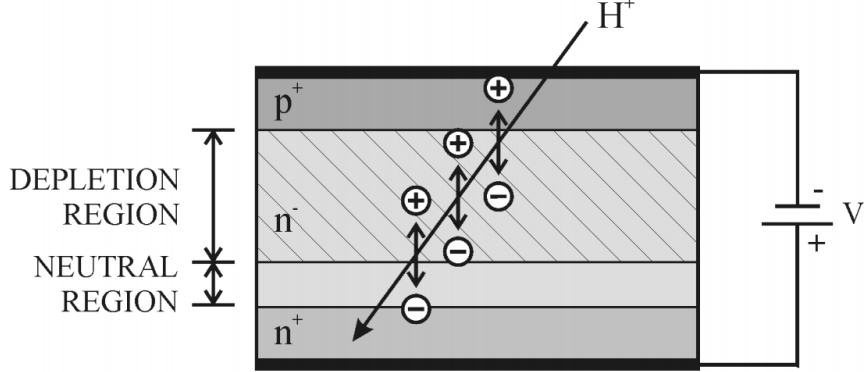


Figure 3-10: The schematic plot explaining how a silicon tracker detects charged particles is shown above.

However, in the CMS silicon tracker, due to the small number of electrons produced in the silicon sensors, the energy loss dE/dx as a function of momentum p of charged particles does not have sufficiently good resolution to separate and identify electron, pion, kaons, and protons. Therefore, we generally do not perform particle identification (PID) for hadrons with the CMS detector in physics analyses.

3.4 Muon System

Named as the “Compact **Muon** Solenoid”, the muon capability is one of the most important features of the CMS experiment. The CMS muon system, with an acceptance coverage of $|\eta| < 2.4$, has 1400 muon chambers including 250 drift tubes and 540 cathode strip chambers to track the positions of the muons and provide a trigger. Its 610 resistive plate chambers form a redundant trigger system. Due to the small energy loss of muon in ECAL and HCAL [4], the muons produced from the LHC usually penetrate through the trackers and calorimeters. Therefore, the muon system is located at the outermost of the CMS detector. Figure 3-11 shows the particles produced at the interaction points and pass through the CMS detector

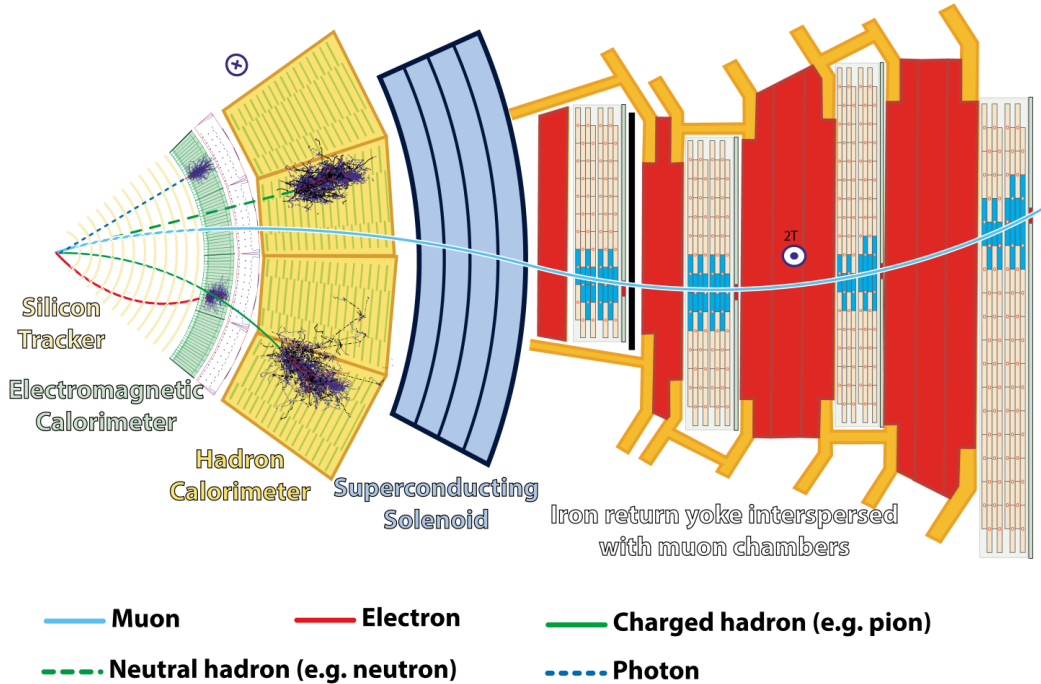


Figure 3-11: The particle flow of long-life particles, such as electrons, muons, photons, charged hadrons: π, K, p , and neutral hadrons: neutrons, in the CMS detector are shown above.

The muon system employs gaseous detector technology. The physical modules of drift tubes, cathode strip proportional planes, and resistive plates are called “chambers”. When a muon passes through the chambers, it will ionize electrons of the gas atoms. Under a strong electric field, the avalanche electrons will be drifted to the anode and the gas ion will be drifted to the cathode. An electronic signal will be generated as this occurs. Figure 3-12 shows schematically how electron avalanches work in a gaseous detector to detect charged particles as well as the design of CMS drift tube to detect muons.

Therefore, with both the tracking system and the muon chambers, the CMS detectors have excellent capabilities of detecting, identifying, and reconstructing muons, which is crucial for heavy flavor physics studies.

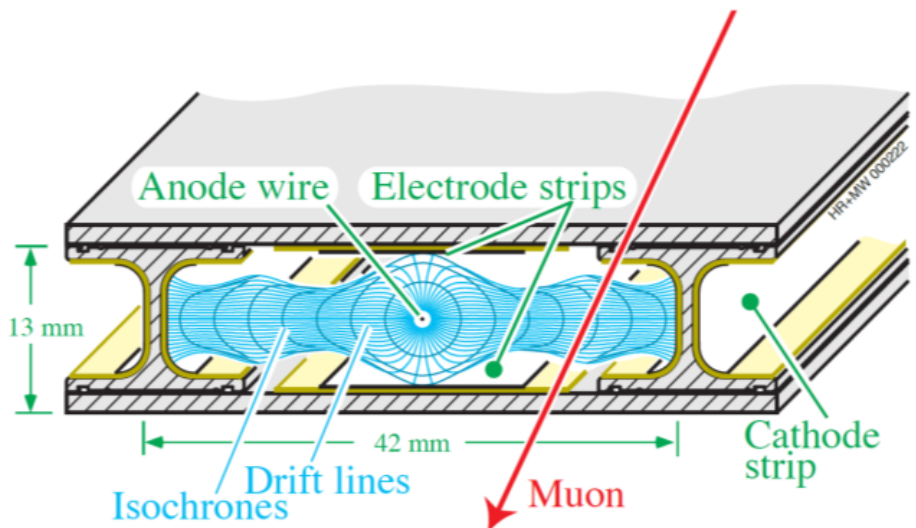
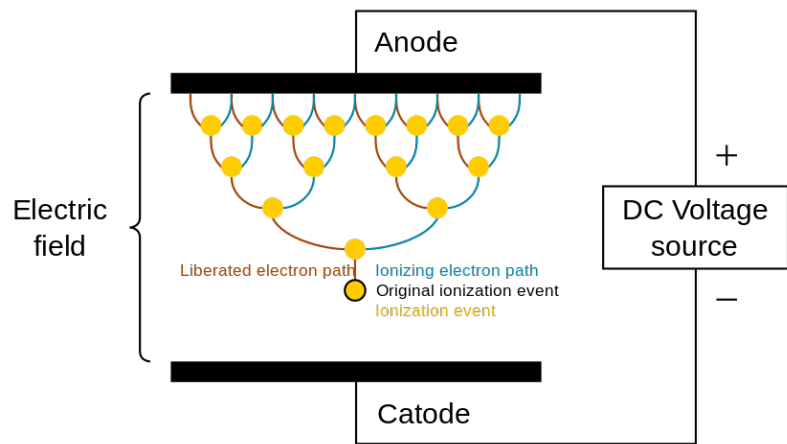


Figure 3-12: A visualization of Townsend Avalanche (top) and schematic plot of the CMS drift tube detecting a muon (bottom) are shown above.

3.5 Calorimeter System

In nuclear and particle physics, a calorimeter is a detector that completely stops particles and measures the total energy deposited. According to the particles, the calorimeters can be divided into electromagnetic calorimeters (ECAL or EMCAL) to measure the energy of electrons and photons and hadronic calorimeters to measure the energy of charged and neutral hadrons. The CMS calorimeter system includes both ECAL and HCAL. It is located in between the tracker and the muon chambers as shown in Figure 3-2.

According to the measurement of the shower energy, calorimeters can typically be classified as sampling calorimeters and homogenous calorimeters. The sampling calorimeters have two components: absorber and scintillator. The absorber is generally made of metals and produces the shower. The scintillator collects a fraction of the total energy from the shower (visible energy) and then corrects the visible energy back to the total energy based on the light collection efficiency. On the other hand, the homogenous calorimeters collect all the energy deposited. Their materials producing the particle shower also measure energy deposition.

3.5.1 ECAL

The CMS ECAL is made of lead tungstate (PbWO_4) crystal and is a homogeneous type calorimeter. High energy electrons and photons interact with the CMS ECAL and undergo bremsstrahlung to produce electrons, positrons, and photons and deposit energy to the ECAL. It has an acceptance coverage of $|\eta| < 1.48$ with a high granularity of $\Delta\eta \times \Delta\phi = 0.0175 \times 0.0175$ in the barrel region and $1.5 < |\eta| < 3.0$ in the endcap region. In addition, the ECAL has an excellent energy resolution of $\frac{\Delta E}{E} = \frac{2.83\%}{\sqrt{E}} \oplus \frac{12.0\%}{E} \oplus 0.26\%$ where E is in the unit of GeV [164] to precisely measure the energy of electrons and photons. It is capable of identifying electrons and detecting photons, which is crucial for heavy flavor physics studies and photon-jet analysis.

3.5.2 HCAL

The CMS HCAL is a sampling type calorimeter made of 926 tons of steel or brass. Over a million World War II brass shell casements are from the Russian Navy. Hadrons interact with the HCAL brass and steel nuclei and produce hadronic showers. A fraction of the shower energy is sampled by the tiles of plastic wavelength shifting scintillators and transferred readout boxes. Generally, particles, except muons and neutrinos, will not be able to penetrate the HCAL. The CMS HCAL system consists of the inner HCAL with barrel (HB) and endcap (HE), the outer HECAL (HO), and the forward HCAL (HF). The acceptance coverages of HB, HE, and HO are $|\eta| < 1.39$, $|\eta| < 1.26$, $1.31 < |\eta| < 3.0$, and $2.85 < |\eta| < 5.19$ respectfully. The HO and HB have a granularity of $\Delta\eta \times \Delta\phi = 0.087 \times 0.087$. The overall energy resolution of HCAL is $\frac{\Delta E}{E} \approx \frac{100\%}{\sqrt{E}}$ [165], which is excellent for jet physics studies.

3.5.3 HF

The forward HCAL is a special component of the CMS HCAL system. It is segmented into 36×13 towers in the $\eta - \phi$ plane. Figure 3-13 shows schematic and physical views of the CMS HF detector [166]

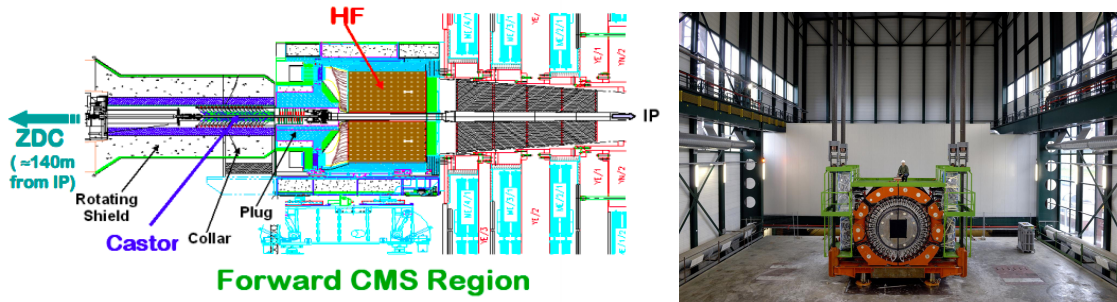


Figure 3-13: The schematic view of the CMS forward region including HF, CASTOR, and ZDC (left) and the physical view of the HF (right) are shown above.

As mentioned above, we have developed the L1 MB trigger based on the HF response to select MB events. In addition, in CMS, centrality is defined based on the activities in the HF [167]. The more activities are there in the HF, the more

remnants of colliding nuclei, the more central the collision event is. Figure 3-14 shows the determination of centrality range from the HF response

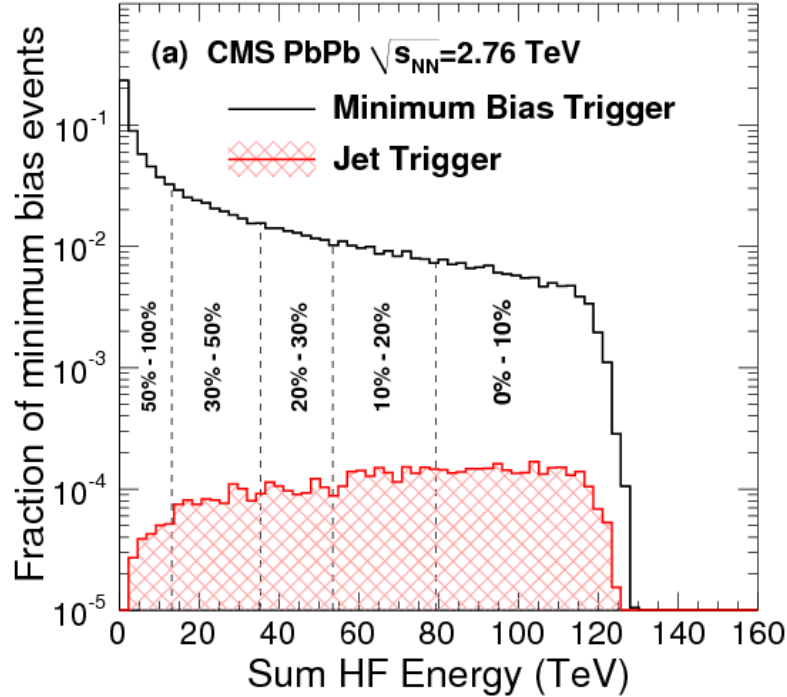


Figure 3-14: The distribution of the sum of HF energy using MB Trigger and Jet Trigger with the classification of centrality binning is shown above. As we can see, the energy of the HF increase as the collision events become more central, which is within our expectation.

In addition to HF, CASTOR ($-6.6 < \eta < -5.2$) and ZDC ($|\eta| > 8.1$) are also calorimeters located at the very forward region [168] as shown above in Figure 3-13. They can help select MB events and trigger ultra-peripheral collision (UPC) events. Figure 3-15 shows the pictures of CASTOR and the ZDC in the very forward direction of the CMS detector

3.6 Relevant Detector Components

In the data analysis of this thesis, the most relevant CMS sub-detectors are the silicon pixel and strip trackers and the muon chambers. We also use HF information to

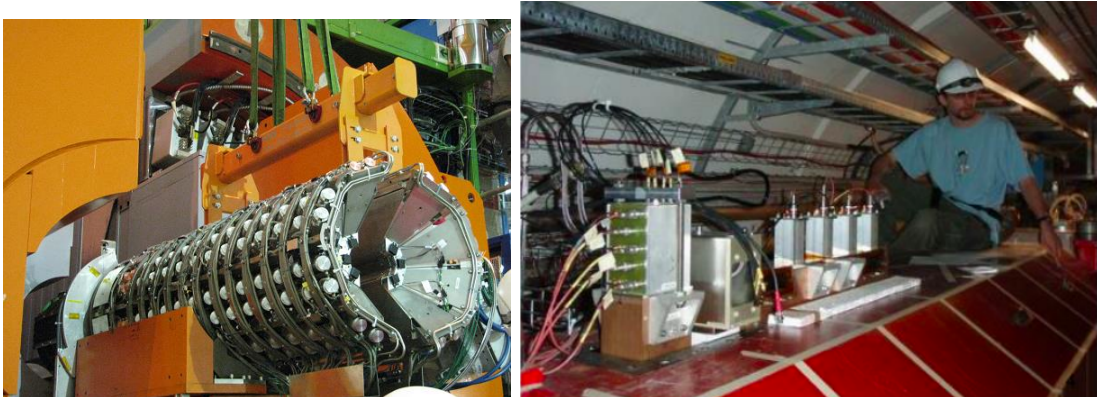


Figure 3-15: The picture of the CASTOR (left) at the CMS underground collision hall and ZDC (right) at 140 m away from the CMS beam interacting point are shown above.

select high-quality events. The datasets we used in the analysis are dimuon triggered datasets. We also use MB triggered samples to estimate the total number of MB events in order to determine the production yield in our analysis. In the next chapter, we will describe the physics objects reconstructed from the detectors and used in our analysis to fully reconstruct B mesons and measure their cross sections.

Chapter 4

Reconstructed Objects

The state-of-the-art CMS detector takes a snapshot of each event and saves the detailed information of the collisions into datasets. In the datasets, we can access event information with reconstructed physics objects including hits, tracks, muons, and vertices, which will be crucial for our data analysis to study B-meson physics in heavy-ion collisions. Below, we will describe, in principle, how these objects with physical meaning are reconstructed from the electronic signals from the CMS detector.

4.1 Events

As mentioned previously, in CMS, an event is defined as a snapshot of one collision at the LHC. Many particles are produced in the collisions and then decay before they are detected in an event. Theoretically, to obtain the complete information of an event, we only need to know the position and momentum of each particle. Experimentally, we detect final state particles and record their kinematics. In high-energy physics experiments, the particles reaching the detectors are e^\pm , μ^\pm , π^\pm , K^\pm , p , n , K_L^0 , γ . All other particles have already decayed into these particles before they can be detected. In order to study them, they need to be reconstructed. Historically, this is used to be done by fast cameras with high resolution. Figure 4-1 shows a famous Ω^- baryon (Strangeness -3: $\Omega = sss$) event reconstructed from one of the pictures taken in the bubble chamber [169].

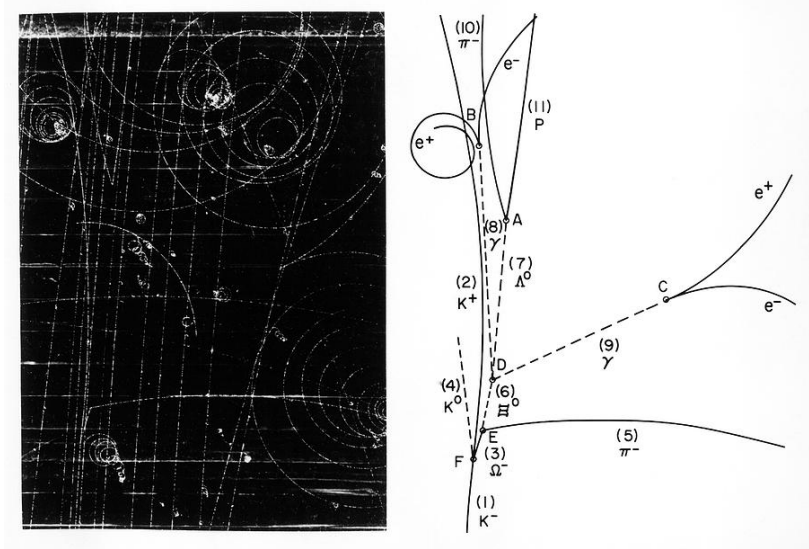


Figure 4-1: The photo of an Ω^- baryon reconstructed from an event: $K^-p \rightarrow K^0K^+\Omega^- \rightarrow \Xi^0\pi^- \rightarrow \Lambda^0\gamma\gamma \rightarrow \pi^-p$ taken from the bubble chamber of the group led by Nicholas Samios at BNL is shown above.

Nowadays, high-speed electronics and semiconductor technologies have advanced. With the development of computing, detector hardware, and readout electronics, high-energy physics experiments are able to collect many events with higher precision of measurements. For instance, the CMS experiment has an event trigger rate of 100 kHz, corresponding to a rate of 100000 events per second with 100 GB/s information [170]. Experimental data have become more digital and abstract instead of pictorial and intuitive. The complete event information is stored in a file format instead of a photograph. Physicists use computers to read experimental data and develop software to analysis each event, extract the physics information from the analysis, and interpret the physics results.

In the following subsections, for simplicity, I will explain the reconstructed objects of events with only one charged particle.

4.2 Hits

All reconstructed objects start from hits as the energy deposition of particles passing through the detectors. Here I will explain the concept of hits based on CMS silicon pixel tracker. Figure 4-2 is the schematic view of a chip with silicon pixels in the CMS tracker

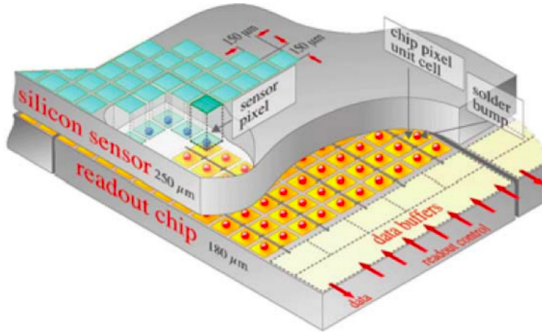


Figure 4-2: The schematic plot of a CMS silicon chip with pixel sensors is shown above.

When a charged particle passes through a layer of the CMS silicon pixel detector, we can look at the charges collected by each pixel on that layer due to the ionization of electron-hole pairs by the high-energy charged particle. Ideally, if a particle enters the tracker at a normal angle, only one pixel is fired. However, in reality, its neighboring pixels may also have some response. When the particle goes through the tracker at a small angle, which frequently happens at the forward region, multiple pixels are expected to fire. Figure 4-3 schematically demonstrates the firing pixels when a particle passing the layer

Here we call each firing pixel a hit, which is demonstrated in Figure 4-3 in red. In CMS pixel tracker, the probability of a pixel firing when a charged particle passing through is greater than 99% [162], which means that it is very unlikely that a hit is missing while a particle passes through the pixel.

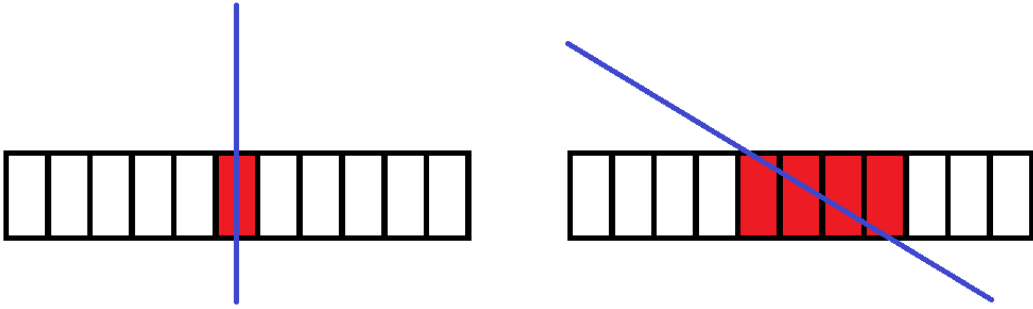


Figure 4-3: The schematic views of a charged particle (blue line) entering the silicon pixel layer (black) at a normal angle (left) and a small tilting angle (right) with the pixels fired (red) are shown above. The left cluster has 1 hit and the right cluster has 4 hits.

4.3 Clusters

Therefore, there should be at least one hit for each layer when a single particle passes through. We define the collection of the adjacent pixel hits in a layer created by one particle as a cluster [162]. The local hits reconstruction algorithm is implemented to obtain clusters. The number of electric charges Q is associated with each hit. We can design an algorithm to determine the center of a cluster according to the charges of each hit. A simple algorithm is to calculate the center of gravity of the cluster taking the weighted averaging of the charge and the position of each hit. In this case, for a cluster with a single hit, its position is simply the center of the pixel. For clusters with many hits, a dedicated algorithm is developed to estimate their positions [162]. The position of a cluster represents a measurement of the charged particle trajectory.

However, in an event with many particles, the occupancy of each layer will be very high and the clusters will become complicated. The CMS collaboration develops a dedicated clustering algorithm to handle such conditions [163]. In CMS terminology, the conversion from the electronic signal of pixels to clusters is called DIGI.

4.4 Tracks

4.4.1 Overview of Basic Principles

In a uniform external magnetic field, the trajectory of a charged particle will be a helix in 3 dimensions. Geometrically, five parameters are needed to parametrize a helix. A parametric curve of a helix in Cartesian coordinates moving along the z direction is written as follows

$$x(t) = R \cos(\omega t) + a \quad (4.1)$$

$$y(t) = R \sin(\omega t) + b \quad (4.2)$$

$$z(t) = vt + c \quad (4.3)$$

Therefore, we need at least 3 clusters to determine all 5 parameters. 3 clusters can determine the radius R and the center of the circle (a and b) and also can determine the straight line in the z -direction. Figure 4-5 shows the helix path of a charged particle in a uniform magnetic field and the fit to determine the center and the radius of the helix.

Moreover, we can determine the transverse momentum of the charged particle according to the R obtained from fit to the center of 3 clusters.

$$p_T = qRB \quad (4.4)$$

In general, the charges of the particles produced in the collision and pass through the tracker are $q = e$. Hence, $p_T = eRB$. For p_T in the unit of GeV, R in the unit of meter (m), and B in the unit of tesla (T), we have

$$p_T \simeq 0.3RB \quad (4.5)$$

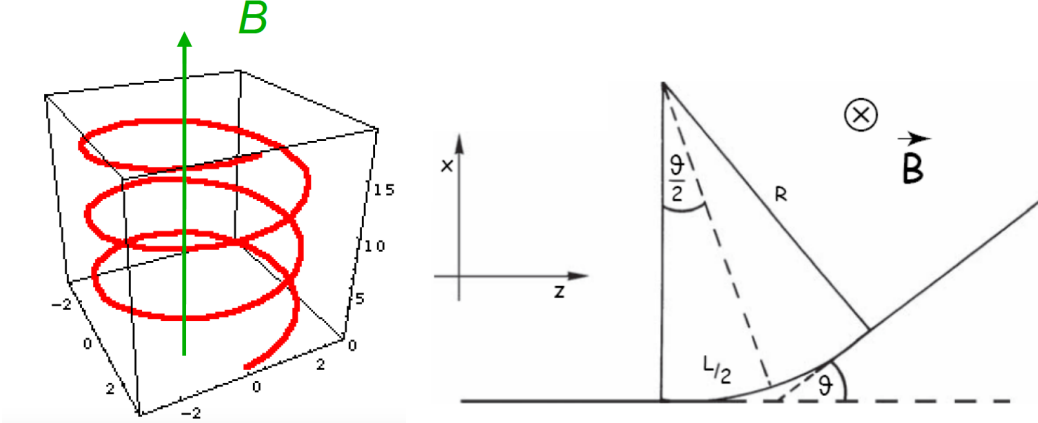


Figure 4-4: The helix motion of a charged particle under a constant and uniform magnetic field \vec{B} pointing in the $+z$ direction (left) and the fit to 3 points to determine the center and the radius of a circle (right) are shown above.

Therefore, as seen above from Figure 4-5, the transverse momentum resolution is driven by the determination of R assuming we have a perfect measurement on the magnetic field \vec{B} .

According to Figure 4-5 on the right, at high p_T , for a 3-cluster case, the tangent lines of the hits on the circular layers are essentially in parallel. In addition, we know that the layers in the pixel track have equal spacing Δr between layers. For CMS pixel tracker, its innermost 3 layers has equal distance $\Delta r = \Delta r_{12} = \Delta r_{23} = 2.9$ cm [171].

Hence, we can see that $L/2 = \Delta r$, which assumes fixed with no uncertainties. Hence, we have

$$\frac{L}{2} = R \sin \frac{\theta}{2} \quad (4.6)$$

Again, at high p_T , the angle θ will be very small since the radius of the circle $R \gg \Delta r$, $\sin \theta \simeq \theta$ and $\cos \theta \simeq 1 - \frac{\theta^2}{2}$. Hence, we can use the small-angle approximation

$$L = 2R \sin \frac{\theta}{2} \simeq R\theta \quad (4.7)$$

Therefore,

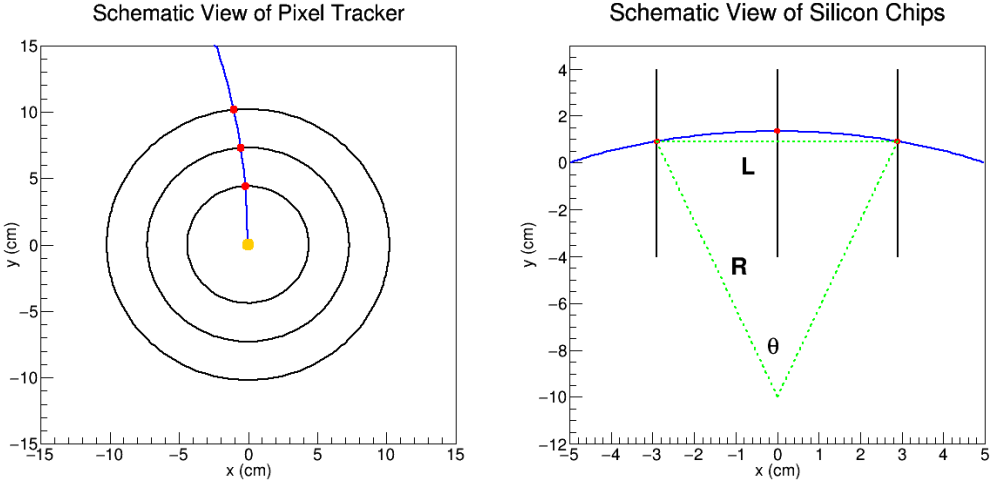


Figure 4-5: A track (blue) initiated from the beam spot (orange) passing through 3 layers of pixel detectors (black) leaving 3 clusters (red) is shown on the left and the circular fit to the 3 clusters with the definition of R , L , and θ is shown on the right.

$$p_T \simeq 0.3RB = 0.3 \frac{BL}{\theta} \quad (4.8)$$

Hence, geometrically, we have

$$s = R - R \cos \frac{\theta}{2} = R(1 - \cos \frac{\theta}{2}) = R(1 - \cos \frac{\theta}{2}) \simeq \frac{L}{\theta} \left\{ 1 - \left[1 - \frac{1}{2} \left(\frac{\theta}{2} \right)^2 \right] \right\} = \frac{L\theta}{8} = \frac{0.3BL^2}{8p_T} \quad (4.9)$$

Thus, the uncertainties on both sides go as

$$\sigma_s = \frac{0.3BL^2}{8p_T^2} \sigma_{p_T} \quad (4.10)$$

Hence, the transverse momentum resolution $\frac{\sigma_{p_T}}{p_T}$ is given by

$$\frac{\sigma_{p_T}}{p_T} = \frac{8\sigma_s}{0.3BL^2 p_T} \quad (4.11)$$

Here, σ_s is effectively the position resolution of the silicon pixel detector. We can see that the transverse momentum resolution gets worse as p_T increases in the high p_T region. Figure 4-6 shows the $\frac{\sigma_{p_T}}{p_T}$ as a function p_T

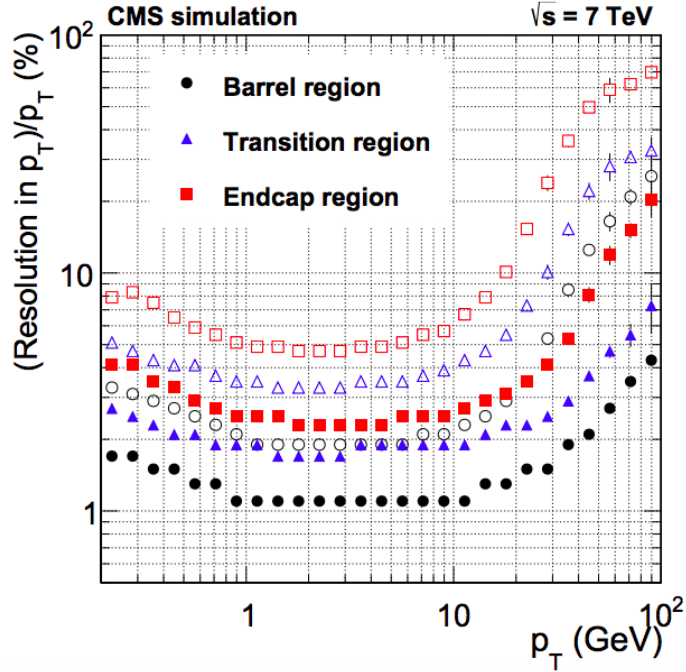


Figure 4-6: The transverse momentum resolution $\frac{\sigma_{pT}}{p_T}$ of a track as a function of transverse momentum p_T is shown above.

We can see that a good agreement with linear growth of $\frac{\sigma_{pT}}{p_T}$ for $p_T > 20 \text{ GeV}/c$ in the high p_T region.

Longitudinally, p_z can be determined by the p_T and the angle $\Delta\theta$ in the transverse direction

$$p_z = \frac{\Delta z}{\frac{R\Delta\theta}{p_T}} = 0.3B \frac{\Delta z}{\Delta\theta} \quad (4.12)$$

At this point, we have obtained the trajectory with complete kinematic information about a particle except for its mass which will require particle identification to determine.

4.4.2 CMS Tracking Algorithm

Because the CMS silicon tracker has 3 pixel and 10 strip layers, a charged particle passing through all 13 layers should leave 13 clusters, which is much more than required hits to determine the helix. Moreover, in reality, in the collision events at

the LHC, many tracks are produced from multiple vertices. In collider physics, we introduce the concept: pileup (PU) events, which is defined as events with more than one vertex. Figure 4-7 shows the number of vertices and the number of tracks in pp collisions at $\sqrt{s_{NN}} = 5.02$ TeV

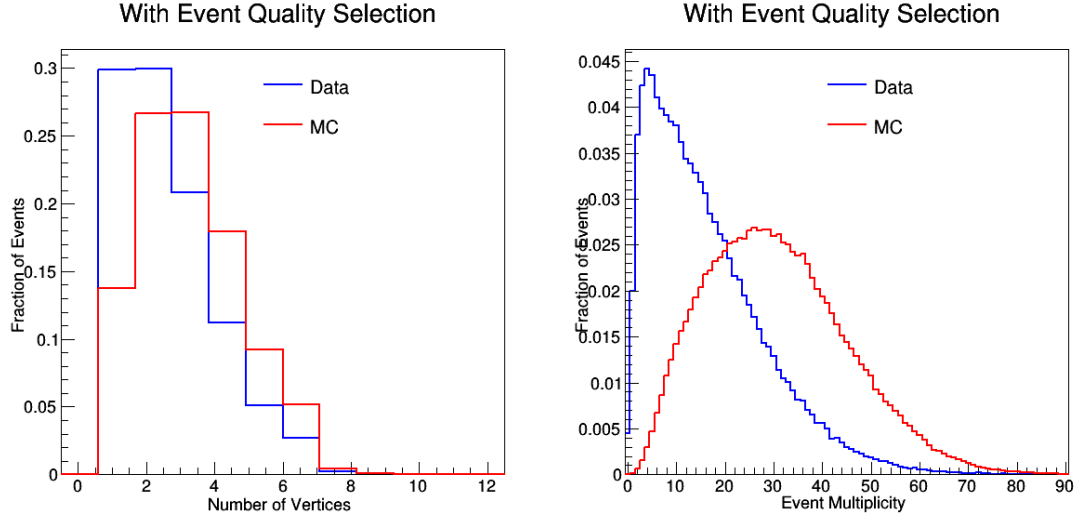


Figure 4-7: The Data (blue) and MC (red) of the number of primary vertex distribution (left) and event multiplicity (right) in 2017 pp dataset are shown above. We can see that an event could have more than one vertex with more than 100 tracks, which makes it very challenging to perform tracking.

Hence, the CMS collaboration has developed the state-of-the-art tracking algorithm to reconstruct the paths and primary vertices of the collisions from the electronic readout signals. The CMS tracking algorithm employs the Combinatorial Track Finder (CTF), an adaptation of the combinatorial Kalman Filter [172–174], which in turn is an extension of the Kalman Filter [175] to allow pattern recognition and track fitting to occur in the same framework. The collection of reconstructed tracks is produced by multiple passes (iterations) of the CTF track reconstruction sequence, in a process called iterative tracking [162]. The CMS tracking workflow and its performance are shown in Figure 4-8 and Figure 4-12

Track Seeding: After reconstructing the hits and obtaining the clusters, the tracking is in the track seeding stage. A dedicated seeding algorithm is designed to select the clusters, either a triplet or a pair, from the pixel layers and other combina-

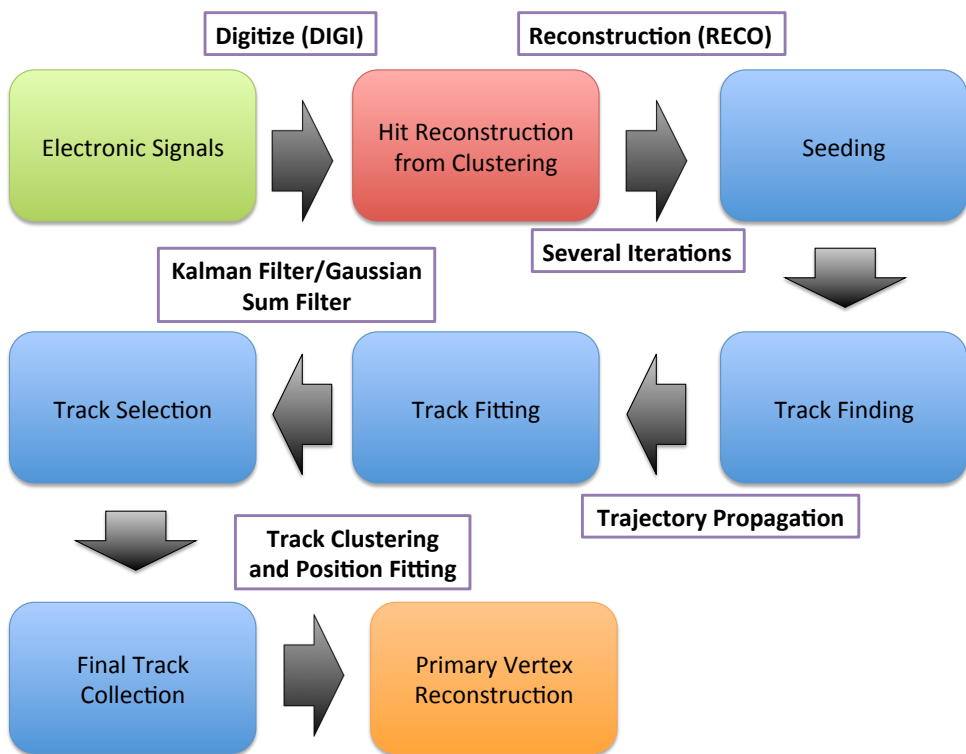


Figure 4-8: The schematic block diagram of CMS tracking workflow is shown above.

tions of pixel and strip layers before fitting [162]. After these steps, preliminary fits to the seeds named trajectory seeds are created.

Track Finding: Then, it moves on to the track finding stage. A six-step iteration process, including navigation, hit search, hit grouping, and trajectory update, is implemented with the application of CFT algorithms based on Kalman Filter to build track candidates. The schematic overviews of the track finding process are shown below in Figure 4-9 and Figure 4-10

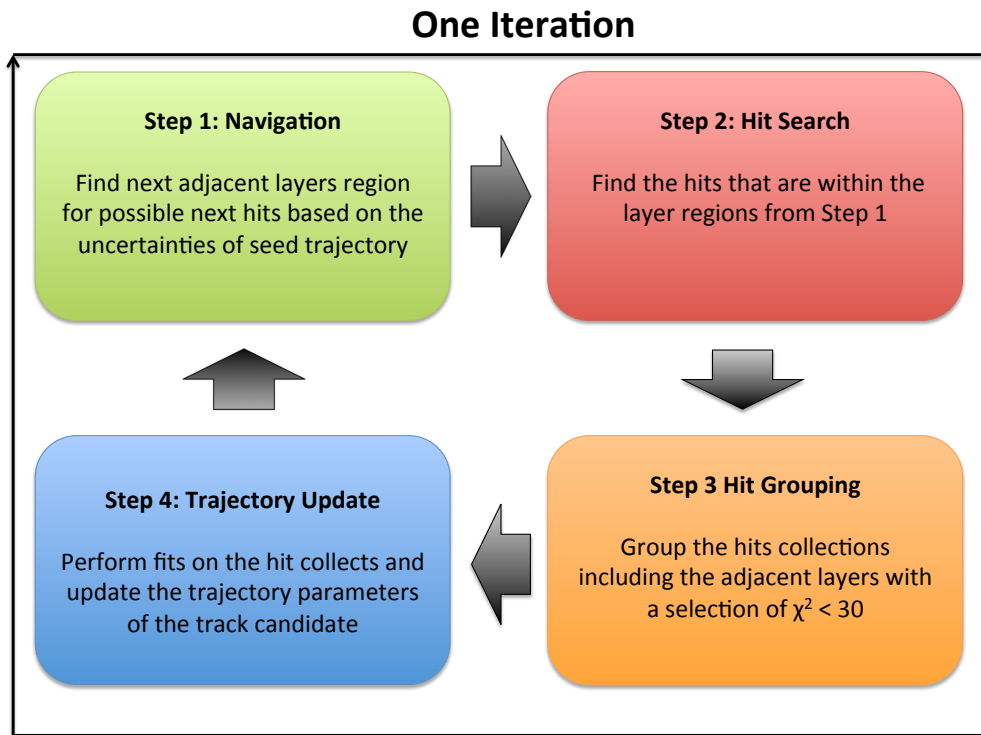


Figure 4-9: The four steps of CMS track finding workflow (left) and the schematic demonstration of each step (right) are shown above.

Track Fitting: Next, the tracking is in the stage of track fitting. Kalman Filter [175] is applied to improve fitting performance. It starts from the innermost location with typically four hits [172–174]. When extrapolating the trajectory from one hit to the next, the filtering and smoothing procedures are carried out with a Rugga-Katta propagator to obtain the best precision. $\chi^2 < 20$ is required of each fit in order to improve its precision and reject fake tracks. Figure 4-11 schematically shows how the

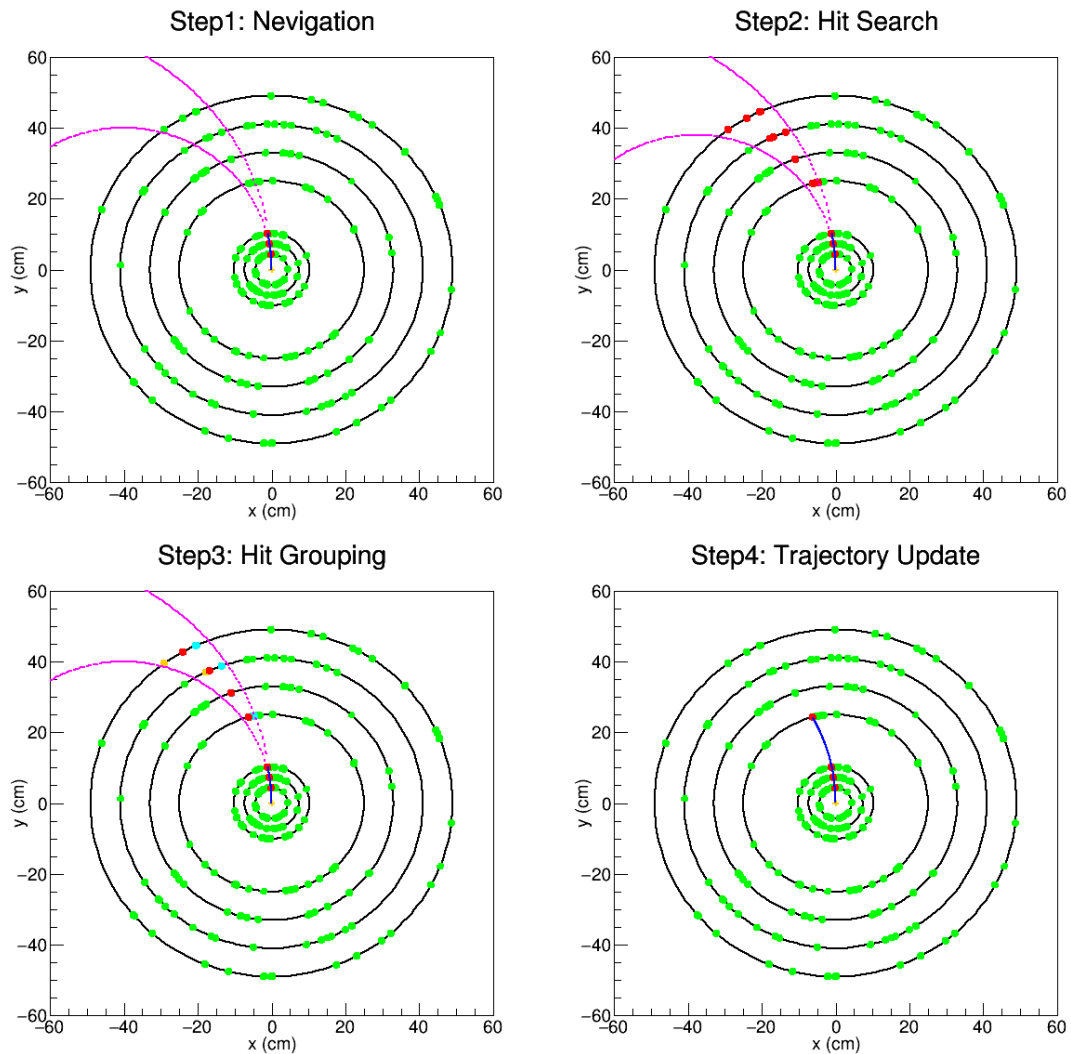


Figure 4-10: The four schematic plots demonstrating each of the four steps for track finding are shown respectfully above.

Kalman Filter fits along with Rugga-Katta propagator are applied in the iterative fitting algorithm for CMS tracking

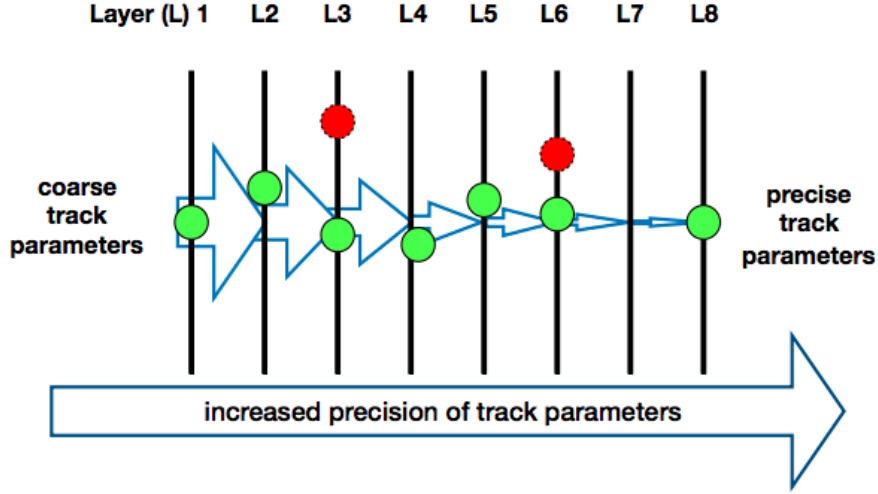


Figure 4-11: The schematic demonstration Kalman Filter along with Rugga-Katta propagator to improve the tracks fitting is shown above.

Track Selection: Subsequently, the tracking is in the stage of track selection. At this point, we have already obtained a preliminary track collection of one event. To improve the track quality and reject fake tracks, further selections based on the track properties will be applied. The following selection criteria are applied to select high-quality tracks [162]

- Minimum number of layers in which the track has at least one associated hit
- Minimum number of layers in which the track has an associated 3D hit
- Maximum number of layers that has no associate hits
- $\chi^2/dof < \alpha_0 N_{layers}$
- $|d_0^{BS}|/\sigma_{d_0(p_T)} < (\alpha_1 N_{layers})^\beta$
- $|z_0^{PV}|/\sigma_{z_0(p_T, \eta)} < (\alpha_2 N_{layers})^\beta$
- $|d_0^{BS}|/\delta d_0 < (\alpha_3 N_{layers})^\beta$

- $|z_0^{PV}|/\delta z_0 < (\alpha_4 N_{layers})^\beta$

Here, α_n and β are configurable constants depending on the selection efficiency and purity requirements. d_0^{BS} is the closest transverse distance of the track to the beam spot and δd_0 is its associated error. z_0^{PV} is the distance along the beam-line from the closest pixel vertex and δz_0^{PV} is its associated error. Hence, $|d_0^{BS}|/\sigma_{d_0(p_T)}$ and $|z_0^{PV}|/\sigma_{z_0(p_T, \eta)}$ are expressed in terms of significance. $\sigma_{d_0(p_T)}$ and $\sigma_{z_0(p_T, \eta)}$ are essentially the associated errors of d_0^{BS} and z_0^{PV} parametrized by the track p_T and η .

Final Track Collection: Finally, after we apply the selections, we have obtained a final track collection for one event. Figure 4-12 shows the general performance of the CMS tracking algorithm

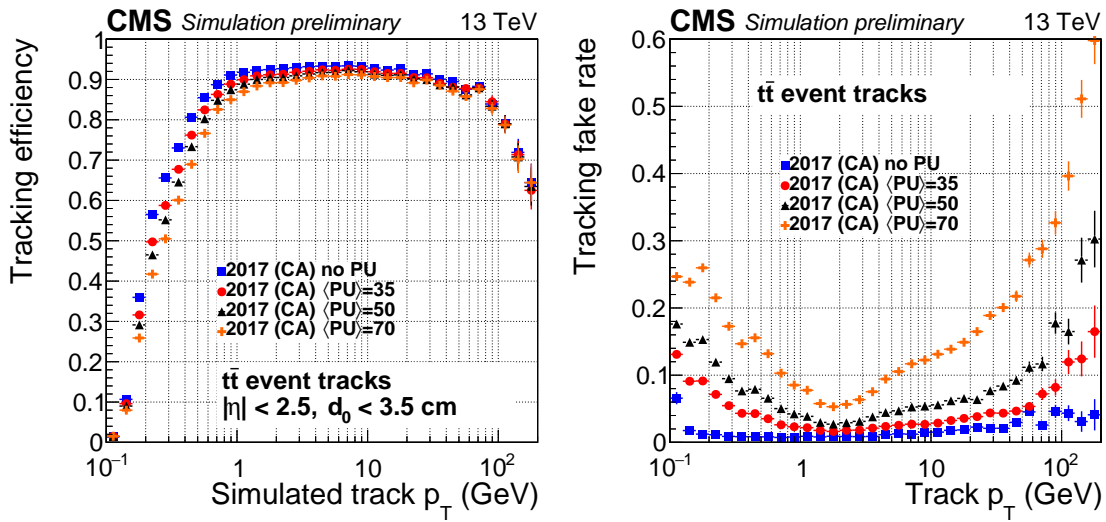


Figure 4-12: The CMS tracking efficiency (left) and fake rate (right) as a function of p_T from simulations of $t\bar{t}$ events at 13 TeV with different pileup conditions are shown above.

We should note that a modified version of the Kalman Filter named Gaussian Sum Filter [176] is applied to improve the tracking performance of electrons [162].

4.5 Muons

The muons in the tracker use essentially the same tracking algorithm as other charged particles [162]. The tracking performance of muons is excellent. For isolated muons

with $1 < p_T < 100$ GeV/c, the tracking efficiency is $> 99\%$ over the full η -range of tracker acceptance and does not significantly depend on p_T while the fake rate is negligible [162]. We can require having hits on the outermost muon chambers to identify muons because other charge particles will be stopped by the calorimeter and should not be able to enter the muon system as shown in Figure 3-11. The muon reconstruction workflow with the muon chambers is shown below in Figure 4-13

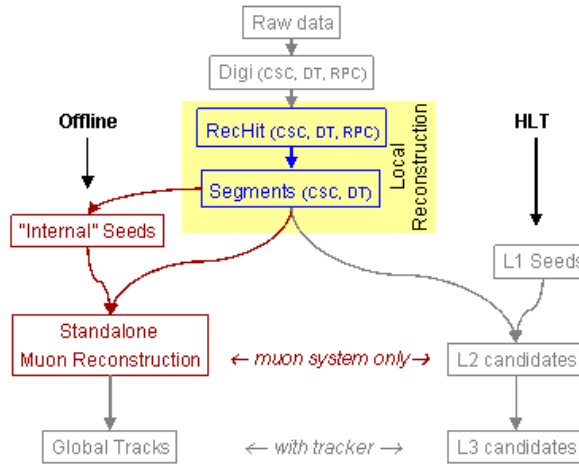


Figure 4-13: The schematic block diagram of muon reconstruction in the CMS muon system is shown above.

In addition, since the muons also deposit some energy to the ECAL and HCAL, we can also access calorimeter information for the muons. Therefore, the CMS detector has excellent capabilities of detecting, identifying, and reconstructing muons, which is crucial for heavy flavor physics studies.

In CMS terminology, there are many types of muons based on their selection requirement in reconstruction. They are classified as follows:

- **Standalone Muons:** the muon segments reconstructed from muon chambers only.
- **Tracker Muons:** the muon segments reconstructed from tracker only but are

also validated with the information from calorimeter and muon systems

- **Global Muons:** the muons reconstructed from the fits to the hits of both trackers and muon systems
- **RPC Muons:** the muons reconstructed with both inner tracker and the resistive plate detector only
- **Calorimeter-based Muons (Calo Muons):** the muons reconstructed with both inner tracker and calorimeters

The relationship between standalone muons, tracker muons, global muons, and calo muons are shown below in Figure 4-14

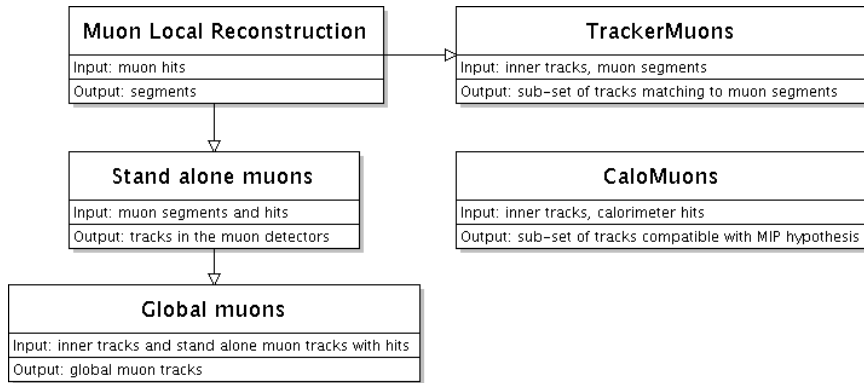


Figure 4-14: The relationship between different reconstructed muon in CMS is shown above

For physics analyses, additional selections including trigger, identification, and acceptance will be applied to muons. We will further discuss them in the analysis chapter.

4.6 Vertices

In particle physics, the term vertex is similar to a vertex in the Feynman diagram where the old incoming particles are destroyed and the new outgoing particles are created via an intersection points at the space-time diagram. This has already been

shown in Figure 4-1 of the Ω^- baryon event where we can clearly see the vertices of Ω^- baryon creation and decay in the reconstructed plot on the right.

4.6.1 Primary Vertices

By definition, in collider experiments, the primary vertex is assumed where the beam particles interact. Therefore, all particles produced in the collisions of that event originate from the primary vertices. With the final track collection for each event, assuming all the tracks are promptly produced at a given interaction point, we can determine the primary vertices by selecting the tracks, performing track clustering, and obtaining the position of each vertex using its associated tracks [162]. The selection criteria for the track to perform primary vertex are as follows:

- $|d_0^{BS}|/\Delta d_0 < 5$
- $N_{pixel} > 2$
- $N_{strip} > 5$
- $\chi^2/dof < 20$

The selections above make sure the tracks used have high quality and are indeed from primary vertices. The deterministic annealing algorithm [177] is the track clustering algorithm that CMS is currently using. An iterative process of minimizing the annealing function of the longitudinal distance between the tracks and the vertices with gradual temperature reduction until dropping to the critical temperature is carried out to determine the number of vertices and their z coordinates [162]. A track can be used for more than one vertex during tracking clustering. Figure 4-15 is a pp collision event display of the CMS detector with reconstructed tracks and primary vertices

After that, we have determined the vertex candidates with z coordinates. Then, for the vertex candidates with at least two tracks, adaptive vertex fitter [178] is applied to compute the best estimate of vertex parameters, including its x , y and z positions,

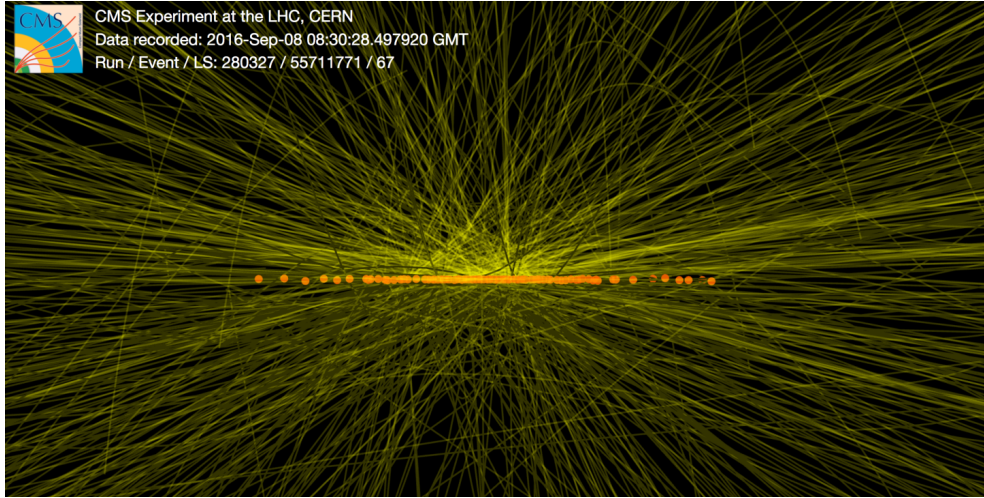


Figure 4-15: A pp collision event display of the CMS detector with reconstructed tracks (green curves) and primary vertices (yellow dots) is shown above.

covariance matrix, and the parameters characterizing the fitting performance such as χ^2 , n_{dof} , vertex fitting probability, and the weights of the tracks used in the vertex. At this point, we have obtained the complete information of an event: a final collection of tracks and the best reconstructed vertices. The track and primary vertex information of each event will be saved in datasets for further physics analyses.

4.6.2 Secondary Vertices

Another object we should mention, particularly in the context of this thesis, is secondary vertex. Again, as seen from Figure 4-1, there are many vertices in the Ω^- baryon event in its decay chain. We can define the displaced vertex from the primary vertex due to the decay of a short-life particle produced at high energy as the secondary vertex. Figure 4-16 below is a schematic plot of the decay topology of a prompt D^0 decay via the decay channel: $D^0 \rightarrow K^-\pi^+$ showing the primary vertex and secondary vertex

The decay length is defined as the distance between primary vertex and secondary vertex. In LHC collisions, since the energy is very high, the particles produced from the primary vertex generally have large momenta, which correspond to a large Lorentz gamma factors $\gamma\beta \simeq 5$. For B mesons produced at the LHC, we estimate their decay

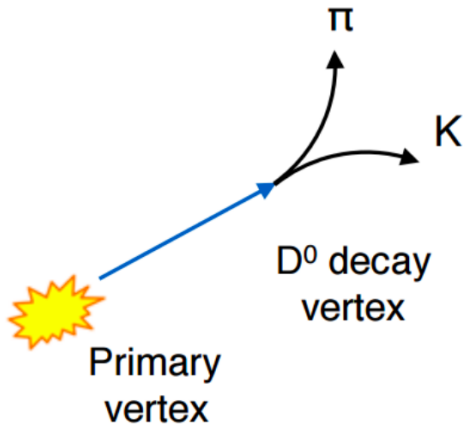


Figure 4-16: The decay of $D^0 \rightarrow K^-\pi^+$ with the definition of the secondary vertex is shown above

length: $\gamma\beta c\tau \simeq 3$ mm due to their relative long lifetimes $c\tau = 500 \mu\text{m}$ [4]. Therefore, the B-meson secondary vertex is well separated from the primary vertex and might even be viewed by the human eyes. The relatively long B-meson decay lengths make them ideal candidates to be fully reconstructed and studied thanks to the excellent vertexing and tracking capabilities of the CMS detector.

Terminologically, we can also call the secondary vertex as the reconstructed mother particle's vertex. For instance, in $B_s^0 \rightarrow J/\psi\phi \rightarrow \mu^+\mu^-K^+K^-$, we can identify 3 secondary vertices. We could call them B_s^0 , J/ψ , and ϕ vertices.

Chapter 5

Data Analysis

5.1 Analysis Tools

In this thesis, the analysis tools include Macbook computers, MIT and CERN high-performance computing facilities, Linux shell script, C++ programming language, and ROOT analysis package for high-energy physics experiments. The machines performing the analysis includes CERN lxplus, MIT Tier-2 submit, and MITHIG Grendel machine. Data files are saved in ROOT files format. Data samples are processed using the crab job submission framework at CERN lxplus system. Analysis jobs are submitted to MIT Tier-2 HTCondor parallel computing system. The core software for data processing is the CMS software (CMSSW_10_3_4). The software for the analysis has been documented on Github and Gitlab. Throughout the analysis, I use the Poisson Statistics model to describe the statistical uncertainties of the data. In the limit of high statistics, it is approximately equivalent to the Gaussian Statistics. These tools are crucial for me to finish the analysis and report the results.

5.2 Analysis Strategies

5.2.1 Physics Goals

The exclusive productions of b hadrons in different collision systems are necessary to study beauty energy loss and hadronization mechanisms. In this thesis, we propose to fully reconstruct B_s^0 ($b\bar{s}$) and B^+ ($\bar{b}u$) mesons in pp and PbPb collisions at $\sqrt{s_{NN}} = 5.02$ TeV with the CMS experiment. We aim at measuring precisely their cross sections, yield ratios, and nuclear modification factors of fully reconstructed B_s^0 and B^+ mesons via the decay channels $B_s^0 \rightarrow J/\psi\phi \rightarrow \mu^+\mu^-K^+K^-$ and $B^+ \rightarrow J/\psi\phi \rightarrow \mu^+\mu^-K^+$ to investigate beauty quark production and hadronization in vacuum and QGP. We hope to have a conclusive measurement of B_s^0/B^+ ratio to pinpoint the effect of strangeness enhancement in QGP on beauty hadronization and test theoretical model calculations [144] with both jet fragmentation [18] and quark coalescence [19] mechanisms. Therefore, we would like to present our experimental measurements over a wide range of p_T and centrality. We are particularly interested in the low and intermediate p_T regions where the slow-moving beauty quarks will pick up nearby light quarks in the color-dense QGP environment while such mechanism is not expected to occur in the vacuum [116]. The R_{AA} down to low p_T will constrain theoretical models and help understand beauty quark energy mechanism in the QGP medium. These studies will be crucial for us to understand the beauty quark diffusion coefficient and probe the inner workings of QGP, providing insights into one of the open questions in high-energy nuclear physics.

5.2.2 General Workflow

Figure 5-1 shows the workflow we designed to fully reconstructed B_s^0 and B^+ mesons from final state particles via the exclusive decay modes. B_s^0 mesons are fully reconstructed from the decay channel of $B_s^0 \rightarrow J/\psi\phi \rightarrow \mu^+\mu^-K^+K^-$, which has a fragmentation fraction of $f(b \rightarrow B_s^0) = 0.103$ and a decay branching fraction $BR(B_s^0 \rightarrow J/\psi\phi \rightarrow \mu^+\mu^-K^+K^-) = 3.17 \times 10^{-5}$. B^+ mesons are reconstructed from the decay channel $B^+ \rightarrow J/\psi K^+ \rightarrow \mu^+\mu^-K^+$ with a fragmentation fraction of $f(b \rightarrow B^+) = 0.001$ and a decay branching fraction $BR(B^+ \rightarrow J/\psi K^+ \rightarrow \mu^+\mu^-K^+) = 1.1 \times 10^{-5}$.

the CMS detector. B^+ mesons are fully reconstructed from the decay channel of $B^+ \rightarrow J/\psi\phi \rightarrow \mu^+\mu^-K^+$, which has a fragmentation fraction of $f(b \rightarrow B^+) = 0.401$ and a decay branching fraction $BR(B^+ \rightarrow J/\psi\phi \rightarrow \mu^+\mu^-K^+K^-) = 6.02 \times 10^{-5}$ $B^+ \rightarrow J/\psi K^+ \rightarrow \mu^+\mu^-K^+$ with the CMS detector.

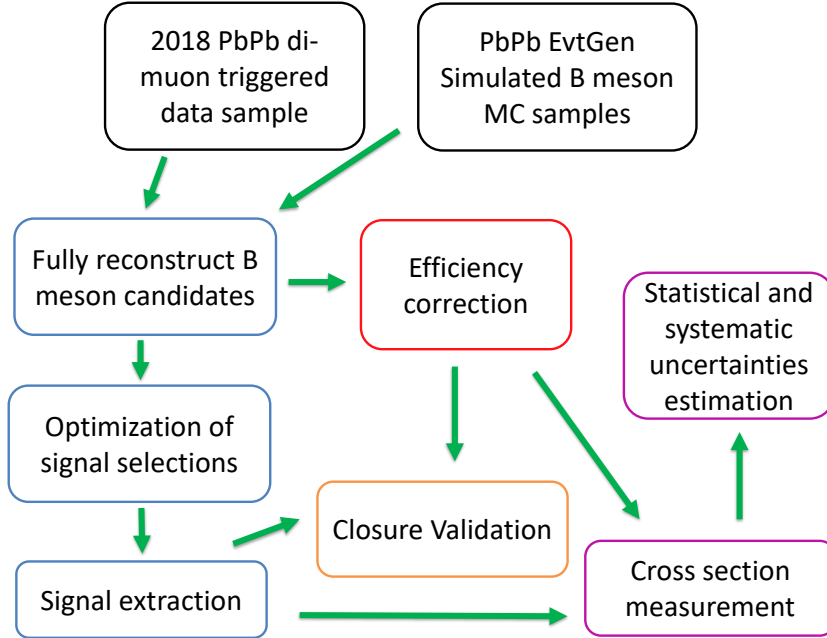


Figure 5-1: The block diagram of the workflow with major steps for B-meson cross section measurements is shown above.

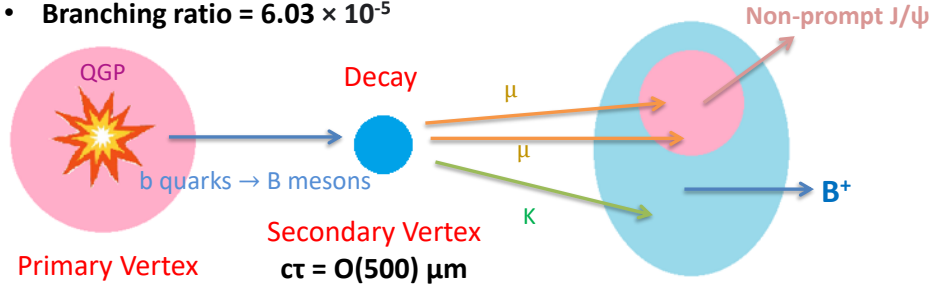
Figure 5-2 shows pictorially the decay topology of fully reconstructed B mesons and our reconstruction strategies

In this thesis, we propose to measure B_s^0 and B^+ cross section in the p_T bin of [7, 10, 15, 20, 50] GeV/c within centrality [0, 90] and centrality bin of [0, 30, 90] with p_T [10, 50]. The rapidity range of B-meson measurements is reported in $|y| < 2.4$.

5.2.3 Technical Challenges

In spite of the excellent muon, tracking, and vertexing capabilities of the CMS detector, there are still many challenges for the analysis. Below is a list of challenges in the B-meson analysis

- B^+ : via the decay channel $B^+ \rightarrow J/\psi K^+ \rightarrow \mu^+ \mu^- K^+$
- Branching ratio = 6.03×10^{-5}



- B_s^0 : using the decay channel $B_s^0 \rightarrow J/\psi \phi \rightarrow \mu^+ \mu^- K^+ K^-$
- Branching ratio = 3.17×10^{-5}

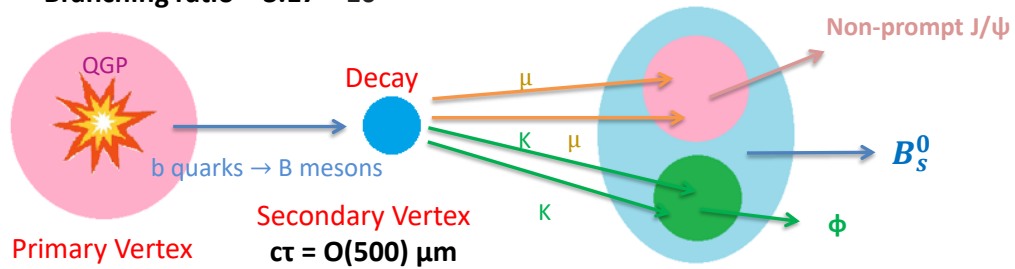


Figure 5-2: The strategies to fully reconstruct B_s^0 and B^+ in the selected exclusive decay modes are shown above.

- The small B-meson decay branching ratio, which is on the order of 10^{-5} , and limited luminosity of the sample: $S \downarrow$
- Huge combinatorial background without hadron particle identification, particularly in PbPb collisions and at low p_T : $B \uparrow$
- Low muon acceptance of at very low p_T : $S \downarrow$
- High fake track rate with low tracking efficiency at very low p_T : $B \uparrow$

Here, S stands for signal and B stands for background. These factors will all lower the signal-to-background ratio, which makes it challenging to fully reconstruct B mesons, particularly at very low p_T . In this thesis, to reduce the signal-to-background ratio and the systematic uncertainties, we will employ a machine learning technique along with multivariate analysis approach and an elaborated single-particle efficiency correction method to perform the measurements.

5.3 Analysis Samples

5.3.1 Dimuon Triggered Datasets

In this part of the thesis, I focus on studying beauty production and hadronization in QGP. Therefore, this analysis is performed using the 2018 PbPb data at $\sqrt{s_{NN}}=5.02$ TeV, which has an integrated luminosity of 1.7 nb^{-1} . The analysis uses the dimuon triggered datasets (*DoubleMu PD*). The full name of the used datasets and their corresponding luminosity can be found in Table 5.1.

Table 5.1: List of PbPb HLT datasets and triggers with the corresponding integrated luminosities used in the analysis.

System	Primary dataset	Trigger	Luminosity
PbPb	/HIDoubleMuonPsiPeri/HIRun2018A-04Apr2019-v1/AOD	HLT_HIL3Mu0NHitQ10_L2Mu0_MAXdR3p5_M1to5_v1	522 nb^{-1}
PbPb	/HIDoubleMuon/HIRun2018A-04Apr2019-v1/AOD	HLT_HIL3Mu0NHitQ10_L2Mu0_MAXdR3p5_M1to5_v1	1124 nb^{-1}
PbPb	Combined All		$1.657 (\sim 1.7) \text{ nb}^{-1}$

The details of the dimuon trigger selections to collect the data sample are explained in 2.2.5. Moreover, a Muon JSON to select good luminosity sections in the PbPb

dataset is applied. Both B_s^0 and B^+ data come from these samples. However, in the later stage, the B-meson candidates are saved in different channels based on different reconstructions.

5.3.2 Monte Carlo Simulations Samples

Dedicated PbPb B_s^0 and B^+ MC samples are generated in order to estimate the acceptance and selection efficiencies, to study the background components, and to evaluate systematic uncertainties. PYTHIA8 Tune CUETPM8 [132, 179], set to generate inclusive (all quark/antiquark, as well as gluon initiated) QCD processes, is used to generate B-meson signal at 5.02 TeV. Several preselections at the generation steps are applied in order to optimize the generation process and conserve resources.

For B_s^0 , only signal events are kept with at least one B_s^0 (forced to decay through the channel $B_s^0 \rightarrow J/\psi\phi \rightarrow \mu^+\mu^-K^+K^-$ by means of the EVTGEN package [180]), with $p_T > 5.0$ GeV/c and $|\eta| < 2.4$. In addition, the J/ψ and ϕ meson, are forced to decay in the two muons and two kaons respectively. Final state radiations are generated using PHOTOS [181]. The selected signal B mesons PYTHIA8 events are embedded into a PbPb background simulated with the HYDJET (version 1.8, tune “Drum” for the prompt and non-prompt J/ψ MC and tune “Cymbal5Ev8” for the B_s^0 signal MC) [182] event generator.

For B^+ , similar requirements for MC generation are applied except a different decay channel $B^+ \rightarrow J/\psi K^+ \rightarrow \mu^+\mu^-K^+$ is used.

For B_s^0 and B^+ , around 50000 events are generated in 5 \hat{p}_T bins: [0, 5, 15, 30, 50] GeV/c in both signal only and embedded samples. The high \hat{p}_T selections are used to enrich the high p_T B-meson statistics in order to perform efficiency correction.

We should note that there are two components in the MC sample. The truth information about the particles generated in the simulation, which is called generated (GEN), and the reconstructed one smeared according to the CMS detector effects, which is called reconstructed (RECO). Due to the nature of MC generation, we will need to reweigh the MC in order to model the data.

In addition to the B_s^0 and B^+ , a sample of inclusive b hadron decay to J/ψ (non-

prompt) MC is also simulated to study the possible background contributions to the B-meson signal region without hadronic PID.

5.3.3 \hat{p}_T Reweighting

As mentioned above, different \hat{p}_T cuts are applied to generate the MC samples. When merging the samplings, a \hat{p}_T weight based on beauty production cross section is required to apply to the MC in order to obtain a smooth distribution that can model the real data. Figure 5-3 shows the generated B-meson p_T distributions of J/ψ , B^+ , and B_s^0 before and after applying the \hat{p}_T weights:

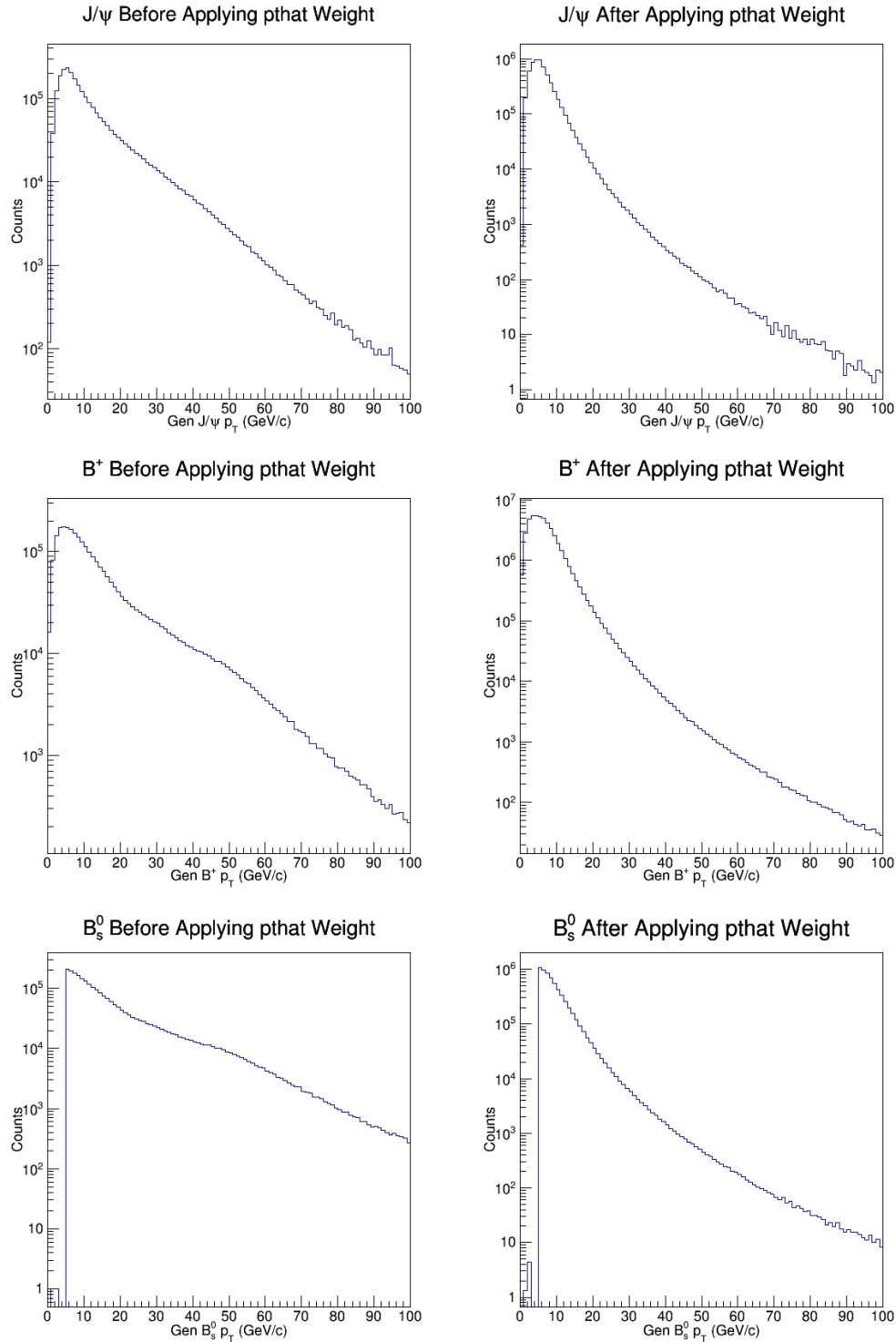


Figure 5-3: J/ψ generated p_T distribution before (upper left) and after (upper right) \hat{p}_T reweighting, B^+ generated p_T distribution before (middle left) and after (middle right) \hat{p}_T reweighting, and B_s^0 generated Gp_T distribution before (lower left) and after (lower right) \hat{p}_T reweighting are shown above.

5.3.4 RECO B-meson p_T Reweighting

Then, we also check if these smooth B-meson generated p_T shapes in fact correspond to a good agreement between the data and MC in the RECO side. Therefore, we take the ratio of the normalized data raw yield to the normalized MC raw yield and perform a variety of functions to fit the distribution. In our studies, we use Linear ($y = p_0 + p_1x$), Quadratic ($y = p_0 + p_1x + p_2x^2$), Linear + Inverse ($y = p_1x + \frac{p_2}{x}$), Linear + Square Root ($y = p_0 + p_1x + p_2\sqrt{x}$), Linear + Log ($y = p_0 + p_1x + p_2 \log x$). The data vs MC raw yield shapes and our fitting results on spectra ratio are shown as follows 5-4 and 5-5 for B_s^0 and B^+ respectfully

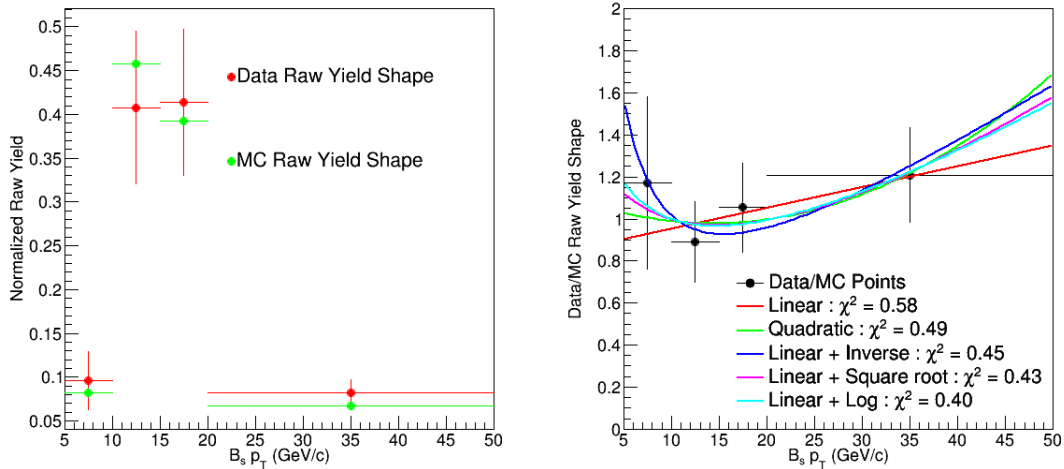


Figure 5-4: B_s^0 p_T normalized raw yields obtained in PbPb MC and Data are shown above on the top left panel. The data/MC ratio and different fitting functions: Linear (Red), Quadratic(Green), Linear + Inverse (Blue), Linear + Square Root (Purple), and Linear + Log (Cyan) and their χ^2 are shown above on the top right panel. The bottom plots are the data/MC reweighed yields with different functions from the fit on the top right panel.

5.3.5 Centrality Reweighting

Because the MC simulations employ PYTHIA embedded into a simulated PbPb background, they do not model the centrality of nucleus-nucleus collision well. Therefore, the MC simulations are also reweighed in order to match the centrality distribution

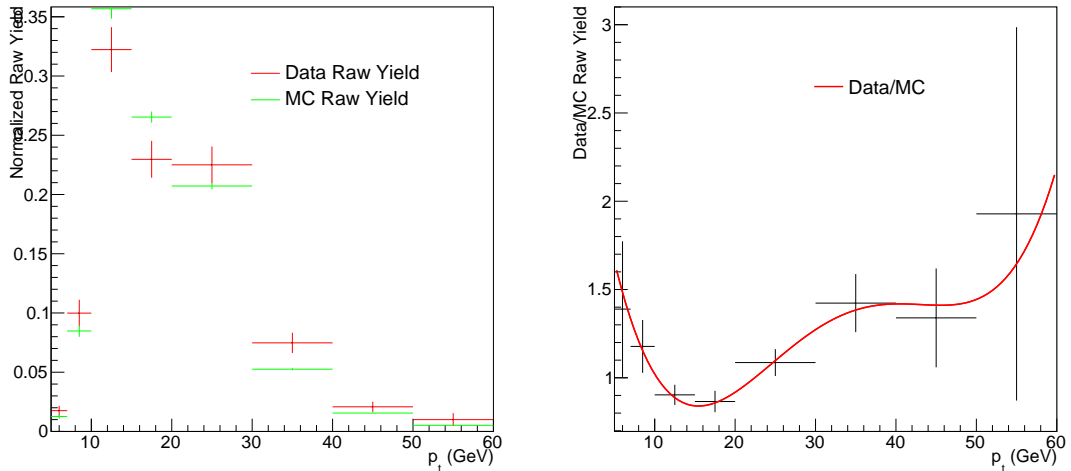


Figure 5-5: The normalized B^+ raw yield in MC (green) and Data (red) as a function RECO B^+ p_T (left) and the fourth-order polynomial fits to their ratio (right) are shown above.

in data. In the middle panel of Figure 5-6, the centrality distribution of the MC simulation (red) is compared to the one in data (blue), before the reweighting. Each unit (hiBin) on the x-axis represents a 0.5% centrality. The number of binary collisions N_{coll} is used as the weight to scale the MC centrality, and the distribution presented in the right panel of Figure 5-6 is obtained.

A better centrality agreement between the data and the MC is seen after the reweighting process.

5.3.6 PV_{*z*} Reweighting

In addition to p_T shape and centrality reweighting, there must be a primary vertex z position (PV_{*z*}) reweighting due to incorrect modeling of the primary vertex location and resolution in the MC simulation. In fact, it is known that the MB samples used to embed for PbPb signal MC samples (with Cymbal5Ev8 tune) have PV_{*z*} offsets. Also, the offsets between data and MC in the X and Y directions are observed in the 2018 PbPb collisions. To remedy this, a Gaussian fit is applied to both data and MC PV_{*z*} distributions shown in Fig. 5-7. The black markers represent the distribution points

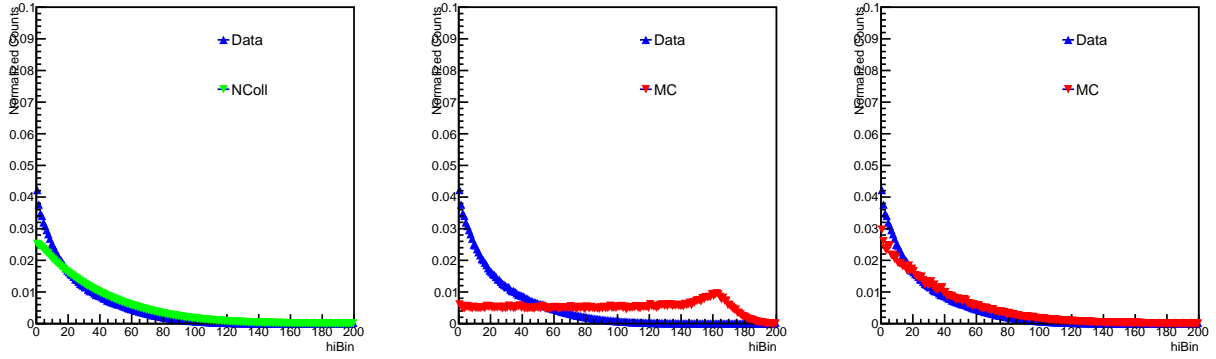


Figure 5-6: The comparison between N_{coll} and Data vs hiBin (left), centrality distribution of MC (red) and data (blue) in PbPb collisions in the centrality interval 0-100% without N_{coll} weight (middle), and with N_{coll} weight (right) are shown above.

for MC (left), and data (right), while the red line represents the fit result. Then, the ratio between the two fit results is taken as the weighting function. The result after this weighting can be found in Fig. 5-7. But we should note that this analysis is not sensitive to the absolute value of the PV position because the reconstruction of the B-meson relies only on the relative distance between PV and reconstructed B-meson secondary vertex, which will be presented in the later sections.

An almost perfect MC-data agreement after PV_z reweighing is observed above. After these standard reweighing procedures, the residue disagreement between MC and data will be considered as a source of systematic uncertainties.

5.4 Global Event Observables

The global event observables characterize general conditions of heavy-ion collisions. In this analysis, we decide to use another set of quantities including the total number of MB events to represent the luminosity and the average number of participants $\langle N_{parts} \rangle$ to represent centrality. In addition, to compare with pp collisions, we also need to scale the cross section in PbPb according to N_{coll} . Therefore, we will determine all the global event observables including the total number of minimum bias events (N_{MB}), centrality, number of participants N_{part} , number of binary nucleon-nucleon

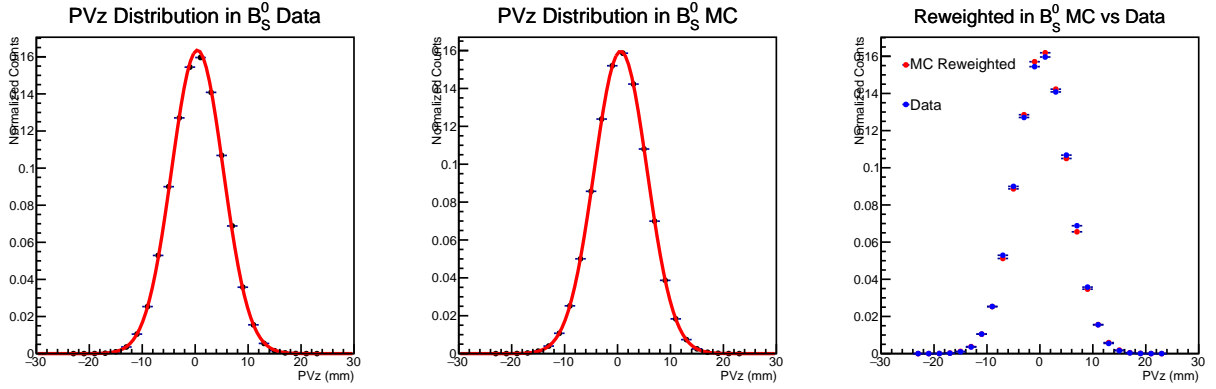


Figure 5-7: The PV_z distributions fitted with Gaussian functions in MC (left) and data (middle), and reweighed with MC to data with the ratio (right) are shown above. The PV_z distributions are well described by the Gaussian functions and the reweighing PV_z reduces the MC-data discrepancy.

collisions N_{coll} , and nuclear overlap function T_{AA} in dimuon PbPb dataset in the following subsections.

5.4.1 Total Number of Events

As seen in Table 5.1, the nominal luminosity of the dimuon PbPb dataset is 1.7 nb^{-1} . However, this nominal luminosity has large uncertainties and should be used in the analysis to measure the cross section. As mentioned previously in Chapter 2.2, the dimuon trigger, based on the MB trigger, will not save events that do not pass trigger selections. Hence, we can use the events of 1 PD MB datasets (PD0) via the following formula to determine the actual number of MB events corresponding to the dimuon PbPb datasets:

$$N_{MB} = \frac{N_{MB}^{\mu\mu json}}{\mathcal{L}_{MBtrigger}^{\mu json}} \mathcal{L}_{\mu\mu trigger}^{\mu json} \quad (5.1)$$

The definitions of the variables in the formula are as follows:

N_{MB} : The number of minimum bias events in dimuon PD with Muon JSON.

$N_{MB}^{\mu json}$: The number of the event of all MB PDs with Muon JSON.

$\mathcal{L}_{MB}^{\mu json}$: The luminosity of all MB PDs with Muon JSON.

$\mathcal{L}_{\mu\mu trigger}^{\mu\mu json}$: The luminosity of dimuon PD with Muon JSON.

For 0 - 90%, $N_{MB}^{\mu\mu json}$ is 161507974. The number of events can then be computed as follows:

$$N_{MB} = \frac{N_{MB}^{\mu\mu json}}{\mathcal{L}_{MB trigger}^{\mu\mu json}} \mathcal{L}_{\mu\mu trigger}^{\mu\mu json} = \frac{1657.1320 \mu b^{-1}}{24.0748 \mu b^{-1}} \times 161507974 = 1.1823737719 \times 10^{10} \simeq \mathbf{11.82 \text{ billion}}$$
(5.2)

Hence, the number of MB events for the 2018 dimuon PbPb dataset is $N_{MB} = 11.82$ billion. Below, in Table 5.2, we compile the number of minimum biased events N_{MB} in 0 - 30%, 30% - 90%, and 0 - 90%.

Table 5.2: Summary table of the total number of MB events and their uncertainties in different centralities

Centrality	N_{MB} (billion)	Uncertainties
0-30%	3.941	1.26%
30-90%	7.882	1.26%
0-90%	11.82	1.26%

5.4.2 Centrality Definition

For the 2018 PbPb dataset, the centrality is given in hiBin with a 0.5% increment. The hiBin is defined based on the HF response (hiHF). According to the Global observable, Figure 5-8 demonstrates the hiHF as a function of centrality with uncertainties.

We can compute the percent deviation nom of final results to estimate systematics due to uncertainties of centrality.

5.4.3 $\langle N_{part} \rangle$, $\langle N_{coll} \rangle$, $\langle T_{AA} \rangle$ vs Centrality

As we discussed in the Glauber Model [56,62] section 1.5.7, the number of participants N_{part} , the number of binary nucleon-nucleon collisions, and nuclear overlap function T_{AA} are all functions of the event centrality. The CMS Global Observable group has

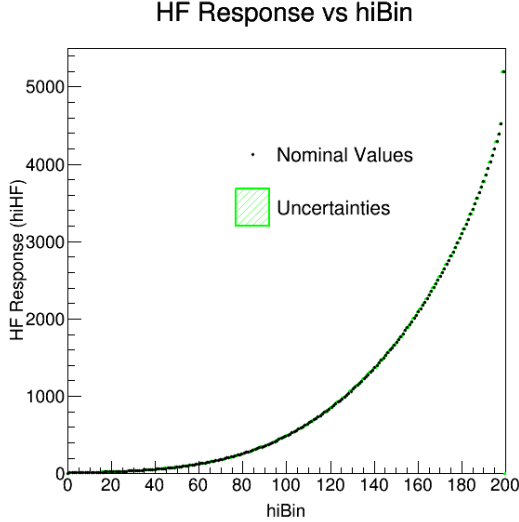


Figure 5-8: The nominal (black) and uncertainties band (green) hiHF vs hiBin for CMS 2018 PbPb dataset are shown above.

computed the average $\langle N_{part} \rangle$, $\langle N_{coll} \rangle$, $\langle T_{AA} \rangle$, and their uncertainties for different centrality bins based on the Glauber Model. The selected results are shown in Table 5.3 below

Table 5.3: A summary table of the total number of MB events vs centrality is shown below. The uncertainties are represented in terms of percentage in the parenthesis.

Centrality	$\langle N_{part} \rangle$	$\langle N_{coll} \rangle$	$\langle T_{AA} \rangle$
0-30%	269.1 (0.39%)	1042 (2.0%)	15.42 (2.0%)
30-90%	54.45 (1.5%)	115.2 (3.6%)	1.704 (3.6%)
0-90%	126.0 (0.67%)	424.1 (2.2%)	6.274 (2.2%)

The global observables N_{MB} , $\langle N_{part} \rangle$, $\langle N_{coll} \rangle$, and $\langle T_{AA} \rangle$ will be used as input for our B-meson analysis.

5.4.4 Event Multiplicity

Aside from N_{MB} , $\langle N_{part} \rangle$, $\langle N_{coll} \rangle$, and $\langle T_{AA} \rangle$, event multiplicity is also an event observable. We count the number of tracks in each event with some track quality selections and use it to interpret the event multiplicity, which characterizes the event activity. The following is the selection criteria

- High purity tracks required
- $|d_z/\sigma_{d_z}| < 3$
- $|d_{xy}/\sigma_{d_{xy}}| < 3$
- $\sigma_{p_T}/p_T < 0.1$
- $p_T > 0.5 \text{ GeV/c}$
- $|\eta| < 2.4 \text{ GeV/c}$

Nevertheless, the event multiplicity is not used in B-meson analysis of the PbPb datasets. Instead, it will be used in pp analysis to study the B_s^0/B^+ ratio as a function of event multiplicity in pp collisions.

5.5 B-meson Reconstruction

Now we look into each event of the PbPb dimuon dataset. It turns out that there is no PU in any event, which means that there is only one primary vertex for each PbPb event. We can then reconstruct the B-meson candidates according to the final state muons and kaons tracks. In CMS, a dedicated software named “*Bfinder*” is developed to perform B-meson reconstruction. Figure 5-9 and Figure 5-10 show the workflow to fully reconstruct *Bfinder* for B_s^0 and B^+ respectfully.

Here, we should note that since we do not have hadronic PID for the kaons, we assume the track to be kaons and assign the charged kaon PDG mass to the tracks [4] to the tracks. Also, the invariant mass of the muon pair is constrained to the nominal J/ψ meson PDG mass ($m_{J/\psi} = 3.096916 \text{ GeV/c}^2$) [4] instead of a distribution of the dimuon mass $m_{\mu\mu}$. The output file format of *Bfinder* is an Ntuple. Finally, we do not distinguish particles and anti-particles during the B-meson reconstruction. Therefore, both B_s^0 and \bar{B}_s^0 as well as B^+ and B^- are reconstructed. Here, for simplicity, we only mention the B_s^0 and B^+ throughout the thesis. Each event will have multiple B-meson candidates as shown in Figure 5-11.

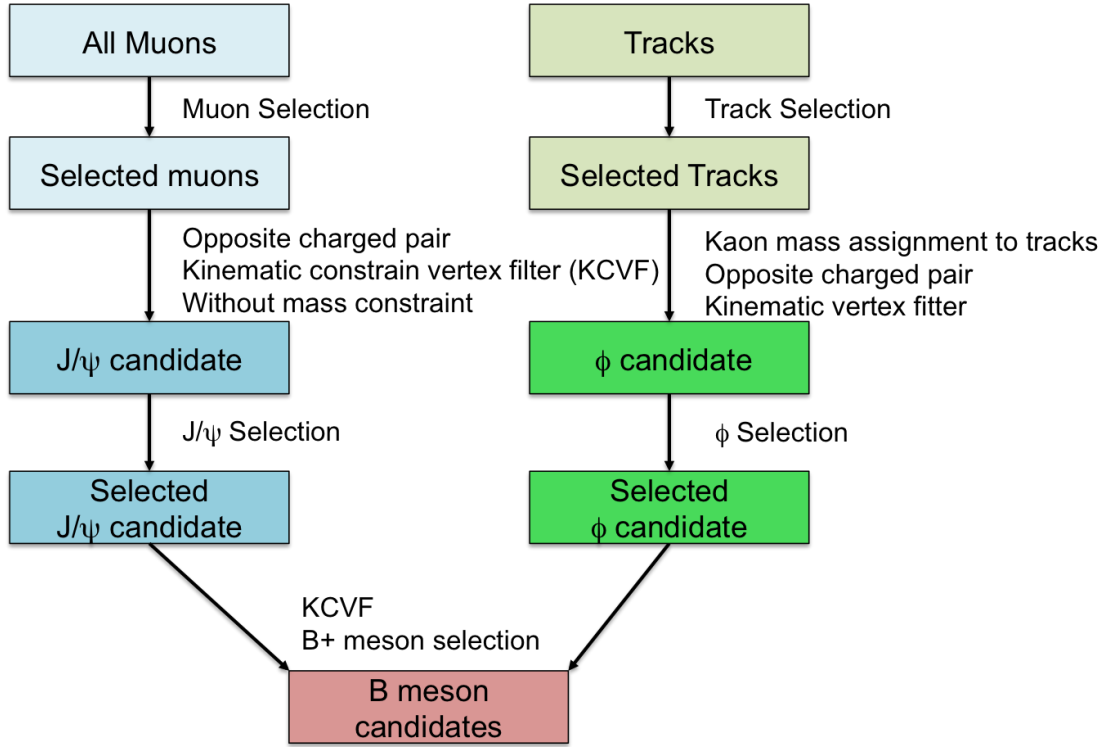


Figure 5-9: The schematic block diagram of the full reconstruction workflows for B_s^0 via the decay channel of $B_s^0 \rightarrow J/\psi\phi \rightarrow \mu^+\mu^-K^+K^-$ in the *Bfinder* is shown above.

Their information, including invariant mass, p_T , and y as well as their daughter particles kinematics such as p_T and η , is saved as a form of vector in each event. In this thesis, we use B-meson Ntuples to perform our analysis.

5.5.1 Event Selections

To ensure the quality of inelastic hadronic collisions events for B-meson reconstruction, we apply the following selections

- At least one reconstructed primary interaction vertex, formed by two or more tracks
- The longitudinal distance from the center of the nominal interaction region of less than 15 cm along the beam axis: $|PV_z| < 15$
- Compatible shapes of the clusters in the pixel detector with those expected from

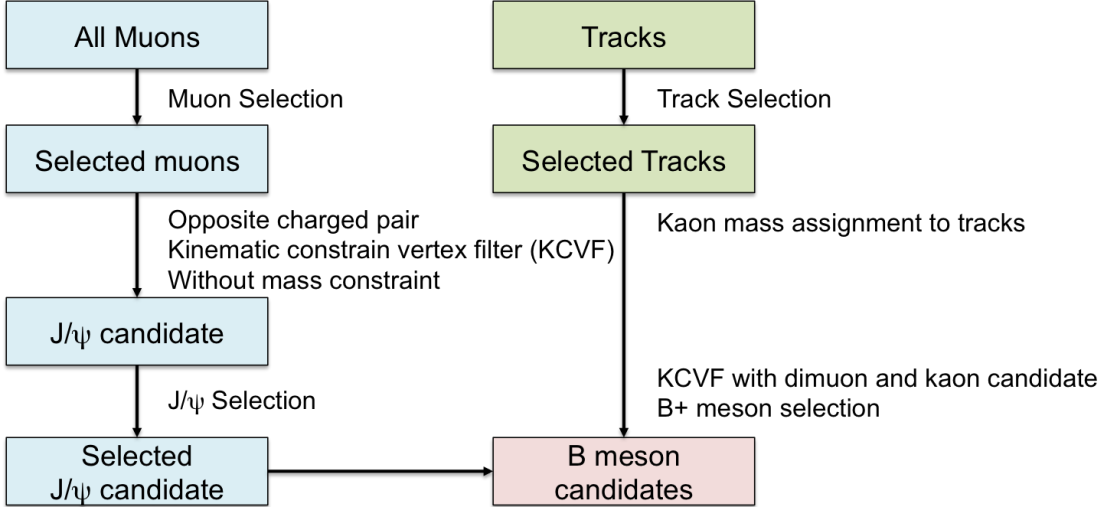


Figure 5-10: The schematic block diagram of the full reconstruction workflows for B^+ via the decay channel of $B^+ \rightarrow J/\psi K^+ \rightarrow \mu^+ \mu^- K^+$ in the *Bfinder* is shown above.

particles produced by a PbPb collision [183]

- At least two towers in each of the HF detectors with energy deposits of more than 4 GeV per tower

5.5.2 Track Selections

In addition to event selections, we also apply track selections to improve the quality of the tracks and reject fake tracks. For B^+ we have the following selections

- General Tracks passing high purity selection (described in section 3.4.2)
- $|\eta| < 2.4$ and $p_T > 1$ GeV/c
- p_T momentum resolution: $\frac{\sigma_{p_T}}{p_T} < 0.1$
- At least 10 hits in the pixel + strip tracker layers: $N_{hit} > 10$
- $(\text{Track } \chi^2/ndf)/(\text{pixel + strip hits}) > 0.18$
- Vertex probability > 0.05

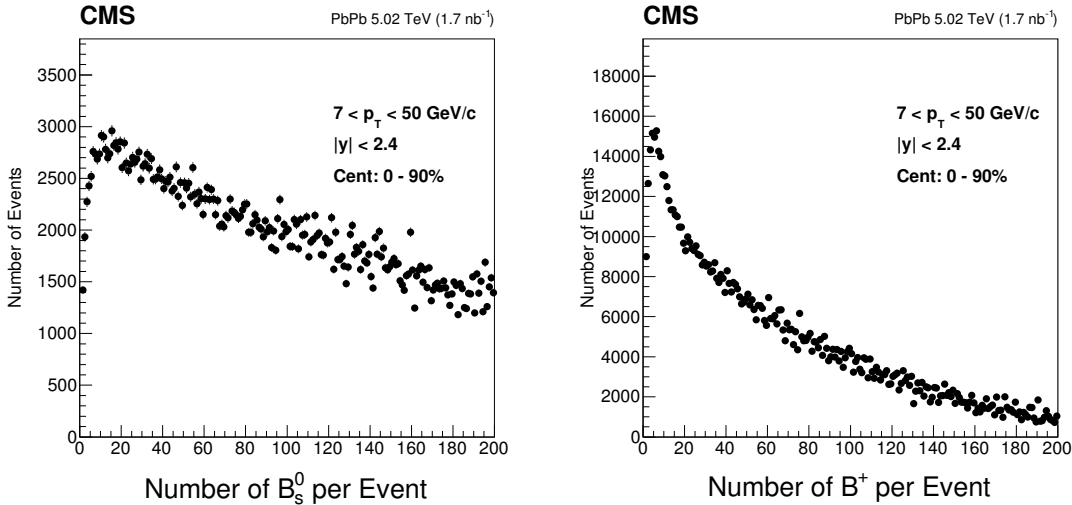


Figure 5-11: The number of reconstructed B-meson candidates per event distributions in the dimuon PbPb dataset for B_s^0 (left) and B^+ (right) are shown above. Multiple B-meson candidates are reconstructed in one event.

For B_s^0 , since we expect it to have a ϕ resonance in the decay chain, we require the mass of the reconstructed dikaon candidates $|p_{K^+} + p_{K^-}| = m_{KK}$ to be $0.015 \text{ GeV}/c^2$ within the ϕ meson PDG mass ($m_\phi = 1.019455 \text{ GeV}/c^2$): $|m_{KK} - m_\phi| < 0.015 \text{ GeV}/c^2$

5.5.3 Muon Selections

The muon candidates are selected according to the *hybrid-soft muon* selection, developed for the muon analysis using CMS 2012 7 TeV pp data [184]. It is adapted from the soft-muon ID developed by the BPH group, with two modifications: a) the purity selection is removed, and b) the muon is required to be also *global*. This selection will be updated for the one developed in 2018. The *hybrid-soft muon* selection includes the following cuts:

- Required to be Global Muon and Tracker Muon (described in section 3.4.3)
- At least one good muons
- Transverse impact parameter $D_{xy} < 0.3 \text{ cm}$
- Longitudinal impact parameter $D_z < 20 \text{ cm}$

- At least 1 muon hits on pixel tracker layers and 5 hits on both the pixel + strip tracker layers

In addition, the muon acceptance selections ensure that the muon candidate will have a total efficiency: $\epsilon^\mu > 10\%$. Table 5.4 shows that the muon acceptance cuts, designed by the CMS muon analysis group, are also applied in our B-meson analysis:

Table 5.4: Summary table of the muon acceptance selection for muon: $|\eta^\mu|$ as a function p_T^μ .

Centrality	$\langle N_{part} \rangle$	$\langle N_{coll} \rangle$	$\langle T_{AA} \rangle$
$ \eta^\mu $	0 – 1.2	1.2 – 2.1	2.1 – 2.4
p_T^μ (GeV/c)	> 3.5	$> 5.47 - 1.89$	$\eta > 1.5$

Table 5.4 comes from the muon analysis in the 2018 PbPb dataset. Figure 5-12 shows the muon reconstruction, identification, and trigger efficiency as a function of p_T^μ and η^μ [185]

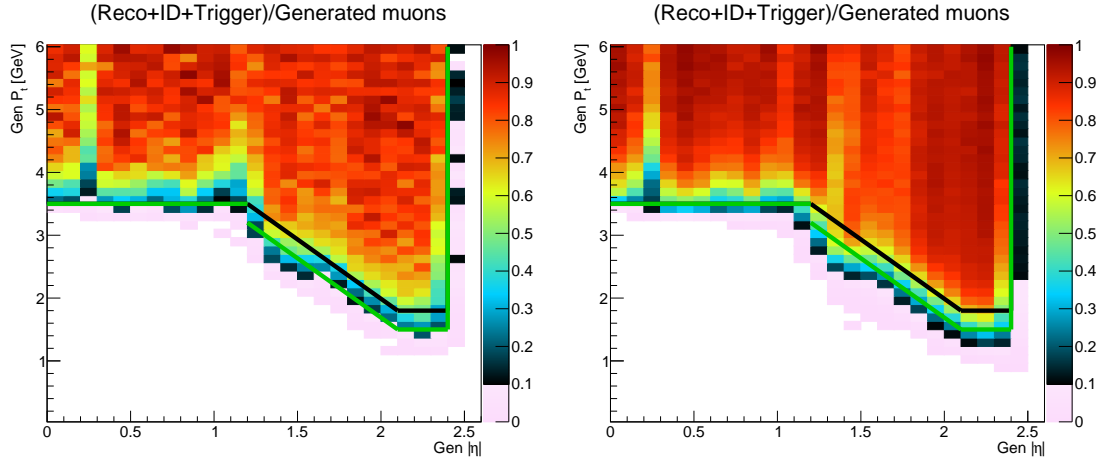


Figure 5-12: The total efficiency, including reconstruction, identification, and trigger, of a single muon in 2018 PbPb (left) and 2017 pp (right) are shown above. The black curve is the 2015 PbPb and pp 90% muon efficiency boundary while the green curve is the 2017 pp and 2018 PbPb 90% muon efficiency boundary. The green boundary is translated to numerical values in Table 5.4

We should note that there is a discontinuity of the muon acceptance selection at $|\eta| = 1.2$. Aside from the single muon selections, the following selections are applied

to the reconstructed dimuon candidates

- Two muons have opposite charges
- Two muons are tracker muons
- The dimuon invariant mass is about $0.15 \text{ GeV}/c^2$ near the J/ψ PDG mass ($m_{J/\psi} = 3.096916 \text{ GeV}/c^2$): $|m_{\mu\mu} - m_{J/\psi}| < 0.15 \text{ GeV}/c^2$
- One muon is L2 muon and the other one is L3 muon (described in section 2.25)
- The probability of the two muon tracks originating from the same decay vertex $> 1\%$

In addition, a B-meson invariant mass window of $4 < m_B < 6 \text{ GeV}/c^2$ is applied since the B_s^0 mass is $m_{B_s^0} = 5.367 \text{ GeV}/c^2$ and the B_s^+ mass is $m_{B_s^+} = 5.279 \text{ GeV}/c^2$ [4]. Anything far away from the mass window should not be considered. After applying all these preliminary selections to improve the quality of our dataset for the analysis, we are ready to perform cut optimization to further reject background candidates based on the decay topology of the B_s^0 and B_s^+ decay chains.

5.6 Cut Optimization

Given the high combinatorial background, particularly in PbPb collision where we have thousands of tracks per event [186], it is not possible to observe the B-meson resonance by simply applying the preselections presented in the previous section. Figure 5-13 shows the invariant mass distribution of fully reconstructed B_s^0 and B_s^+ at $7 < p_T < 50 \text{ GeV}/c$ after the event, track, and muon selections.

No clear B-meson signal is observed from the data. Therefore, aside from the preselections, a multivariate analysis (MVA) approach [187] is thus conducted in order to develop optimal selections to separate B-meson signal from the background and reconstruct significant resonances in the invariant mass distributions from the data. The fitting performance is further related to both the amount of signal and background presented in the B-meson invariant mass spectra.

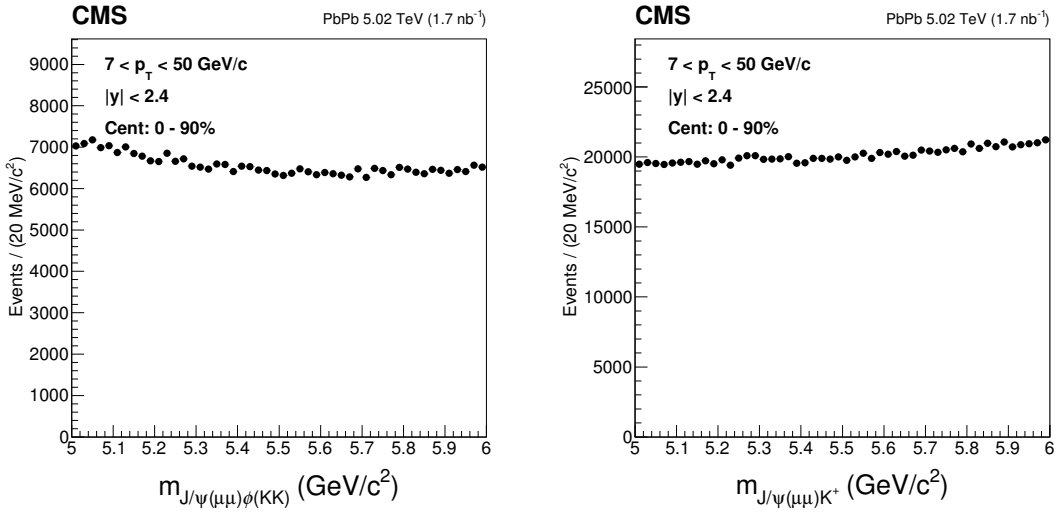


Figure 5-13: The invariant mass distributions of fully reconstructed B_s^0 (left) and B^+ (right) after preselection are shown above.

5.6.1 Topological Variables

By an MVA analysis, one can then find the proper selection criteria optimized for this purpose. Several variables related to the kaon tracks and B mesons decay topology are applied to reduce the combinatorial background that arises from a random combination of tracks and muons. The topological variables used in B-meson analyses to be optimized by are listed as follows:

Topological Variables for B_s^0 :

- Kaon track p_T
- Kaon track transverse distance to closest approach (DCA) significance: $DCA_{xy}/\sigma_{DCA_{xy}}$
- Kaon track longitudinal distance to closest approach (DCA) significance: DCA_z/σ_{DCA_z}
- Dikaon invariant mass distance to the ϕ meson PDG mass: $|m_{KK} - m_\phi|$
- The B_s^0 meson decay length [or the distance between primary vertex (PV) and secondary vertex (SV)] significance: $|\vec{D}(SV, DV)|/|\sigma_{\vec{D}(SV, DV)}|$
- The open angle between the B-meson decay length vector and its three momentum: $\alpha : \cos(\alpha) = \frac{\vec{D}(SV, DV) \cdot \vec{p}}{|\vec{D}(SV, DV)| |\vec{p}|}$

- The cosine angle of the opening angle in the transverse direction: $\theta_B : \cos(\theta_B) = \frac{D(SV, DV)_{xy} \cdot p_T}{|D(SV, DV)_{xy}| |p_T|}$

- Vertex fitting probability: the χ^2 value of the vertex fitting

For B^+ , we also apply some addition rectangular selections before cut optimization. After that, we use the following topological variables in the cut optimization.

Topological Variables for B^+ :

- Kaon track p_T
- Kaon track $|\eta|$
- Kaon track transverse distance to closest approach (DCA) significance: $DCA_{xy}/\sigma_{DCA_{xy}}$
- The B^+ meson decay length [or the distance between primary vertex (PV) and secondary vertex (SV)] significance: $|\vec{D}(SV, DV)|/|\sigma_{\vec{D}(SV, DV)}|$
- The open angle between the B-meson decay length vector and its three momentum: $\alpha : \cos(\alpha) = \frac{\vec{D}(SV, DV) \cdot \vec{p}}{|\vec{D}(SV, DV)| |\vec{p}|}$
- The cosine angle of the opening angle in the transverse direction: $\theta_B : \cos(\theta_B) = \frac{D(SV, DV)_{xy} \cdot p_T}{|D(SV, DV)_{xy}| |p_T|}$
- Vertex fitting probability: the χ^2 value of the vertex fitting

Figure 5-14 and Figure 5-15 show the definitions of topological variables of B_s^0 and B^+ decay chains respectfully

These topological variables will become the inputs to the multivariate analysis to optimize the signal significance.

5.6.2 Multivariate Analysis

In statistics, many data analysis techniques only focus on one or two variables individually. Multivariate analysis (MVA) analyzes more than two variables simultaneously to improve the data analysis. Figure 5-16 shows schematically the advantages of MVA

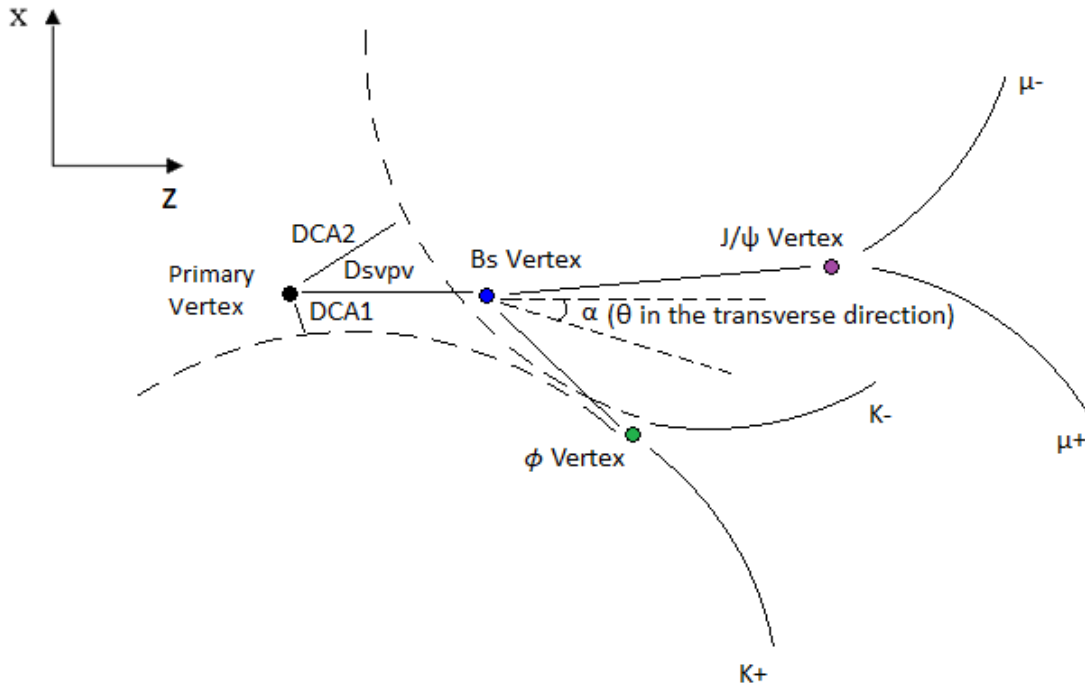


Figure 5-14: The definitions of topological variables in the decay of $B_s^0 \rightarrow J/\psi\phi \rightarrow \mu^+\mu^-K^+K^-$ (left) are schematically shown above.

to traditional statistical techniques in data analysis to separate the signal from the background with two variables.

We can see that in multivariate analysis, an MVA value as a function of two independent variables x and y : $MVA = f(x, y)$ is able to select signal out from the background with higher purity (larger S/B ratio) than the rectangular selection function $x_1 < x < x_2$ and $y_1 < y < y_2$. Table 5.5 shows the performance of MVA and traditional rectangular selections

Table 5.5: The numerical values of the comparison between the traditional rectangular selections and MVA.

Analysis Techniques	S	B	S/B
Rectangular	174	135	1.29
MVA	215	114	1.89

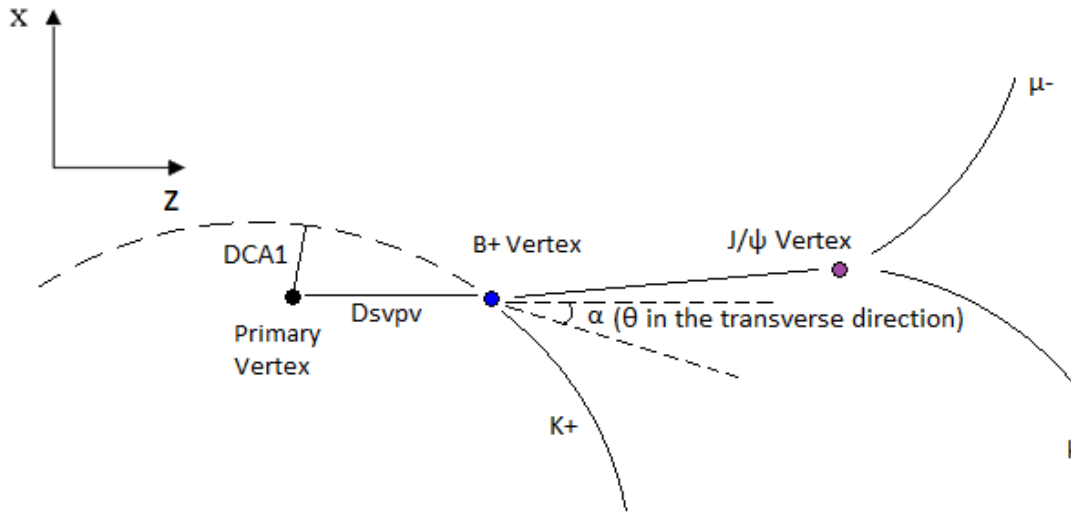


Figure 5-15: The definitions of topological variables in the decay of $B^+ \rightarrow J/\psi K^+ \rightarrow \mu^+ \mu^- K^+$ are schematically shown above.

5.6.3 Machine Learning Techniques

Machine learning, as a branch of artificial intelligence, is the science that gets computers to learn what human beings do. It is an automating data analysis method for model building to solve practical problems. Figure 5-17 demonstrates the data analysis problems including classification, regression, and clustering, where machine learning could be applied.

In this analysis, our goal is to separate B-meson signal out of the background. Therefore, it is a classification problem. Machine learning can be a powerful tool to solve our problems. We will apply supervised machine learning to train the computer and let them find the optimal selections for B-meson analyses for us.

5.6.4 Terminologies

The following list explains the technical jargons of machine learning techniques along with MVA that may be mentioned later in this thesis:

- **Training samples:** the input samples including both background and signal to train the computer. In this thesis, we use the B-meson candidates coming

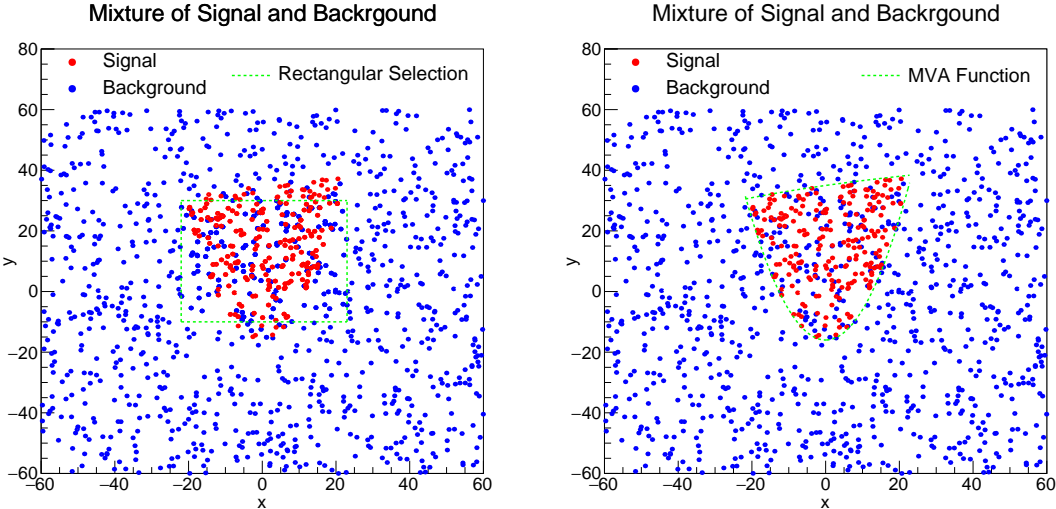


Figure 5-16: The performance of traditional rectangular selection with a range of x and y (left) compared to the MVA method of a curve as a function of X and Y (right) are shown above. Here, we have the total signal $S = 215$ and the background $B = 1000$.

from our selected B-meson decay channels (GEN Matched) in MC as the signal input and the B-meson candidates from the invariant mass sideband region with a distance of greater than $0.2 \text{ GeV}/c^2$ to the PDG B-meson mass as the background input to the *TMVA* framework

- **Testing samples:** the samples including both background and signal going to be tested with the output from the training. The testing sample should not be the same as the training sample.
- **Correlation matrix:** the linear correlation between the input variables for training
- **ROC curve:** the curve of signal efficiency as a function of the background rejection (equivalent to $1 - \text{background efficiency}$) for a given MVA value. Here the efficiency is defined as: efficiency = the number of candidates with the given MVA cut/number of candidates without the MVA cut.
- **Overtraining:** A Kolmogorov-Smirnov test [188] comparing the shape of the MVA distributions of training and test samples. It returns probabilities for both

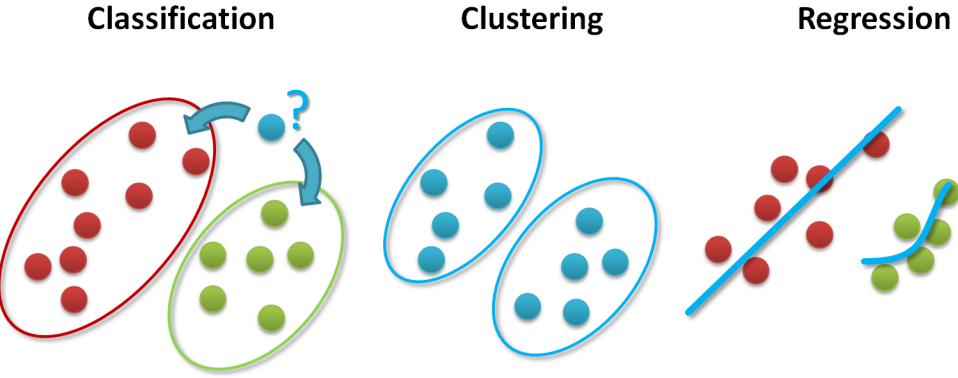


Figure 5-17: The solutions to classification, regression, and clustering problems with supervised and unsupervised machine learning approaches are shown schematically above.

signal and background between 0 and 1. The closer to 0, the poor the matching, the more the overtraining will be.

Figure 5-18 shows the definition of signal and background regions in B_s^0 and B^+ invariant mass plot.

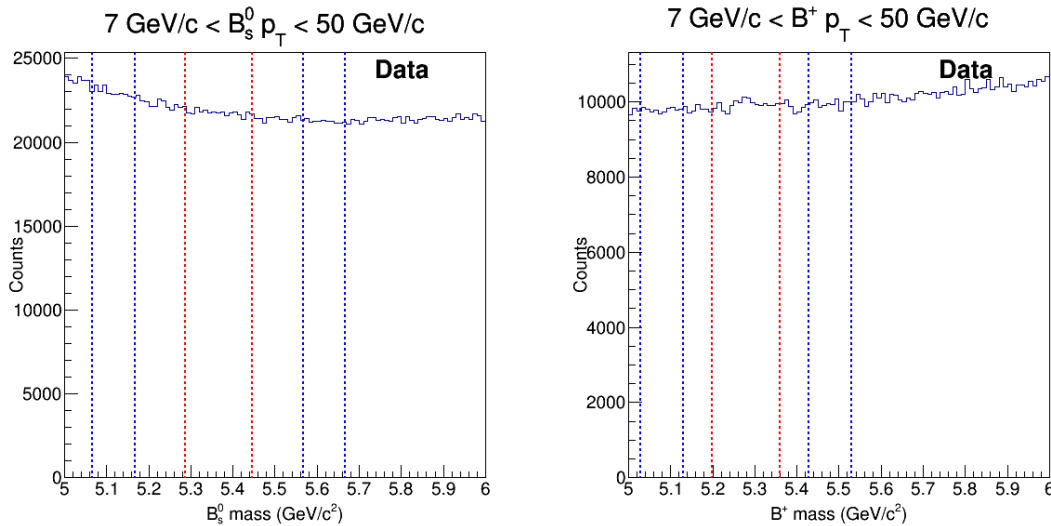


Figure 5-18: The definitions of signal (red band) and background region (blue band) in the fully reconstructed B-meson invariant mass distribution for B_s^0 (left) and B^+ (right) are shown above.

The signal region is $|m_B - m_B^{PDG}| < 0.08$ GeV/c and the background region is

$0.20 < |m_B - m_B^{PDG}| < 0.30$ GeV/c² for B_s^0 and $0.15 < |m_B - m_B^{PDG}| < 0.25$ GeV/c² for B^+ .

5.6.5 Boosted Decision Tree Algorithm

Nowadays, machine learning has become more and more sophisticated. There are many well developed machine learning algorithms such as Rectangular Cut (CutsSA), Linear Discriminant (LD), Boosted Decision Tree (BDT), Neural Network Feed-Forward Multilayer Perceptrons with Recommended ANN with BFGS Training Method and Bayesian Regulator (MLPBNN), and Deep Learning in the market. Here, I will give a brief introduction about the BDT algorithm in terms of *Boosted* and *Decision Tree*

Boosted: Boosted here refers to the “boosting” factor α in the hypothesis function to let the machine learn and correctly model the actual curve [189]. According to supervised machine learning, in order to use the boosting method, we first assign an ensemble of many weak learners to create a strong learner. The idea of boosting is to keep reweighing the function to enhance the classification and regression and performance by applying an MVA algorithm subsequently to the reweighed version of the training data in a sequential matter. Eventually, the hypothesis will converge a function that can describe the actual data. Figure 5-19 below shows schematically the boosting scheme

Decision Tree: A decision tree, sometimes called a regression tree, is a binary decision support tool using a tree-like model of decisions and list their possible consequences. Starting from a sample to analyze, it sets up criteria for selections to decide the likelihood of signal and background based on the pure signal and background input samples. Then, it makes binary decisions (Yes/No), in each branch to select a subset of samples out of the current sample, which can be either sequentially or in parallel. It will then iterate multiple times until the subsamples are considered as signal or background. In *TMVA* machinery, the number of iteration is called *NTree*. Figure 5-20 is a schematic demonstration of a decision tree with *NTree* = 4

In general, the performance of BDT will improve as *NTree* become larger. How-

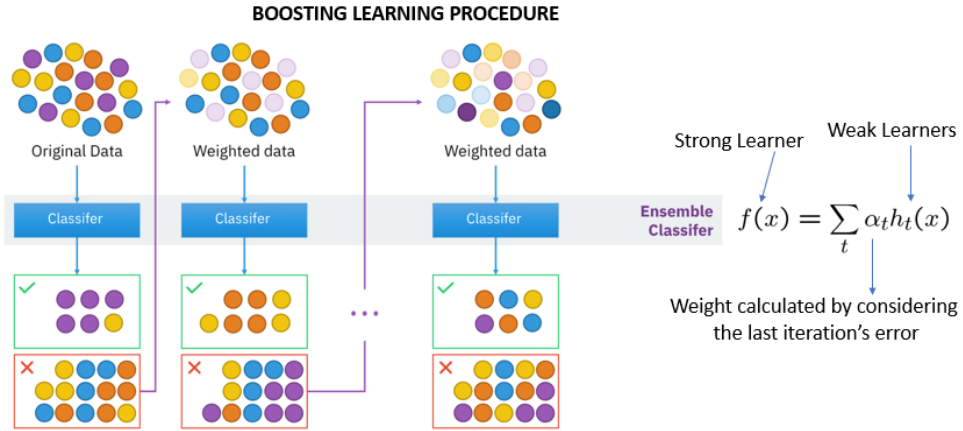


Figure 5-19: The schematic illustration of boosting procedures in machine learning is shown above.

ever, we should note that normally NTree is required to be smaller than the sample statistics. Otherwise, overtraining may occur and could induce biases in data analysis. We should also note that the BDT scores range from -1 to 1.

5.6.6 TMVA Training

To perform machine learning, I use the Toolkit for Multivariate Data Analysis with ROOT (*TMVA*) [190], a dedicated ROOT base machine learning software framework on C++ programming language, to train the computer to find the optimal MVA value as a function of the topological variables in our B-meson analyses. We propose to optimize B_s^0 in the p_T binning of [7, 10, 15, 20, 50] GeV/c and B^+ in the p_T binning of [5, 7, 10, 15, 20, 30, 40, 50, 60] GeV/c individually. The following procedures are carried out:

Step 1: identify sufficient signal and background samples to train the computer within *TMVA* machinery.

Step 2: choose the training algorithms to use. Here, we choose CutsSA, CutsGA, BDT, MLP, and MLPBNN2 algorithms

Step 3: decide the training parameters for each training algorithm.

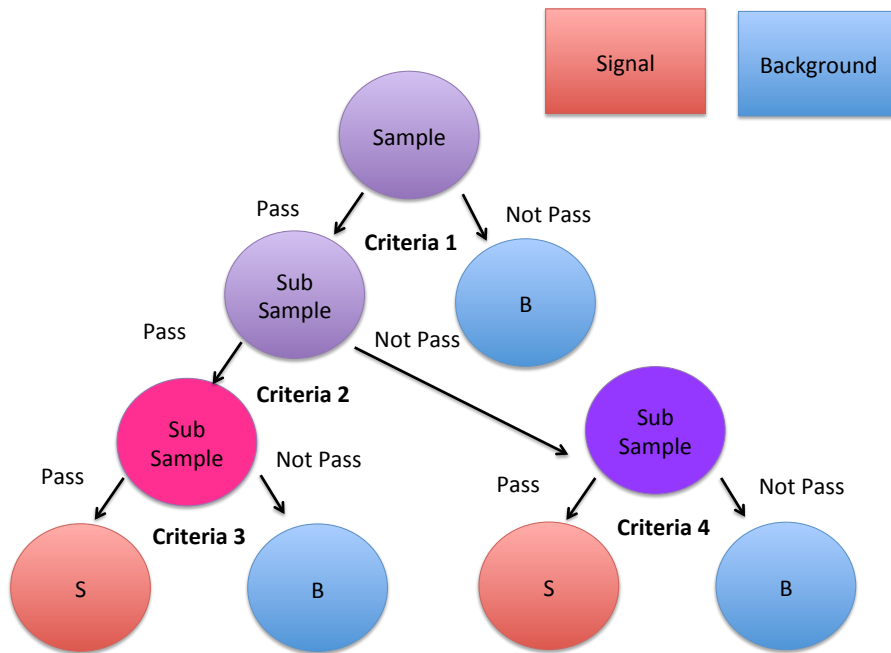


Figure 5-20: The schematic block diagram of a binary decision tree with $NTree = 4$ to separate signal and background in a training sample.

Step 4: run the TMVA machinery and generate the performance plots

Step 5: choose the best algorithm according to the performance

5.6.7 Training Performance

After finishing the TMVA training procedure, we are ready to look at the training performance. First, we produce the correlation between the input topological variables. Figure 5-21 shows the correlation matrices of B_s^0 and B^+ topological variables for B-meson $10 < p_T < 15$ GeV/c.

No significant correlation among the topological variables is observed except for the opening angle α and the cosine its transverse projection $\cos \theta$, which is known to be correlated. Therefore, the variable sets we input to the TMVA training are good.

Next, we compare the overall performance of the algorithms. Figure 5-22 below shows the ROC curves for B_s^0 TMVA training from $10 < p_T < 15$ GeV/c.

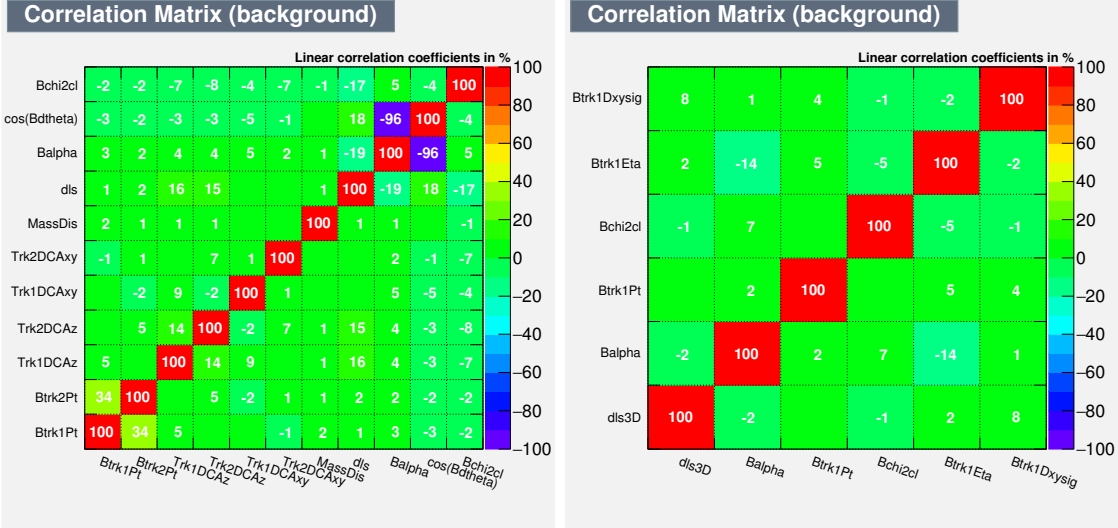


Figure 5-21: The correlation matrices of B_s^0 (left) and B^+ (right) in data at $10 < p_T < 15$ GeV/c are shown above.

We should note that the number of trees for BDT here is NTree = 2000. From Figure 5-22, we can see that BDT has the best performance compared to other algorithms in the given parameter settings. Basically, for a given background rejection efficiency, the BDT curve has the highest signal efficiency. Or, in other words, the area of BDT ROC curve is the largest among all other algorithms, demonstrating that BDT has the best performance. The BDT ROC curve is closer to the upper right corner where the best algorithm lies. Therefore, we decide to use the BDT algorithm to look for the optimal selections in all p_T bins in both B_s^0 and B^+ analysis.

Finally, before implementing the BDT algorithm to the analysis, we also check the overtraining and make sure that no significant overtraining is observed. Figure 5-23 show the overtraining test for both B_s^0 and B^+ BDT at $10 < p_T < 15$ GeV/c.

According to Figure 5-23, neither signal nor background of B_s^0 and B^+ BDT is vanishing. Hence, no significant overtraining is observed. The BDT training is valid to use in the B_s^0 and B^+ analysis.

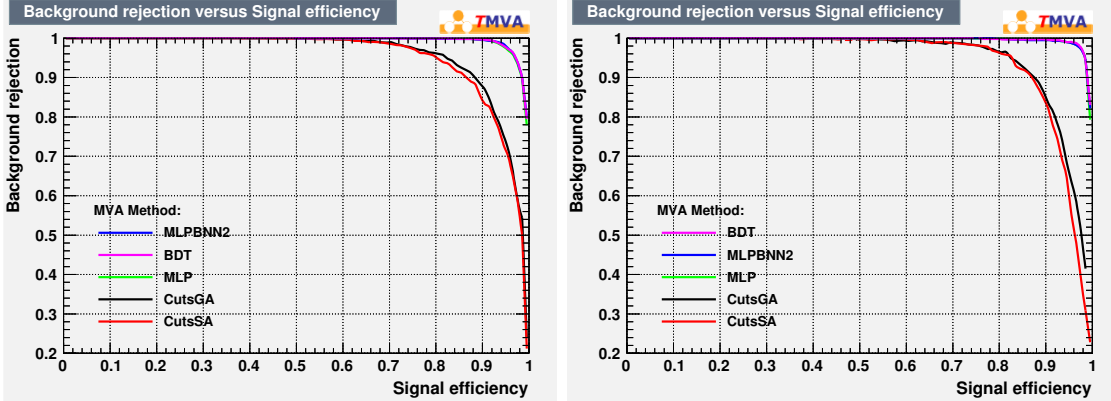


Figure 5-22: The B_s^0 ROC curves of CutsSA, CutsGA, BDT, MLP, and MLPBNN2 algorithms are shown above.

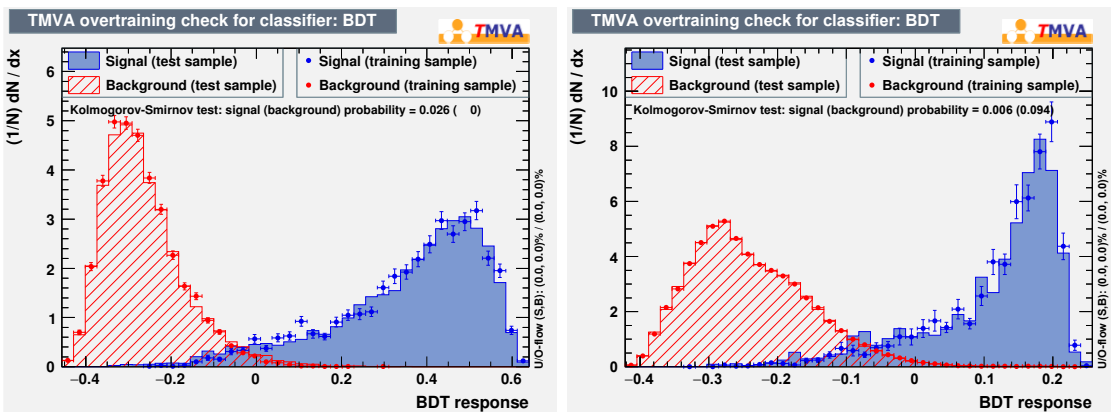


Figure 5-23: The Kolmogorov-Smirnov overtraining tests on the signal (blue) and background (red) in B_s^0 (left) and B^+ (right) at $10 < p_T < 15 \text{ GeV}/c$ are shown on the right. These plots suggest that they both pass the tests.

5.6.8 Working Point Determination

Now with the BDT training results, next step is to choose the BDT selections that can give us the best analysis results. We decide to use the statistical significance as the figure of merit, which is as follows

$$Sig = \frac{S}{\sqrt{S + B}} \quad (5.3)$$

We estimate S and B for a set of BDT cuts and choose the BDT scores that return to the maximum statistical significance in each p_T bin. We can directly estimate the

background B according to the data sideband region width scaled to the signal region band width

$$B = \frac{w_S}{w_B} N_B \epsilon_B \quad (5.4)$$

To determine the signal S , we do not directly look at the data. Instead, we use FONLL cross section [108] shown in 1-34 and the MC to determine the signal S as follows

$$S = 2R_{AA}^{2015Ref} L \sigma_{FONLL}^{pp \rightarrow b\bar{b}} \epsilon_{pre} \epsilon_S f(b \rightarrow B) BR \quad (5.5)$$

We know that since B^+ is more abundantly produced with large reconstructed efficiency since it has only one kaon track compared to B_s^0 . Therefore, the B_s^0 signal statistics is more limited. Table 5.6 summarizes our calculations of B_s^0 S , B , and S/B after the event, track, and muon pre-selections.

Table 5.6: The summary table of signal and background estimation of B_s^0 in each p_T and centrality bin in the analysis.

Centrality (%)	$B_s^0 p_T$ (GeV/c)	Signal (S)	Background (B)	S/B Ratio
0 – 90	7 – 10	12	24234	0.000495
0 – 90	10 – 15	47	14230	0.00330
0 – 90	15 – 20	24	2457	0.00977
0 – 90	20 – 50	25	698	0.0358
0 – 30	10 – 50	64	16697	0.00383
30 – 90	10 – 50	32	688	0.0465
0 – 90	10 – 50	96	17385	0.00552

Now, we scan through a series of BDT values from -1 to 1 and compute their corresponding statistical significance. Figure 5-24 shows the statistical significance as a function of BDT for B_s^0 and B^+ from $10 < p_T < 15$ GeV/c

For B_s^0 , our optimal selection returns us with an $S = 38$ and $B = 5$, which has a remarkable background-to-signal rejection of more than $10^3 : 1$.

Table 5.11 and Table We can see tha 5.8 document the optimal BDT selections maximizing the statistical significance in each p_T bin for B_s^0 and B^+ respectfully.

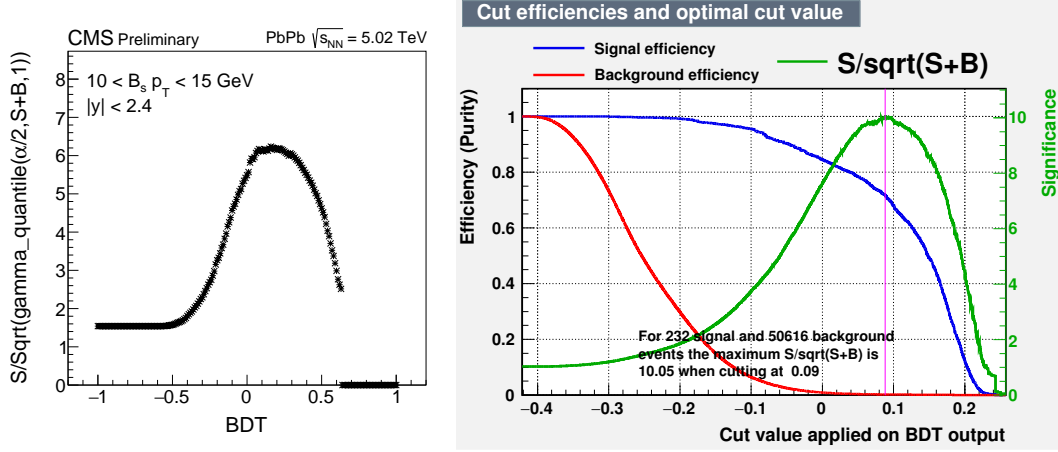


Figure 5-24: The significance: $Sig = \frac{S}{\sqrt{S+B}}$ as a function of BDT in B_s^0 from $10 < p_T < 15$ GeV/c are shown above. We can see that B_s^0 BDT peaks near 0.32 while B^+ peaks near 0.09.

Table 5.7: The summary of optimal BDT selection maximizing the B_s^0 statistical significance.

B_s^0 p_T (GeV/c)	5 – 10	10 – 15	15 – 20	20 – 50
BDT Cut Values	> 0.32	0.29	0.35	0.33

5.6.9 Optimal Selection Performance

To check the performance BDT selections, we look at the dimuon and dikaon invariant mass distributions to see if J/ψ and ϕ resonance are observed. Figure 5-25 shows the results after applying the selections

We can see clear J/ψ and ϕ peaks after applying the selections in both data and MC, which suggests that our selections are reasonable. Now we can also look at the invariant mass distributions of B_s^0 and B^+ in Figure 5-26

Again, we can see very clear signals after the optimal BDT selections in both B_s^0 and B^+ invariant mass distributions. With the optimal BDT selections and clear B-meson signals, we are ready to study its background and signal before extracting the raw yield for B-meson cross section measurement.

Table 5.8: The summary of optimal BDT selection maximizing the B^+ statistical significance.

$B^+ p_T$ (GeV/c)	5 – 7	7 – 10	10 – 15	15 – 20	20 – 30	30 – 40	40 – 50	50 – 60
BDT Cut Values	> 0.02	0.03	0.09	0.07	0.10	0.16	0.20	0.27

5.7 Background Studies

5.7.1 Overview

The productions of J/ψ mesons occur in three ways. The prompt J/ψ produced directly in pp collision, indirectly via the decay of heavier charmonium states, and non-prompt J/ψ from the decay of a b hadron. Non-prompt J/ψ mesons lead to a measurement of the b-hadron cross section. According to PDG, so far physicists have observed thousands of known decay modes of b hadrons [4]. Without hadronic PID, we can envision that potential background feed-down sources coming from other b-hadron decays contribute to the B-meson invariant mass spectra. For instance, the decay of $B^0 \rightarrow J/\psi K^{*0}(892) \rightarrow \mu^+ \mu^- K\pi$ could contribute to the $B_s^0 \rightarrow J/\psi \phi \rightarrow \mu^+ \mu^- K^+ K^-$ due to misidentification of π to K . We call such background as “non-prompt (NP) background”, to distinguish them from the combinatorial background due to random combinations of decay daughter tracks when reconstructing B mesons. NP background generally forms a peaking structure in the region of interests. A dedicated inclusive NP J/ψ from b-hadron decays MC is simulated to determine the NP background component within our B-meson invariant mass regions. We then classify each reconstructed B-meson candidate by their GEN-level particle, e.g. whether it is coming from a B_s^0 , B^+ , or other decays that fall into the B-meson reconstruction workflow, in order to measure their individual contribution to the peaking structure.

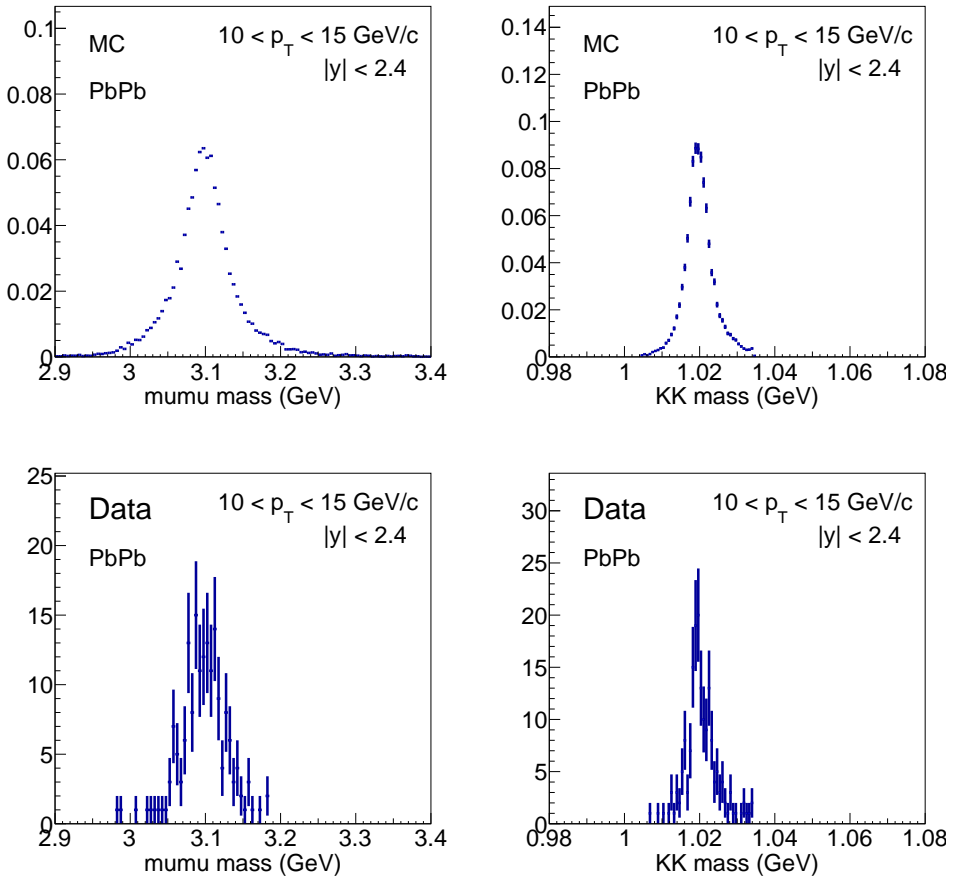


Figure 5-25: The J/ψ (left) and ϕ (right) meson mass distributions after applying $BDT > 0$ for MC (top) and data (bottom) in B_s^0 analysis are shown above.

5.7.2 Individual Channel NP Background Studies

Many small contributions form the peaking background structure. We can not identify each of them individually but most of the contributed ones are determined. Below is a list of example processes composing the majority of the peaking background:

- Case 1: $X \rightarrow J/\psi\pi^-K^+$, here pion is misidentified as kaon
- Case 2: $B_s^0 \rightarrow J/\psi K^+K^-$, in which both kaons are not coming from the decay of an intermediate ϕ meson resonance.
- Case 3: $B^+ \rightarrow J/\psi K^+$, added extra K^-
- Case 4: $X \rightarrow J/\psi\pi^+\pi^-$, pions misidentified as kaons.

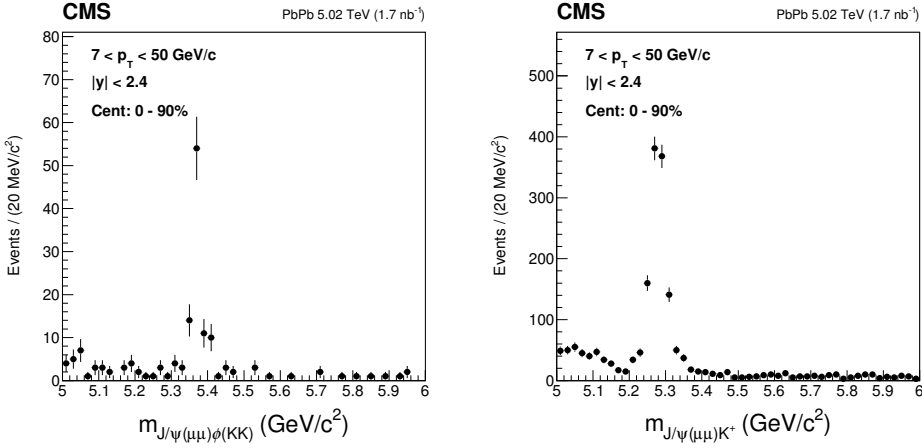


Figure 5-26: The B_s^0 (left) and B^+ (right) invariant mass distributions after applying optimal BDT selections from $10 < p_T < 50 \text{ GeV}/c$ in data are shown above.

- Case 5: $B_s^0 \rightarrow J/\psi K^+ K^- X$
- Case 6: $B_s^0 \rightarrow J/\psi \phi \pi \pi$
- Case 7: $B^0 \rightarrow J/\psi K^{*0}$

Figure 5-27 shows the contribution of the determined channels with respect to the total background after applying optimal cuts for PbPb for $10 < p_T < 15 \text{ GeV}/c$, $15 < p_T < 20 \text{ GeV}/c$, $20 < p_T < 50 \text{ GeV}/c$, as well as the inclusive $10 < p_T < 50 \text{ GeV}/c$. The peak at the B_s^0 signal region has been investigated. We have found that the mostly contributing channels are $B^0 \rightarrow J/\psi K^{*0}(892)$ in grey color and $B_s^0 \rightarrow J/\psi K^+ K^-$ in black color.

Figure 5-28 also includes the signal component in the distribution. We can see that the non-prompt background is insignificant compared to the total inclusive background and the inclusive background is low comparing to the $B_s \rightarrow J/\psi \phi \rightarrow J/\psi K^+ K^-$ signal in our studies.

5.7.3 B-meson contribution of NP Background to B_s^0

From the non-prompt background studies above, we can see that there are many small contributions. Those small components together summed up constructing a

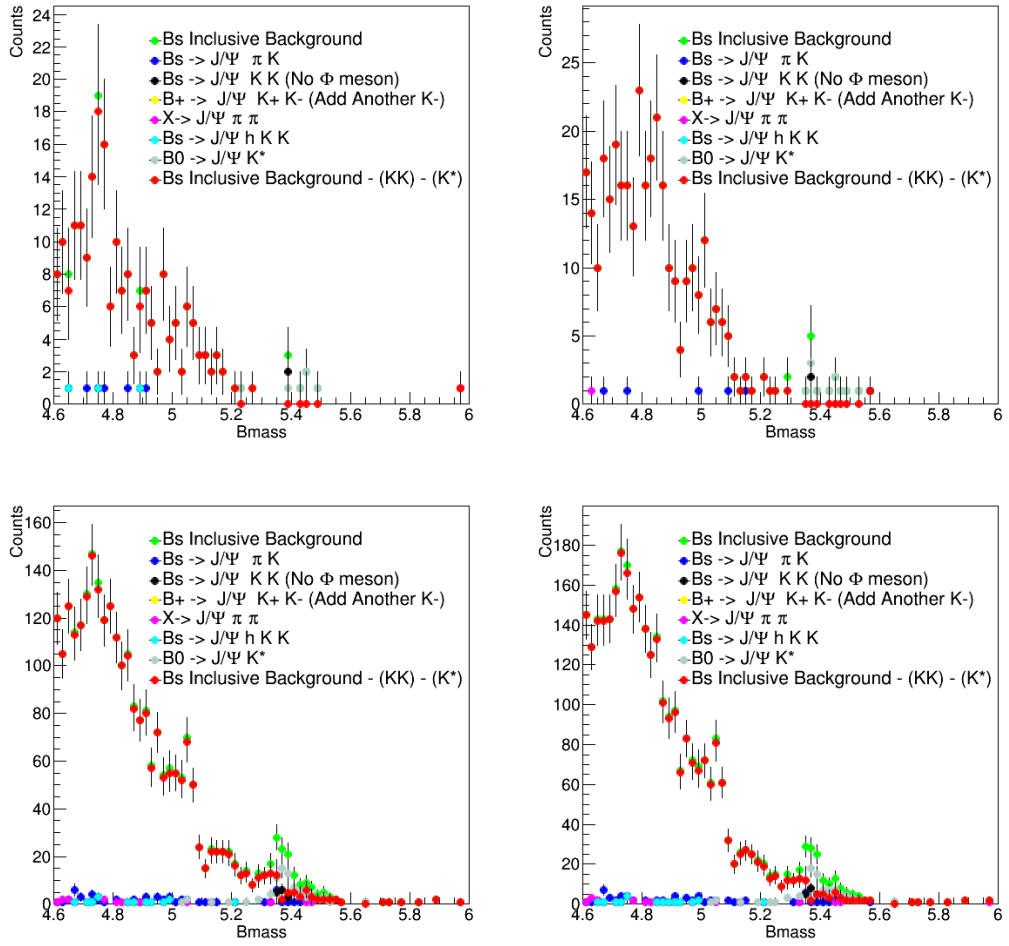


Figure 5-27: Individual NP background contributions with respect to the total background components from 10 to 15 GeV (top left), 15 to 20 GeV (top right), 20 to 50 GeV (bottom left), and 10 to 50 GeV (bottom right) in B_s^0 invariant mass distributions. The non-prompt background from all channels listed above is negligible compared to the inclusive background. Also, no peak near the B_s^0 resonance is observed when the $B^0 \rightarrow J/\psi K^{*0}$ and $B_s \rightarrow J/\psi K^+ K^-$ components subtract from inclusive background.

large background and we can not identify all of them individually. Under this circumstances, another definition of individual component is used. The new definition of the NP background components are listed below

- Case 1: $B^+ \rightarrow J/\psi X$, all contributions from B^+
- Case 2: $B_s^0 \rightarrow J/\psi X$, all contributions from B_s^0

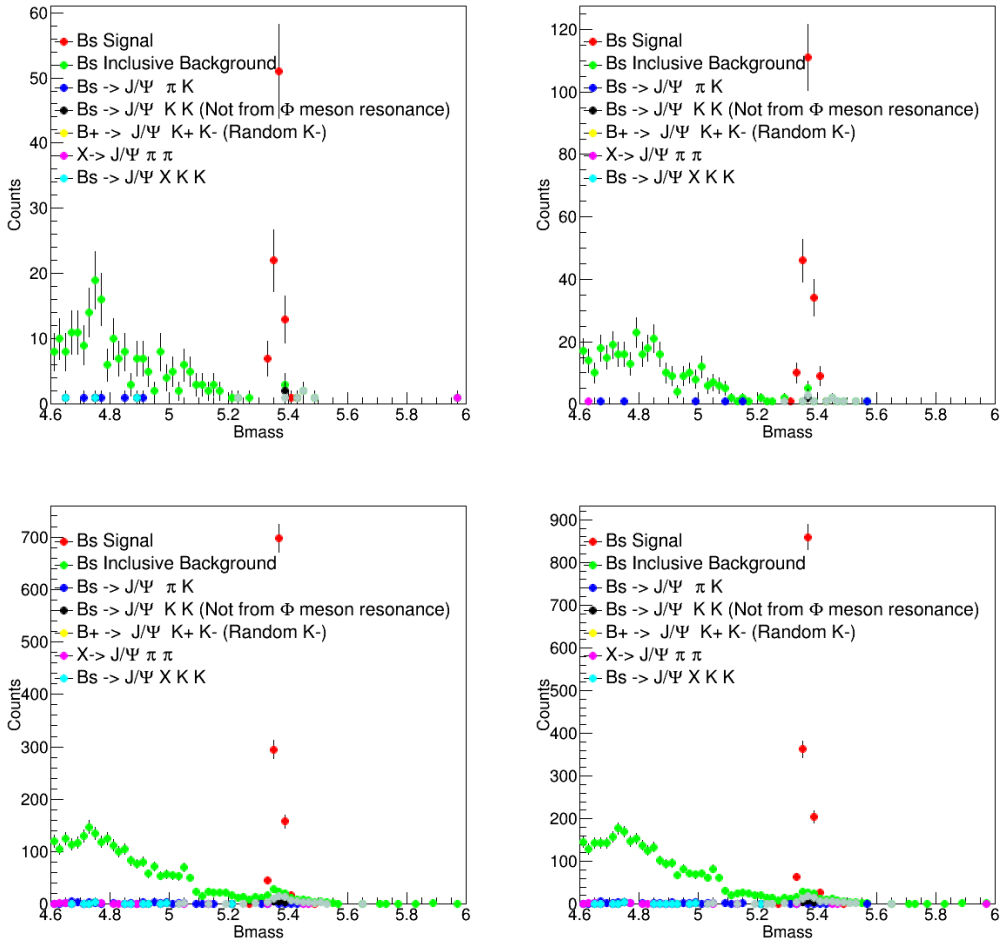


Figure 5-28: Individual Non-prompt background contributions with respect to the total background components and the signal channel from 10 to 15 GeV (top left), 15 to 20 GeV (top right), 20 to 50 GeV (bottom left), and 10 to 50 GeV (bottom right). We can see that the inclusive background is small compared to the signal in our studies.

- Case 3: $B^0 \rightarrow J/\psi X$, all contributions from B^0
- Case 4: Other contributions

In Figure 5-29, the signal region is dominated by the B^0 , B^+ , and B_s^0 decays while the other channels are contributed on the left side of the mass spectrum.

Hence, the conclusion is that the NP peaking background contribution to the B_s^0 is negligible due to the $K^{*0}(892)$ veto cut: $|m_{KK} - m_\phi| < 0.015 \text{ GeV}/c^2$. We estimate that it may only contribute around 4% uncertainties to the signal yield, negligible

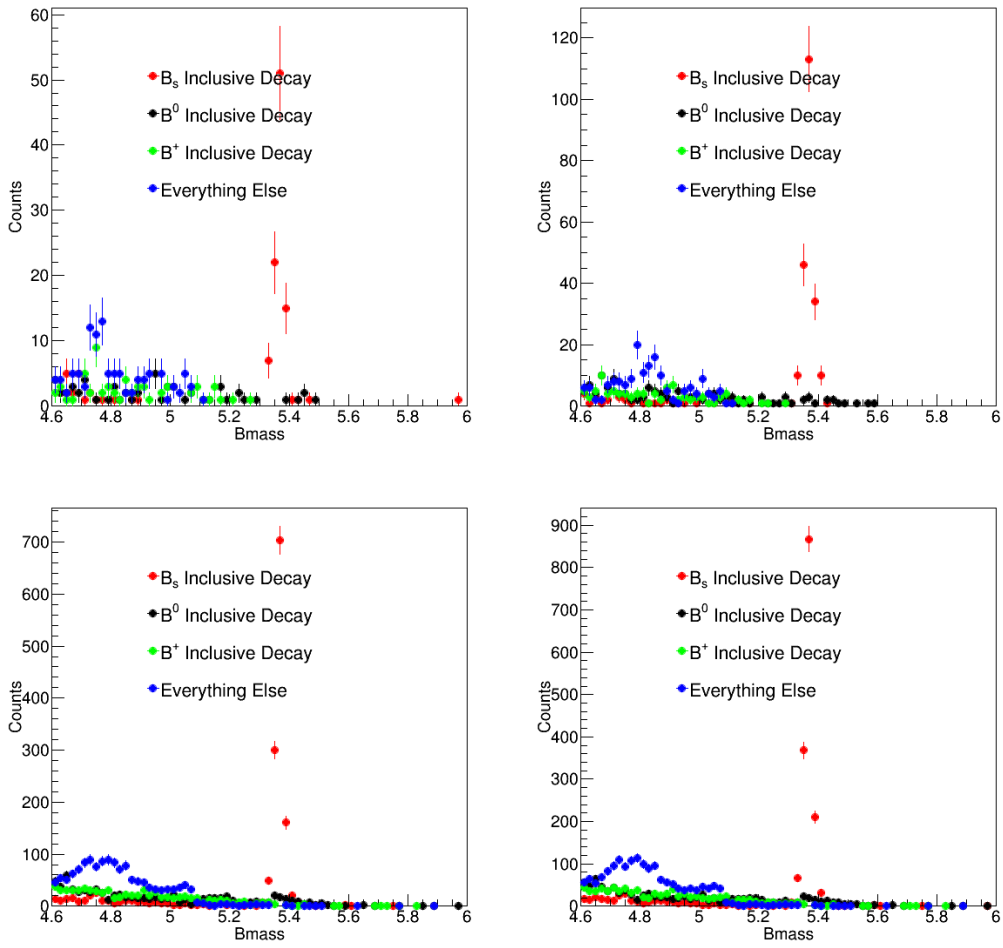


Figure 5-29: B^+ , B_s^0 , B^0 channels make nearly equal contribution in the signal region for all p_T bins 10 - 15 GeV/c, 15 - 20 GeV/c, 20 - 50 GeV/c, and 10 - 50 GeV/c.

compared to the statistical uncertainties of the B_s^0 signal, which is on the order of 10%. Hence, there is no need to develop a specific function to model the NP background component for B_s^0 .

5.7.4 B-meson Contribution of NP Background to B^+

We veto the candidates from the inclusive NP J/ψ MC sample that are matched to a genuine B^+ signal. The resulting B candidate mass spectrum in the inclusive p_T range (5-100 GeV/c) is shown in Figure 5-30 for PbPb MC samples.

It is clear that these sources create a peaking structure in the region of $m_{B^+} < 5.20$

GeV/c^2 as seen in Figure 5-26 after applying the optimal selections. This structure can be nicely fitted with an error function as done previously in B-meson pp analyses [191]. In addition, there is a minor peak on the right shoulder ($\approx 5.34 \text{ GeV}/c^2$) of the nominal signal ($\approx 5.28 \text{ GeV}/c^2$), and this can be fitted with a Gaussian function. The additional combinatorial background can be fitted with an exponential decay function. This contribution is absorbed in the total combinatorial background of our nominal channel of the main analysis. This will be described in detail in Section 5.8. The shape of the NP background model function is used as a template in fit to perform the signal extraction.

Further MC studies have been carried out to identify different channels that give rise to the non-prompt peaking structure in the B^+ invariant mass distribution. Several main processes have been identified as follows:

- Case 1: 4-body B^+ decays which occur via resonant decay channels e.g. $B^+ \rightarrow J/\psi K^{*+}(892)$. In these cases, we treat the kaons coming from the $K^{*+}(892)$ decays as coming from a signal $B^+ \rightarrow J/\psi K^+$ decay.
- Case 2: 4-body B^0 decays channels e.g. $B^0 \rightarrow J/\psi K^{*0}(892)$.
- Case 3: $B^+ \rightarrow J/\psi \pi^+$ decays in which we have misidentified the π^+ as a K^+ .

The different contributions are presented in Fig.5-31. The contribution from $B^+ \rightarrow J/\psi \pi^+$ clearly forms a peaking structure on the right shoulder of the nominal decay channel B^+ decay. However, the overall magnitude of this component is tiny compared to the other two sources, and negligible compared to the nominal signal. As a consequence, we can barely see the contribution of this peaking structure in the invariant mass plot of B^+ nominal channel.

The conclusion from these studies is that we need to use a function to model the NP background component. Its template shape should be determined according to the B^+ NP J/ψ MC sample and applied to the data with a scale parameter. According to our studies, such function is the error function in the left-hand shoulder (lower than the B^+ PDG mass) and a double Gaussian in the B^+ signal region.

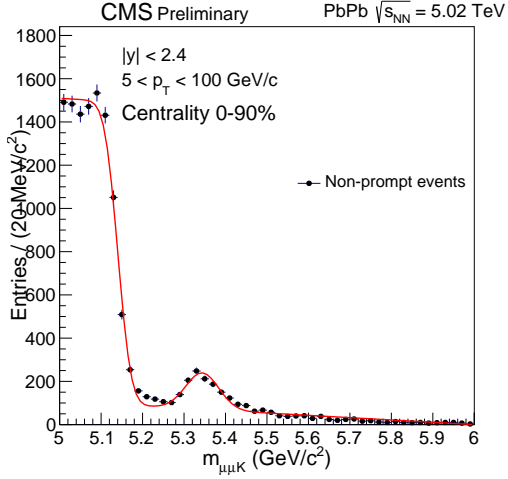


Figure 5-30: B^+ invariant mass distributions obtained from inclusive B-meson MC production after vetoing the contribution of genuine B^+ signal candidates is shown above.

5.8 Signal Extraction

Now, equipped with the optimal BDT selections and the NP background studies, we are ready to extract the signal raw yield from the B-meson invariant distribution and measure the cross section. Also, since we see very clear B_s^0 signals, we can estimate the B_s^0 significances and check if they lead to an observation.

5.8.1 Fitting Models

Raw yields are extracted through the extended unbinned maximum likelihood fits to the invariant mass of reconstructed B_s^0 meson candidates, which is performed using the *Roofit* package [192]. The unbinned fit can reduce the potential bias due to the binning artifact. We develop the probability density function (PDF) to fit to the B-meson invariant mass distributions to extract their signal raw yields. In the PDF, the signal region for both B_s^0 and B^+ are described by Gaussian functions with the same means but different widths while the combinatorial background is modeled with an exponential decay function. For B^+ , an additional error function in the left-hand shoulder (lower than the B^+ PDG mass) and a double Gaussian in the B^+ signal

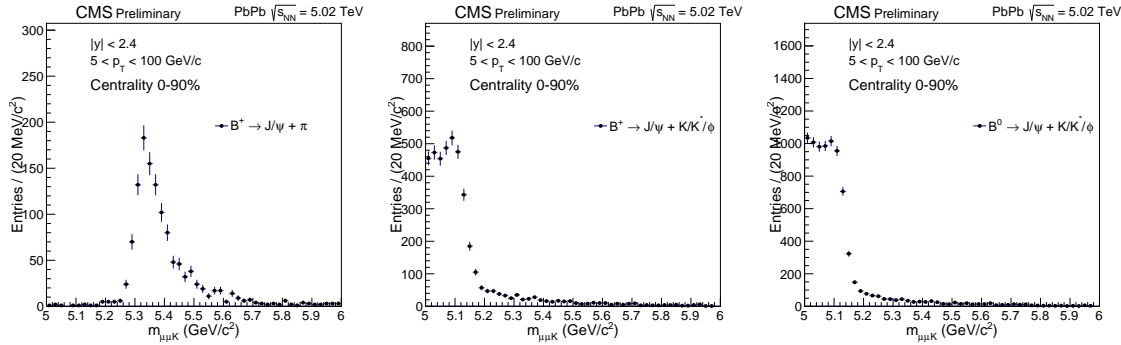


Figure 5-31: Peaking background contribution from $B^+ \rightarrow J/\psi\pi$ and from $K^{*0}(892)$ and $K^{*+}(892)$ resonant decay channels of B^0 and B^+ are shown above.

region to fit NP peaking background due to the b-hadron feed down based on the template fits to inclusive NP J/ψ MC sample in Section 5.7.

Hence, the generic event likelihood in data is described by the formula below

$$\mathcal{L}(m; N_S) = N_S \cdot (\alpha G(m; M, \sigma_1) + (1 - \alpha)G(m; M, \sigma_2)) + N_B \cdot E(m; \lambda_m) \quad (5.6)$$

$$G(m; M, \sigma) = \frac{1}{\sqrt{2\pi}\sigma} \exp^{-\frac{(m-M)^2}{2\sigma^2}} \quad (5.7)$$

$$E(m; \lambda_m) = \exp^{-\lambda_m m} \quad (5.8)$$

Where m is the candidate mass (input). M and σ_i are the signal mass means and widths (resolution); G and E denote respectively Gaussian and Exponential functions, normalized in the fitting mass window; N_S denotes the signal raw yield (the parameter of interest), N_B is the background yield, while α and λ_m are nuisance parameters (describing the signal fractions and exponential decay constants).

It should note that the main reason for using double Gaussian functions instead of a single Gaussian is that the reconstructed B_s^0 signal width varies as a function of B-meson p_T due to the p_T dependence of the track p_T resolution. Figure 5-32 shows the B_s^0 and B^+ invariant mass width as a function of p_T in the MC

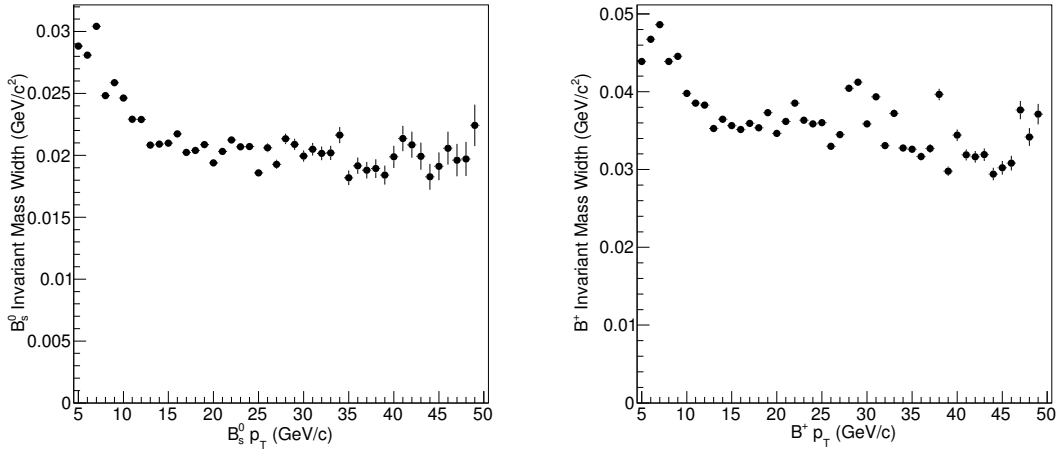


Figure 5-32: The signal B_s^0 (left) and B^+ (right) invariant mass widths as a function of p_T are shown above. We could see a rather large variation of the B-meson mass width from low to high p_T .

5.8.2 Raw Yield Extraction

To obtain the signal raw yields and their statistical uncertainties from B_s^0 and B^+ invariant mass distributions, the following fitting procedures are carried out within the B-meson invariant mass window of $5 < m < 6 \text{ GeV}/c^2$.

- First, a fit is performed, with a double Gaussian function to the MC invariant mass distribution of the genuine B-meson signals.
- For B^+ , the shape of the NP background component is obtained using the dedicated NP J/ψ MC samples.
- The fit is performed to the data with the fixed shapes (widths and relative proportion of the two Gaussians) same with the Gaussians obtained from the MC fit.
- For systematic uncertainty check, add a free parameter (a), which is commonly multiplied by the widths of the signal Gaussians, serving as a scale factor of the resolution that parametrizes data and MC signal shape difference. However, in the nominal fit, this is set to be unity ($a = 1$), which means the widths of the

data signal are set to be identical to the ones of the MC signal.

- The parameters of the background PDF and the mean of the signal Gaussians are the free parameters of the fit.

Figure 5-33 shows the fitting results of B_s^0 in the p_T range of [7, 10, 15, 20, 50] GeV/c.

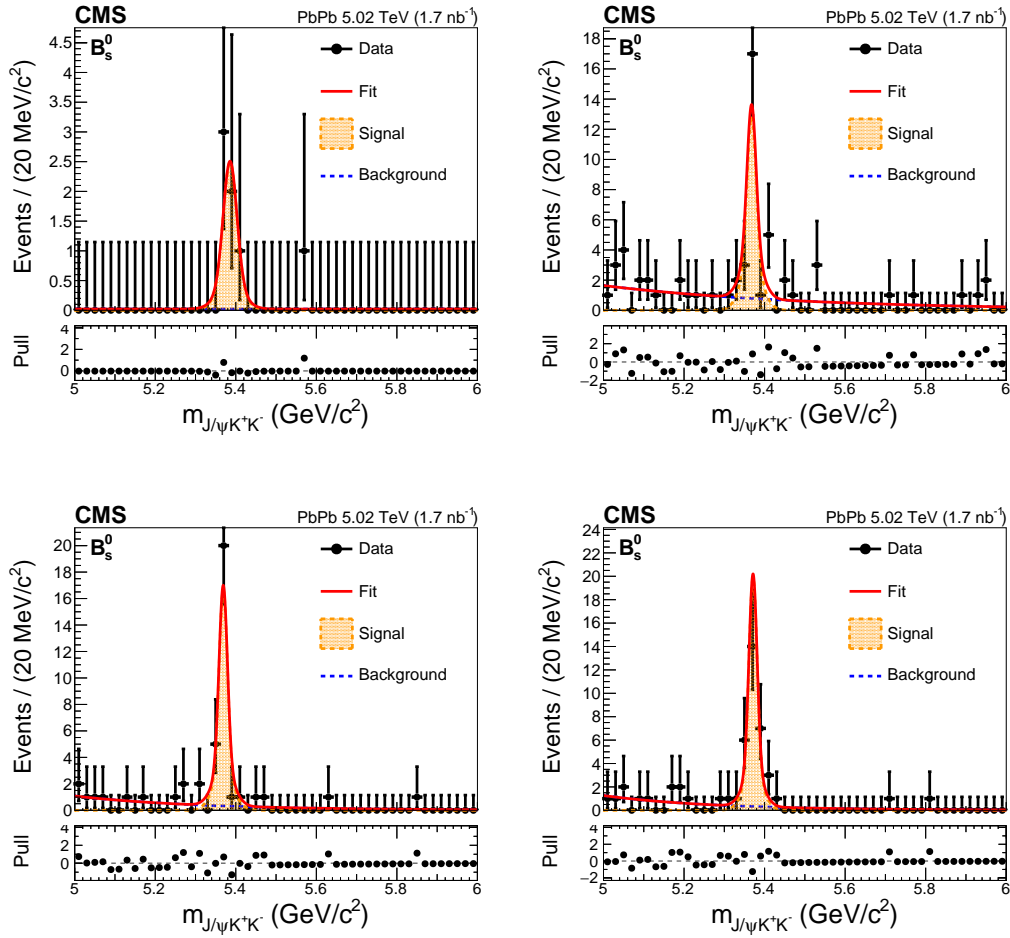


Figure 5-33: The B_s^0 invariant mass distributions as well as the fits to extract the signal raw yield N_S in different p_T bins are shown above.

Figure 5-34 shows the fitting results of B_s^0 in the centrality range of [0, 30, 90] % in PbPb collisions.

Figure 5-35 shows the fitting results of B^+ in the p_T range of [7, 10, 15, 20, 50] GeV/c.

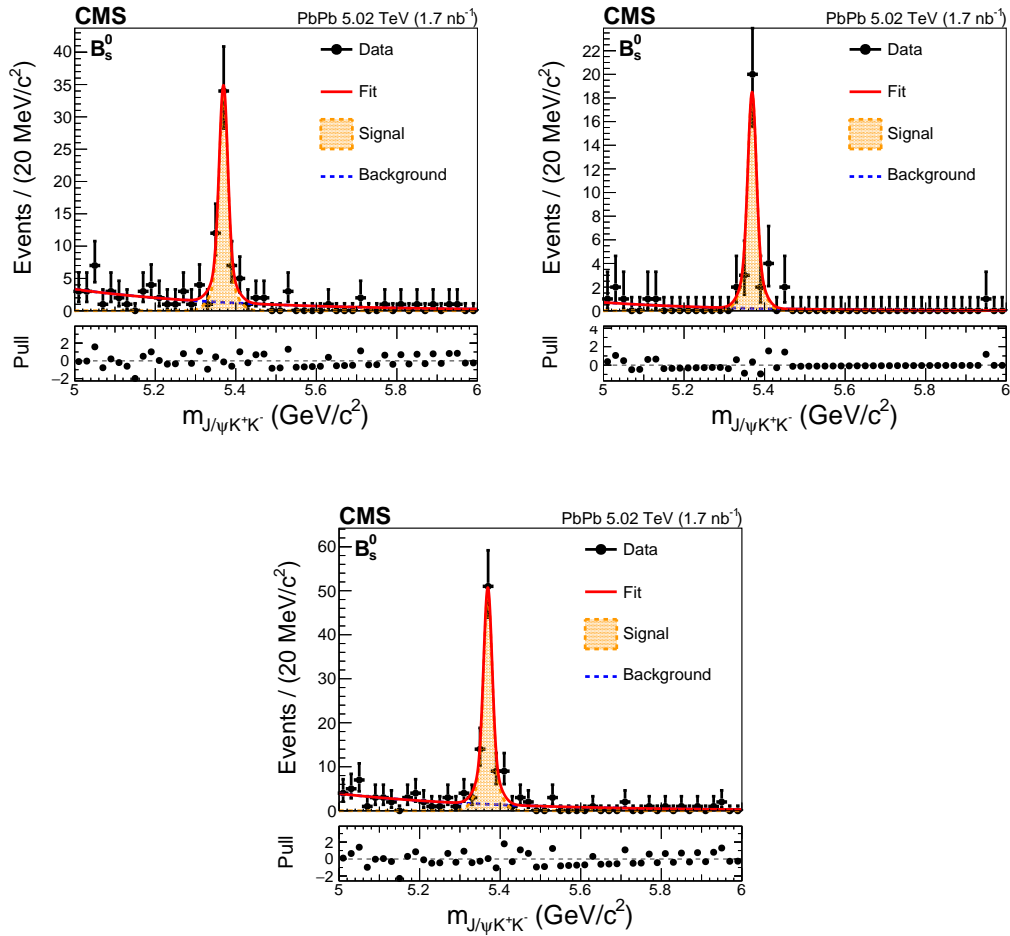


Figure 5-34: The B_s^0 invariant mass distributions as well as the fits to extract the signal raw yield N_S in centrality bins 0 - 30%, 30 - 90%, and 0 - 90% are shown above.

Figure 5-36 shows the fitting results of B_s^0 in the centrality range of [0, 30, 90] % in PbPb collisions.

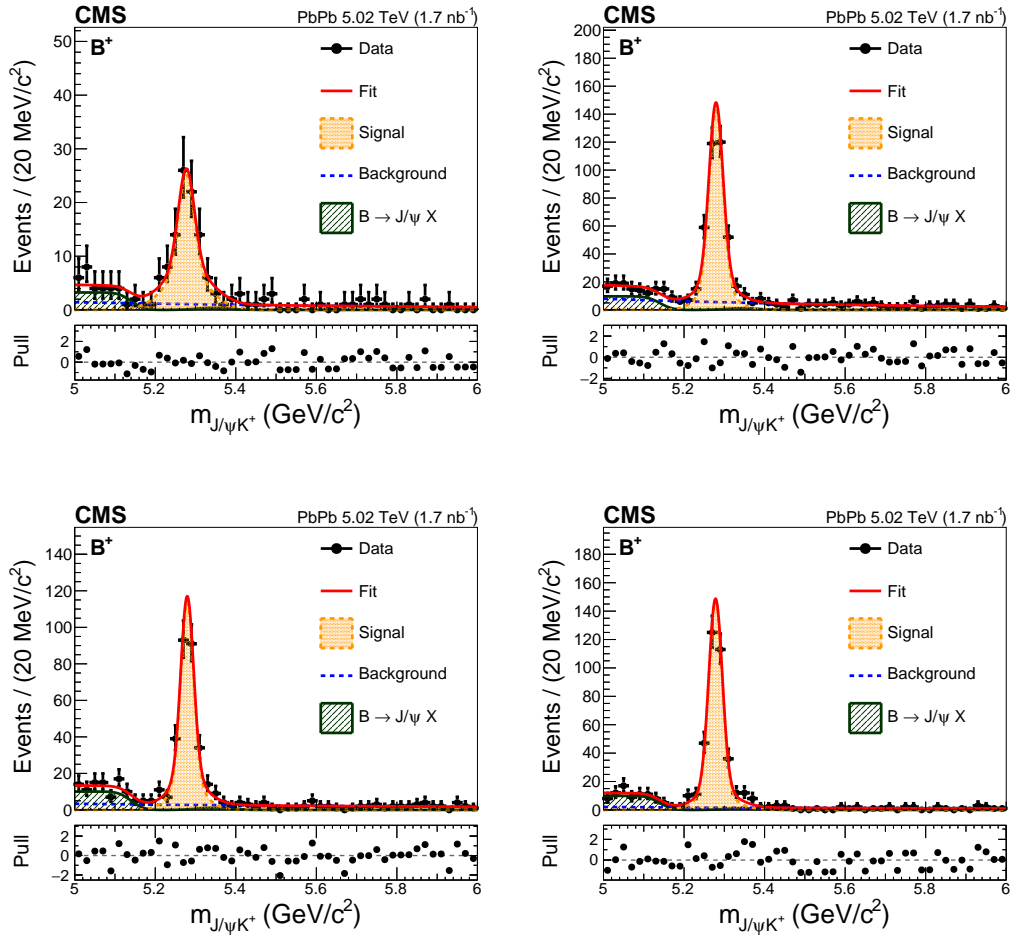


Figure 5-35: The B^+ invariant mass distributions as well as the fits to extract the signal raw yield N_S in different p_T bins are shown above.

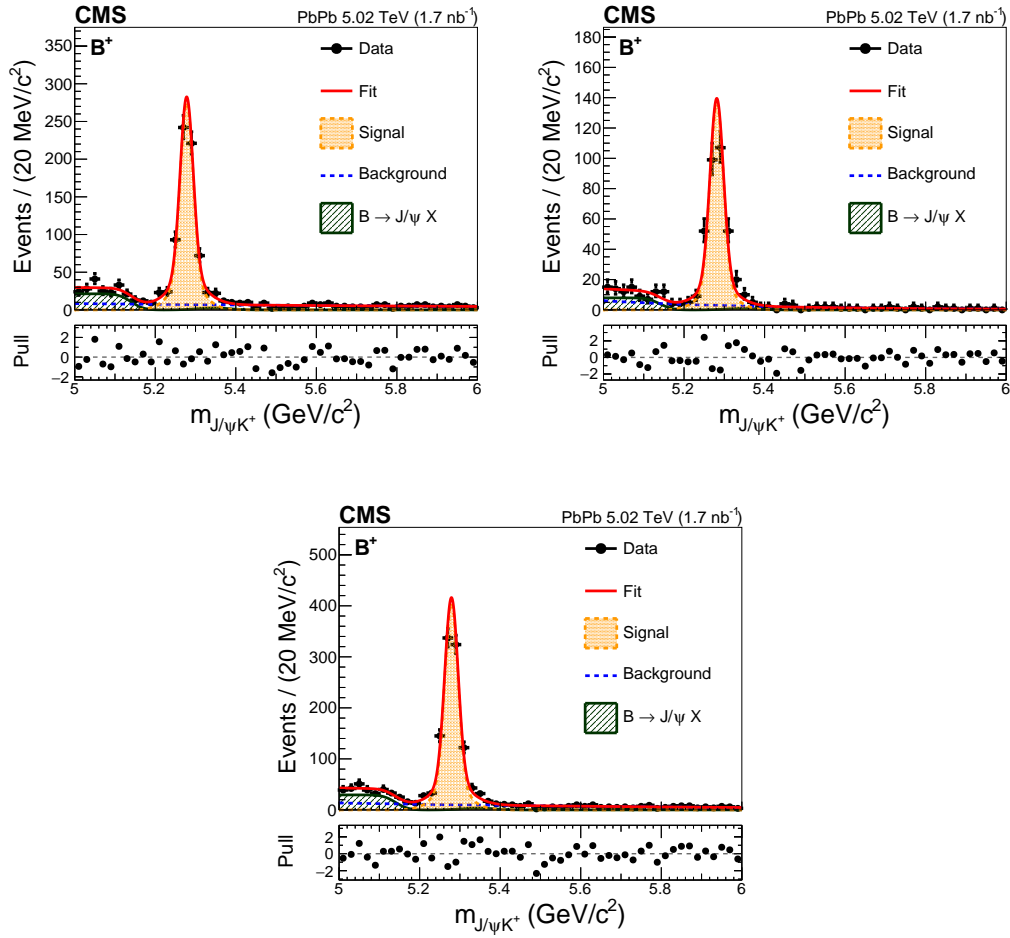


Figure 5-36: The B^+ invariant mass distributions as well as the fits to extract the signal raw yield N_S in centrality bins 0 - 30%, 30 - 90%, and 0 - 90% are shown above.

Table 5.9 and 5.10 below summarize the selected fit parameters and their error extracted from the fits of B_s^0 and B^+ respectfully

Table 5.9: The summary table of B_s^0 fits results of Gaussian mean, signal raw yield, and background raw yield as well as their uncertainties.

Centrality (%)	$B_s^0 p_T$ (GeV/c)	Gaus Mean (GeV/c ²)	Sig Yield (N_S)	Bkgd Yield (N_B)
0 – 90	7 – 10	5.386 ± 0.007	5.94 ± 2.43	1.06 ± 1.03
0 – 90	10 – 15	5.368 ± 0.003	23.41 ± 5.28	35.59 ± 6.28
0 – 90	15 – 20	5.369 ± 0.002	26.70 ± 5.31	16.33 ± 4.20
0 – 90	20 – 50	5.371 ± 0.003	30.19 ± 5.73	16.82 ± 4.39
0 – 30	10 – 50	5.369 ± 0.002	54.64 ± 7.86	60.35 ± 8.19
30 – 90	10 – 50	5.370 ± 0.003	29.88 ± 5.58	10.13 ± 3.37
0 – 90	10 – 50	5.369 ± 0.002	80.25 ± 9.43	68.74 ± 8.79

Table 5.10: The summary table of B^+ fits results of Gaussian mean, signal raw yield, and background raw yield as well as their uncertainties.

Centrality (%)	$B^+ p_T$ (GeV/c)	Gaus Mean (GeV/c ²)	Sig Yield (N_S)	Bkgd Yield (N_B)
0 – 90	7 – 10	5.277 ± 0.004	92.33 ± 10.88	7.90 ± 2.33
0 – 90	10 – 15	5.279 ± 0.001	354.6 ± 20.68	39.9 ± 6.28
0 – 90	15 – 20	5.279 ± 0.001	26.70 ± 5.31	16.33 ± 4.20
0 – 90	20 – 50	5.278 ± 0.001	30.19 ± 5.73	16.82 ± 4.39
0 – 30	10 – 50	5.278 ± 0.001	657.7 ± 27.7	53.46 ± 5.28
30 – 90	10 – 50	5.281 ± 0.001	327.0 ± 19.5	19.57 ± 4.69
0 – 90	10 – 50	5.279 ± 0.001	971.6 ± 33.9	74.16 ± 6.91

At a glance, we can see that our fits all look good. In addition to the fits, the pulls, defined as the ratios of the difference between the data and the fit to the statistical uncertainties of the data, are also shown above in Figure 5-33, Figure 5-34, Figure 5-35, and Figure 5-36. We can see that the pulls are basically consistent with 0 with a 2σ fluctuation, which again suggests that our fits good. A dedicated closure test on the fits will be conducted later to further validate our fits.

5.8.3 Signal Significance Estimation

The significance (Z) is calculated through a likelihood method, which follows the formula below:

$$Z = \sqrt{2 \log \frac{L_{S+B}}{L_B}} \quad (5.9)$$

Here, L_{S+B} is the likelihood of each fit and L_B is the likelihood when the number of signal N_S parameter is fixed to 0. Figure 5-37 show the likelihood scan of B_s^0 in 4 p_T bins and 3 centrality bins

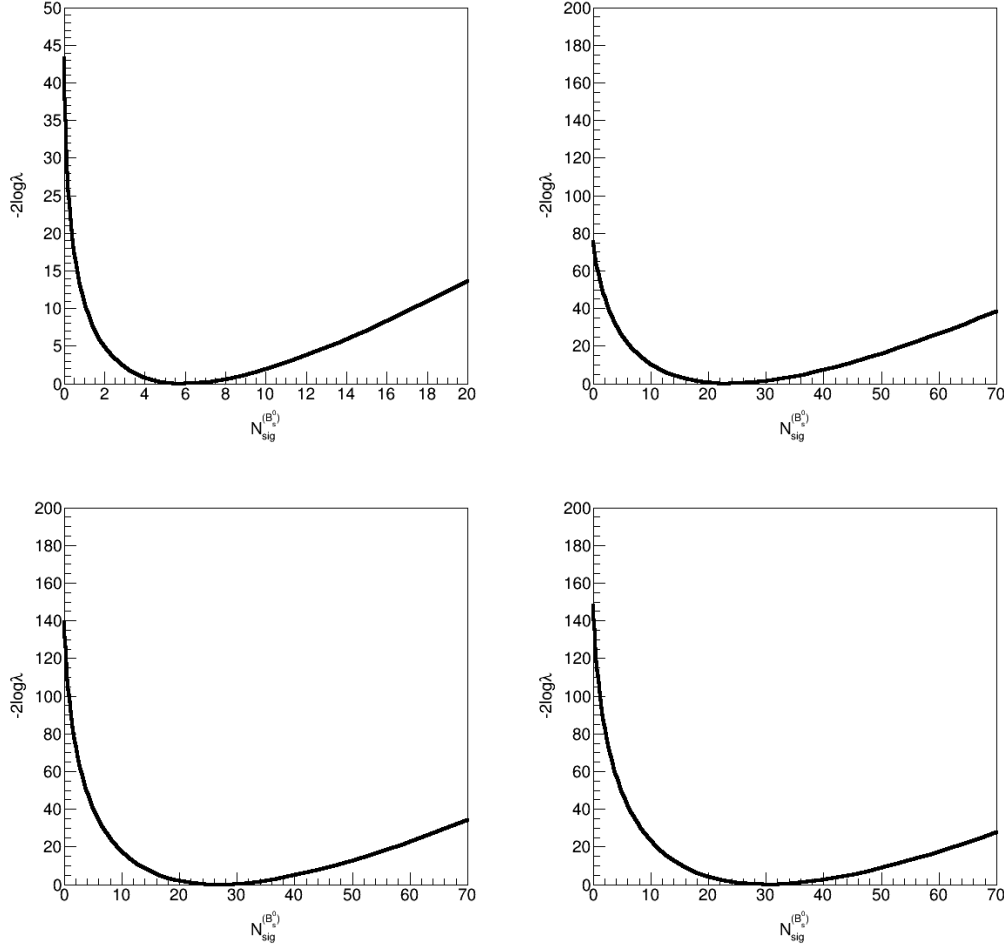


Figure 5-37: The significance vs signal yield for p_T bins from 7 – 10, 10 – 15, 15 – 20, and 20 – 50 GeV/c for 0 - 90% centrality are shown above

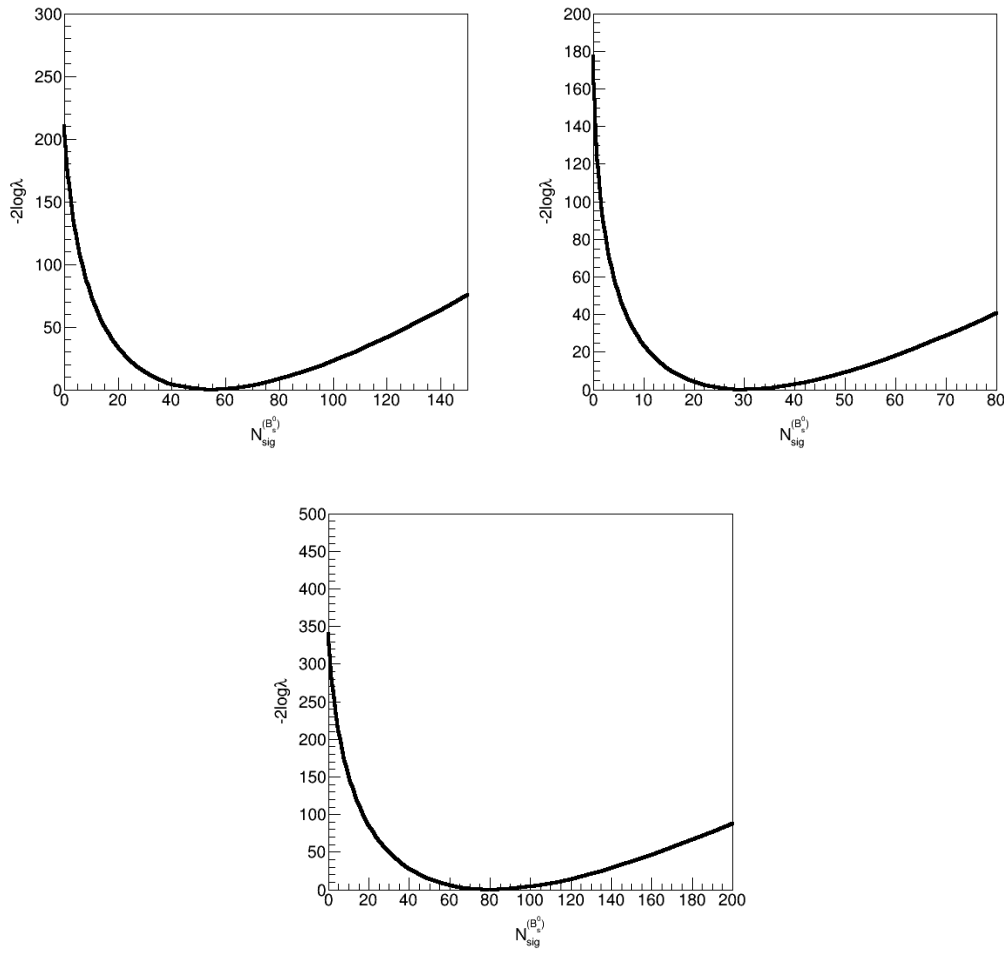


Figure 5-38: The significance vs signal yield for centrality bins in 0 - 30%, 30% - 90% 0 - 90% for p_T from 10 - 50 GeV/c are shown above

Table 5.11 summarizes the significance of B_s^0 according to our likelihood estimation.

We can see that B_s^0 mesons have significances of greater than 5σ for all p_T and centrality bins. In fact, this is the first observation of fully reconstructed B_s^0 meson in nucleus-nucleus collisions with greater than 5σ significance.

Table 5.11: The summary table of B_s^0 likelihood significance for each p_T and centrality bin.

Centrality (%)	$B_s^0 p_T$ (GeV/c)	Likelihood Significance (Z)
0 – 90	7 – 10	5.3
0 – 90	10 – 15	7.9
0 – 90	15 – 20	10
0 – 90	20 – 50	10
0 – 30	10 – 50	14
30 – 90	10 – 50	11
0 – 90	10 – 50	16

5.9 B-Meson Candidates MC-Data Comparison

5.9.1 Overview

Ideally, if the simulation is impeccable, the RECO distribution in the MC should match perfectly with the data. Nevertheless, there are always limitations in the MC simulations because of the incorrect modeling of physics processes in the generation side or the poor implementation of detector effects on the reconstruction side. The discrepancy should be quantified as a source of systematic uncertainties. The MC simulation plays a crucial role in data analysis and could affect our final results significantly. In order to compare the consistency between data and MC, we need to look at the B-meson signal-only candidates. In the MC, we can simply apply the GEN-Match selection to select all B-meson signal candidates. In the data, we need to perform the background subtraction to extract the signal. After that, we can normalize the distributions of the data and MC to compare their shapes.

5.9.2 Splot Techniques

To carry out MC-Data comparison studies, a dedicated *Splot* method is used. It is a likelihood-based method by which we reweigh the data using the unbinned fit results. The weights are added to the dataset based on models and yield extraction variables. Each event has two weights: the probability of belonging to the signal given its mass

and probability of belonging to the background given its mass. The *Splot* class gives us the distributions of our variables for given species (signal or background). The advantage of using this method is that we use the full dataset for the comparison in contrast to the sideband subtraction method where one should select the investigation range of signal and background. Furthermore, we use likelihood to describe the behavior of the events in contrast to the potential misidentification of signal events in the background region which might occur in the sideband subtraction method.

In order to obtain the *Splot* weight, we first need to fit the data using a discriminating variable, namely the B-meson candidates invariant mass. This method, like the one described in the previous section, assumes that the discriminating variables chosen are independent of the variables we wish to study. We then use the fit to attribute to each event two weights: w_S , which corresponds to the probability of it belonging to the signal, and w_B , which corresponds to the probability of fit belonging to the background. The weights are qualitatively demonstrated in Figure 5-39.

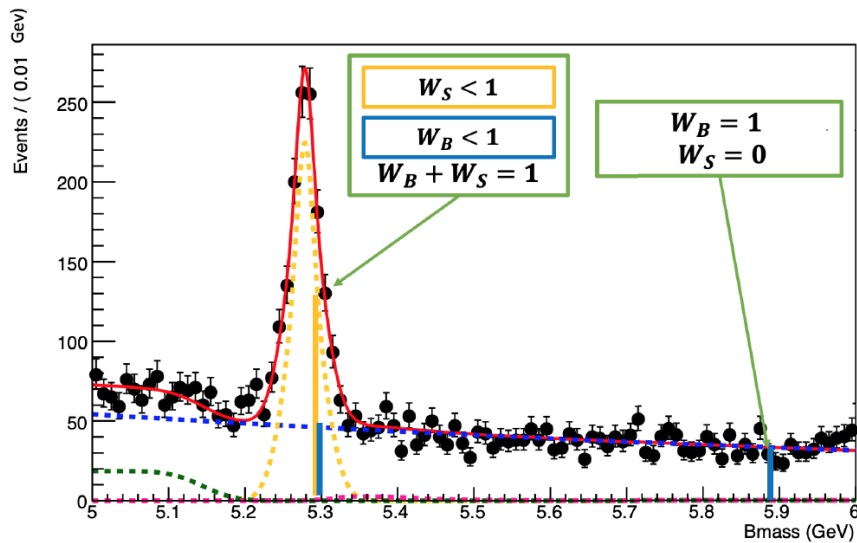


Figure 5-39: The illustration of *Splot* techniques via an unbinned fit to B^+ invariant mass distribution using our fitting model to extract the *Splot* weights w_S and w_B is shown above.

5.9.3 Splot Variable Correlation Studies

First, in order to apply *Splot* to perform Data-MC comparison, we need to confirm that our variables are indeed not correlated to the invariant mass. Therefore, the correlation matrices for BDT variables vs B_s^0 and B^+ invariant mass (Bmass) for data and MC are shown in Figure 5-40 and Figure 5-41 respectively

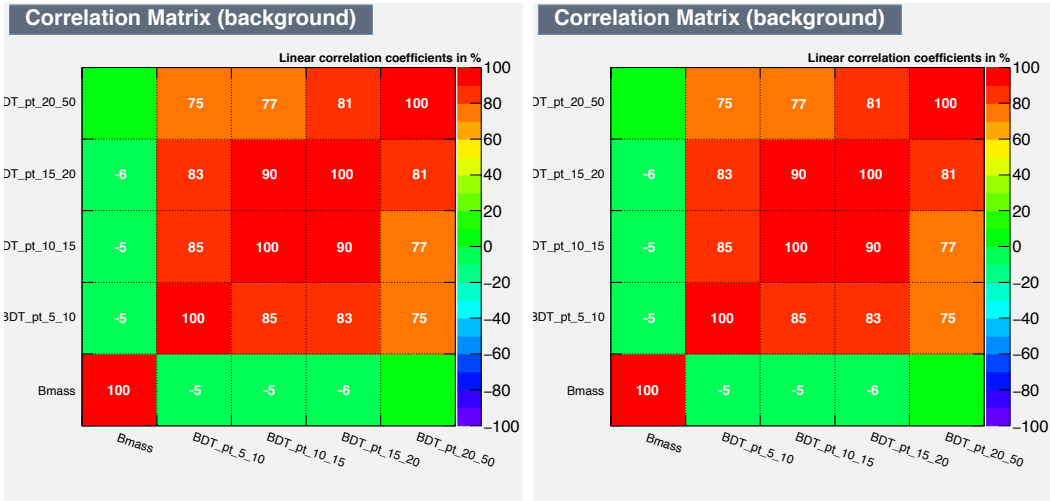


Figure 5-40: The correlation matrices in data (left) and MC (right) of B_s^0 .

5.9.4 Splot Results for Data-MC Comparison

No significant correlation between the BDT variables and the invariant mass is observed in either B_s^0 and B^+ , which also validates their BDT training. Therefore, *Splot* will be applicable to compare data and MC. Here, we focus on BDT values that are directly used in our signal extraction and related to MC distribution validation, rather than the individual topological variables used in BDT training. In a wide range of BDT, the two distributions show good agreement. We only focus on the region where BDT is greater than the working point and is smaller than the maximum values of the candidates.

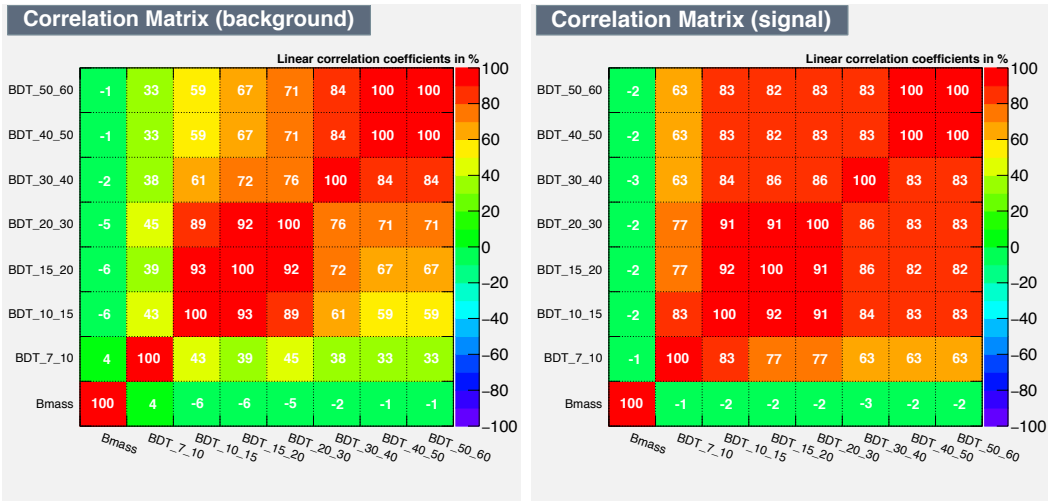


Figure 5-41: The correlation matrices in data (left) and MC (right) of B^+ .

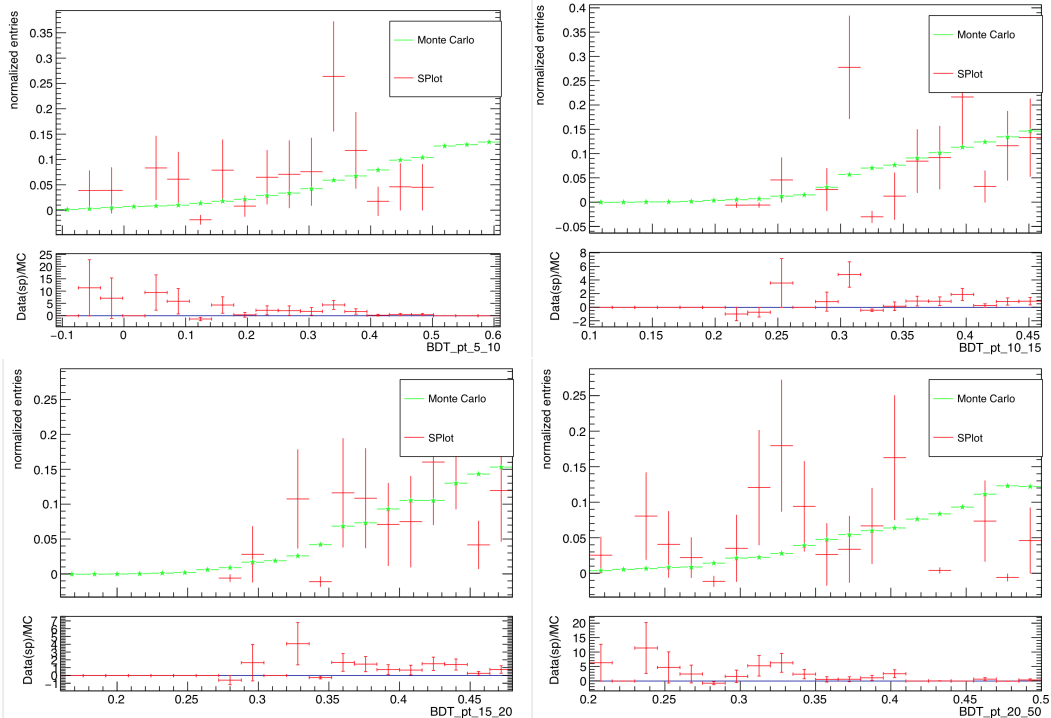


Figure 5-42: Comparison of B_s^0 BDT distributions in data (red) and MC (green) using the *Splot* method.

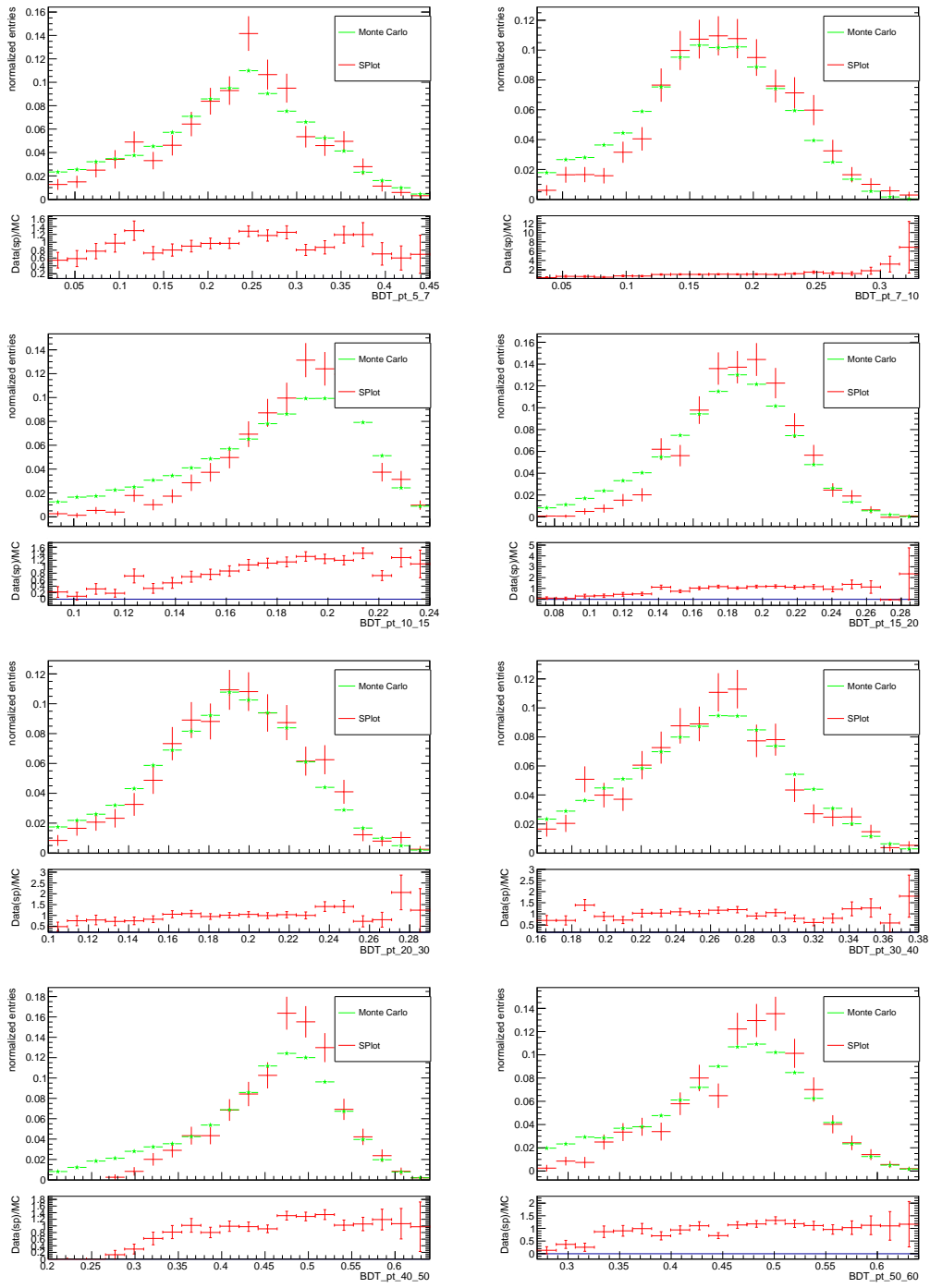


Figure 5-43: Comparison of B^+ BDT distributions in data (red) and MC (green) using the *Splot* method.

From Figure 5-43, the B^+ BDT variables in for all p_T bins have overall reasonably good agreement between data and MC. Their ratios are near unity with some fluctuations due to limited statistics. In the systematic section, we will quantify the discrepancy between data and MC as a source of systematic uncertainties. For B_s^0 , unlike B^+ whose statistics is in general > 100 , the total number of signal B_s^0 candidates is < 100 , which results in large error bars shown in Figure 5-42. Nonetheless, the ratios of data to MC shapes are still overall near unity within. Nevertheless, since the events used by B_s^0 and B^+ are essentially the same and their tracks are very similar, the overall good B^+ Data-MC agreement can provide an indirect validation for B_s^0 . The CMS analysis note AN-19-219 [193] documents more details on the general descriptions of the *Splot* method applied to this analysis.

5.10 Acceptance and Efficiency Correction

5.10.1 Overview

Now, we have clearly seen B-meson signals and extracted their signal raw yields N_S from their invariant distributions. In the next step, we need to correct the acceptance and selection efficiency of the B mesons in order to obtain the cross section. The following procedures define the method we use to determine B-meson acceptance and selection efficiency using B-meson MC samples:

First, We count the total number of GEN-level B-meson candidates reweighed by the centrality, PV_z , and \hat{p}_T as **NBGen** within the given B-meson rapidity region $|y| < 2.4$.

Next, we count the number of generated B-meson candidates passing the following selections

Muon track selections:

$$\begin{aligned}
p_T^\mu > 3.5 \text{ GeV/c} && \text{for } |\eta^\mu| < 1.2 \\
p_T^\mu > (5.47 - 1.89 \times |\eta^\mu|) \text{ GeV/c} && \text{for } 1.2 \leq |\eta^\mu| < 2.1 \\
p_T^\mu > 1.5 \text{ GeV/c} && \text{for } 2.1 \leq |\eta^\mu| < 2.4
\end{aligned} \tag{5.10}$$

Kaon track selections:

$$\begin{aligned}
p_T^K > 0.9 \text{ GeV/c} \\
|\eta^K| < 2.4
\end{aligned} \tag{5.11}$$

We denote those generated B-meson candidates passing selections as **NPassAcc**.

Finally, we apply all the selections on the GEN-matched RECO B mesons. We count the reconstructed B-meson candidates passing the selections mentioned in Section 5.5 “Muon and J/ψ candidates selections” and the optimal BDT selections in Table 5.7 and Table 5.8 in Section 5.6.9 and denote the number as **NSelPass**.

The acceptance is defined by: **acceptance** = **NPassAcc**/**NBGen**.

The selection efficiency is defined by: **selection efficiency** = **NSelPass**/**NPassAcc**.

Here, we denote α as **the acceptance** and ϵ as **the selection efficiency** and their product, which is $\alpha \times \epsilon = \mathbf{NSelPass}/\mathbf{NBGen}$, is call (total) efficiency.

5.10.2 Tag & Probe Techniques

The previous subsection mentioned the efficiency correction for B-meson using MC simulations only. However, we know that both B_s^0 and B^+ decay to J/ψ . A dedicated analysis technique called *tag & probe* is developed to correct the B-meson efficiency in a data-driven way. The tag-&-probe method uses *scale factors* defined as the ratio of data/MC for L2 and L3 triggered single muon efficiency tagged from the J/ψ resonance [194]. There are three scale factors: identification (id), tracking (trk), and trigger (trg). Figure 5-44 shows the workflow for the tag-&-probe method in B-meson analysis

The total scale factor (SF) of two muons ($SF^{\mu\mu}$) is given by the following formula

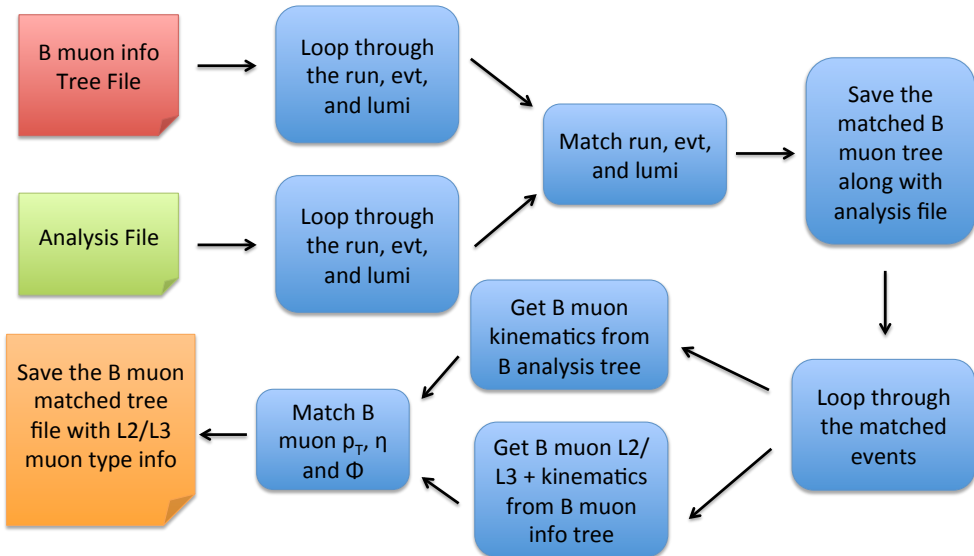


Figure 5-44: The workflow to obtain L2 and L3 muons in order to apply the tag-&-probe method is shown above.

$$SF^{\mu\mu} = id^{\mu_1} \times trk^{\mu_1} \times trg^{\mu_1} \times id^{\mu_2} \times trk^{\mu_2} \times trg^{\mu_2} \quad (5.12)$$

It should note that, as mentioned in Section 2.2.5, the dimuon PbPb triggered datasets consist of one L2 muon and one L3 muon. In our analysis, the two muons used to reconstruct B-meson are made of either one L2 muon and one L3 muon (L2, L3) or two L3 muons (L3, L3). The muon type (either L2 or L3) only affects the trg SF. In the (L2, L3) case, we simply correct the scale factor according to the individual scale factor values of the muon legs. However, in the (L3, L3) case, we can treat them as the combination of (L2, L3) and (L3, L2) by considering one of the muon legs as L2 muon. Then we compute the SF for both cases and take the average of the two SF as the SF for (L3, L3).

5.10.3 Traditional Efficiency Correction Results

Traditionally, we simply compute the efficiency as functions of binned p_T and centrality and use it to correct the signal raw yield within the p_T and centrality bins. The B_s^0 and B^+ acceptance, selection efficiency, and total efficiency as a function of p_T and centrality are shown respectfully below in Figure 5-45 and Figure 5-46

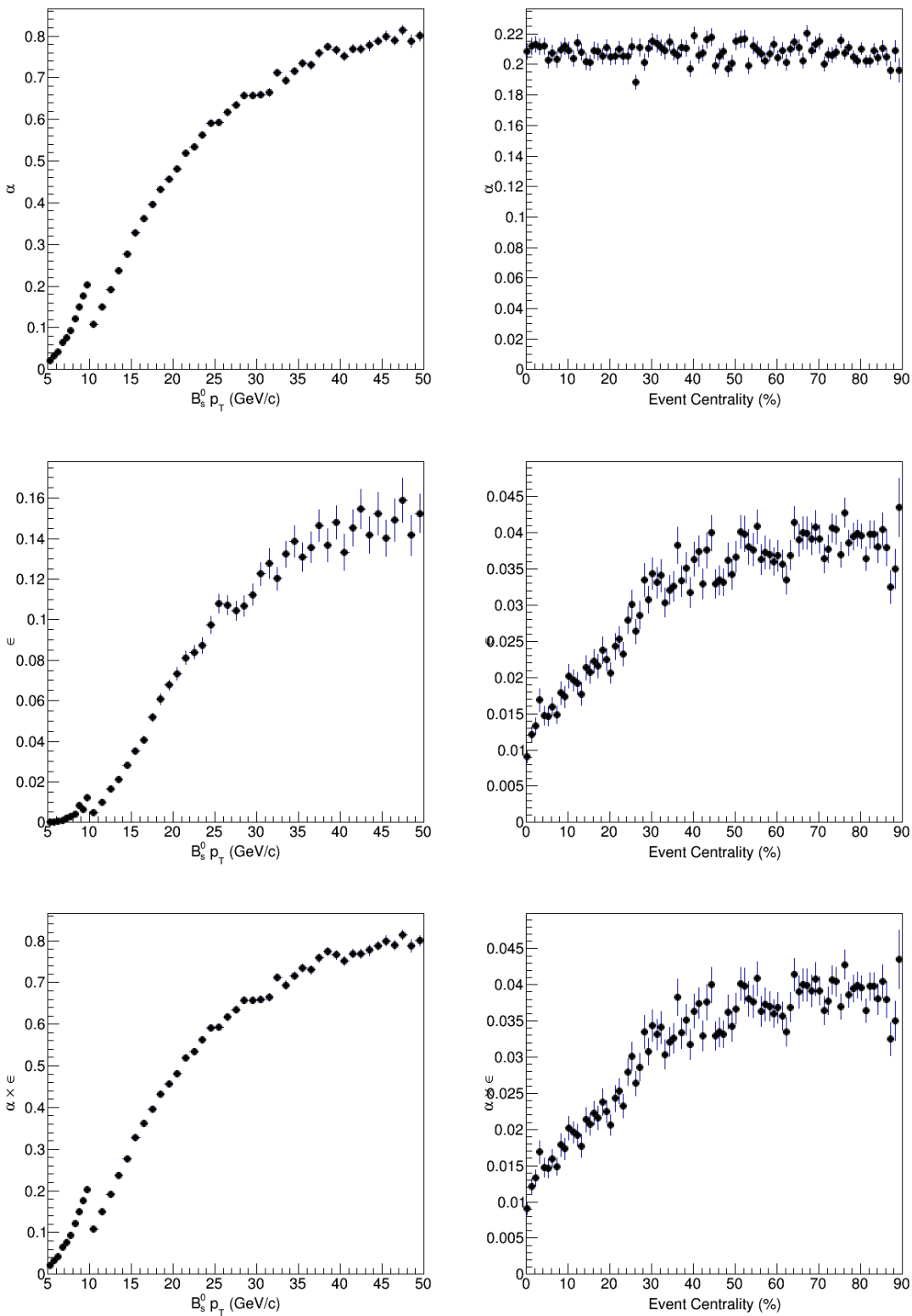


Figure 5-45: The B_s^0 acceptance (top), selection efficiency (middle), and efficiency (bottom) as a function of p_T (left) and event centrality (right) are shown respectfully above. We should note that there is no significant centrality dependence on the B_s^0 acceptance, which makes sense.

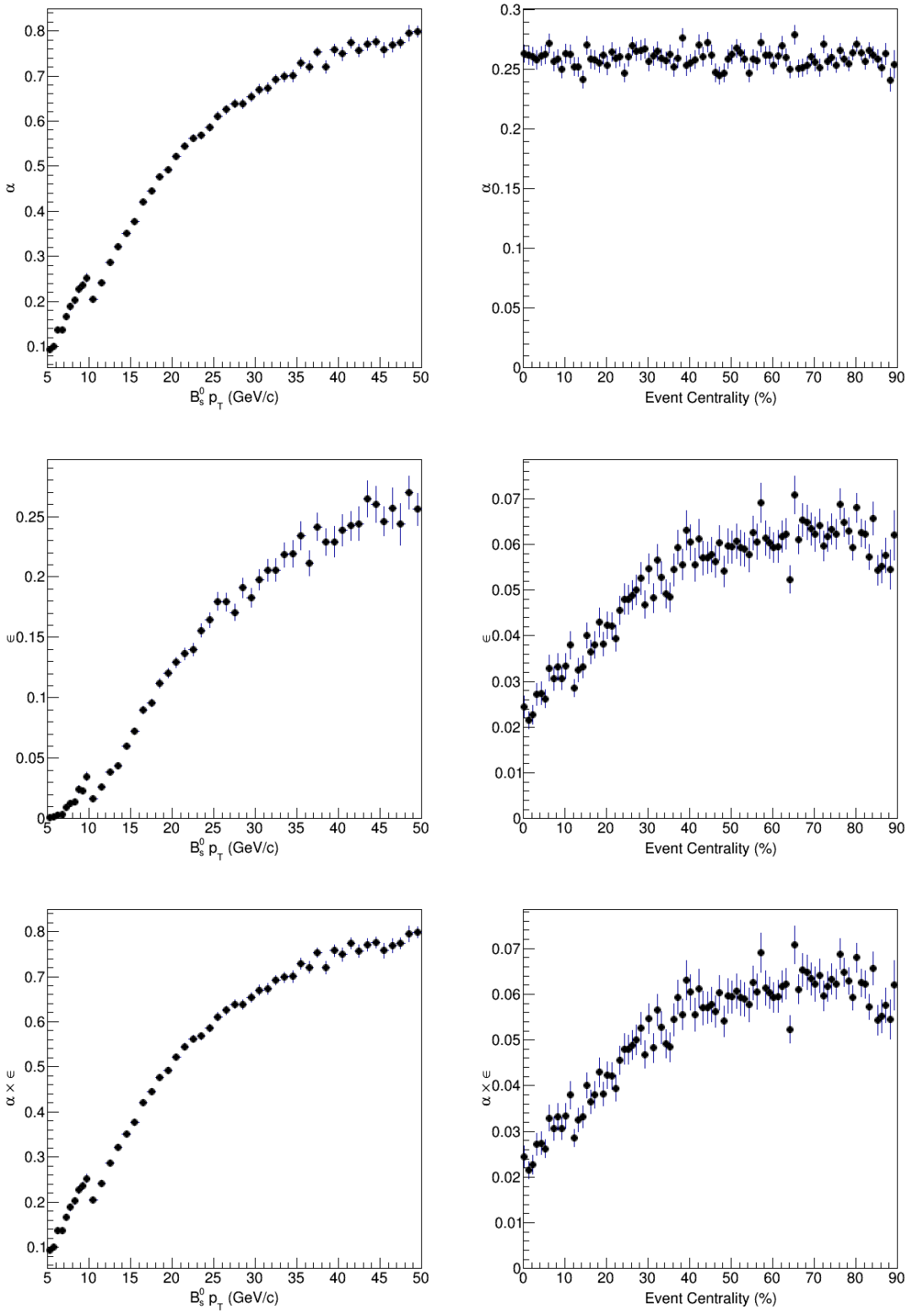


Figure 5-46: The B^+ acceptance (top), selection efficiency (middle), and efficiency (bottom) as a function of p_T (left) and event centrality (right) are shown respectfully above. We should note that there is no significant centrality dependence on the B^+ acceptance, which makes sense.

5.10.4 Analysis Challenges

Although B-meson p_T and y distributions are reasonably modeled by FONLL in pp collisions, the precise B-meson p_T and y distribution shapes are still unknown in PbPb, which could significantly affect the efficiency determination. In the following, we demonstrate how the unknown shape of the generated B-meson kinematics can affect the efficiency.

Since we know the efficiency is given by $\alpha \times \epsilon = \text{NSelPass}/\text{NBGen}$. NBGen in the simulation could not represent the truth. A weight function $w(x)$ is defined as the ratio between the generated B-meson cross section to the cross section of actual B-meson in PbPb for some kinematic variable x as follows

$$w(x) = \frac{\sigma_B^{MC}(x)}{\sigma_B^{PbPb}(x)} \quad (5.13)$$

Therefore, this weight function needs to be applied to both GEN-level $G(x)$ and RECO-level $R(x)$ in order to obtain the correct selection efficiency as a function of B mesons p_T .

$$\epsilon_{corr}(x) = \frac{\langle R(x) \rangle}{\langle G(x) \rangle} = \frac{\int R(x)w(x)dx}{\int G(x)w(x)dx} \quad (5.14)$$

Experimentally, the data are discreet. Therefore, the measurement is done in bins. Now considering a bin of $[x_1, x_2]$, the expression above is written as

$$\epsilon_{corr}(x_1 < x < x_2) = \frac{\int_{x_1}^{x_2} R(x)w(x)dx}{\int_{x_1}^{x_2} G(x)w(x)dx} \quad (5.15)$$

When $x_1 \rightarrow x_2$, we have

$$\epsilon_{corr}(x_1 < x < x_2) = \frac{\int_{x_1}^{x_2} R(x)w(x)dx}{\int_{x_1}^{x_2} G(x)w(x)dx} \sim \frac{R(x)w(x)(x_2 - x_1)}{G(x)w(x)(x_2 - x_1)} = \frac{R(x)}{G(x)} = \epsilon(x) \quad (5.16)$$

We can see that, for any non-trivial $w(x)$, in very fine bins, the effect of $w(x)$ will disappear. When we measure B-meson over a large p_T range, this effect could

be significant, particularly for the B_s^0 mesons where the change of efficiency between $7 - 10$ GeV/c and $10 - 15$ GeV/c and the slope of uncertainties on $w(x)$ both are huge. Hence, in order to eliminate the uncertainties due to unknown the B-meson kinematics, we can bin the efficiency finely.

5.10.5 Fiducial Measurement

In fact, to better estimate B-meson efficiency, we should use 2D efficiency maps as functions of B-meson p_T and $|y|$. Figure 5-47 shows reconstructed B_s^0 and B^+ distribution in the MC

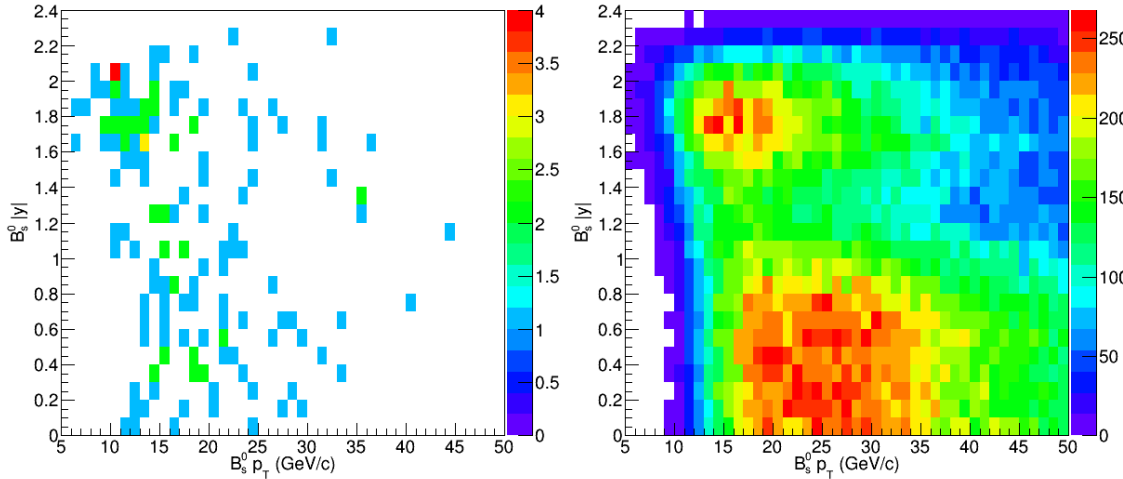


Figure 5-47: The finely binned 2D B-meson candidates distribution vs p_T and $|y|$ for data (left) and MC (right) in centrality 0 - 90% are shown respectfully above.

For B-meson p_T below 10 GeV/c, very few B mesons are reconstructed at the rapidity region of $|y| < 1.5$. This is due to the limited acceptance of muons because the muon tracks at low p_T cannot reach the muon systems. Hence, a fiducial measurement is carried out. For B mesons from $p_T < 10$ GeV/c, we only correct the efficiency within $1.5 < |y| < 2.4$ instead of $|y| < 2.4$. For $p_T > 10$ GeV/c, we still correct them to $|y| < 2.4$. The fiducial B-meson measurements will be carried out throughout this thesis.

5.10.6 Finely Binned 2D Efficiency Map

After significantly reducing the unknown B-meson kinematics effects on efficiency correction and choosing the fiducial region for our measurement, we propose to measure the inverse of the total efficiency: $\frac{1}{\alpha \times \epsilon}$ as a function of p_T and $|y|$ to correct the B-meson raw yield to production yield. We implement the following workflow in Figure 5-48 to estimate $\langle \frac{1}{\alpha \times \epsilon} \rangle$

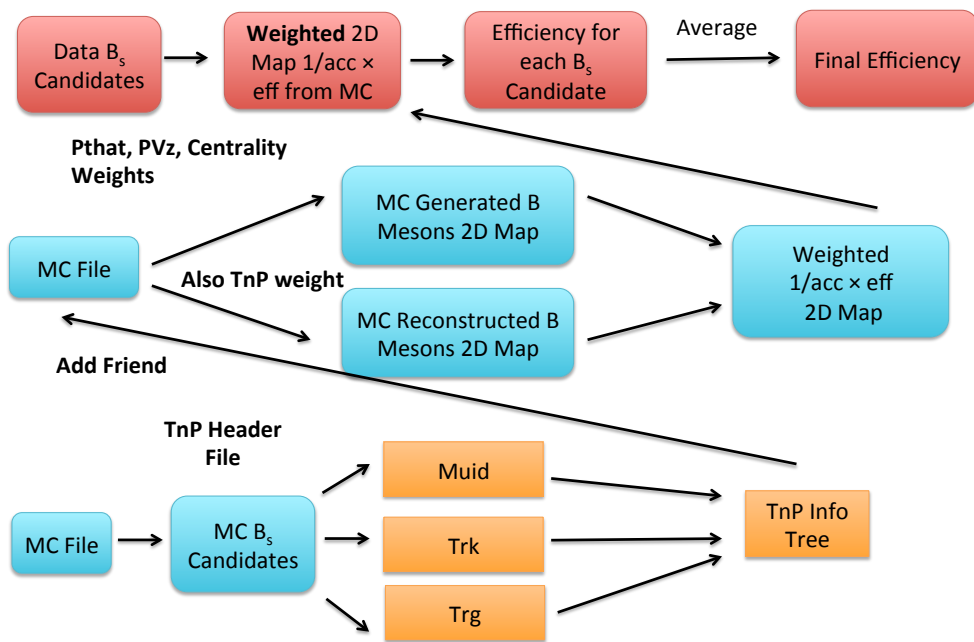


Figure 5-48: The workflow for the efficiency correction including the data-driven tag-&-probe approach in B-meson analysis is shown above.

The $\frac{1}{\alpha \times \epsilon}$ applied with the tag-&-probe SFs as functions of p_T and $|y|$ for B_s^0 and B^+ are shown on Figure 5-49 and Figure 5-50 respectfully

The p_T bin width is 0.5 GeV/c from 5 - 10 GeV/c and 1 GeV/c from 10 - 50 GeV/c. The $|y|$ binning is [0, 1.2, 1.8, 2.1, 2.4].

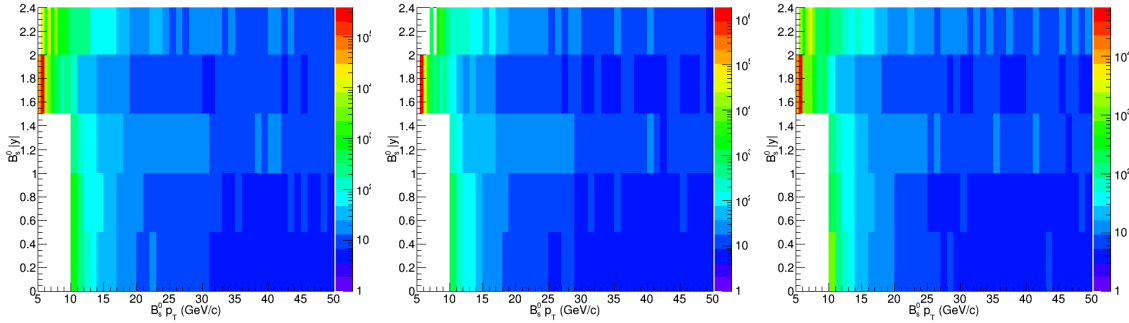


Figure 5-49: The finely binned 2D $\frac{1}{\alpha \times \epsilon}$ vs $B_s^0 p_T$ and $B |y|$ in centrality 0 - 90% (top), 0 - 30% (middle), and 30% - 90% (bottom) are shown respectfully above.

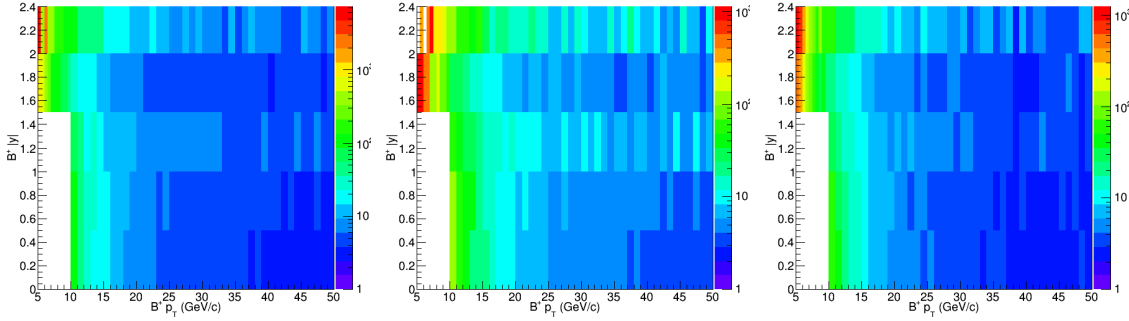


Figure 5-50: The finely binned 2D $\frac{1}{\alpha \times \epsilon}$ vs $B^+ p_T$ and $B |y|$ in centrality 0 - 90% (top), 0 - 30% (middle), and 30% - 90% (bottom) are shown respectfully above.

5.10.7 Data-Drive Efficiency Correction

Finally, we propose to correct the efficiency with a data-driven method. We correct the signal B-meson candidate efficiency. This can be done by looping B-meson data signal region candidates on the 2D $\frac{1}{\alpha \times \epsilon}$ map according to their p_T and $|y|$. Then, referring to techniques of the published J/ψ analysis [194], we compute the average on the efficiency of all signal B-meson candidates: $\langle \frac{1}{\alpha \times \epsilon} \rangle$ within the p_T and centrality bins. Here, we call $\langle \frac{1}{\alpha \times \epsilon} \rangle$ as the efficiency correction factor. Mathematically, it is written as

$$\langle \frac{1}{\alpha \times \epsilon} \rangle = \frac{1}{N} \sum_{i=1}^N \frac{1}{\alpha_i \times \epsilon_i} \quad (5.17)$$

It should note that the reason why we will measure $\langle \frac{1}{\alpha \times \epsilon} \rangle$ instead of $\frac{1}{\langle \alpha \times \epsilon \rangle}$ is because $\langle \frac{1}{\alpha \times \epsilon} \rangle$ has better closure. A dedicated closure test on this approach will be carried out and the results discussed will be in Section 5.11.

Also, there are some background contaminations even the candidates are restricted within the signal region. This could be improved by the *Splot* method. However, it turns out that the difference in the efficiency between applying Splot and not applying Splot is very small. We do not consider using the *Splot* method in this measurement.

Finally, this method only gives nominal results. The statistical uncertainties turn out to be correlated with both the data and MC statistics. A dedicated data bootstrapping approach to estimate the statistical uncertainties of the efficiency correction factor $\langle \frac{1}{\alpha \times \epsilon} \rangle$ will be carried out in Section 4.12.

5.10.8 Results

After applying a data-driven method to compute the efficiency correction factor, we obtain Figure 5-51 and Figure 5-52 showing $\langle \frac{1}{\alpha \times \epsilon} \rangle$ as functions of p_T and centrality for both B_s^0 and B^+ .

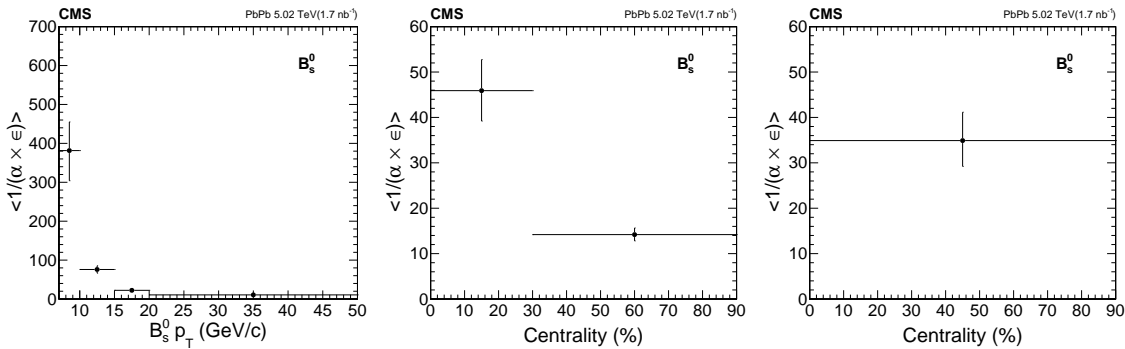


Figure 5-51: The B_s^0 efficiency correction factor $\langle \frac{1}{\alpha \times \epsilon} \rangle$ vs p_T (left) and 0 – 30 % and 30 – 90% centrality (middle) and the inclusive 0 – 90% centrality (right) are shown above.

Table 5.12 and 5.13 summarize the nominal efficiency of B_s^0 and B^+ respectfully and their upper and lower asymmetric statistical uncertainties obtained from Section 5.12.

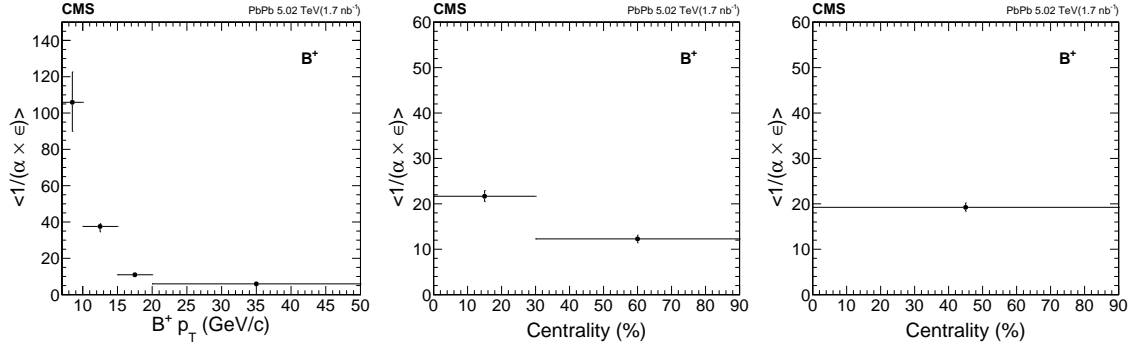


Figure 5-52: The B^+ efficiency correction factor $\langle \frac{1}{\alpha \times \epsilon} \rangle$ vs p_T (left) and 0 – 30 % and 30 – 90% centrality (middle) and the inclusive 0 – 90% centrality (right) are shown above.

Table 5.12: The summary table of B_s^0 efficiency correction factor $\langle \frac{1}{\alpha \times \epsilon} \rangle$ for each p_T and centrality bin.

Centrality (%)	B_s^0 p_T (GeV/c)	$\langle \frac{1}{\alpha \times \epsilon} \rangle$	$\langle \frac{1}{\alpha \times \epsilon} \rangle$ Error Up (+)	$\langle \frac{1}{\alpha \times \epsilon} \rangle$ Error Down (-)
0 – 90	7 – 10	381.5	19.3%	20.3%
0 – 90	10 – 15	75.92	12.4%	12.3%
0 – 90	15 – 20	22.35	6.41%	6.47%
0 – 90	20 – 50	10.63	5.90%	6.20%
0 – 30	10 – 50	45.90	14.9%	14.6%
30 – 90	10 – 50	14.19	10.3%	9.78%
0 – 90	10 – 50	34.90	17.9%	16.3%

At this point, we have all the ingredients to measure the B-meson cross section and study the physics.

5.11 Cross Section Measurement

The goal of this thesis is to measure the cross section of B-meson in PbPb collisions as functions of B mesons p_T and PbPb collision event centrality. Here, in high-energy heavy-ion physics, cross section really means production yield.

In terms of B-meson p_T , the cross section is defined mathematically as follows:

Table 5.13: The summary table of B^+ efficiency correction factor $\langle \frac{1}{\alpha \times \epsilon} \rangle$ for each p_T and centrality bin.

Centrality (%)	$B^+ p_T$ (GeV/c)	$\langle \frac{1}{\alpha \times \epsilon} \rangle$	$\langle \frac{1}{\alpha \times \epsilon} \rangle$ Error Up (+)	$\langle \frac{1}{\alpha \times \epsilon} \rangle$ Error Down (-)
0 – 90	7 – 10	105.9	15.8%	15.1%
0 – 90	10 – 15	37.55	4.10%	7.95%
0 – 90	15 – 20	10.94	6.54%	6.50%
0 – 90	20 – 50	5.932	6.90%	5.26%
0 – 30	10 – 50	21.67	5.81%	5.54%
30 – 90	10 – 50	12.28	6.71%	7.06%
0 – 90	10 – 50	19.23	5.06%	4.54%

$$\frac{1}{T_{AA}} \frac{dN}{dp_T} = \frac{1}{T_{AA}} \frac{1}{2} \frac{1}{\Delta p_T} \frac{1}{N_{MB} BR} N_S \langle \frac{1}{\alpha \times \epsilon} \rangle \quad (5.18)$$

In terms of PbPb collision event centrality, the cross section is defined as mathematically as follows:

$$\frac{1}{T_{AA}} N = \frac{1}{T_{AA}} \frac{1}{2} \frac{1}{N_{MB} BR} N_S \langle \frac{1}{\alpha \times \epsilon} \rangle \quad (5.19)$$

The definitions of the variables above are shown below:

- N : B-meson production yield
- T_{AA} : nuclear overlapping function - here is for spherical nucleus $^{208}_{82}\text{Pb}$
- N_{MB} : number of minimum biased events corresponding to the dimuon PbPb datasets
- $\frac{1}{2}$: divide by 2 for the purpose of normalizing particle and antiparticle
- BR : B-meson decay branching ratio
- Δp_T : B-meson transverse momentum bin width
- N_S : signal raw yield
- $\langle \frac{1}{\alpha \times \epsilon} \rangle$: the data-drive efficiency correction factor

It should be pointed out that we aim at measuring the p_T differential cross section as a function B mesons p_T while as we plan to present the p_T integrated cross section as a function of event centrality in this thesis. Before presenting our final results of the cross section measurement, we need to validate our signal raw yield N_S and efficiency correction factor $\langle \frac{1}{\alpha \times \epsilon} \rangle$ measurements and estimate the correct statistical and systematic uncertainties of the B-meson measurements.

5.12 Validation Tests

Before presenting the final results, some more validation tests need to complete to ensure our results are unbiased.

5.12.1 Mass Scraping Test

From Figure 5-40, we see that the BDT variables are essentially uncorrelated to the B_s^0 invariant mass. However, uncorrelation is not equivalent to independence. We need to make sure that in the BDT training procedures, no significant invariant mass dependence is introduced. This effect is called the mass scraping effect. Therefore, we propose the following tests to explicitly quantify the B_s^0 BDT variables dependence on the B_s^0 invariant mass.

- We look at the BDT shape in different B_s^0 data invariant mass sideband regions (both left- and right-hand side) that are far away from the B_s^0 PDG mass
- Then we take the ratio from other BDT shape with respect to one sideband to produce the ratio as a function of the BDT in different invariant mass regions
- We fit each BDT shape with a linear function, which is treated as a weight as a function of the BDT: $w(BDT)$
- We apply the weight $w(BDT)$ to each B_s^0 candidate and plot their invariant mass distributions with the weights

- We fit the $w(BDT)$ weighted invariant mass distribution and extracted the $w(BDT)$ weighted yield N_S^w
- We count the total number of candidates in both $w(BDT)$ unweighted and weighted case N and N^w
- We compute the percent difference δ from the rescaled $w(BDT)$ B_s^0 signal raw yield $\frac{N}{N^w} N_S^w$ to the unweighted nominal B_s^0 signal raw yield N_S

$$\delta = \frac{\frac{N}{N^w} N_S^w - N_S}{N_S} \times 100\% \quad (5.20)$$

Table 5.14 shows the nominal and linearly weighted rescaled signal raw yields and the percent deviation of the variated signal raw yield from nominal raw yield in each p_T and centrality bin.

Table 5.14: The summary table of BDT vs mass dependence systematics on the background yields from the fits in different p_T and centrality bins are shown below.

Centrality	$B_s^0 p_T$ (GeV/c)	$\frac{N}{N^w} N_S^w$	N_S	Percent Deviation (δ)
0 - 90%	7 - 10	6.831	6.787	0.64%
0 - 90%	10 - 15	27.14	27.23	0.33%
0 - 90%	15 - 20	26.69	26.78	0.34%
0 - 90%	20 - 50	31.26	31.41	0.48%
0 - 30%	10 - 50	59.25	60.19	1.59%
30 - 90%	10 - 50	29.88	30.04	0.20%
0 - 90%	10 - 50	84.95	86.07	0.14%

We can see the mass scraping effect on B_s^0 raw yield extraction is less than 2%, which is negligible. This fully validates that our B-meson BDT variables have little to no dependence on B-meson invariant mass.

5.12.2 Raw Yield Closure

In addition, we test the closure of the unbinned fits to extract signal raw yields and make sure they are good. 5000 MC toy samples are generated according to the means

and uncertainties of the B-meson invariant distributions. Then, each sample is fitted with our models and produces a signal raw yield value, error, and pull. The pull of a fit parameter is related to its value p_i and the error σ_{p_i} and the mean of the total dataset \bar{p} as follows:

$$Pull = \frac{p_i - \bar{p}}{\sigma_{p_i}} \quad (5.21)$$

Finally, we plot the pull distributions of all 5000 samples and perform the Gaussian fits to the pull distributions to obtain their means and widths. We expect each Gaussian fit to have a mean $\mu = 0$ and the width $\sigma = 1$, which is called a unit pull. Figure 5-53, 5-54, 5-55 and 5-56 show the pull distributions and the Gaussian fits for B_s^0 and B^+ signal raw yield parameter N_S for each p_T and centrality bin respectfully

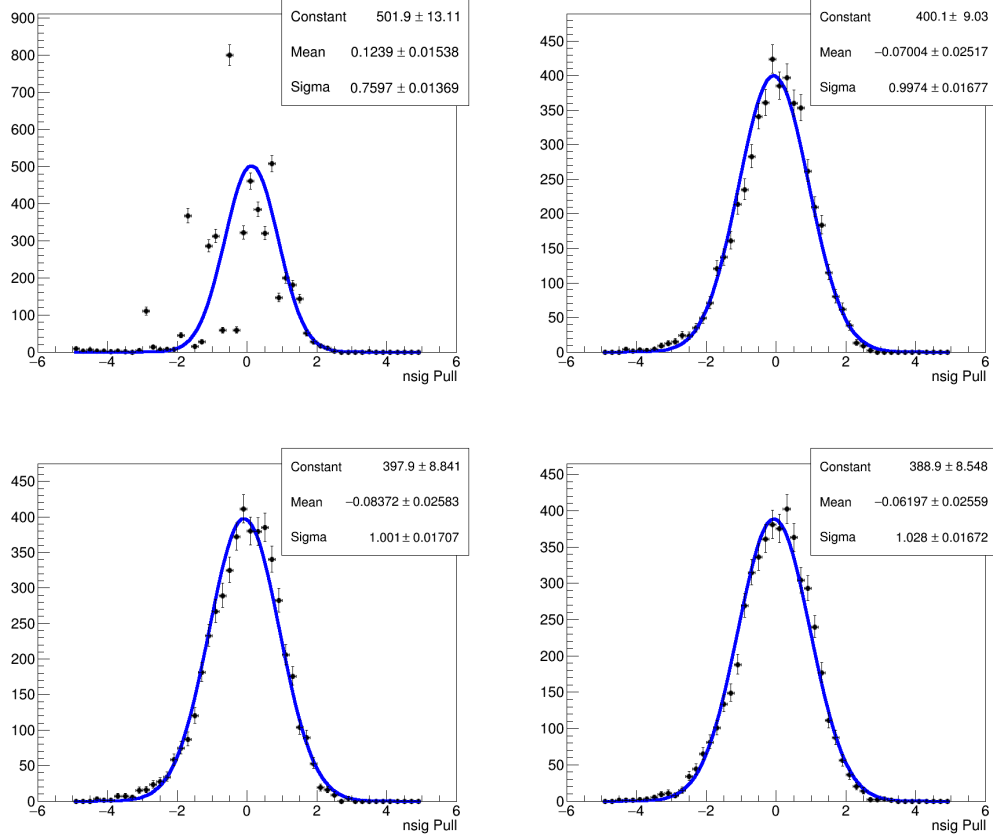


Figure 5-53: The B_s^0 pull distributions and the Gaussian fits for 0 - 90% from p_T 7 - 10, 10 - 15, 15 - 20, 20 - 50 GeV/c are shown respectfully above.

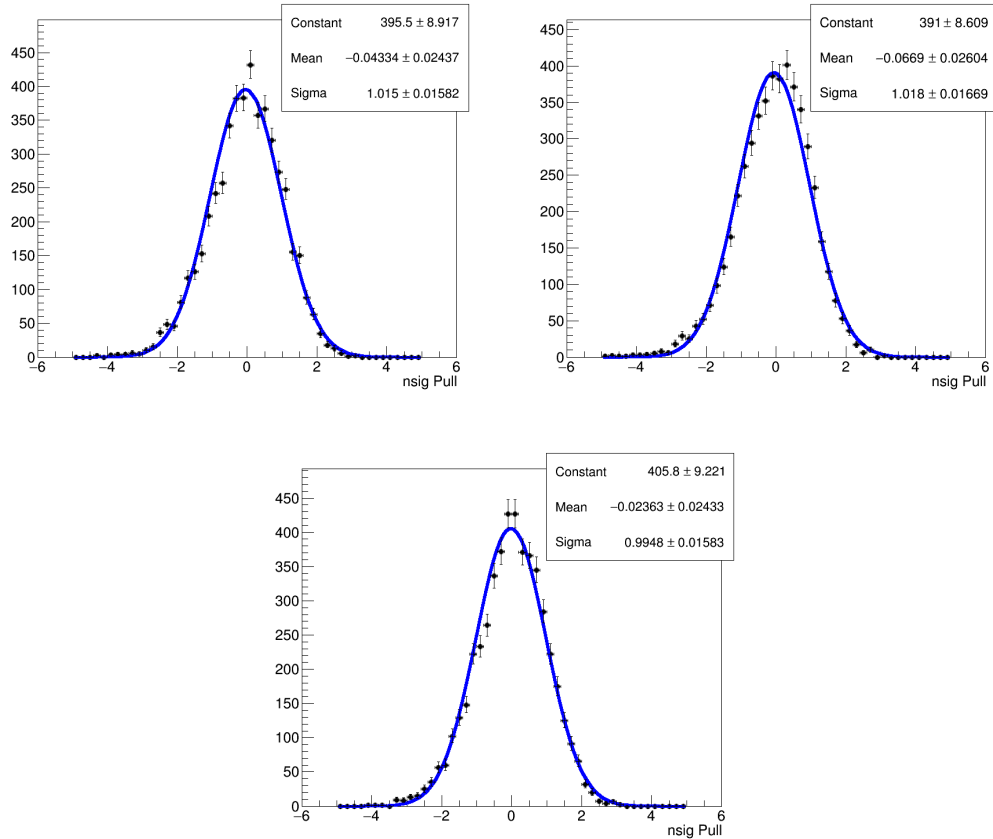


Figure 5-54: The B_s^0 pull distributions and the Gaussian fits in 0 - 30%, 30 - 90%, and 0 - 90% event centrality are shown respectfully above.

According to the results of the fits, all pulls appear to be unit pulls. This validates the closure of our fits and confirms our signal raw yield N_S has the correct mean and error yield.

5.12.3 Efficiency Closure

Next, after validating the fit closure for B-meson signal raw yield extraction, we also need to validate the efficiency correction approach to explicitly show that the efficiency correction factor $\langle \frac{1}{\alpha \times \epsilon} \rangle$ are indeed consistent with the truth efficiency to avoid potential bias. To perform this study, we use the $\hat{p}_T = 5$ GeV/c MC sample. Here, we consider both cases. The high statistics case: one whole $\hat{p}_T = 5$ GeV/c MC sample. The low statistics case: 2000 split data-like $\hat{p}_T = 5$ GeV/c MC samples same

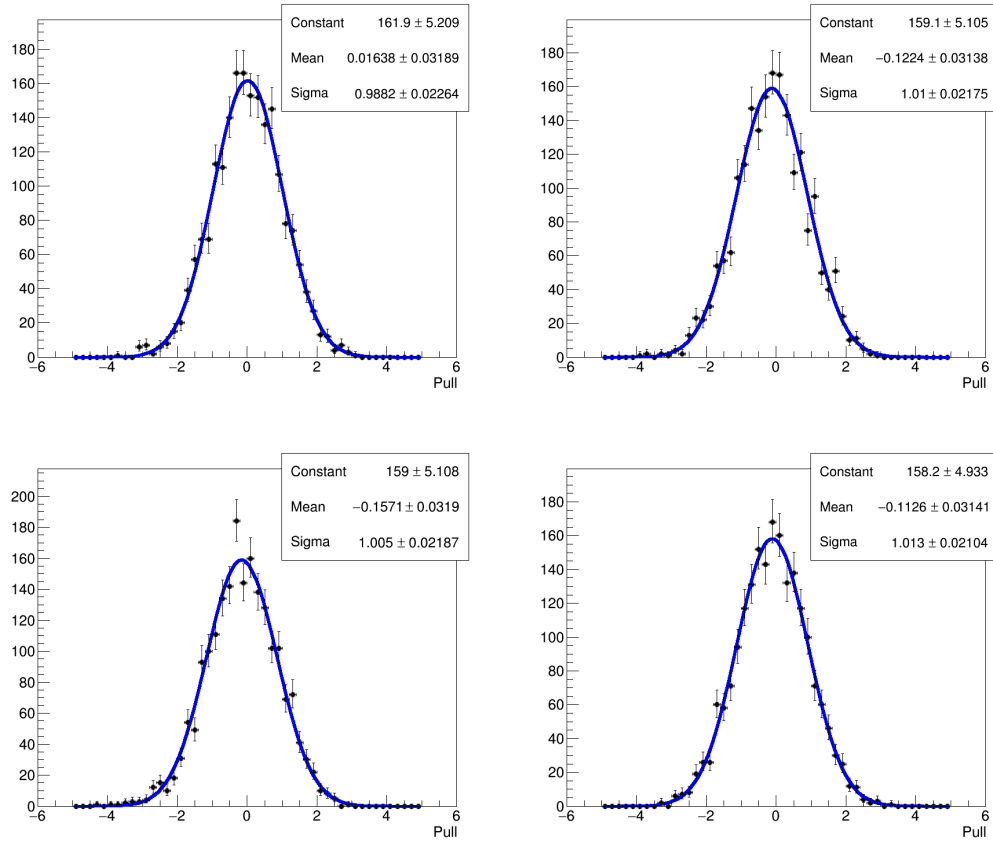


Figure 5-55: The B^+ pull distributions and the Gaussian fits for 0 - 90% at p_T 7 - 10, 10 - 15, 15 - 20, 20 - 50 GeV/c are shown respectfully above.

as the raw yield fit studies. In both cases, we use the same 2D $\frac{1}{\alpha \times \epsilon}$ efficiency correction maps without tag-&-probe weights from the input MC samples. We compare the $\langle \frac{1}{\alpha \times \epsilon} \rangle$ to the expected value, which is the total number of generated B_s /total number of reconstructed B mesons. Then we compute the

$$\%Dev = \frac{\langle \frac{1}{\alpha \times \epsilon} \rangle - GEN/RECO_{truth}}{GEN/RECO_{truth}} \times 100\% \quad (5.22)$$

to quantify the potential bias of the efficiency correction factor $\langle \frac{1}{\alpha \times \epsilon} \rangle$ in the analysis.

High Statistics Limit

The efficiency closure test results in high statistics limit of B_s^0 and B^+ are sum-

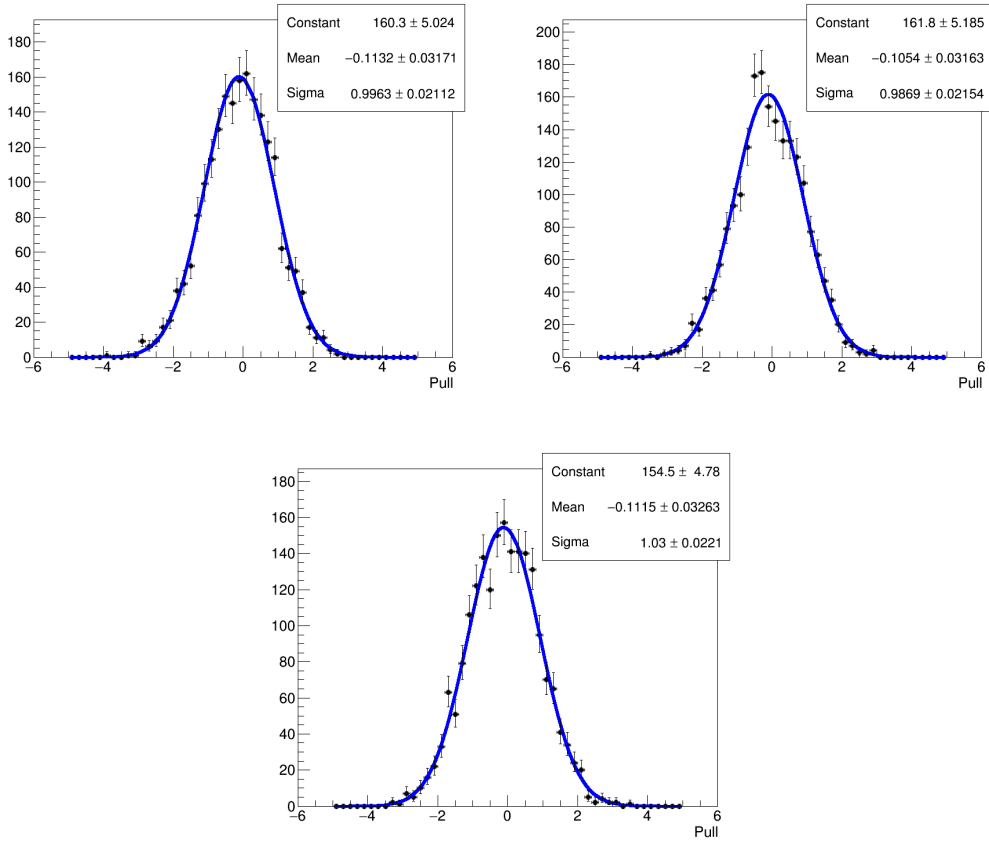


Figure 5-56: The B^+ pull distributions and the Gaussian fits for 0 - 30%, 30 - 90%, and 0 - 90% event centrality are shown respectfully above.

marized in table 5.15 and 5.16 respectfully below

In conclusion, we can see that the biases of the $\langle \frac{1}{\alpha \times \epsilon} \rangle$, which are all below 3.5%, are negligible compared to other sources of uncertainties. On the contrary, the efficiency correction factor $\frac{1}{\langle \alpha \times \epsilon \rangle}$ has a large bias. That also explains why we use $\langle \frac{1}{\alpha \times \epsilon} \rangle$ instead of $\frac{1}{\langle \alpha \times \epsilon \rangle}$ in our B-meson data analysis.

Low Statistics Limit

We compute the efficiency correction factor $\langle \frac{1}{\alpha \times \epsilon} \rangle$ on each of the 2000 data-like MC samples. Then, we plot their percent deviation for all p_T and centrality bins and compute their mean values. Our results are shown in Figure 5-57 and Figure 5-58

Table 5.15: The results of B_s^0 efficiency factors $\langle \frac{1}{\alpha \times \epsilon} \rangle$ and $\frac{1}{\langle \alpha \times \epsilon \rangle}$ and their percent deviations are shown above.

Centrality	$B_s^0 p_T$ (GeV/c)	NRECO	GEN/RECO	$\langle \frac{1}{\alpha \times \epsilon} \rangle$	% Dev	$\frac{1}{\langle \alpha \times \epsilon \rangle}$	% Dev
0 - 90%	7 - 10	12102	117.495	112.958	-3.4%	80.5755	-30.6%
0 - 90%	10 - 15	1788	43.3865	43.1728	-0.493%	27.6409	-36.3%
0 - 90%	15 - 20	4577	13.7835	13.639	-1.05%	12.6465	-8.25%
0 - 90%	20 - 50	35980	6.38043	6.36748	-0.203%	5.9658	-6.50%
0 - 90%	10 - 50	9522	12.2694	12.2668	-0.0212%	6.5642	-28.3%
0 - 30%	10 - 50	33143	7.70383	7.70087	-0.0384%	8.79954	-24.2%
30 - 90%	10 - 50	42453	8.72094	8.71793	-0.0345%	5.8419	-24.7%

Table 5.16: The results of B^+ efficiency factors $\langle \frac{1}{\alpha \times \epsilon} \rangle$ and $\frac{1}{\langle \alpha \times \epsilon \rangle}$ and their percent deviations are shown above.

Centrality	$B^+ p_T$ (GeV/c)	NRECO	GEN/RECO	$\langle \frac{1}{\alpha \times \epsilon} \rangle$	% Dev	$\frac{1}{\langle \alpha \times \epsilon \rangle}$	% Dev
0 - 90%	7 - 10	12102	117.495	112.958	-3.4%	80.5755	-30.6%
0 - 90%	10 - 15	1788	43.3865	43.1728	-0.493%	27.6409	-36.3%
0 - 90%	15 - 20	4577	13.7835	13.639	-1.05%	12.6465	-8.25%
0 - 90%	20 - 50	35980	6.38043	6.36748	-0.203%	5.9658	-6.50%
0 - 90%	10 - 50	9522	12.2694	12.2668	-0.0212%	6.5642	-28.3%
0 - 30%	10 - 50	33143	7.70383	7.70087	-0.0384%	8.79954	-24.2%
30 - 90%	10 - 50	42453	8.72094	8.71793	-0.0345%	5.8419	-24.7%

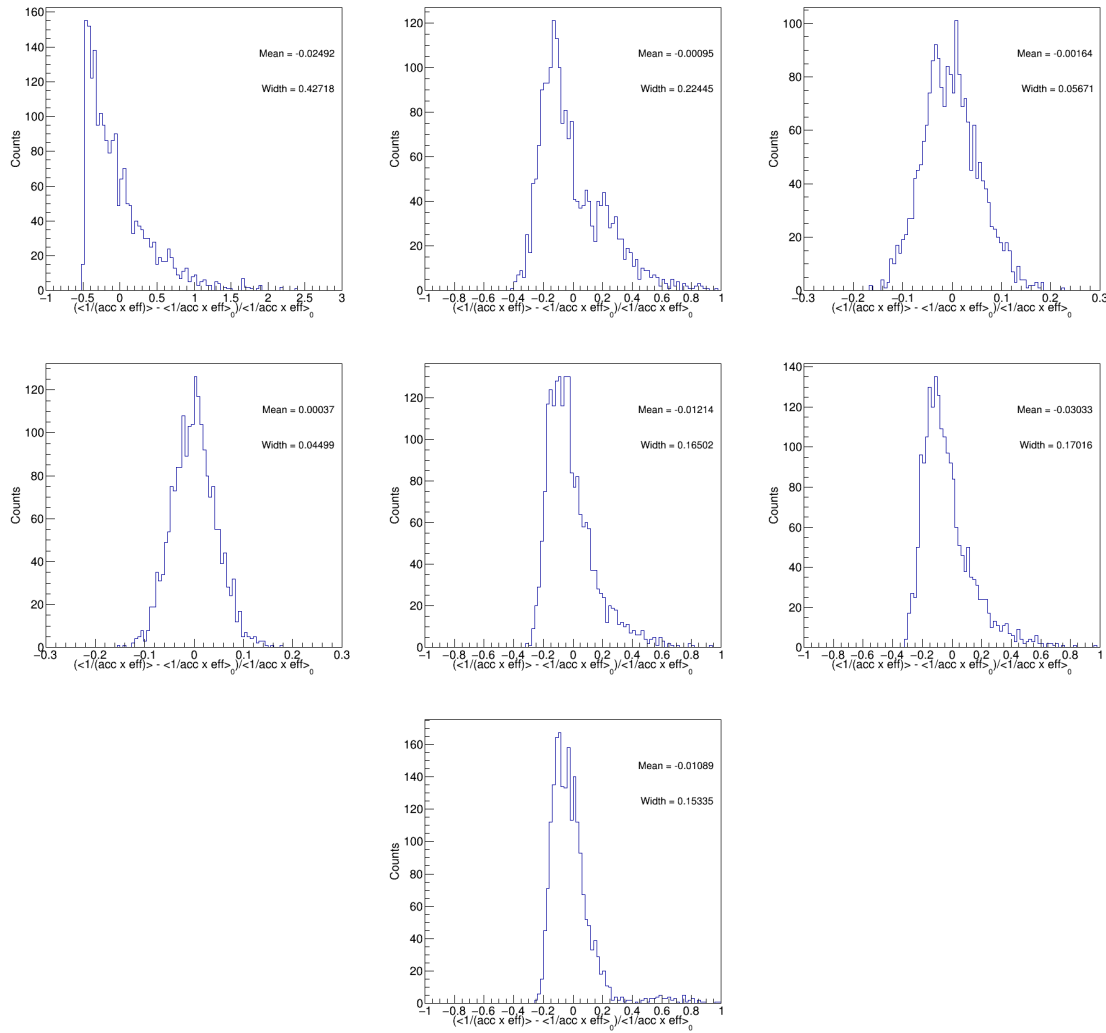


Figure 5-57: The percent deviation distributions of $B_s^0 \langle \frac{1}{\alpha \times \epsilon} \rangle$ to RECO/GEN for the data-like randomly constructed MC samples in centrality 0 - 90% from 7 - 10, 10 - 15, 15 - 20, and 20 - 50 GeV/c as well as 0 - 90%, 0 - 30%, and 30 - 90% event centrality from 10 - 50 GeV/c are shown respectfully above.

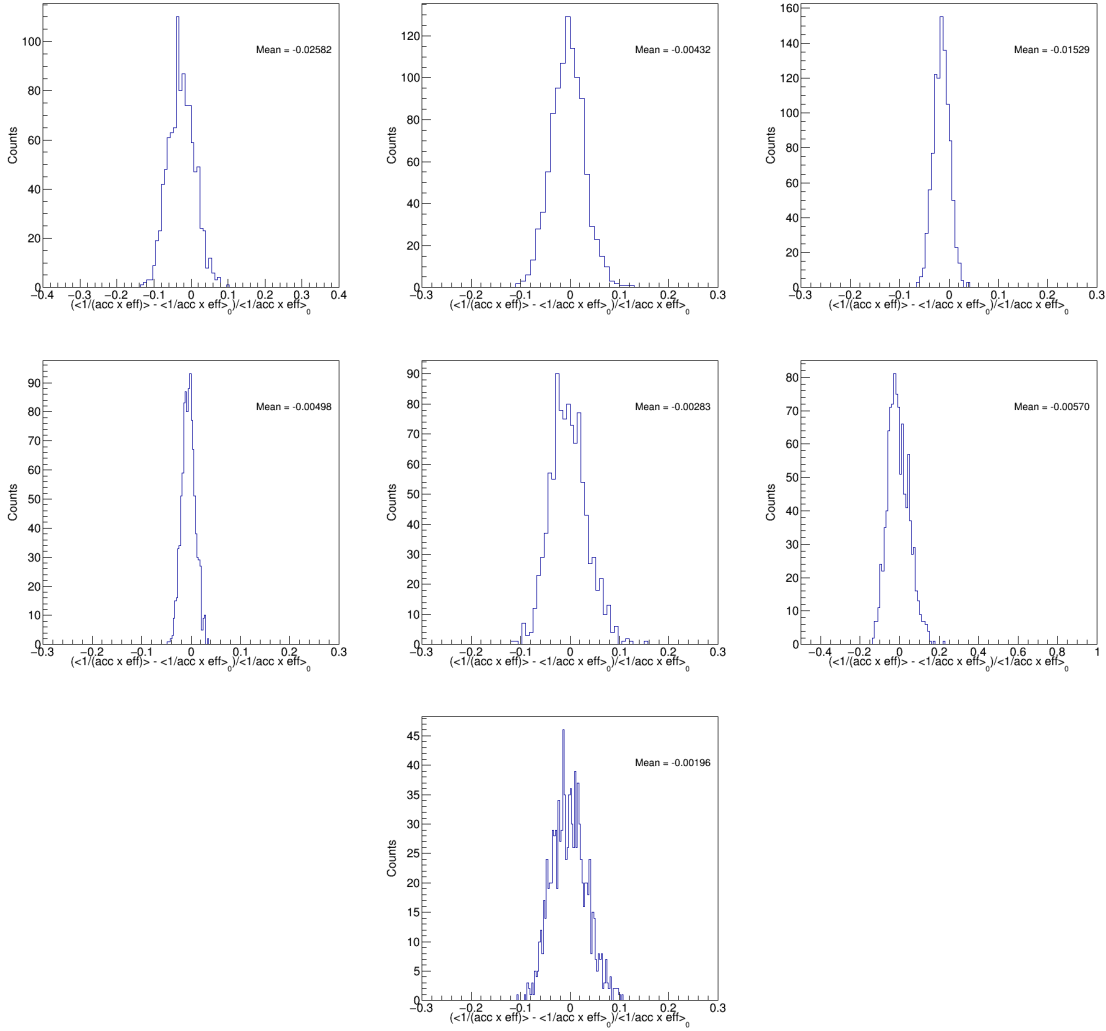


Figure 5-58: The percent deviation distributions of $B^+ \langle \frac{1}{\alpha \times \epsilon} \rangle$ to RECO/GEN for the data-like randomly constructed MC samples in centrality 0 - 90% from 7 - 10, 10 - 15, 15 - 20, and 20 - 50 GeV/c as well as 0 - 90%, 0 - 30%, and 30 - 90% event centrality from 10 - 50 GeV/c are shown respectfully above.

The percent deviations of B_s^0 and B^+ efficiency correct factors $\langle \frac{1}{\alpha \times \epsilon} \rangle$ are summarize in the Table 5.17 and Table 5.18 respectfully

In conclusion, we can see that, even in the limit of low statistics, which is similar to the statistics in our B-meson data analysis, the $\langle \frac{1}{\alpha \times \epsilon} \rangle$ correction method still gives us satisfying closure within 3% of bias. All these show that the efficiency correction factor $\langle \frac{1}{\alpha \times \epsilon} \rangle$ will not introduce significant bias in both B_s^0 and B^+ analyses.

Table 5.17: The percent deviation of B_s^0 efficiency factors from the expected value in the statistics similar to the data analysis is shown above.

Centrality	$B_s^0 p_T$ (GeV/c)	% Dev
0 - 90%	7 - 10	-2.49%
0 - 90%	10 - 15	-0.10%
0 - 90%	15 - 20	-0.16%
0 - 90%	20 - 50	+0.03%
0 - 90%	10 - 50	-1.09%
0 - 30%	10 - 50	-1.21%
30 - 90%	10 - 50	-3.03%

Table 5.18: The percent deviation of B^+ efficiency factors from the expected value in the statistics similar to the data analysis is shown above.

Centrality	$B^+ p_T$ (GeV/c)	% Dev
0 - 90%	7 - 10	-2.58%
0 - 90%	10 - 15	-0.43%
0 - 90%	15 - 20	-1.53%
0 - 90%	20 - 50	-0.50%
0 - 90%	10 - 50	-0.28%
0 - 30%	10 - 50	-0.57%
30 - 90%	10 - 50	-0.20%

5.12.4 *Splot* Closure on Efficiency

Finally, we will validate the efficiency correction factor $\langle \frac{1}{\alpha \times \epsilon} \rangle$ using all signal region data candidates. We compare our nominal $\langle \frac{1}{\alpha \times \epsilon} \rangle$ to the results with *Splot* weights w^S , which are obtained from the *Splot* analysis techniques shown in Section 4.9. Figure 5-59 shows the *Splot* weight distributions of B_s^0 and B^+ candidates

We can see that most of the candidates are either background-like (near 0) and signal-like (near 1). But some candidates are in between. Hence, the *Splot* weighted efficiency correction factor $\langle \frac{1}{\alpha \times \epsilon} \rangle'$ is given by

$$\langle \frac{1}{\alpha \times \epsilon} \rangle' = \frac{\sum_{i=1}^N \frac{w_i^S}{\alpha_i \times \epsilon_i}}{\sum_{i=1}^N w_i^S} \quad (5.23)$$

We can compute the *Splot* weighted efficiency correction factor $\langle \frac{1}{\alpha \times \epsilon} \rangle'$ and look at

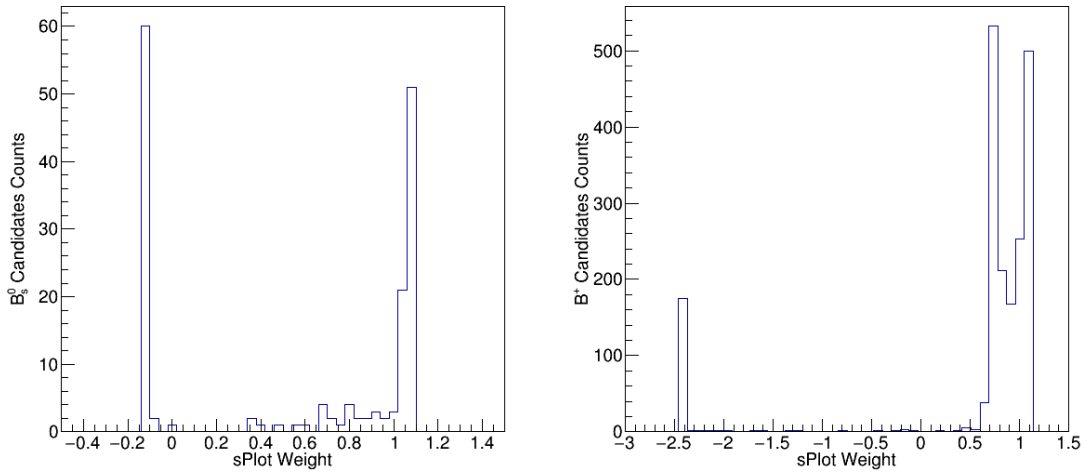


Figure 5-59: The sPlot weight distributions for B_s^0 (left) and B^+ (right) candidates are shown above.

its deviation from the nominal efficiency correction factor $\langle \frac{1}{\alpha \times \epsilon} \rangle'$.

$$\%Dev = \frac{\langle \frac{1}{\alpha \times \epsilon} \rangle' - \langle \frac{1}{\alpha \times \epsilon} \rangle}{\langle \frac{1}{\alpha \times \epsilon} \rangle} \times 100\% \quad (5.24)$$

The percent deviations of B_s^0 and B^+ Splot weighted efficiency correct factor $\langle \frac{1}{\alpha \times \epsilon} \rangle'$ to the nominal efficiency correction factor $\langle \frac{1}{\alpha \times \epsilon} \rangle$ are summarized in Table 5.19 and Table 5.20 respectively

Table 5.19: The B_s^0 Splot weighted efficiency correct factor $\langle \frac{1}{\alpha \times \epsilon} \rangle'$, nominal unweighed $\langle \frac{1}{\alpha \times \epsilon} \rangle$, and their percent deviation for each p_T and centrality bin are summarized below.

Centrality	$B_s^0 p_T$ (GeV/c)	$\langle \frac{1}{\alpha \times \epsilon} \rangle'$ (Weighed)	$\langle \frac{1}{\alpha \times \epsilon} \rangle$ (Nominal)	Percent Deviation (% Dev)
0 - 90%	7 - 10	386.5	381.5	1.31%
0 - 90%	10 - 15	77.34	75.92	1.88%
0 - 90%	15 - 20	22.24	22.35	0.49%
0 - 90%	20 - 50	10.71	10.63	0.75%
0 - 30%	10 - 50	46.20	45.90	0.63%
30 - 90%	10 - 50	14.27	14.19	0.56%
0 - 90%	10 - 50	35.15	34.90	0.72%

Table 5.20: The B^+ *Splot* weighted efficiency correct factor $\langle \frac{1}{\alpha \times \epsilon} \rangle'$, nominal unweighed $\langle \frac{1}{\alpha \times \epsilon} \rangle$, and their percent deviation for each p_T and centrality bin are summarized below.

Centrality	$B^+ p_T$ (GeV/c)	$\langle \frac{1}{\alpha \times \epsilon} \rangle'$ (Weighed)	$\langle \frac{1}{\alpha \times \epsilon} \rangle$ (Nominal)	Percent Deviation (% Dev)
0 - 90%	7 - 10	104.1	105.9	1.72%
0 - 90%	10 - 15	37.51	37.55	0.11%
0 - 90%	15 - 20	10.95	10.94	0.09%
0 - 90%	20 - 50	5.932	5.932	0.01%
0 - 30%	10 - 50	21.65	21.67	0.09%
30 - 90%	10 - 50	12.15	12.28	1.06%
0 - 90%	10 - 50	19.17	19.23	0.31%

Since the percent deviations are within 2%, there is no need to implement *Splot* weight to compute the efficiency correct factor $\langle \frac{1}{\alpha \times \epsilon} \rangle$. Up to here, our analysis procedures have been fully validated.

5.13 Statistical Uncertainties Determination

5.13.1 Data Bootstrapping

After showing that there is no explicit bias throughout the entire analysis, the next step is to evaluate the statistical uncertainties of the analysis. To estimate the statistical uncertainties of measurements, we can simply follow the toy approach. We can repeat the counting experiments with identical conditions and randomly sample the statistics according to the Poisson distribution defined as follows:

$$P(\mu, x) = \frac{\mu^N e^{-\mu}}{N!} \quad (5.25)$$

In order to estimate the statistical uncertainties, we develop the following procedures named as “Data Bootstrapping”, to quantify the statistical uncertainties of the final cross section measurement, which is defined in Equations 5.18 and 5.19 in Section 5.11:

- Randomly resample the data after passing the selections for each p_T and centrality bin. Each resampled data has the number of B mesons according to Poisson distribution with the same mean as the signal raw yield in data analysis.
- Construct 1000 randomly resampled datasets. Here, we allow events to repeat in the resampled dataset.
- Carry out the same analysis workflows on each of the resampled datasets as the data analysis and compute the corrected yield, which is defined as the product of the signal raw yield N_S and efficiency correction factor $\langle \frac{1}{\alpha \times \epsilon} \rangle$
- Plot the B-meson corrected yield distribution and compute the mean and RMS for each p_T and centrality bin
- Quote the RMS/Mean values of the distributions as the percent statistical uncertainties

Figure 5-60 and 5-61 show the corrected yield distribution of 1000 B_s^0 and B^+ resampled datasets respectfully

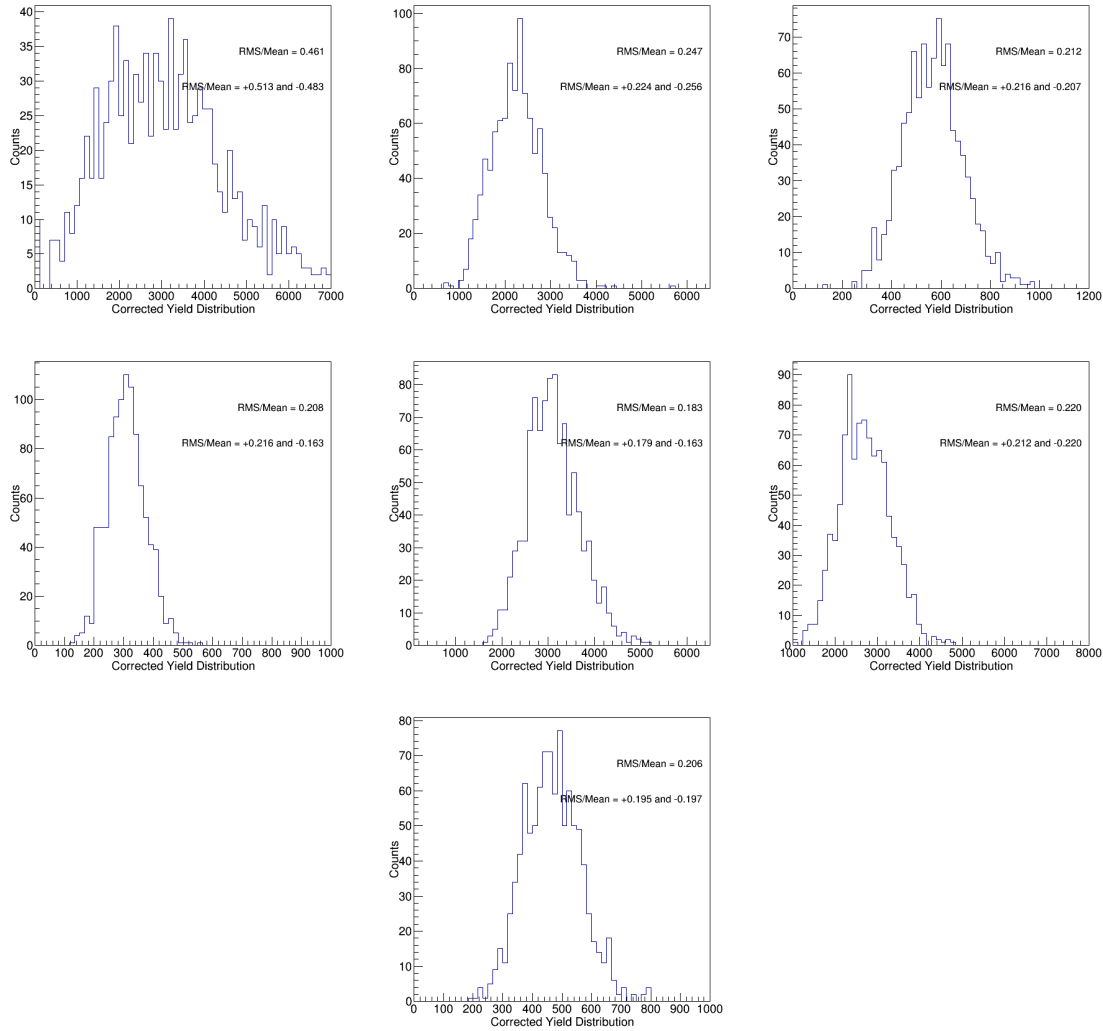


Figure 5-60: The B_s^0 corrected yield distributions of the 1000 data-like randomly resampled datasets for centrality in 0 - 90% in the p_T range of 7 - 10, 10 - 15, 15 - 20, and 20 - 50 GeV/c as well as 0 - 90%, 0 - 30%, and 30 - 90% in the p_T range of 10 - 50 GeV/c are shown above.

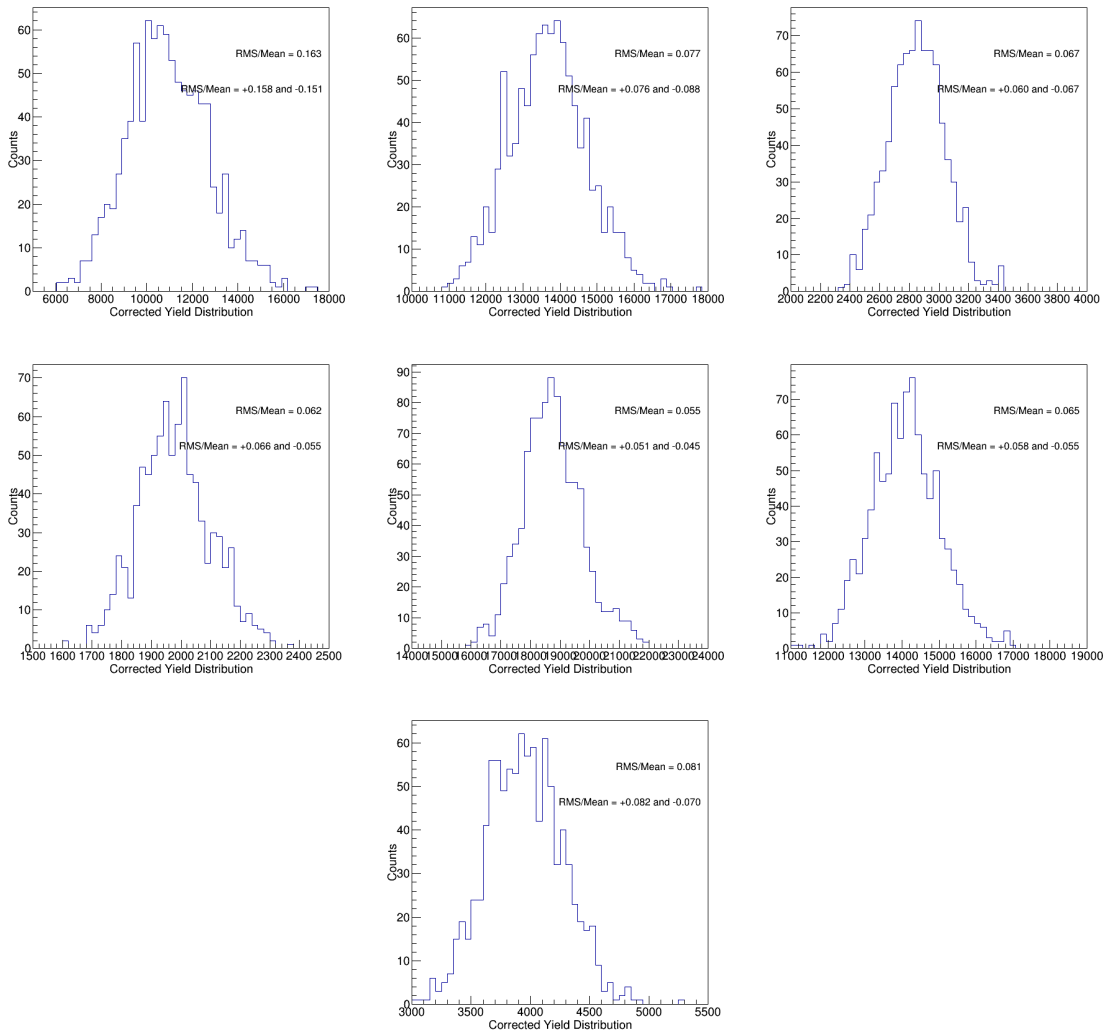


Figure 5-61: The B^+ corrected yield distributions of the 1000 data-like randomly resampled datasets for centrality in 0 - 90% in the p_T range of 7 - 10, 10 - 15, 15 - 20, and 20 - 50 GeV/c as well as 0 - 90%, 0 - 30%, and 30 - 90% in the p_T range of 10 - 50 GeV/c are shown above.

5.13.2 Statistical Uncertainties Interpretation

More refinement is needed as we see from Figure 5-60 and Figure 5-61 that the corrected yield distributions are indeed asymmetric. Hence, asymmetric statistical uncertainties will be introduced in our B-meson cross section measurements. To quantify the asymmetric statistical uncertainties, we do the following

- Find the location of the bin corresponding to the mean of corrected yield distribution
- Integrate the up/down (+/-) side by increasing/decreasing the bin number from the mean bin
- Take integral count from the mean bin ratio to the total up/down side counts from the mean so that they reach 1σ , which is $34.14\% \times 2 = 68.28\%$. Mathematically, the method is shown below:

$$\frac{\int_{\langle Y \rangle}^{Y^+} f(x)dx}{\int_{\langle Y \rangle}^{\infty} f(x)dx} = 68.28\% \quad (5.26)$$

- Read out the corresponding up/down corrected yield values, for instance, Y^+ as shown on the equation above
- Compute the percent deviations (% Dev) from the mean values for both up/down corrected yields and quote the deviations as up/down statistical uncertainties

$$\%Dev^{\pm} = \frac{Y^{\pm} - \langle Y \rangle}{\langle Y \rangle} \times 100\% \quad (5.27)$$

Table 5.21 and Table 5.22 summarize the estimations of statistical uncertainties for B_s^0 and B^+ cross sections in each p_T and centrality bin

Table 5.21: The B_s^0 RMS/Mean and their asymmetric up and down statistical uncertainties of the corrected yield distributions are summarized below.

Centrality	$B_s^0 p_T$ (GeV/c)	RMS/Mean	Stat. Up (+)	Stat Down (-)
0 - 90%	7 - 10	46.1%	51.3%	48.3%
0 - 90%	10 - 15	24.7%	22.4%	25.6%
0 - 90%	15 - 20	21.2%	21.6%	20.7%
0 - 90%	20 - 50	20.8%	21.6%	16.3%
0 - 30%	10 - 50	22.0%	21.2%	22.0%
30 - 90%	10 - 50	20.6%	19.5%	19.7%
0 - 90%	10 - 50	18.3%	17.9%	16.3%

Table 5.22: The B^+ RMS/Mean and their asymmetric up and down statistical uncertainties of the corrected yield distributions are summarized below.

Centrality	$B^+ p_T$ (GeV/c)	RMS/Mean	Stat. Up (+)	Stat Down (-)
0 - 90%	7 - 10	16.4%	15.8%	15.1%
0 - 90%	10 - 15	7.70%	7.60%	8.77%
0 - 90%	15 - 20	6.72%	6.00%	6.66%
0 - 90%	20 - 50	6.19%	6.64%	5.49%
0 - 30%	10 - 50	6.52%	5.81%	5.54%
30 - 90%	10 - 50	8.10%	8.22%	6.97%
0 - 90%	10 - 50	5.49%	5.06%	4.54%

5.14 Systematic Uncertainties Estimation

The final step is to estimate the systematic uncertainties of the B-meson measurements. We know that systematic uncertainties always exist in experiments due to the imperfection of apparatus conditions, unknown variation in the experiments, and limitation of the analysis techniques, which cannot be cured even with infinite statistics. They mainly come from 3 parts: the common constant scale factors for both B_s^0 and B^+ mesons, the signal raw yield extraction, and the efficiency correction. Based on the formula to obtain the cross section (Equations 5.18 and 5.19), we can identify the main sources of systematic uncertainties in terms of percentage and the method to estimate each of them in the following subsections.

5.14.1 Global Observables

The uncertainties of global observables T_{AA} and N_{MB} are summarized in Table 5.3 and Table 5.2. We simply quote the uncertainties from them in our cross section measurements.

5.14.2 Branching Ratios

According to PDG 2018 [195], the relevant decay branching ratio and their uncertainties are listed as follows:

- $BR(B_s^0 \rightarrow J/\psi\phi) = (1.08 \pm 0.08) \times 10^{-3}$
- $BR(B^+ \rightarrow J/\psi K^+) = (1.010 \pm 0.029) \times 10^{-3}$
- $BR(J/\psi \rightarrow \mu^+\mu^-) = (5.961 \pm 0.033)\%$
- $BR(\phi \rightarrow K^+K^-) = (49.2 \pm 0.5)\%$

Hence, we can compute the total branching ratios of the B-meson decay chains by multiply the partial decays. The uncertainties on the BR will propagate in an uncorrelated manner.

- $BR(B_s^0 \rightarrow J/\psi\phi \rightarrow \mu^+\mu^- K^+ K^-) = (3.17 \pm 0.24) \times 10^{-5}$
- $BR(B^+ \rightarrow J/\psi K^+ \rightarrow \mu^+\mu^- K^+) = (6.03 \pm 0.18) \times 10^{-5}$

Hence, we can compute the percent uncertainties of the B_s^0 and B^+ branching ratios. The systematic uncertainties due to decay branching ratio of B_s^0 are **7.50%** and B^+ is **2.92%**.

5.14.3 Tracking Efficiency

The difference in the track reconstruction efficiency in data and simulation is estimated by comparing 3-prong D^* decay $D^* \rightarrow K\pi\pi$ and 5-prong D^* decay $D^* \rightarrow K\pi\pi\pi\pi$ [196]. According to CMS tracking group studies, this results in **5%** for each

track. Hence, the systematic uncertainties due to tracking efficiency are **5%** for B^+ since it has only one kaon track and **10%** for B_s^0 since it has two kaon tracks. These apply to all p_T and centrality bins.

5.14.4 Muon Efficiency

The systematic uncertainties due to muon efficiency can be quantified by taking the up and down cases of the tag-&-probe scale factors determined by the CMS dilepton group. Figure 5-62 shows the workflow to carry out the systematic uncertainties studies using the tag-&-probe method in this analysis:

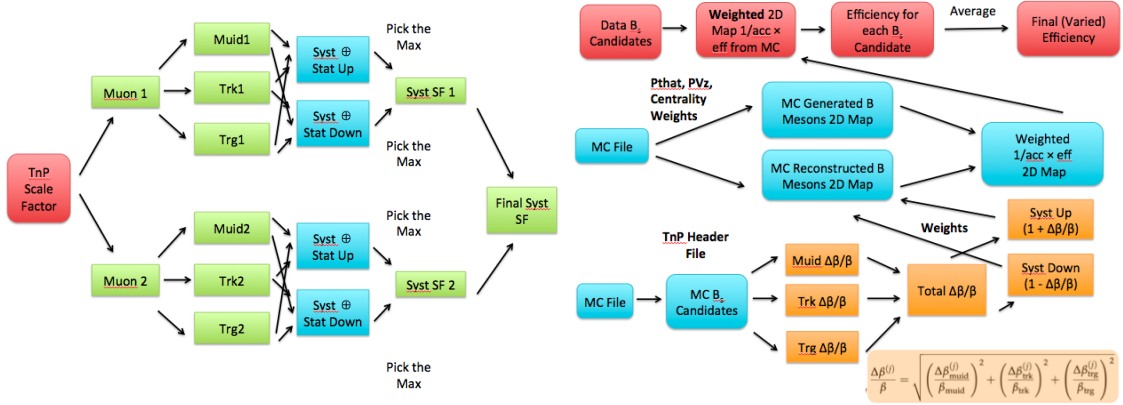


Figure 5-62: The schematic block diagrams demonstrating the calculations of the uncertainties on tag-&-probe scale factors (left) and the asymmetric systematic uncertainties due to muon efficiency on the efficiency correction factor (right) are shown above.

Table 5.23 and Table 5.24 summarize the systematic uncertainties due to muon efficiency on B_s^0 and B^+ respectfully

Table 5.23: The B_s^0 systematic uncertainties due to muon efficiency for each p_T and centrality bin are summarized below.

Centrality	$B_s^0 p_T$ (GeV/c)	Uncertainty Up (+)	Uncertainty Down (-)
0 - 90%	7 - 10	8.88%	7.49%
0 - 90%	10 - 15	5.97%	5.24%
0 - 90%	15 - 20	3.73%	3.46%
0 - 90%	20 - 50	3.91%	3.60%
0 - 30%	10 - 50	5.52%	4.85%
30 - 90%	10 - 50	4.63%	4.19%
0 - 90%	10 - 50	5.29%	4.70%

Table 5.24: The B^+ systematic uncertainties due to muon efficiency for each p_T and centrality bin are summarized below.

Centrality	$B^+ p_T$ (GeV/c)	Uncertainty Up (+)	Uncertainty Down (-)
0 - 90%	7 - 10	7.21%	6.28%
0 - 90%	10 - 15	4.29%	3.92%
0 - 90%	15 - 20	3.83%	3.53%
0 - 90%	20 - 50	3.87%	3.56%
0 - 30%	10 - 50	4.18%	3.83%
30 - 90%	10 - 50	4.14%	3.80%
0 - 90%	10 - 50	4.16%	3.81%

5.14.5 Selection Efficiency

Next, we will estimate uncertainties due to B-meson selection efficiency. The efficiency correction heavily relies on the MC performance. The poor descriptions of detector performance in the MC simulation, the limited MC statistics, and the poor underlying physics processes modeling of the MC B-meson spectra will contribute to the uncertainties in efficiency correction. In fact, this is the major systematic uncertainty throughout the analysis.

Data-MC Discrepancy

We have previously compared the data and MC distributions of B_s^0 and B^+ BDT scores. To quantify the systematic uncertainties due to data-MC discrepancy, we can simply apply the *Splot* weights w obtained by *Splot* techniques in the BDT distributions to get a weighted 2D efficiency correction map $\frac{w}{\alpha \times \epsilon}$. Then, we compute the weighted efficiency correction factor $\langle \frac{1}{\alpha \times \epsilon} \rangle_w$. Finally, we take the percent deviation (% Dev) of the BDT *Splot* weighted $\langle \frac{1}{\alpha \times \epsilon} \rangle_w$ to the nominal efficiency correction factor $\langle \frac{1}{\alpha \times \epsilon} \rangle$ as the systematic uncertainties.

$$\%Dev = \frac{\langle \frac{1}{\alpha \times \epsilon} \rangle_w - \langle \frac{1}{\alpha \times \epsilon} \rangle}{\langle \frac{1}{\alpha \times \epsilon} \rangle} \times 100\% \quad (5.28)$$

This method works for B^+ since it has sufficient statistics. However, for B_s^0 , due to its limited statistics, we decide to apply the *Splot* weights obtained from kinematic variables of the kaon tracks of B^+ to the efficiency correction factor and quote the largest one as the systematic uncertainties. The list of kinematic variables are shown below:

- The transverse distance of closest approach the kaon track to the primary vertex
- The error on the transverse distance of closest approach the kaon track to the primary vertex
- The longitudinal distance of closest approach the kaon track to the primary vertex

- The error on the longitudinal distance of closest approach the kaon track to the primary vertex
- The kaon track pseudorapidity
- The kaon track rapidity
- The kaon track transverse momentum

Table 5.25 and Table 5.26 summarize the systematic uncertainties due to data-MC discrepancy on B_s^0 and B^+ respectfully

Table 5.25: The B_s^0 systematic uncertainties due to data-MC discrepancy for each p_T and centrality bin are summarized below.

Centrality	$B_s^0 p_T$ (GeV/c)	% Dev
0 - 90%	7 - 10	34.65%
0 - 90%	10 - 15	5.64%
0 - 90%	15 - 20	4.66%
0 - 90%	20 - 50	10.24%
0 - 30%	10 - 50	3.09%
30 - 90%	10 - 50	3.66%
0 - 90%	10 - 50	3.19%

Table 5.26: The B^+ systematic uncertainties due to data-MC discrepancy for each p_T and centrality bin are summarized below.

Centrality	$B^+ p_T$ (GeV/c)	% Dev
0 - 90%	7 - 10	4.17%
0 - 90%	10 - 15	15.25%
0 - 90%	15 - 20	3.01%
0 - 90%	20 - 50	1.65%
0 - 30%	10 - 50	13.28%
30 - 90%	10 - 50	8.49%
0 - 90%	10 - 50	11.51%

Finite MC Statistics

Another source of uncertainties on the selection efficiency is the statistics of the MC samples. Ideally, this kind of uncertainty should be 0 because we can in principle simulate as many MC events as we want. However, in reality, we only generated about 2.5 million MC events, which is finite. Particularly, when we create the finely binned 2D maps of efficiency vs B-meson p_T and $|y|$, due to the limited acceptance and fine binning, very low p_T B mesons will have very few candidates.

To quantify the systematic uncertainties due to limited B-meson MC events, the following procedures are carried out

- Generate 10000 2D maps of efficiency vs B-meson p_T and $|y|$ and smear them with Gaussian distribution according to the means and errors of the nominal 2D maps
- Carry out the analysis workflow to obtain the efficiency correct factors for $\langle \frac{1}{\alpha \times \epsilon} \rangle$ all 10000 2D maps using the same B-meson experimental data input
- Plot the distributions of the efficiency correct factors $\langle \frac{1}{\alpha \times \epsilon} \rangle$
- Compute the RMS/Mean of the distributions and quote them as the systematic uncertainties due to finite MC statistics

Figure 5-63 and Figure 5-64 show the $\langle \frac{1}{\alpha \times \epsilon} \rangle$ distributions for B_s^0 and B^+ respectively

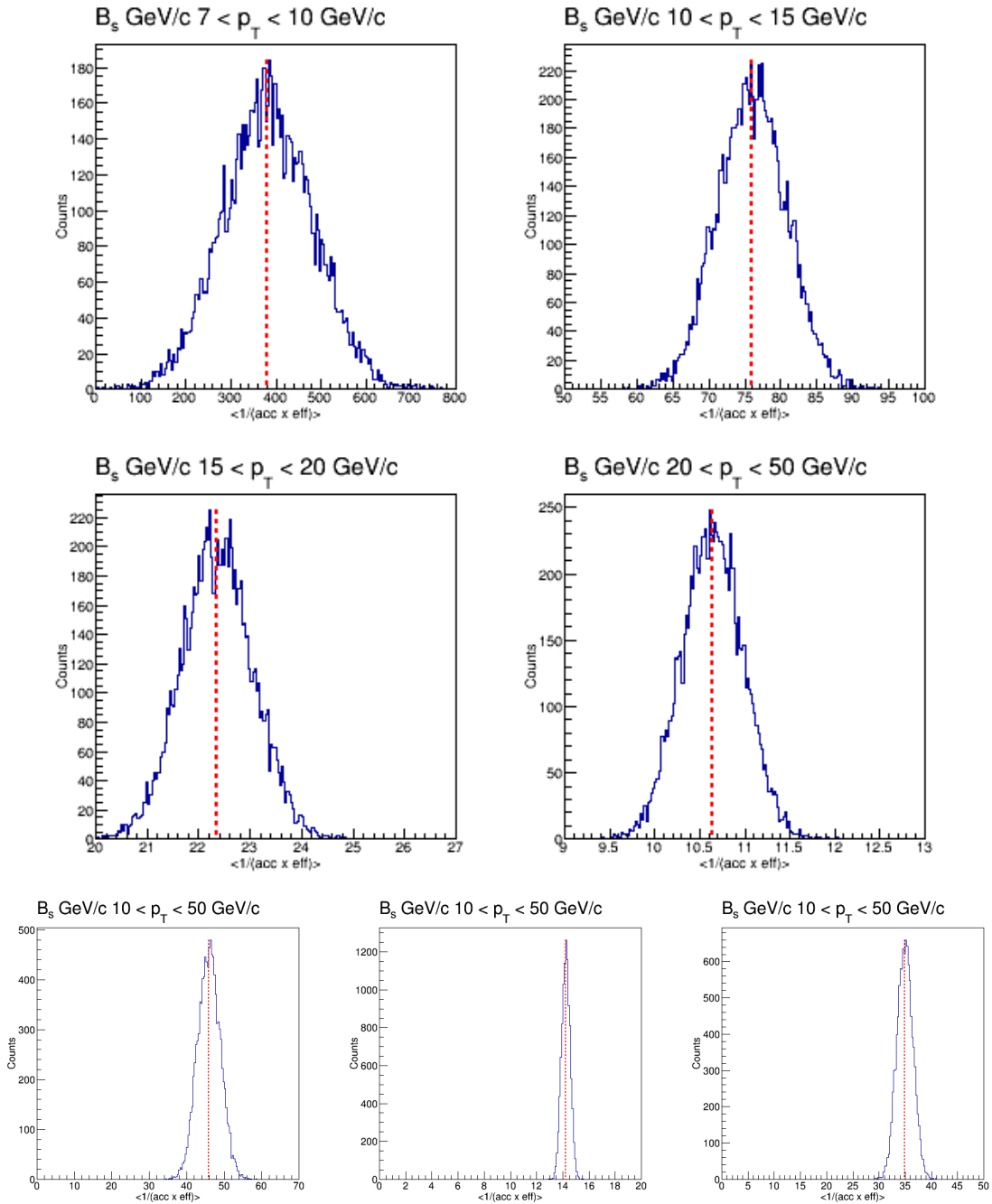


Figure 5-63: The distributions of $B_s^0 \langle \frac{1}{\text{acc} \times \text{eff}} \rangle$ for centrality in 0 - 90% in the p_T range of 7 - 10, 10 - 15, 15 - 20, and 20 - 50 GeV/c as well as 0 - 90%, 0 - 30%, and 30 - 90% in the p_T range of 10 - 50 GeV/c are shown above. The red dash lines are our nominal values for efficiency correction.

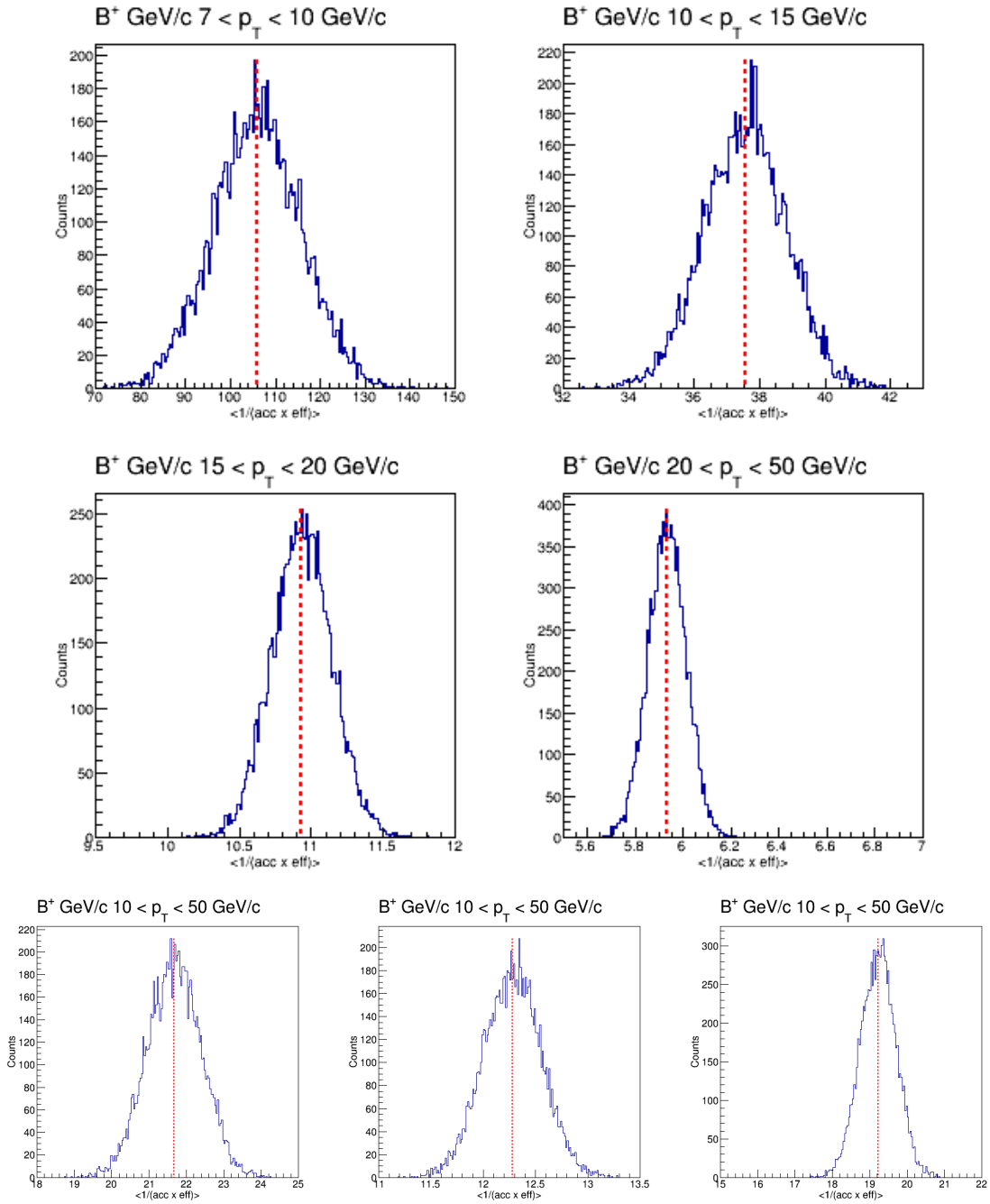


Figure 5-64: The distributions of $B^+ \langle \frac{1}{\text{acc} \times \text{eff}} \rangle$ for centrality in 0 - 90% in the p_T range of 7 - 10, 10 - 15, 15 - 20, and 20 - 50 GeV/c as well as 0 - 90%, 0 - 30%, and 30 - 90% in the p_T range of 10 - 50 GeV/c are shown above. The red dash lines are our nominal values for efficiency correction.

As expected, the distributions have symmetric Gaussian shapes. The means of the distributions agree with the nominal values of $\langle \frac{1}{\alpha \times \epsilon} \rangle$ in the analysis, which makes sense and thus validates the procedures. Table 5.27 and Table 5.28 summarize the RMS/Mean results of the distributions for B_s^0 and B^+ respectfully

Table 5.27: The B_s^0 systematic uncertainties due to limited MC sample statistics for each p_T and centrality bin are summarized below.

Centrality	$B_s^0 p_T$ (GeV/c)	% Dev
0 - 90%	7 - 10	26.5%
0 - 90%	10 - 15	6.28%
0 - 90%	15 - 20	3.08%
0 - 90%	20 - 50	3.21%
0 - 30%	10 - 50	6.59%
30 - 90%	10 - 50	2.27%
0 - 90%	10 - 50	4.37%

Table 5.28: The B^+ systematic uncertainties due to MC sample statistics for each p_T and centrality bin are summarized below.

Centrality	$B^+ p_T$ (GeV/c)	% Dev
0 - 90%	7 - 10	9.22%
0 - 90%	10 - 15	3.36%
0 - 90%	15 - 20	1.92%
0 - 90%	20 - 50	1.35%
0 - 30%	10 - 50	3.37%
30 - 90%	10 - 50	2.26%
0 - 90%	10 - 50	2.49%

The systematic uncertainties due to finite MC simulation events are particularly large at low p_T due to the limited acceptance.

Residue p_T Shape Effects

According to the B-meson fragmentation fraction measurement in pp collisions from LHCb in Figure 1-35, no significant rapidity dependence is observed. Assuming similar insignificant rapidity dependence also holds in PbPb collisions, the rapidity should

not contribute to the weigh function $w(x)$. Hence, only B-meson p_T shapes play an important role in creating the systematic uncertainties to selection efficiency.

As demonstrated in Section 5.10.4, in the limit of zero bin width, the uncertainties due to the unknown B-meson kinematics will be completely eliminated. However, since we have a very fine but still finite p_T binning, there could still be residue effects on systematic uncertainties due to the B-meson p_T shape. To quantify the uncertainties, we simply apply the B-meson p_T weights obtained in Section 5.3.4 according to the fit functions obtained in Figure 5-4 and Figure 5-5.

We apply the B-meson p_T weights to the 2D $\frac{1}{\alpha \times \epsilon}$ map. Then, we compute different $\langle \frac{1}{\alpha \times \epsilon} \rangle^{w_{pT}}$ and take the percent deviation to the nominal efficiency correction factor $\langle \frac{1}{\alpha \times \epsilon} \rangle$. Next, we choose the largest percent deviated from 0 and quote them as the systematic uncertainties due to the B-meson p_T shape. Table 5.29 and Table 5.30 summarize the results

Table 5.29: The B_s^0 systematic uncertainties due to unknown B-meson p_T shape in PbPb collisions for each p_T and centrality bin are summarized below.

Centrality	$B_s^0 p_T$ (GeV/c)	% Dev
0 - 90%	7 - 10	0.015%
0 - 90%	10 - 15	0.050%
0 - 90%	15 - 20	0.010%
0 - 90%	20 - 50	0.022%
0 - 30%	10 - 50	0.067%
30 - 90%	10 - 50	0.015%
0 - 90%	10 - 50	0.037%

We can see that the remaining p_T shape systematic uncertainties are essentially negligible, which demonstrates the success of $\langle \frac{1}{\alpha \times \epsilon} \rangle$ efficiency correction approach.

Total Uncertainties on Selection Efficiency

Hence, in summary, the total uncertainties due to selection efficiency are simply the sum of uncertainties due to data-MC discrepancy, finite MC events, and the remaining B-meson p_T shape in quadrature: selection efficiency = data-MC discrepancy \oplus finite

Table 5.30: The B^+ systematic uncertainties due to unknown B-meson p_T shape in PbPb collisions for each p_T and centrality bin are summarized below.

Centrality	$B^+ p_T$ (GeV/c)	% Dev
0 - 90%	7 - 10	0.166%
0 - 90%	10 - 15	0.198%
0 - 90%	15 - 20	0.009%
0 - 90%	20 - 50	0.005%
0 - 30%	10 - 50	0.158%
30 - 90%	10 - 50	0.093%
0 - 90%	10 - 50	0.140%

MC events \oplus remaining B-meson p_T shape. Table 5.31 and Table 5.32 summarize the selection efficiency systematic uncertainties of B_s^0 and B^+ respectfully

Table 5.31: The B_s^0 selection efficiency uncertainties are summarized below.

Centrality	$B_s^0 p_T$ (GeV/c)	MC-Data	MC Stat.	p_T Shape	Total Uncertainties
0 - 90%	7 - 10	34.65%	26.5%	0.015%	43.62%
0 - 90%	10 - 15	5.64%	6.28%	0.050%	8.44%
0 - 90%	15 - 20	4.66%	3.08%	0.010%	5.85%
0 - 90%	20 - 50	10.24%	3.21%	0.022%	10.73%
0 - 30%	10 - 50	3.09%	6.59%	0.067%	7.28%
30 - 90%	10 - 50	3.66%	2.27%	0.015%	4.31%
0 - 90%	10 - 50	3.19%	4.37%	0.037%	5.41%

5.14.6 Signal Extraction

Finally, there are also systematic uncertainties due to signal extraction. To evaluate the uncertainties, we try different models for the signal and background components in the unbinned fit to the B-meson invariant mass distributions. Then, we quote the percent deviations (% Dev) of the variated signal raw yields N'_S from the nominal signal raw yields N_S as the systematic uncertainties.

Table 5.32: The B^+ selection efficiency uncertainties are summarized below.

Centrality	B^+ p_T (GeV/c)	MC-Data	MC Stat.	p_T Shape	Total Uncertainties
0 - 90%	7 - 10	4.17%	9.22%	0.166%	10.12%
0 - 90%	10 - 15	15.25%	3.36%	0.198%	15.62%
0 - 90%	15 - 20	3.01%	1.92%	0.009%	3.57%
0 - 90%	20 - 50	1.65%	1.35%	0.005%	2.13%
0 - 30%	10 - 50	13.28%	3.37%	0.158%	13.70%
30 - 90%	10 - 50	8.49%	2.26%	0.093%	8.79%
0 - 90%	10 - 50	11.51%	2.49%	0.140%	11.78%

Signal PDF Variation

For the signal component, we consider several variations listed as follows.

- Switch double Gaussian to triple Gaussian
- Fix the mean of the double Gaussian to be the mean from the MC fits
- Increase/decrease the widths nominal double Gaussian function by 10%: $\sigma_{1,2} \rightarrow (1 + \pm 10\%) \sigma_{1,2}$

Figure 5-65 and Figure 5-66 show the examples of signal PDF variation performed in B_s^0 and B^+ invariant mass fits to estimate the systematic uncertainties due to signal extraction

Next, we simply take the largest percent variations of the variated signal raw yields compared to the nominal ones and quote them as the systematic uncertainties.

Table 5.33 and Table 5.34 summarize the signal PDF systematic uncertainties

Background PDF Variation

The variation of background is simpler. We replace the nominal exponential decay function with first-, second-, and third-order polynomials. Again, same as the signal PDF variation, we quote the percent deviation from the variated signal raw yield to the nominal signal raw yield as the background PDF systematic uncertainties.

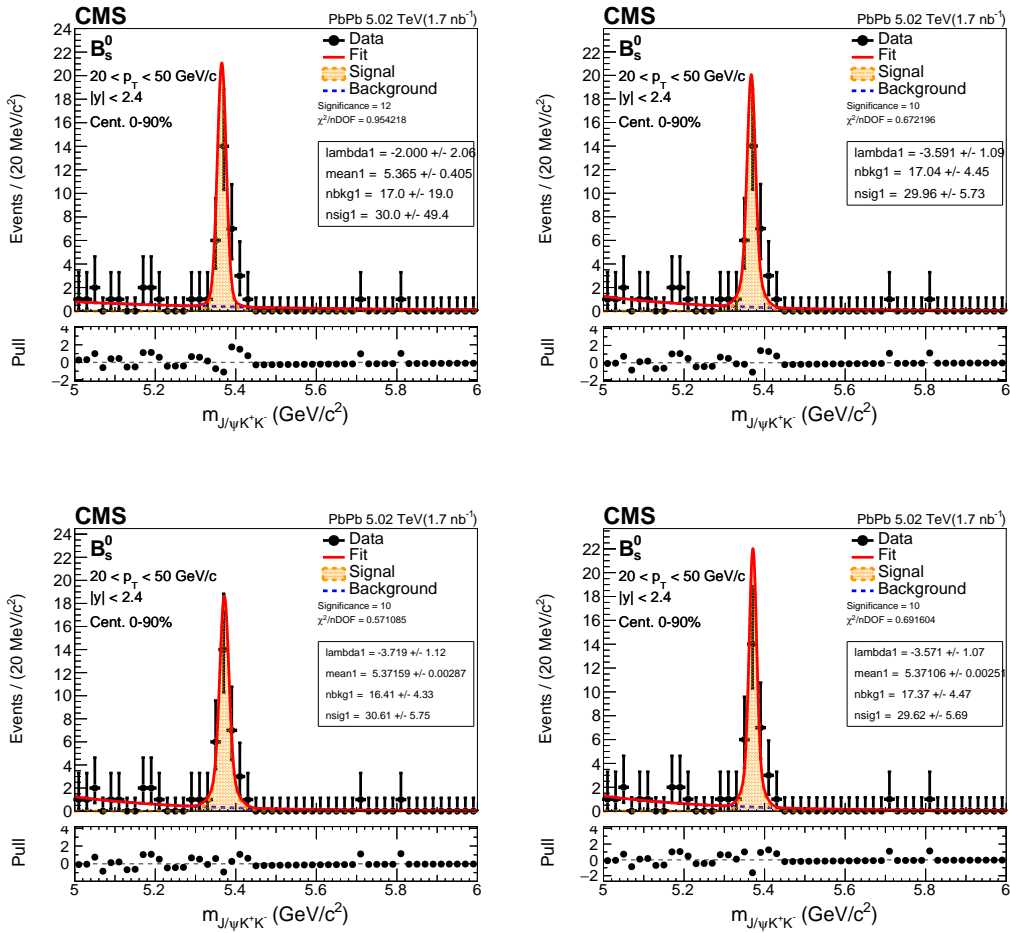


Figure 5-65: The fits of B_s^0 invariant mass distributions for p_T from 20 - 50 GeV/c and centrality from 0 - 90% are shown above. The signal PDFs are gaussian (with widths and relative proportions fixed from MC), double gaussian with all the parameters fixed (including the mean), increased width ($a=1.1$), and decreased width ($a=0.9$) from top left to bottom right.

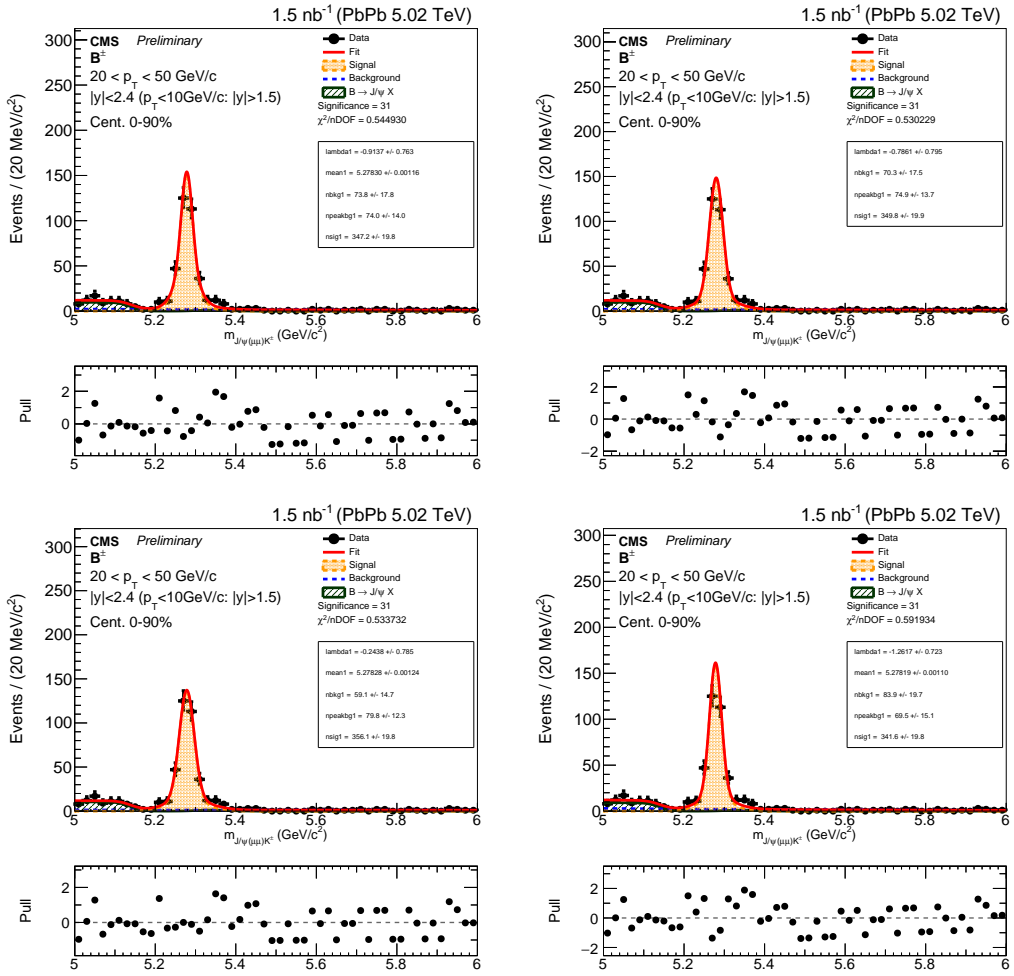


Figure 5-66: The fit of B_s^0 invariant mass distributions for p_T from 20 - 50 GeV/c and centrality from 0 - 90% are shown above. The signal PDFs are gaussian (with widths and relative proportions fixed from MC), double gaussian with all the parameters fixed (including the mean), increased width ($a=1.1$), and decreased width ($a=0.9$) from top left to bottom right.

Table 5.33: The B_s^0 systematic uncertainties due to signal PDF variation in p_T and centrality bin are summarized below.

Centrality	$B_s^0 p_T$ (GeV/c)	Triple Gaussian	Fixed Mean	+10% Width	-10% Width
0 - 90%	7 - 10	0.862%	0.762%	0.066%	0.056%
0 - 90%	10 - 15	0.144%	0.137%	1.83%	2.34%
0 - 90%	15 - 20	0.110%	0.066%	1.02%	1.00%
0 - 90%	20 - 50	0.629%	0.056%	1.40%	1.88%
0 - 30%	10 - 50	0.241%	0.192%	1.47%	1.74%
30 - 90%	10 - 50	2.96%	0.208%	0.840%	0.767%
0 - 90%	10 - 50	1.56%	0.20%	1.33%	1.65%

Table 5.34: The B^+ systematic uncertainties due to signal PDF variation in p_T and centrality bin are summarized below.

Centrality	$B^+ p_T$ (GeV/c)	Triple Gaussian	Fixed Mean	+10% Width	-10% Width
0 - 90%	7 - 10	0.004%	1.13%	3.84%	4.46%
0 - 90%	10 - 15	0.235%	0.046%	2.27%	2.67%
0 - 90%	15 - 20	0.050%	0.025%	2.32%	2.74%
0 - 90%	20 - 50	0.750%	0.010%	1.79%	2.36%
0 - 30%	10 - 50	0.415%	0.155%	2.12%	2.50%
30 - 90%	10 - 50	0.370%	0.064%	2.10%	2.57%
0 - 90%	10 - 50	0.494%	0.060%	2.19%	2.60%

Figure 5-67 and Figure 5-68 show the examples of background PDF variation done in B_s^0 and B^+ invariant mass fits to estimate the systematic uncertainties due to background extraction

Again, we simply take the largest percent variations of the variated signal raw yields compared to the nominal ones and quote them as the systematic uncertainties. Table 5.35 and Table 5.36 summarize the background PDF systematic uncertainties

Total PDF Variation

To calculate the total PDF variation, we simply add the PDF variations of the signal and background into quadrature: signal extraction uncertainties = PDF variation of

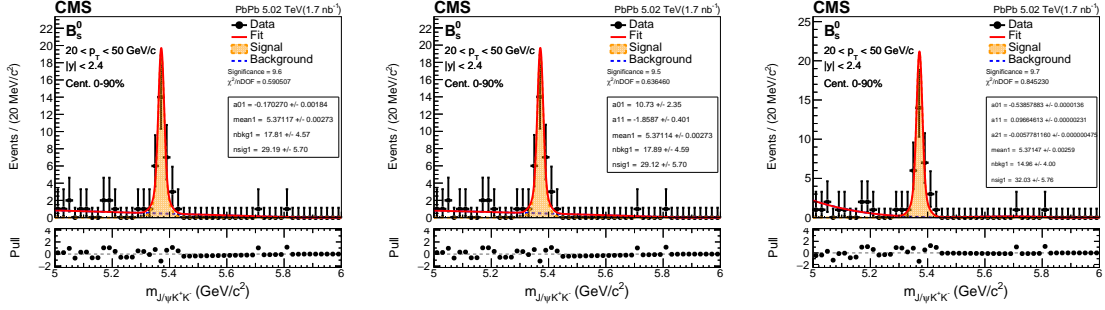


Figure 5-67: The Invariant mass fits to B_s^0 candidates for $B_s^0 p_T$ from 20 - 50 GeV/c and centrality from 0 to 90% in 5.02 TeV PbPb. The background PDFs from left to right are first-, second-, and third-order polynomials.

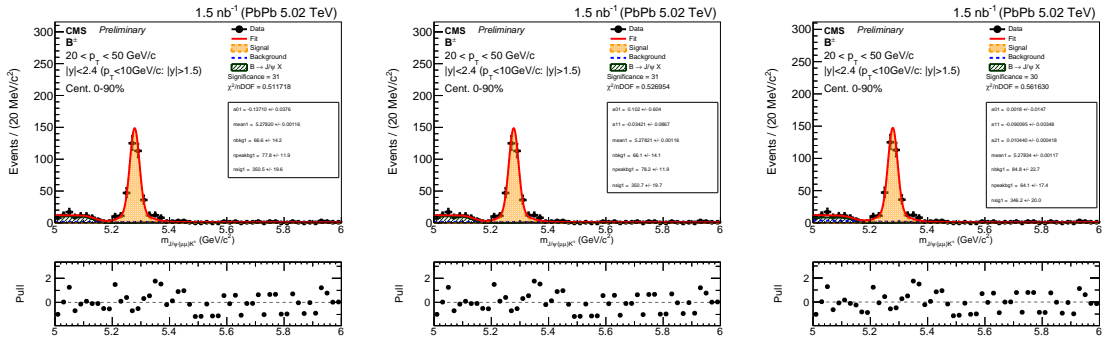


Figure 5-68: The Invariant mass fits to B^+ candidates for $B^+ p_T$ from 20 - 50 GeV/c and centrality from 0 to 90% in 5.02 TeV PbPb. The background PDFs from left to right are first-, second-, and third-order polynomials.

Table 5.35: The B_s^0 systematic uncertainties due to background PDF variation in p_T and centrality bin are summarized below.

Centrality	$B_s^0 p_T$ (GeV/c)	First Order	Second Order	Third Order
0 - 90%	7 - 10	0.02%	0.92%	0.96%
0 - 90%	10 - 15	1.45%	2.69%	2.64%
0 - 90%	15 - 20	1.45%	1.36%	0.28%
0 - 90%	20 - 50	3.30%	3.54%	6.11%
0 - 30%	10 - 50	1.83%	0.495%	0.029%
30 - 90%	10 - 50	1.14%	1.33%	0.912%
0 - 90%	10 - 50	1.58%	0.773%	0.592%

Table 5.36: The B^+ systematic uncertainties due to background PDF variation in p_T and centrality bin are summarized below.

Centrality	$B^+ p_T$ (GeV/c)	First Order	Second Order	Third Order
0 - 90%	7 - 10	0.021%	0.117%	0.093%
0 - 90%	10 - 15	0.312%	0.380%	0.546%
0 - 90%	15 - 20	0.386%	0.432%	0.576%
0 - 90%	20 - 50	0.196%	0.238%	1.03%
0 - 30%	10 - 50	0.157%	0.245%	0.412%
30 - 90%	10 - 50	1.13%	0.065%	0.102%
0 - 90%	10 - 50	0.384%	0.427%	0.422%

signal \oplus background. Table 5.37 and Table 5.38 summarize the total PDF systematic uncertainties contributing to B_s^0 and B^+ signal extraction respectfully.

5.14.7 Summary

Finally, we collect all studies above and add all sources of systematic uncertainties into quadrature to obtain the total systematic uncertainties. We compile summary tables for the systematic uncertainties in B_s^0 and B^+ cross section measurements in each p_T and centrality bin. Table 5.41 and Table 5.42 show B^{+0}_s p_T and centrality cross section measurements respectfully

Table 5.41 and Table 5.42 show B^+ p_T and centrality cross section measurements respectfully

Table 5.37: The B_s^0 signal extraction systematic uncertainties due to PDF variation in p_T and centrality bin are summarized below.

Centrality	$B_s^0 p_T$ (GeV/c)	Signal PDF	Background PDF	Total Uncertainties
0 - 90%	7 - 10	0.762%	0.96%	1.23%
0 - 90%	10 - 15	2.34%	2.69%	3.57%
0 - 90%	15 - 20	1.02%	1.45%	1.77%
0 - 90%	20 - 50	1.88%	6.11%	6.39%
0 - 30%	10 - 50	1.74%	1.83%	2.53%
30 - 90%	10 - 50	2.96%	1.33%	3.25%
0 - 90%	10 - 50	1.65%	1.58%	2.28%

Table 5.38: The B^+ signal extraction systematic uncertainties due to PDF variation in p_T and centrality bin are summarized below.

Centrality	$B^+ p_T$ (GeV/c)	Signal PDF	Background PDF	Total Uncertainties
0 - 90%	7 - 10	4.46%	0.117%	4.46%
0 - 90%	10 - 15	2.67%	0.546%	2.73%
0 - 90%	15 - 20	2.74%	0.576%	2.80%
0 - 90%	20 - 50	2.36%	1.03%	2.57%
0 - 30%	10 - 50	2.50%	0.412%	2.53%
30 - 90%	10 - 50	2.57%	1.13%	2.81%
0 - 90%	10 - 50	2.60%	0.427%	2.64%

Table 5.39: Summary of systematic uncertainties in each $B_s^0 p_T$ bin. All the values are reported in percentage.

$B_s^0 p_T$ (GeV/c)	7 - 10	10 - 15	15 - 20	20 - 50
Tracking Efficiency	10%	10%	10%	10%
Muon Efficiency	+8.88% -7.49%	+5.97% -5.24%	+3.73% -3.46%	+3.91% -3.60%
Selection Efficiency	43.62%	8.44%	5.85%	10.73%
Signal Extraction	1.23%	3.57%	1.77%	6.39%
Total	+45.64% -45.39%	+14.82% -14.54%	+12.18% -12.10%	+16.47% -16.40%
N_{MB}	1.26%	1.26%	1.26%	1.26%
T_{AA}	2.2%	2.2%	2.2%	2.2%
Branching Ratio	7.5%	7.5%	7.5%	7.5%
Global Systematics	7.92%	7.92%	7.92%	7.92%

Table 5.40: Summary of systematic uncertainties in each B_s^0 centrality bin. All the values are reported in percentage.

PbPb Collision Centrality	0 - 30%	30 - 90%	0 - 90%
Tracking Efficiency	10%	10%	10%
Muon Efficiency	+5.52% -4.85%	+4.63% -4.19%	+5.29% -4.70%
Selection Efficiency	7.28%	4.31 %	5.41%
Signal Extraction	2.53%	3.25%	2.28%
T_{AA}	2%	3.6%	2.2%
N_{MB}	1.26%	1.26%	1.26%
Total	+13.68% -13.52%	+12.71% -12.60%	+13.00% -12.77%
Branching fractions	7.5%	7.5%	7.5%
Global Systematics	7.5%	7.5%	7.5%

Table 5.41: Summary of systematic uncertainties in each B^+ p_T bin. All the values are reported in percentage.

$B^+ p_T$ (GeV/c)	7 - 10	10 - 15	15 - 20	20 - 50
Tracking Efficiency	5%	5%	5%	5%
Muon Efficiency	+7.21% -6.28%	+4.29% -3.92%	+3.83% -3.53%	+3.87% -3.56%
Selection Efficiency	10.12%	15.62%	3.57%	2.13%
Signal Extraction	4.46%	2.73%	2.80%	2.57%
Total	+14.04% -13.59%	+17.14% -17.05%	+7.75% -7.61%	+7.15% -6.99%
N_{MB}	1.26%	1.26%	1.26%	1.26%
T_{AA}	2.2%	2.2%	2.2%	2.2%
Branching Ratio	2.9%	2.9%	2.9%	2.9%
Global Systematics	3.85%	3.85%	3.85%	3.85%

Table 5.42: Summary of systematic uncertainties in each B^+ centrality bin. All the values are reported in percentage.

PbPb Collision Centrality	0 - 30%	30 - 90%	0 - 90%
Tracking Efficiency	10%	10%	10%
Muon Efficiency	+4.18%	+4.14%	+4.16%
	-3.83%	-3.80%	-3.81%
Selection Efficiency	13.70%	8.79%	11.78%
Signal Extraction	2.53%	2.81%	2.64%
T_{AA}	2%	3.6%	2.2%
N_{MB}	1.26%	1.26%	1.26%
Total	+15.53%	+11.89%	+13.92%
	-15.43%	-11.77%	-13.82%
Branching fractions	2.92%	2.92%	2.92%
Global Systematics	2.92%	2.92%	2.92%

Finally, Figure 5-69 and Figure 5-70 below illustrate the plot of all sources of B_s^0 and B^+ systematic uncertainties respectively for each p_T and centrality bin.

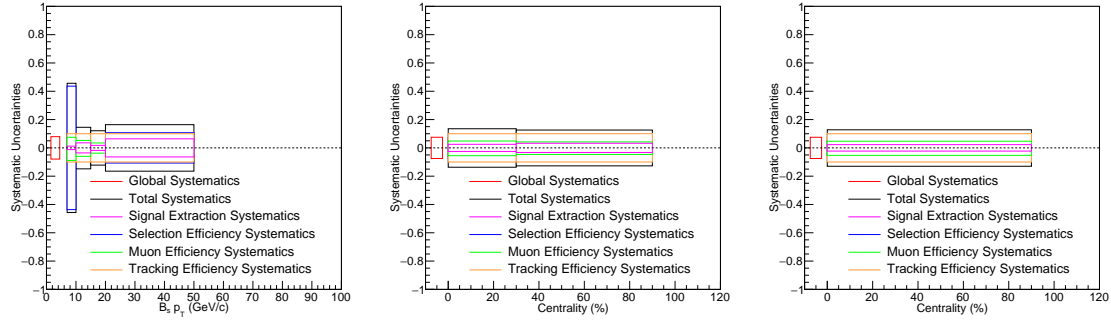


Figure 5-69: The summary of B_s^0 systematic uncertainties plotted as a function of p_T (left), centrality in 0 - 30% and 30 - 90% (middle), and the inclusive centrality bin 0 - 90% (right) are shown above.

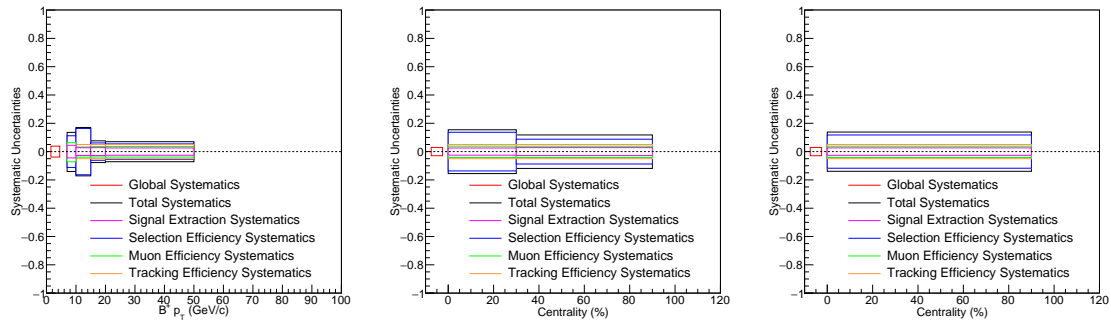


Figure 5-70: The summary of B^+ systematic uncertainties plotted as a function of p_T (left), centrality in 0 - 30% and 30 - 90% (middle), and the inclusive centrality bin 0 - 90% (right) are shown above.

5.15 Final Results

5.15.1 Overview

At this point, we have fully validated the analysis with detailed evaluations of both statistical and systematic uncertainties. We are ready to report the experimental measurements of B_s^0 and B^+ cross section and the B_s^0/B^+ ratios as functions of p_T and PbPb collision centrality.

5.15.2 B_s^0 and B^+ Cross Sections

When the B-meson cross section measurements as a function of p_T plots are created, the abscissa of each data point is set to the mean value of the corresponding p_T distribution after background subtraction via *Splot*. Figure 5-71 shows B_s^0 and B^+ p_T differential cross section $\frac{1}{T_{AA}} \frac{dN}{dp_T}$ as a function B-meson p_T in PbPb collisions at $\sqrt{s_{NN}} = 5.02$ TeV with the CMS detector using the 2018 dimuon PbPb dataset.

Table 5.43 and Table 5.44 summarize the B-meson cross section as functions of p_T :

Table 5.43: The numerical values and uncertainties of the B_s^0 cross section as a function of p_T are summarized below.

p_T (GeV/c)	$\frac{1}{T_{AA}} \frac{dN}{dp_T}$ (pb c/GeV)	Stat. Up (+)	Stat. Down (-)	Syst. Up (+)	Syst. Down (-)
7 - 10	160432	51.3%	48.3%	45.6%	45.4%
10 - 15	75523.7	22.4%	25.6%	14.8%	14.5%
15 - 20	25355	21.6%	20.7%	12.2%	12.1%
20 - 50	2272.18	21.6%	16.3%	16.5%	16.4%

We should again point out that for the p_T bin from 7 - 10 GeV/c, the measurement is a fiducial measurement correcting to B-meson rapidity only up to $1.5 < |y| < 2.4$. The B-meson measurements have a p_T range of 7 - 50 GeV/c. The uncertainties are large for B_s^0 p_T from 7 to 10 GeV/c due to the very limited statistics.

Figure 5-72 shows B_s^0 and B^+ p_T integrated cross section as a function of average

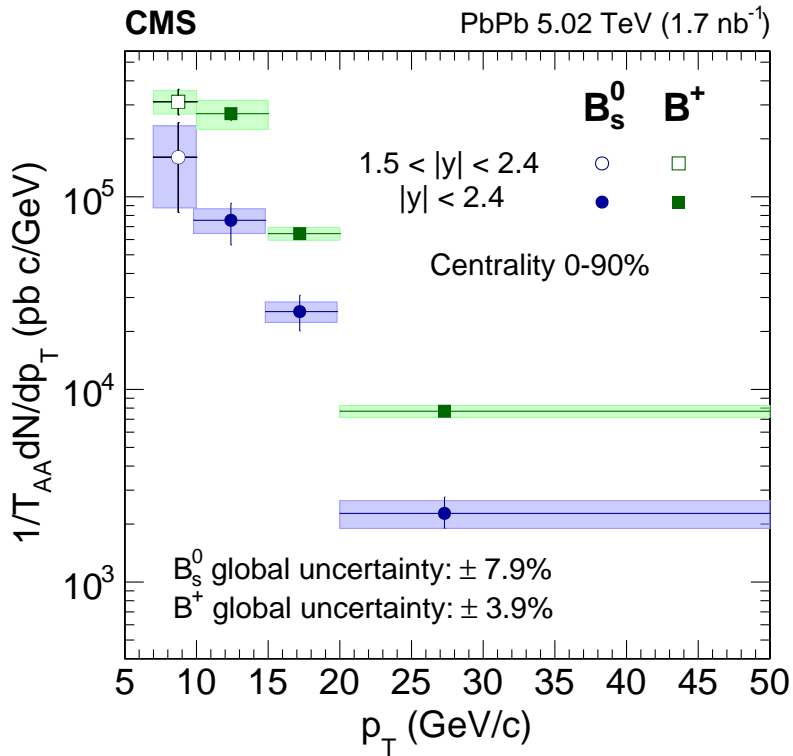


Figure 5-71: The measurement of B_s^0 and B^+ p_T differential cross section $\frac{1}{\tau_{AA}} \frac{dN}{dp_T}$ as a function of B-meson p_T within 0 - 90% centrality is shown above. It should be pointed out that the cross section results are plotted in the unit of pb c/GeV since τ_{AA} is in the unit of pb^{-1} while the p_T is in the unit of GeV/c. The open markers from 7 - 10 GeV/c stand for the fiducial measurements in the B-meson rapidity of $1.5 < |y| < 2.4$.

Table 5.44: The numerical values and uncertainties of the B^+ cross section as a function of p_T are summarized below.

p_T (GeV/c)	$\frac{1}{T_{AA}} \frac{dN}{dp_T}$ (pb c/GeV)	Stat. Up (+)	Stat. Down (-)	Syst. Up (+)	Syst. Down (-)
7 - 10	311668	15.9%	14.3%	14.0%	13.6%
10 - 15	270167	6.63%	7.95%	17.1%	17.1%
15 - 20	64384.4	6.54%	6.50%	7.75%	7.61%
20 - 50	7704.11	6.90%	5.26%	7.15%	6.99%

number of participants $\langle N_{part} \rangle$, with the corresponding PbPb collision centralities labeled in the plot

Table 5.45 and Table 5.46 summarize the B_s^0 and B^+ cross section as functions of centrality and their statistical and systematic uncertainties.

Table 5.45: The numerical values and uncertainties of B_s^0 cross section as a function of centrality are summarized below.

Centrality	$\frac{1}{T_{AA}} N$ (pb)	Stat. Up (+)	Stat. Down (-)	Syst. Up (+)	Syst. Down (-)
0 - 30%	650790	21.2%	22.0%	14.0%	13.7%
30 - 90%	497359	19.5%	19.7%	12.8%	12.7%
0 - 90%	595064	17.9%	16.3%	13.0%	12.8%

Table 5.46: The numerical values and uncertainties of B^+ cross section as a function of centrality are summarized below.

Centrality	$\frac{1}{T_{AA}} N$ (pb)	Stat. Up (+)	Stat. Down (-)	Syst. Up (+)	Syst. Down (-)
0 - 30%	1780710	5.52%	6.72%	15.5%	15.4%
30 - 90%	2286890	6.71%	7.06%	11.9%	11.8%
0 - 90%	1936560	4.47%	4.76%	13.9%	13.8%

It also should note that this is the first centrality differential measurement of fully reconstructed B_s^0 with the CMS experiment. From the cross section above, we can see that the nominal values of the cross section are lower for both B_s^0 and B^+ in more

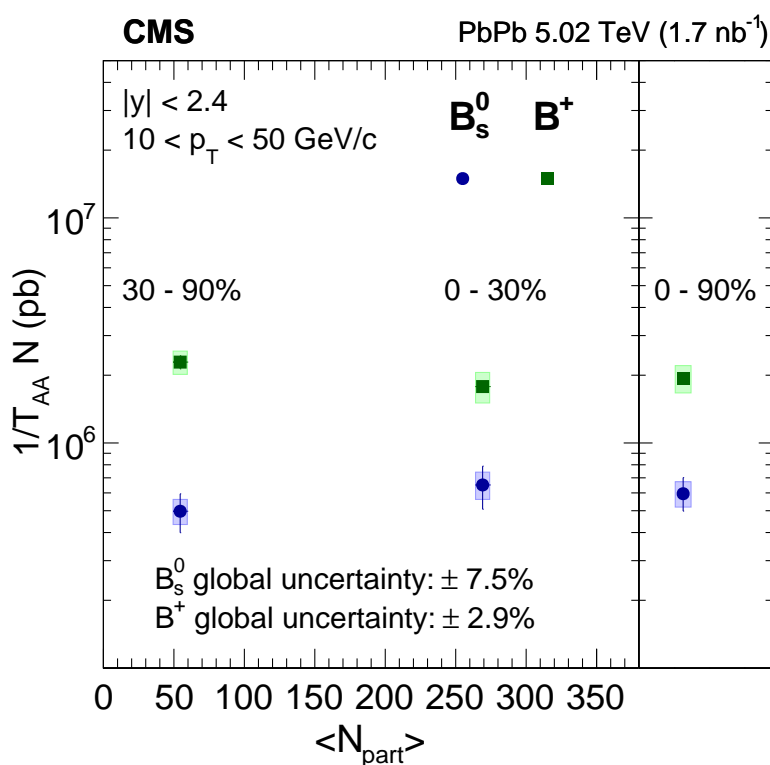


Figure 5-72: The measurement of B_s^0 and B^+ cross section $\frac{1}{T_{AA}} N$ as a function of $\langle N_{\text{part}} \rangle$ in different PbPb collision centralities within B-meson p_T from $10 - 50 \text{ GeV}/c$ is shown above.

central collision (0 - 30%) than the peripheral collision (30 - 90%). However, given the large uncertainties, we could not draw a conclusion that such suppression is due to the hot QGP medium effect.

5.15.3 B_s^0/B^+ Ratios

Since we have measured the B_s^0 and B^+ cross section, the next step is to obtain their ratio, which is an experimental observable to study beauty hadronization mechanism as mentioned in Section 1.8.4. We should note that when we take the ratio between B_s^0 to B^+ , the systematic uncertainties of T_{AA} and N_{MB} will be canceled. Also, the systematic uncertainties of tracking efficiency are reduced to 5% instead of adding into quadrature. Finally, the systematic uncertainties of muon efficiency are treated as perfectly correlated. This means we both vary the B_s^0 and B^+ cross sections with the muon efficiency systematics up and down and compute the ratios. Then, we calculate the percent deviations of up and down variated B_s^0/B^+ to the nominal B_s^0/B^+ and quote those numbers as the systematic uncertainties. Other sources of systematic uncertainties in B_s^0 and B^+ cross sections are added into quadrature for B_s^0/B^+ ratio.

Figure 5-73 shows the B_s^0/B^+ ratio as a function of B-meson p_T

Table 5.47 summarizes B_s^0/B^+ ratio as a function of B-meson p_T

Table 5.47: The numerical values and uncertainties of B_s^0/B^+ cross section ratio as a function of p_T are summarized below.

p_T (GeV/c)	Abc. (GeV/c)	B_s^0/B^+	stat. up (+)	stat. down (-)	syst. up (+)	syst. down (-)
(7,10)	8.75	0.5148	53.7%	50.4%	46.0%	46.1%
(10,15)	12.6	0.2795	22.3%	26.8%	19.3%	19.3%
(15,20)	17.4	0.3938	22.6%	21.7%	9.10%	9.11%
(20,50)	27.3	0.2949	22.7%	17.1%	13.9%	13.9%

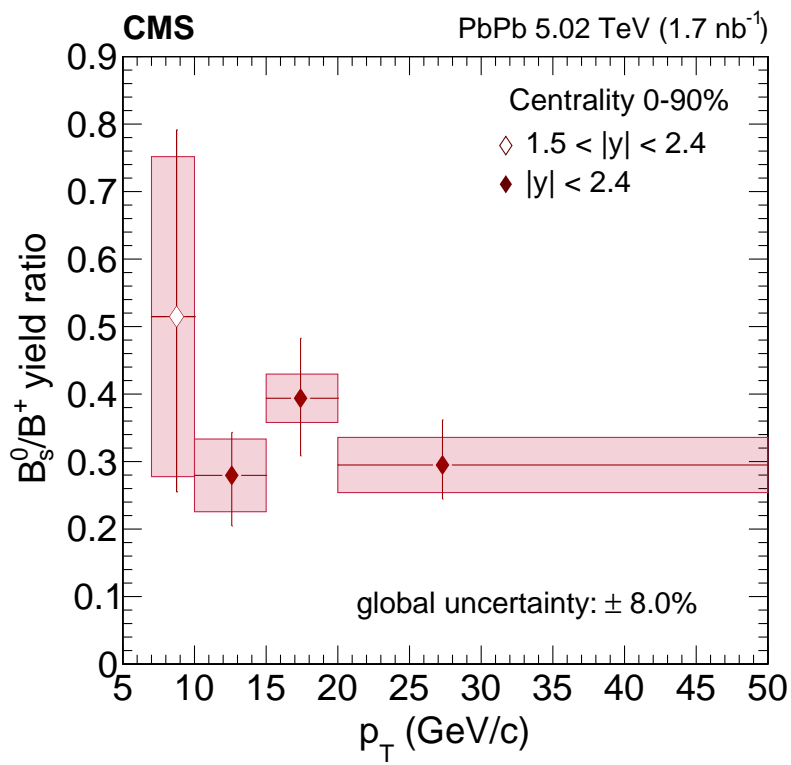


Figure 5-73: The measurement of B_s^0/B^+ as a function of p_T is shown above. The open markers from 7 - 10 GeV/c stand for the fiducial measurements in B-meson rapidity of $1.5 < |y| < 2.4$.

Figure 5-74 shows the B_s^0/B^+ ratio as a function of PbPb collision centrality

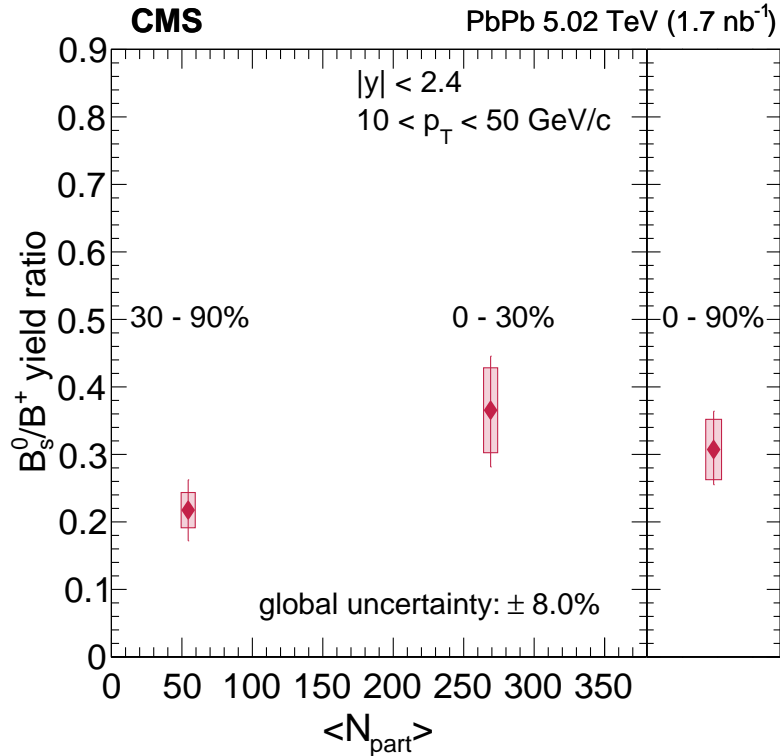


Figure 5-74: The measurement of B_s^0/B^+ as a function of p_T is shown above.

Table 5.48 summarizes B_s^0/B^+ ratio as a function of PbPb collision centrality

Table 5.48: The numerical values and uncertainties of B_s^0/B^+ cross section ratio as a function of centrality are summarized below.

Centrality	B_s^0/B^+	stat. up (+)	stat. down (-)	syst. up (+)	syst. down (-)
0 - 30%	0.3655	21.9%	23.0%	17.2%	17.2%
30 - 90%	0.2175	20.6%	20.9%	12.0%	12.0%
0 - 90%	0.3073	18.4%	17.0%	14.5%	14.6%

Finally, we can also cross check our measurement with the 2015 published B_s^0/B^+ ratio. Figure 5-75 shows the direct comparisons of B_s^0/B^+ ratio as a function p_T

Within uncertainties, we can see that our new results are fully consistent with the 2015 published results but can provide much more information since our measurement is more precise and differential.

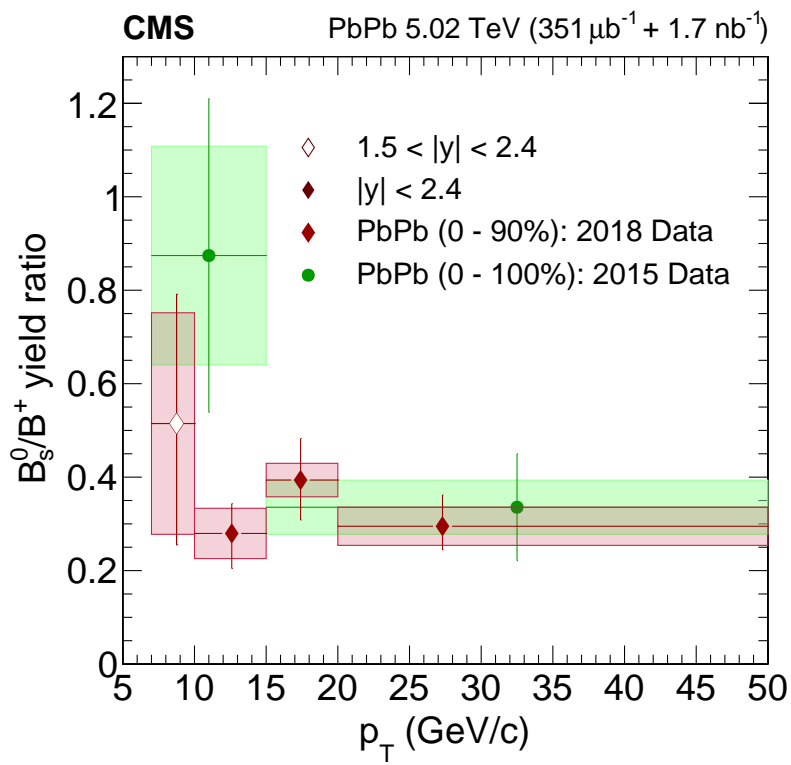


Figure 5-75: The comparison of B_s^0/B^+ as a function of p_T between the CMS 2018 PbPb datasets in centrality 0 - 90% (red) and the 2015 PbPb dataset in centrality 0 - 100% (green) is shown above.

Hence, we have reported the measurements of B_s^0 and B^+ mesons cross section and the B_s^0/B^+ ratio in PbPb collisions at $\sqrt{s_{NN}} = 5.02$ TeV with the CMS experiment. Moreover, we have successfully reproduced our data with the 2015 published results with enhanced performance. In the next chapter, we will answer the questions raised in Section 2.6 through the comparison of our data with other experimental references and theoretical predictions.

Chapter 6

Conclusions

With fully reconstructed B_s^0 and B^+ measurements in PbPb collisions, we can study the beauty hadronization mechanism and answer the questions raised in Section 2.6.

6.1 pp References and Theoretical Models

Because our fully reconstructed B-meson analysis in pp , which serves as the reference for PbPb, is still ongoing, in order to understand our PbPb data, we need to add B-meson pp measurements from other experiments at the LHC. The pp references comparing with our PbPb measurement are described below:

LHCb 7 TeV pp results at $2 < |y| < 5$: This reference is chosen because it is one of the most precise B_s^0/B^+ measurements with energy closest to 5.02 TeV in our analysis [113]. The original results are presented as the corrected yield ratio $\mathcal{R} = \frac{N(B_s^0 \rightarrow J/\psi\phi)}{N(B^+ \rightarrow J/\psi K^+)} \cdot \frac{\epsilon(B^+ \rightarrow J/\psi K^+)}{\epsilon(B_s^0 \rightarrow J/\psi\phi)}$ [113]. We multiply \mathcal{R} by the branching ratios of $BR(B_s^0 \rightarrow J/\psi\phi \rightarrow \mu^+\mu^-K^+K^-)/BR(B^+ \rightarrow J/\psi K^+ \rightarrow \mu^+\mu^-K^+)$ and make them the same quantity as our B_s^0/B^+ measurement.

ATLAS 7 TeV pp results at $|y| < 2.5$: This reference is chosen because it is measured over a rapidity range similar to our measurement range [197]. The original results are the ratios of the fragmentation fraction f_s/f_d . Using the isospin symmetry, we get $f_d = f_u$. So $f_s/f_d = f_s/f_u$. In addition, the ATLAS paper uses the QCD calculations $BF(QCD) = \frac{BR(B_s^0 \rightarrow J/\psi\phi)}{BR(B^0 \rightarrow J/\psi K^{*0})} = 0.83$ instead of directly quoting the PDG

the branching ratios $BF(PDG) = \frac{BR(B_s^0 \rightarrow J/\psi\phi)}{BR(B_s^0 \rightarrow J/\psi K^*0)} = 0.85$. Hence, we relate ATLAS f_s/f_d to our B_s^0/B^+ ratio via $B_s^0/B^+ = BF(PDG)/BF(QCD) \times f_s/f_d$ and compare the ATLAS scaled pp data to our data.

The pp references of LHCb and ATLAS are at different rapidity. However, since the rapidity dependence is not significant in B_s^0/B^+ ratio as demonstrated in Figure 1-35 according to the LHCb publication [113], assuming it is also insignificant in PbPb, we can use the pp references at different rapidity ranges as references for our B_s^0/B^+ measurement.

In addition to the pp references, we also include the theoretical predictions from TAMU (labeled as “PbPb: TAMU” in orange) and Cao, Sun, Ko (labeled as “PbPb: Langevin” in green) models which have been introduced in Section 1.6. Figure 6-1 shows the comparison between our B_s^0/B^+ measurement with pp references and theoretical model calculations.

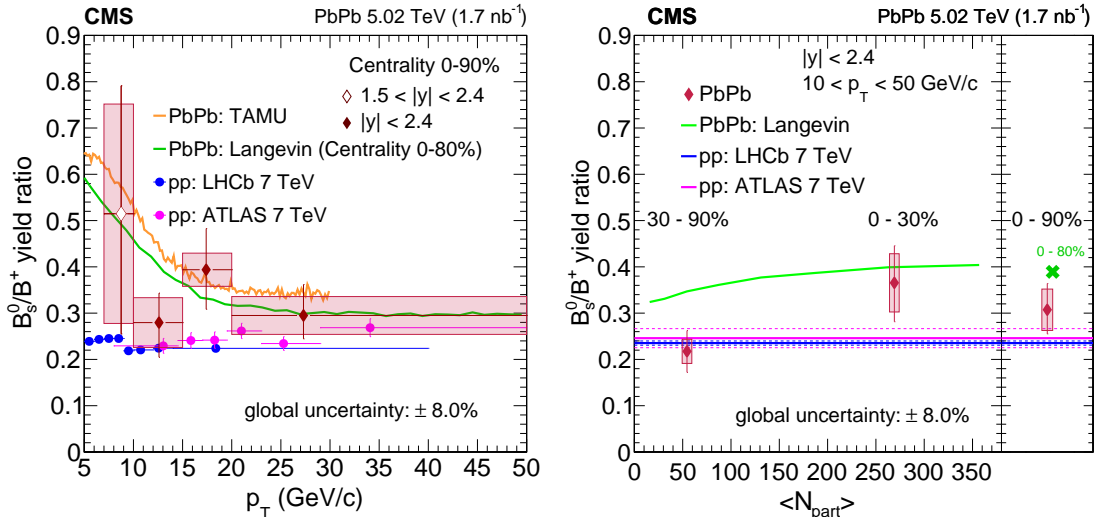


Figure 6-1: The fully reconstructed B_s^0/B^+ ratio (right) as a function of p_T (left) and PbPb event centrality (right) using the 2018 CMS dimuon PbPb dataset are shown above. Both plots include the ATLAS (magenta) and LHCb (blue) 7 TeV pp references. The TAMU model (orange) has only p_T dependent predictions shown on the left figure while the Cao, Sun, Ko model (green) has both p_T and centrality predictions plotted on both figures.

6.2 Implications from the Experimental Data

Figure 6-1 conveys a lot of information. The physics messages from comparison of the PbPb data with the pp references and theoretical model prediction are discussed below:

Substantial Uncertainties at Low p_T : Both statistical and systematic uncertainties of B_s^0/B^+ ratio are large in $7 < p_T < 10$ GeV/c. They mostly come from B_s^0 . However, we know that the statistics of B_s^0 in the p_T range 7 - 10 GeV/c is indeed very small. In fact, from the FONLL calculation, we expect to get only about 12 B_s^0 signal candidates. Unfortunately, some of the systematic uncertainties, for instance, the one due to finite MC simulation statistics, which contributes a lot (26.5%) to the total systematic uncertainties (46%) can be in principle further reduced but reduced due to limited computing resources.

No Significant p_T Dependence: According to B_s^0/B^+ ratio as a function of B-meson p_T , apparently, there is no significant change of the central values for $p_T > 10$ GeV/c. For 7 - 10 GeV/c, the central value jumps from 0.28 up to 0.51. However, the uncertainties of the measurement are also very large. Taking into account all the uncertainties, we do not observe significant p_T dependence on the B_s^0/B^+ ratio.

Good Agreement with Theoretical Models: Both the TAMU and Cao, Sun Ko model calculations for the B_s^0/B^+ ratio vs p_T agree reasonably well with the PbPb data. They both predict the trend of the central values of the data, which first decreases and then approaches flat values as p_T increases. The TAMU Model always lies above the Cao, Sun, Ko Model due to the different applications of fragmentation hadronization mechanisms in the models.

However, we know that in the limit $p_T \rightarrow \infty$, the B_s^0/B^+ in PbPb collisions should be very similar to pp collisions since the fast-moving beauty quarks traverse through the medium within a very short time and are not likely to combine with any quarks in the medium because their speeds are very different. Beauty quarks tend to radiate soft gluons and hadronize via fragmentation. Hence, fragmentation hadronization dominates in b-hadron production at very high p_T .

As for the centrality measurement, the Cao, Sun, Ko model predictions are also reasonably consistent to our data in the range of 0 - 30% and 0 - 90%. However, in the peripheral 30 - 90% collisions, the Cao, Sun, Ko model overshoots B_s^0/B^+ ratio, roughly 2σ above our data point that lies right on the pp references.

Compatible to pp References: While the centers of the B_s^0/B^+ data points lie systematically above the pp references, considering all uncertainties, they are within about 1σ except the peripheral 30 - 90% bin, which behaves like pp because of the very small number of participants. However, it should note that the energy of pp references are higher than the PbPb data. LHCb has reported that the B_s^0/B^+ ratio slightly increases as energy goes up [113]. Therefore, it would make the comparison much better if we could also perform B_s^0/B^+ measurement in pp collisions with CMS and compare the results directly to the PbPb measurements.

6.3 Conclusions

With the physics messages obtained from the discussions, we are prepared to answer the questions raised in Section 2.6 and draw the conclusions of our studies to this thesis:

First Observation of B_s^0 in Nucleus-Nucleus Collisions: In the analysis, we have fully reconstructed B_s^0 with greater 5σ significances in all p_T and centrality bins. Therefore, we have improved our measurements compared to the 2015 published results and declared the first observed fully reconstructed B_s^0 in heavy-ion collisions.

Significant Improvement of the Previous Results: We have successfully reproduced the published results using 2015 datasets with higher precision. Moreover, we measure B_s^0/B^+ as a function of centrality for the first time. In addition, thanks to the higher statistics of the dataset, we are able to measure four p_T bins, providing more information about the p_T dependence of the B_s^0/B^+ ratio. In our measurements, we find no significant p_T dependence of B_s^0/B^+ down to at least 10 GeV/c. In addition, there is a hint of suppression of B-meson cross section in central collision compared to peripheral collisions, which will be confirmed with larger statistics later.

Inconclusive about Strangeness Enhancement: There is a weak hint of potential strangeness enhancement for beauty quark hadronization in PbPb collisions, particularly at low p_T , compared to pp collisions. The B_s^0/B^+ ratios in PbPb collisions are systematically higher than pp collisions for about $(1 - 1.3)\sigma$. However, the hint is not strong enough. We will need more statistics to confirm this hint in the future.

The Fragmentation Hadronization Mechanism Alone Not Enough to Describe Our Data: We can see that the quark coalescence effect must be considered because our data points lie systematically above the pp references. Looking at the most central collision from 0 - 30 %, the B_s^0/B^+ ratio is about 1.25σ above the LHCb pp reference, which corresponds to about 80% confidence. The explicit computation is shown as follows:

$$\%Dev = (0.3655 - 0.2353)/(0.3655 * \sqrt{0.23^2 + 0.172^2}) \simeq 1.25 \quad (6.1)$$

Not Enough Precision to Constrain Theoretical Models: Base on the uncertainties of our data, we find that the theoretical models using quark coalescence to describe hadronization, for instance, the TAMU and Cao, Sun, Ko models, are all in reasonable agreement with the PbPb data, both in terms of central values and the decreasing trends as p_T increases.

Missing the B-meson Measurement in pp with CMS as A Reference: Currently, the B-meson analysis using the 2017 CMS pp dataset is still working in progress. More results will be coming in the near future to answer the questions such as the beauty energy loss mechanism in the QGP and hadronization mechanism in small systems. Our B-meson R_{AA} measurements will be able to constrain the heavy-quark spatial diffusion coefficient and the jet transport parameter to probe the inner workings of the QGP.

In conclusion, the larger PbPb datasets that should be accumulated in upcoming LHC Run 3 and high-luminosity (HL) LHC heavy-ion runs will provide greater precision and allow more differential B-meson measurements not only on traditional observables with but also on modern observables such as $B - \bar{B}$ angular correlations

with more fully reconstructed b-hadron species such as Λ_b , B_c^0 , and Ω_b . In addition, the CMS MIP Timing Detector (MTD) upgrade [198] will allow us to perform hadronic PID. We will be able to fully reconstruct beauty hadrons down very low p_T and carry out measurements with high precision. These future b-hadron measurements could help further investigate beauty hadronization in vacuum and QGP.

6.4 Future Outlooks

As mentioned previously, our B-meson data analysis in pp collisions is still ongoing. Figure 6-2, Figure 6-3, and Figure 6-4 show our ongoing analysis of fully reconstructed B^+ , B^0 , and B_s^0 using the 2017 pp datasets at $\sqrt{s_{NN}} = 5.02$ TeV at very low p_T respectfully

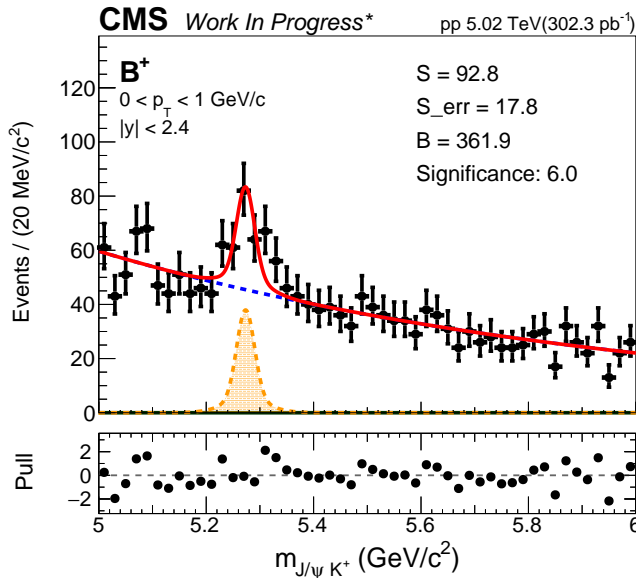


Figure 6-2: The fully reconstructed B^+ via the decay channel of $B^+ \rightarrow J/\psi K^+ \rightarrow \mu^+ \mu^- K^+$ in the p_T range of 0 - 1 GeV/c using the full CMS 2017 pp dataset is shown above. The statistical significance is about 6. The selection is optimized with the BDT algorithm using a subset of topological variables in PbPb B^+ studies.

Thanks to the powerful machine learning algorithms, even without hadronic PID, very clear B-meson signals have still been observed down to $p_T = 0$. The estimated

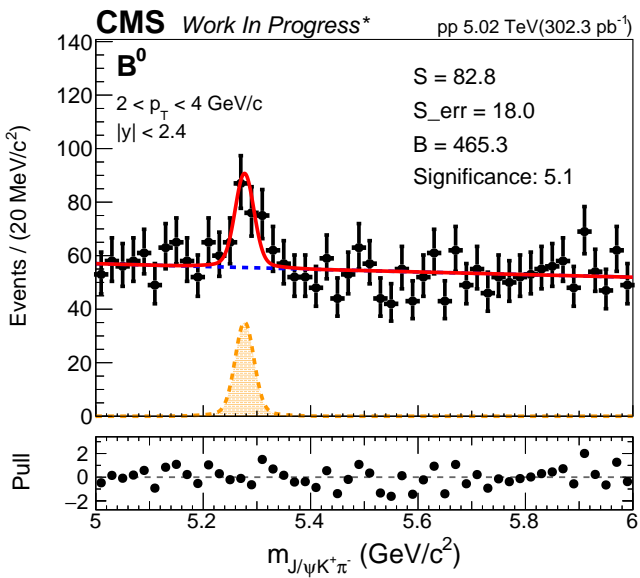


Figure 6-3: The fully reconstructed B^0 via the decay channel of $B^0 \rightarrow J/\psi K^{0*} \rightarrow \mu^+ \mu^- K\pi$ in the p_T range of 2 - 4 GeV/c using the full CMS 2017 pp dataset is shown above. The statistical significance is about 5.1. The selection is optimized with the BDT algorithm using a subset of topological variables in PbPb B_s^0 studies.

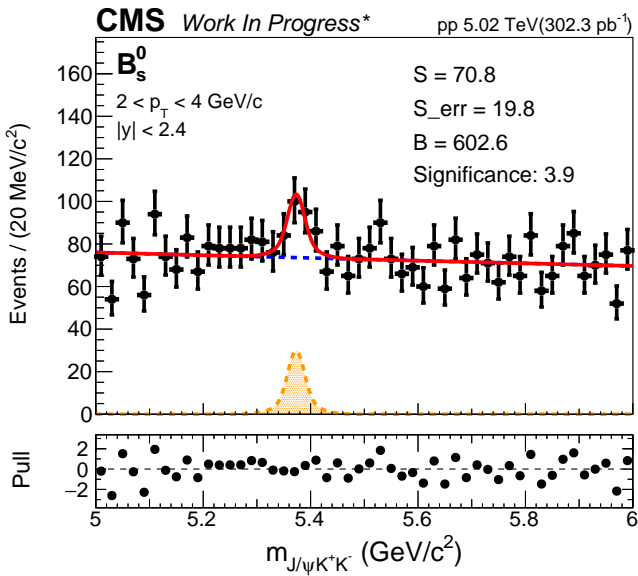


Figure 6-4: The fully reconstructed B_s^0 via the decay channel of $B_s^0 \rightarrow J/\psi \phi \rightarrow \mu^+ \mu^- K^+ K^-$ in the p_T range of 2 - 4 GeV/c using the full CMS 2017 pp dataset is shown above. The statistical significance is about 3.9. The selection is optimized with the BDT algorithm using a subset of topological variables in PbPb B_s^0 studies.

significances are all greater than 4. With these significant signals, we can perform precise measurement on B^+ cross section in pp collisions down to $p_T = 0$, which allows us to study inclusive beauty production cross section. In addition, we will also be able to measure B_s^0/B^+ ratio down to 2 GeV/c. Finally, according to the multiplicity studies, we can also measure B_s^0/B^+ as a function of multiplicity up to about 150, which helps us answer many questions raised in Section 2.6. These fully B-meson measurements down to very low p_T and up to very high multiplicity will be very important to study the beauty quark hadronization mechanisms in vacuum and QGP.

In the future era of LHC Run 3 and HL LHC, much more data will be collected to perform exciting measurements on fully reconstructed B_c^+ and Λ_b hadrons. Meanwhile, at RHIC, as the sPHENIX experiment is taking data in 2023, we can also fully reconstruct b hadrons at lower energies to study a QGP medium at lower temperatures and higher baryon chemical potentials. The fully reconstructed b-hadron measurements at RHIC will be complementary to the measurements at the LHC. Together, these will help determine the heavy-quark diffusion coefficient at different temperatures, constrain the fundamental property of QGP η/s , and probe the inner workings of QGP. Lots of challenges and opportunities are waiting ahead for us to explore and overcome. A bright and exciting chapter of relativistic heavy-ion physics is just around the corner!

References

- [1] S. Weinberg, “A Theory of Leptons”, Phys. Rev. Lett. 19, 1264-1266 (1967)
- [2] M. K. Gaillard, P. D. Grannis, and F. J. Sciulli, “The Standard Model of Particle Physics”, Rev. Mod. Phys. 71 (1999)
- [3] C. D. Roberts, “Nonperturbative effects in QCD at Finite Temperature and Density”, Phys. Part. Nucl. 30 (1999)
- [4] P. A. Zyla et. al. (Particle Data Group), “Review of Particle Physics”, Prog. Theor. Exp. Phys. 2020, 083 C01 (2020)
- [5] J. Gross and F. Wilczek, “Ultraviolet behavior of non-abelian gauge theories”, Phys. Rev. Lett. 30, 1343 (1973)
- [6] S. Dürr et. al. “Ab-Initio Determination of Light Hadron Masses”, Science 322 1224-1227 (2008)
- [7] N. Fettes, U.-G. Meißner, and S. Steininger, “Pion-nucleon scattering in chiral perturbation theory I: Isospin-symmetric case”, Nucl. Phys. A 640 199-234 (1998)
- [8] P. Navrtil and E. Caurier, “Nuclear structure with accurate chiral perturbation theory nucleon-nucleon potential: Application to $\frac{6}{3}Li$ and $\frac{10}{5}B$ ”, Phys. Rev. C 69, 014311 (2004)
- [9] C. Alexandrou, M. Constantinou, K. Hadjyiannakou, K. Jansen, C. Kallidonis, G. Koutsou, and A. V. Avilés-Casco, “Nucleon spin structure from lattice QCD”, PoS DIS2018, 148 (2018)

- [10] J. C. Collins, D. E. Soper, and G. F. Sterman, “Factorization of Hard Processes in QCD”, *Adv. Ser. Direct. High Energy Phys.* 5, 1-91 (1989)
- [11] D. E. Soper, “Parton distribution functions”, *Nucl. Phys. B Proc. Suppl.* 53, 69-80 (1997)
- [12] A. Metz and A. Vossen, “Parton Fragmentation Functions”, *Prog. Part. Nucl. Phys.* 91, 136-202 (2016)
- [13] J. J. Ethier and E. R. Nocera, “Parton Distributions in Nucleons and Nuclei”, *Ann. Rev. Nucl. Part. Sci.* 70, 43-76 (2020)
- [14] Francesco Becattini, “What is the meaning of the statistical hadronization model?”, *J. Phys. Conf. Ser.* 5 (2005)
- [15] B. Andersson, G. Gustafson, G. Ingelman, and T. Sjöstrand, “Parton fragmentation and string dynamics”, *Phys. Rep.* 97 (1983)
- [16] B. R. Webber, “A QCD Model for Jet Fragmentation Including Soft Gluon Interference”, *Nucl. Phys. B* 238 492-528 (1984)
- [17] R. J. Fries, V. Greco, and P. Sorensen, “Coalescence Models For Hadron Formation From Quark Gluon Plasma”, *Ann. Rev. Nucl. Part. Sci.* 58 (2008)
- [18] B.R. Webber, “Fragmentation and hadronization”, *Int. J. Mod. Phys. A* 15S1 577-606 (2000)
- [19] R. C. Hwa and C. B. Yang, “Scaling distributions of quarks, mesons and proton for all p_T , energy and centrality”, *Phys. Rev. C* 67, 064902 (2003)
- [20] B. Alver and G. Roland, “Collision geometry fluctuations and triangular flow in heavy-ion collisions”, *Phys. Rev. C* 81, 054905 (2010)
- [21] J. Jalilian-Marian and X.N. Wang, “Shadowing of gluons in perturbative QCD: A comparison of different models”, *Phys. Rev. D* 63, 096001 (2001)

- [22] European Muon Collaboration, “The ratio of the nucleon structure functions F_2^N for iron and deuterium”, Phys. Lett. B 123, 275-278 (1983)
- [23] E. Wang and X.-N. Wang, “Jet Tomography of Hot and Cold Nuclear Matter”, Phys. Rev. Lett. 89, 162301 (2002)
- [24] F. Wilczek, “QCD In Extreme Conditions”, Contribution to: 9th CRM Summer School: Theoretical Physics at the End of the 20th Century, 567-636
- [25] E. d’Enterria et al., “CMS physics technical design report: Addendum on high density QCD with heavy ions”, J. Phys.G 34 (2007)
- [26] E. Altman, “Many-body localization and quantum thermalization”, Nat. Phys. 14, 979 - 983 (2018).
- [27] M. P. Heller, R. A. Janik, and P. Witaszczyk, “Characteristics of Thermalization of Boost-Invariant Plasma from Holography”, Phys. Rev. Lett. 108, 201602 (2012)
- [28] G. Parisi, “Some considerations on the Quark-Gluon Plasma”, Quark Matter 2018 Conference (2018)
- [29] H.C. Chandola, G. Punetha, and H. Dehnen, “Dual QCD thermodynamics and quark-gluon plasma”, Nucl. Phys. A 945 (2016)
- [30] H. S. Chung, J. Lee, and D. Kang, “Cornell potential parameters for S-wave heavy quarkonia”, J. Korean Phys. Soc. 52 (2018)
- [31] P. K. Srivastava, O. S. K. Chaturvedi, and L. Thakur, “Heavy quarkonia in a potential model: binding energy, decay width, and survival probability”, Eur. Phys. J. C 78 6, 440 (2018)
- [32] J. Harris and B. Muller, “The Search for the quark-gluon plasma”, Ann. Rev. Nucl. Part. Sci. 46 (1996)
- [33] A. Dumitru, Y. Guo, A. Mócsy, and M. Strickland, “Quarkonium states in an anisotropic QCD plasma”, Phys. Rev. D 79 (2009)

- [34] C.A. Dominguez, “Color Deconfinement in QCD at Finite Temperature”, Nucl. Phys. B Proc. Suppl. 15 (1990)
- [35] S. M. Sanches Jr., F. S. Navarra, and D. A. Fogaca, “The quark gluon plasma equation of state and the expansion of the early Universe”, Nucl. Phys. A 937 (2015)
- [36] A. Tawfik and T. Harko, “Quark-Hadron Phase Transitions in Viscous Early Universe”, Phys. Rev. D 85 (2012)
- [37] S. A. Chin, “Transition to Hot Quark Matter in Relativistic Heavy Ion Collision”, Phys. Lett. B 78, 552-555 (1978)
- [38] F. Karsch, “Lattice QCD at High Temperature and Density”, Lect. Notes Phys. 583, 209-249 (2002)
- [39] P. Braun-Munzinger and J. Wambach, “The Phase Diagram of Strongly-Interacting Matter”, Rev. Mod. Phys. Vol 81, 1031-1050 (2009)
- [40] S. Gupta, X. Luo, B. Mohanty, H. G. Ritter, and N. Xu, “Scale for the Phase Diagram of Quantum Chromodynamics”, Science 332 1525-1528 (2011)
- [41] U. Heinz, “The Little Bang: Searching for quark-gluon matter in relativistic heavy-ion collisions”, Nucl. Phys. A 685, 414-431, 2001
- [42] R. X. Xu, “Strange quark stars - A Review”, IAU Symp. 214 (2003)
- [43] Y.-Z. Fan, Y.-W. Yu, D. Xu, Z.-P. Jin, X.-F. Wu, D.-M. Wei, and B. Zhang, “A supra-massive magnetar central engine for short GRB 130603B”, Astrophys. J. Lett. 779 (2013)
- [44] Z. G. Dai, S. Q. Wang, J. S. Wang, L. J. Wang, and Y. W. Yu, “The Most Luminous Supernova ASASSN-15lh: Signature of a Newborn Rapidly-Rotating Strange Quark Star”, Astrophys. J. 817 (2016)
- [45] B. Paczyński and P. Haensel, “Gamma-ray bursts from quark stars”, Mon. Not. Roy. Astron. Soc. 362 1, 4 - 7 (2005)

- [46] D. Trbojevic and S. Peggs, “Required Accuracy of the RHIC Circumference”, United States: N. p., Web. doi:10.2172/1119398 (1993)
- [47] M. J. Rhoades-Brown, “The Heavy Ion Injection Scheme for RHIC”, Proc. of the Workshop on the RHIC Performance (1988)
- [48] D. B. Steski, J. Alessi, J. Benjamin, C. Carlson, M. Manni, P. Thieberger, and M. Wiplich, “Operation of the Relativistic Heavy Ion Collider Au^- ion source”, Review of Scientific Instruments 73, 797 (2002)
- [49] D.B. Steski and P. Thieberger, “Stripping foils at RHIC”, Nucl. Instrum. Meth. A 613 (2010)
- [50] P. Thieberger, L. Ahrens, J. Alessi, J. Benjamin, M. Blaskiewicz, J. M. Brennan, K. Brown, C. Carlson, C. Gardner, W. Fischer, D. Gassner, J. Glenn, W. Mac Kay, G. Marr, T. Roser, K. Smith, L. Snydstrup, D. Steski, D. Trbojevic, N. Tsoupas, V. Zajic, and K. Zeno, “Improved gold ion stripping at 0.1 and 10 GeV/nucleon for the Relativistic Heavy Ion Collider”, Phys. Rev. ST Accel. Beams 11, 011001 (2008)
- [51] L. Evans, “The Large Hadron Collider”, Phil. Trans. R. Soc. A 370 (2012)
- [52] J. Brewer, A. Mazeliauskas, and W. van der Schee, “Opportunities of OO and pO collisions at the LHC”, CERN Theory Report: CERN-TH-2021-028 (2021)
- [53] M. Schaumann, R. Alemany-Fernandez, H. Bartosik, T. Bohl, R. Bruce, G-H Hemelsoet, S. Hirlaender, J. Jowett, V. Kain, M. Krasny, J. Molson, G. Papotti, M.S. Camillocci, H. Timko, and J. Wenninger, “First partially stripped ions in the LHC ($^{208}Pb^{81+}$)” J. Phys. Conf. Ser. 1350, 012071 (2019)
- [54] C.Y. Wong, “Introduction to high-energy heavy-ion collisions”, Singapore, Singapore: World Scientific (1994) 516 p
- [55] Z.-T. Liang and X.-N. Wang, “Globally Polarized Quark-Gluon Plasma in Non-central A + A Collisions”, Phys. Rev. Lett. 96, 039901 (2006)

- [56] M. L. Miller, K. Reygers, S. J. Sanders, and P. Steinberg, "Glauber modeling in high energy nuclear collisions", Ann. Rev. Nucl. Part. Sci. 57, 205 (2007)
- [57] I. Altsybeev and V. Kovalenko, "Classifiers for centrality determination in proton-nucleus and nucleus-nucleus collisions", EPJ Web Conf. 137, 11001
- [58] P. Cortese, "Performance of the ALICE Zero Degree Calorimeters and upgrade strategy", J. Phys. Conf. Ser. 1162, 012006 (2019)
- [59] Oliver Suranyi, "Study of Very Forward Neutrons with the CMS Zero Degree Calorimeter", Universe 5 10, 210 (2019)
- [60] P. Dmitrieva and I. Pshenichnov, "On the performance of Zero Degree Calorimeters in detecting multinucleon events", Nucl. Instrum. Meth. A 906 (2018)
- [61] Star Collaboration, <https://www.star.bnl.gov/public/tpc/tpc.html>
- [62] R. J. Glauber, "Quantum Optics and Heavy Ion Physics", Nucl. Phys. A 774 (2006)
- [63] J. Chauvin, D. Bebrun, A. Lounis, and M. Buenerd, "Low and intermediate energy nucleus-nucleus elastic scattering and the optical limit of Glauber theory", Phys. Rev. C. 28, 1970 (1983)
- [64] T. Wibig and D. Sobczynska, "Proton-nucleus cross section at high energies", J. Phys. G: Nucl. Part. Phys. 24, 2037 (1998)
- [65] B. B. Back, "Studies of multiplicity in relativistic heavy-ion collisions", J. Phys. Conf. Ser. 5 (2000)
- [66] A. Milov, "Electroweak probes with ATLAS", PoS High-pT2017 016 (2019)
- [67] L. Van Hove, "Theoretical prediction of a new state of matter, the "quark-gluon plasma" (also called "quark matter")", Part of Multiparticle Dynamics. Proceedings, 17th International Symposium, Seewinkel, Austria, June 16-20, 801-818 (1986)

- [68] S. A. Bass, M. Gyulassy, H. Stoecker, and W. Greiner, “Signatures of Quark-Gluon-Plasma formation in high energy heavy-ion collisions: A critical review”, J. Phys. G 25 R1-R57 (1999)
- [69] C. Quigg and J. L. Rosner, “Quantum Mechanics with Applications to Quarkonium”, Phys. Rept. 56 167-235 (1979)
- [70] P. Petreczky, “Quarkonium in Hot Medium”, J. Phys. G 37, 094009 (2010)
- [71] G. S. Bali, H. Neff, T. Duessel, T. Lippert, and K. Schilling, “Observation of string breaking in QCD”, Phys. Rev. D 71, 114513 (2005)
- [72] P. Petreczky, “Quarkonium in Hot Medium”, J. Phys. G 37, 094009 (2010)
- [73] STAR Collaboration, “Measurement of inclusive J/ψ suppression in Au+Au collisions at $\sqrt{s_{NN}} = 200$ GeV through the dimuon channel at STAR”, Phys. Lett. B 797, 134917 (2019)
- [74] A. Andronic et. al., “Heavy-flavour and quarkonium production in the LHC era: from proton-proton to heavy-ion collisions”, Eur. Phys. J. C 76, 107 (2016)
- [75] STAR Collaboration, “Suppression of Υ production in d+Au and Au+Au collisions at $\sqrt{s_{NN}} = 200$ GeV”, Phys. Lett. B 735, 127-137 (2014)
- [76] CMS Collaboration, “Suppression of $\Upsilon(1S)$, $\Upsilon(2S)$, and $\Upsilon(3S)$ production in PbPb collisions at $\sqrt{s_{NN}} = 200$ GeV”, Phys. Lett. B 770 357-379 (2017)
- [77] ZEUS Collaboration, “Forward jet production in deep inelastic ep scattering and low-x parton dynamics at HERA”, Phys. Lett. B 632 13-26 (2006)
- [78] R. A. Gerwin, “Energy loss of a relativistic electron beam in a plasma”, The Physics of Fluids 18, 614 (1975)
- [79] STAR Collaboration, “Disappearance of back-to-back high p_T hadron correlations in central Au+Au collisions at $\sqrt{s_{NN}} = 200$ GeV”, Phys. Rev. Lett. 90, 082302 (2003)

- [80] ALICE Collaboration, “Measurements of inclusive jet spectra in pp and central Pb-Pb collisions at $\sqrt{s_{NN}} = 5.02$ TeV”, Phys. Rev. C 101, 034911 (2020)
- [81] C. McGinn, “Mapping the redistribution of jet energy in PbPb collisions at the LHC with CMS”, MIT PhD Thesis (2019)
- [82] A. M. Poskanzer and S.A. Voloshin, “Methods for analyzing anisotropic flow in relativistic nuclear collisions”, Phys. Rev. C 58 1671-1678 (1998)
- [83] P. Bozek and I. Wyskiel, “Directed flow in ultrarelativistic heavy-ion collisions”, Phys. Rev. C 81, 054902 (2010)
- [84] CMS Collaboration, “Constraints on the chiral magnetic effect using charge-dependent azimuthal correlations in pPb and PbPb collisions at the CERN Large Hadron Collider”, Phys. Rev. C 97, 044912 (2018)
- [85] R. S. Bhalerao and J.-Y. Ollitrault, “Eccentricity fluctuations and elliptic flow at RHIC”, Phys. Lett. B 641, 260-264 (2006)
- [86] P. F. Kolb and U. Heinz, “Hydrodynamic description of ultrarelativistic heavy-ion collisions”, Part of Quark-gluon plasma 4, 634-714 (2003)
- [87] STAR Collaboration, “Elliptic flow in Au+Au collisions at $\sqrt{s_{NN}} = 130$ GeV”, Phys. Rev. Lett. 86, 402-407 (2001)
- [88] ALICE Collaboration, “Elliptic flow of charged particles in Pb-Pb collisions at 2.76 TeV”, Phys. Rev. Lett. 105, 252302 (2010)
- [89] J. Rafelski and B. Muller, “Strangeness Production in the Quark-Gluon Plasma”, Phys. Rev. Lett. 48, 1066 (1982)
- [90] STAR Collaboration, “Measurements of ϕ meson production in relativistic heavy-ion collisions at RHIC”, Phys. Rev. C 79, 064903 (2009)
- [91] ALICE Collaboration, “Enhanced production of multi-strange hadrons in high-multiplicity proton-proton collisions”, Nature Phys. 13, 535-539 (2017)

- [92] C. Markert, R. Bellwied, and I. Vitev, “Formation and decay of hadronic resonances in the QGP”, Phys. Lett. B 669, 92-97 (2008)
- [93] T. Kodama, “Hunt for the quark-gluon plasma: 20 years later”, Braz. J. Phys. 34, 205-210 (2004)
- [94] A. Kurkela and A. Mazeliauskas, “Kinetic and Chemical Equilibration of Quark-Gluon Plasma”, Springer Proc. Phys. 250, 177-181 (2020)
- [95] J. L. Nagle, “The Letter S (and the sQGP)”, Eur. Phys. J. C 49, 275-279 (2007)
- [96] S. M. Sanches, F. S. Navarra, and D.A. Fogaca, “The quark gluon plasma equation of state and the expansion of the early Universe”, Nucl. Phys. A 937, 1-16 (2015)
- [97] J. Bjorken, “Highly Relativistic Nucleus-Nucleus Collisions: The Central Rapidity Region”, Phys.Rev.D 27 140-151 (1983)
- [98] U. Heinz, C. Shen, and H. Song, “The viscosity of quark-gluon plasma at RHIC and the LHC”, AIP Conf. Proc. 1441, 766-770 (2012)
- [99] G. Policastro, D. T. Son, and A. O. Starinets, “Shear viscosity of strongly coupled N=4 supersymmetric Yang-Mills plasma”, Phys. Rev. Lett. 87, 081601 (2001)
- [100] B. V. Jacak and B. Müller, “The Exploration of Hot Nuclear Matter”, Science 337, 310-314 (2012)
- [101] A. Adil and M. Gyulassy, “Energy systematics of jet tomography at RHIC: $\sqrt{s_{NN}} = 62.4$ vs. 200 AGeV”,
- [102] Heavy Ion Collisions: The Big Picture, and the Big Questions, “Heavy Ion Collisions: The Big Picture, and the Big Questions”, Ann. Rev. Nucl. Part. Sci. 68, 339-376 (2018)
- [103] X. Dong, Y.-J. Lee, and R. Ralf, “Open Heavy-Flavor Production in Heavy-Ion Collisions”, Ann. Rev. Nucl. Part. Sci. 69, 417-445 (2019)

- [104] M. Cacciari, M. Greco, and P. Nason, “The p_T spectrum in heavy flavor hadroproduction”, JHEP 05 007 (1998)
- [105] M. Cacciari, S. Frixione, and P. Nason, “The p_T spectrum in heavy flavor photoproduction”, JHEP 03 006 (2001)
- [106] R. S. Thorne, “A Variable-flavor number scheme for NNLO”, Phys. Rev. D 73, 054019 (2006)
- [107] S. Alioli, P. Nason, C. Oleari, and E. Re, “A general framework for implementing NLO calculations in shower Monte Carlo programs: the POWHEG BOX”, JHEP 06 043 (2010)
- [108] M. Cacciari, S. Frixione, N. Houdeau, M. L. Mangano, P. Nason, and G. Ridolfi, “Theoretical predictions for charm and bottom production at the LHC”, JHEP 10 137 (2012)
- [109] CMS Collaboration, “Nuclear modification factor of D^0 mesons in PbPb collisions at $\sqrt{s_{NN}} = 5.02$ TeV”, Phys. Lett. B 782, 474-496 (2018)
- [110] CMS Collaboration, “Measurement of the B^\pm Meson Nuclear Modification Factor in Pb-Pb Collisions at $\sqrt{s_{NN}} = 5.02$ TeV”, Phys. Rev. Lett. 119 15, 152301 (2017)
- [111] S. J. Brodsky, H. J. Pirner, and J. Raufeisen “Scaling properties of high p_T inclusive hadron production”, Phys. Lett. B 637, 58-63 (2006)
- [112] C. Peterson, D. Schlatter, I. Schmitt, and P. M. Zerwas, Phys. Rev. D 27 105 (1983)
- [113] LHCb Collaboration, “Measurement of f_s/f_u variation with proton-proton collision energy and B-meson kinematics”, Phys. Rev. Lett. 124, 122002 (2020)
- [114] ALICE Collaboration, “Charm-quark fragmentation fractions and production cross section at midrapidity in pp collisions at the LHC”, CERN-EP-2021-088

- [115] Y. Liu, C. M. Ko, and F. Li, “Heavy quark correlations and the effective volume for quarkonia production”, Phys. Rev. C 93, 034901 (2016)
- [116] F. Prino and R. Rapp, “Open Heavy Flavor in QCD Matter and in Nuclear Collisions”, J. Phys. G 43, 093002 (2016)
- [117] A. M. Adare, M. P. McCumber, J. L. Nagle, and P. Romatschke, “Tests of the Quark-Gluon Plasma Coupling Strength at Early Times with Heavy Quarks”, Phys. Rev. C 90, 024911 (2014)
- [118] Y. Akiba, “Quest for the quark-gluon plasma - hard and electromagnetic probes” Prog. Theor. Exp. Phys. 2015, 03A105 (2015).
- [119] K. M. Burke et al. (JET Collaboration), “Extracting the jet transport coefficient from jet quenching in high-energy heavy-ion collisions”, Phys. Rev. C 90, 014909 (2014)
- [120] J. Casalderrey-Solana, D. C. Gulhan, J. G. Milhano, D. Pablos, and K. Rajagopal, “Predictions for boson-jet observables and fragmentation function ratios from a hybrid strong/weak coupling model for jet quenching”, JHEP 053 (2016)
- [121] S. S. Gubser, “Drag force in AdS/CFT”, Phys. Rev. D 74, 126005 (2006)
- [122] A. Ficnar, J. Noronha, and M. Gyulassy, “Non-conformal Holography of Heavy Quark Quenching”, Nucl. Phys. A 855 (2011)
- [123] H. Bichsel and H. Schindler, “The Interaction of Radiation with Matter”, In: Fabjan C., Schopper H. (eds) Particle Physics Reference Library. Springer, Cham. (2020)
- [124] Y. L. Dokshitzer and D. E. Kharzeev, “Heavy quark colorimetry of QCD matter”, Phys. Lett. B 519, 199 (2001)
- [125] JET Collaboration, “Extracting the jet transport coefficient from jet quenching in high-energy heavy-ion collisions”, Phys. Rev. C 90, 014909 (2014)

- [126] S.-Q. Li, W.-J. Xing, F.-L. Liu, S. Cao, and C.-Y. Qin, “Heavy flavor quenching and flow: the roles of initial condition, pre-equilibrium evolution, and in-medium interaction”, Chin. Phys. C 44, 114101 (2020)
- [127] M. He, R. J. Fries, and R. Rapp, “Heavy flavor at the large hadron collider in a strong coupling approach”, Phys. Lett. B 735, 445 - 450 (2014)
- [128] S. Cao et. al., “Charmed hadron chemistry in relativistic heavy-ion collisions”, Phys. Lett. B 807, 135561 (2020)
- [129] J. Song, H.-H. Li, and F.-L. Shao, “New feature of low p_T charm quark hadronization in pp collisions at $\sqrt{s} = 7$ TeV”, Eur. Phys. J. C 78 4, 344 (2018)
- [130] F. Riek and R. Rapp, “Quarkonia and heavy-quark relaxation times in the quark-gluon plasma”, Phys. Rev. C 82, 035201 (2010).
- [131] M. He, R. J. Fries, and R. Rapp, “Heavy-quark diffusion and hadronization in quark-gluon plasma”, Phys. Rev. C 86, 014903 (2012)
- [132] T. Sjostrand, S. Mrenna, and P. Z. Skands, “PYTHIA 6.4 Physics and Manual”, JHEP 0605, 026 (2006)
- [133] S. Cao, G.-Y. Qin, and S. A. Bass, “Heavy-quark dynamics and hadronization in ultrarelativistic heavy-ion collisions: Collisional versus radiative energy loss”, Phys. Rev. C 88, 044907 (2013)
- [134] S. Cao, G.-Y. Qin, and S. A. Bass, “Energy loss, hadronization, and hadronic interactions of heavy flavors in relativistic heavy-ion collisions”, Phys. Rev. C 92, 024907 (2015)
- [135] M. He and R. Rapp, “Hadronization and Charm-Hadron Ratios in Heavy-Ion Collisions”, Phys. Rev. Lett. 124, 042301 (2020)
- [136] Z. Tang, L. Yi, L. Ruan, M. Shao, H. Chen, C. Li, B. Mohanty, P. Sorensen, A. Tang, and Z. Xu, “Statistical Origin of Constituent-Quark Scaling in the QGP hadronization”, Chin. Phys. Lett. 30 031201(2013)

- [137] STAR Collaboration, “Measurement of D^0 Azimuthal Anisotropy at Midrapidity in Au + Au Collisions at $\sqrt{s_{NN}} = 200$ GeV”, Phys. Rev. Lett. 118, 212301 (2017)
- [138] CMS Collaboration, “Elliptic Flow of Charm and Strange Hadrons in High-Multiplicity $p+Pb$ Collisions at $\sqrt{s_{NN}} = 8.16$ TeV”, Phys. Rev. Lett. 121, 082301 (2018)
- [139] ALICE Collaboration, “Elliptic Flow of Electrons from Beauty-Hadron Decays in Pb-Pb Collisions at $\sqrt{s_{NN}} = 5.02$ TeV”, Phys. Rev. Lett. 126, 162001 (2021)
- [140] ATLAS Collaboration, “Measurement of azimuthal anisotropy of muons from charm and bottom hadrons in Pb+Pb collisions at $\sqrt{s_{NN}} = 5.02$ TeV with the ATLAS detector”, Phys. Lett. B 807, 135595 (2020)
- [141] ALICE Collaboration, “D-meson production in pPb collisions at $\sqrt{s_{NN}} = 5.02$ TeV and in pp collisions at $\sqrt{s} = 7$ TeV”, Phys. Rev. C 94, 054908 (2016)
- [142] CMS Collaboration, “Study of B Meson Production in p + Pb Collisions at $\sqrt{s_{NN}} = 5.02$ TeV Using Exclusive Hadronic Decays”, Phys. Rev. Lett. 116 032301 (2016)
- [143] STAR Collaboration, “Observation of D^0 Meson Nuclear Modifications in Au+Au Collisions at $\sqrt{s_{NN}} = 200$ GeV”, Phys. Rev. Lett. 113, 142301 (2014)
- [144] I. Kuznetsova and J. Rafelski, “Heavy flavor hadrons in statistical hadronization of strangeness-rich QGP”, Eur. Phys. J. C 51, 113-133 (2007)
- [145] Y. Oh, C. M. Ko, S. H. Lee, and S. Yasui, “Heavy baryon/meson ratios in relativistic heavy-ion collisions”, Phys. Rev. C 79, 044905 (2009)
- [146] STAR Collaboration, “Observation of D^\pm/D^0 enhancement in Au+Au collisions at $\sqrt{s_{NN}} = 200$ GeV”, Arxiv 2101.11793
- [147] ALICE Collaboration, “Measurement of D^0 , D^+ , D^{*+} , and D_s^+ production in Pb - Pb collision at $\sqrt{s_{NN}} = 5.02$ TeV”, JHEP 10 174 (2018)

- [148] CMS Collaboration, “Measurement of B_s^0 meson production in pp and PbPb collisions at $\sqrt{s_{NN}} = 5.02$ TeV”, Phys. Lett. B 796 168-190 (2019)
- [149] STAR Collaboration, “First measurement of Λ_c baryon production in AuAu collisions at $\sqrt{s_{NN}} = 200$ GeV”, Phys. Rev. Lett. 124, 172301 (2020)
- [150] ALICE Collaboration, “ Λ_c^+ production in Pb - Pb collisions at $\sqrt{s_{NN}} = 5.02$ TeV”, Phys.Lett.B 793, 212-223 (2019)
- [151] LHCb Collaboration, “Measurement of B^+ , B^0 and Λ_b^0 production in pPb collisions at $\sqrt{s_{NN}} = 8.16$ TeV”, Phys. Rev. D 99, 052011 (2019)
- [152] CMS Collaboration, “Studies of charm quark diffusion inside jets using PbPb and pp collisions at $\sqrt{s_{NN}} = 5.02$ TeV”, Phys. Rev. Lett. 125, 102001 (2020)
- [153] F. Colamaria, “Study of azimuthal correlations between D mesons and charged particles with the ALICE experiment”, J. Phys. Conf. Ser. 612, 012024 (2015)
- [154] STAR Collaboration, “Measurement of D^0 meson + hadron two-dimensional angular correlations in Au+Au collisions at $\sqrt{s_{NN}} = 200$ GeV”, Phys. Rev. C 102, 014905 (2020)
- [155] H. van Hees and R. Rapp, “Thermalization of heavy quarks in the quark-gluon plasma”, Phys. Rev. C 71, 034907 (2005)
- [156] CMS Collaboration, “The CMS experiment at the CERN LHC”, JINST 3 S08004 (2008).
- [157] CMS Collaboration, “A New Boson with a Mass of 125 GeV Observed with the CMS Experiment at the Large Hadron Collider”, Science 338, 1569-1575 (2012)
- [158] CMS Collaboration, “The CMS trigger system”, JINST 12 01, P01020 (2017)
- [159] Y. Chao, “Minimum-Bias and Underlying Event Studies at CMS”, Proceedings, 28th International Conference on Physics in Collision (PIC 2008) : Perugia, Italy, June 25-28, (2008)

- [160] Z. Shi, “Measurement of B_s^0 and B^+ meson yields in PbPb collisions at $\sqrt{s_{NN}} = 5.02$ TeV”, CMS-PAS-HIN-19-011
- [161] CMS Collaboration, “The Phase-2 Upgrade of the CMS Tracker”, CERN-LHCC-2017-009
- [162] M. Swartz, D. Fehling, G. Giurgiu, P. Maksimovic, and V. Chiochia, “A new technique for the reconstruction, validation, and simulation of hits in the CMS pixel detector”, PoS VERTEX2007 035 (2007)
- [163] CMS Collaboration, “Description and performance of track and primary-vertex reconstruction with the CMS tracker”, JINST 9 10, P10009 (2014)
- [164] CMS Collaboration, “The CMS ECAL performance with examples”, JINST 9 C02008 (2014)
- [165] CMS Collaboration, “The CMS hadron calorimeter project: Technical Design Report”, CERN-LHCC-97-031 (1997)
- [166] A. Penzo and Y. Onel, “The CMS-HF quartz fiber calorimeters”, J. Phys. Conf. Ser. 160, 012014 (2009)
- [167] CMS Collaboration, “Observation and studies of jet quenching in PbPb collisions at nucleon-nucleon center-of-mass energy = 2.76 TeV”, Phys. Rev. C 84, 024906 (2011)
- [168] B. Roland, “Forward Physics Capabilities of CMS with the CASTOR and ZDC detectors”, Part of Proceedings, 17th International Workshop on Deep-Inelastic Scattering and Related Subjects (DIS 2019), Madrid, Spain, April 26-30 (2009)
- [169] N. P. Samios, “Baryon spectroscopy and the omega minus”, International conference on the history of original ideas and basic discoveries in particle physics, Erice, Italy (1994)
- [170] T. Bawej el. at., “The New CMS DAQ System for Run-2 of the LHC”, IEEE Trans. Nucl. Sci. 62, 1099-1103 (2015)

- [171] CMS Collaboration, “Commissioning and performance of the CMS pixel tracker with cosmic ray muons”, JINST 5 T03007 (2010)
- [172] P. Billoir, “Progressive track recognition with a Kalman like fitting procedure”, Comput. Phys. Commun. 57, 390 (1989)
- [173] P. Billoir and S. Qian, “Simultaneous pattern recognition and track fitting by the Kalman filtering method”, Nucl. Instrum. Meth. A 294, 219 (1990)
- [174] R. Mankel, “A Concurrent track evolution algorithm for pattern recognition in the HERA-B main tracking system”, Nucl. Instrum. Meth. A 395, 169 (1997)
- [175] R. Fruhwirth, “Application of Kalman filtering to track and vertex fitting”, Nucl. Instrum. Meth. A 262, 444 (1987)
- [176] W. Adam, R. Fruhwirth, A. Strandlie, and T. Todorov, “Reconstruction of electrons with the Gaussian-sum filter in the CMS tracker at LHC”, J. Phys. G 31 N9 (2005)
- [177] K. Rose, “Deterministic Annealing for Clustering, Compression, Classification, Regression and related Optimisation Problems”, Proceedings of the IEEE 86 (1998)
- [178] R. Fruhwirth, W. Waltenberger, and P. Vanlaer, “Adaptive vertex fitting”, J. Phys. G 34 N343 (2007)
- [179] R. Field, “Early LHC Underlying Event Data - Findings and Surprises”, in Hadron collider physics. Proceedings, 22nd Conference, HCP 2010, Toronto, Canada, August 23-27 (2010)
- [180] D. Lange, “The EvtGen particle decay simulation package”, Nucl. Instrum. Meth. A 462 (2001)
- [181] E. Barberio, B. van Eijk, and Z.Was, “PHOTOS: A Universal Monte Carlo for QED radiative corrections in decays”, Comput. Phys. Commun. 66 115 -128 (1991)

- [182] I. P. Lokhtin and A. M. Snigirev, “A model of jet quenching in ultrarelativistic heavy ion collisions and high-pT hadron spectra at RHIC”, Eur. Phys. J. C45 211(2006)
- [183] CMS Collaboration, “Transverse momentum and pseudorapidity distributions of charged hadrons in pp collisions at $\sqrt{s} = 0.9$ and 2.76 TeV”, JHEP 02 041 (2010)
- [184] CMS Collaboration, “Performance of CMS muon reconstruction in pp collision events at $\sqrt{s} = 7$ TeV”, JINST 7 P10002 (2012)
- [185] CMS Collaboration, “Muon performance studies in 2017 pp and 2018 PbPb 5.02TeV data”, CMS Analysis Note: AN-18-316 (2020)
- [186] CMS Collaboration, “Dependence on pseudorapidity and centrality of charged hadron production in PbPb collisions at $\sqrt{s_{NN}} = 2.76$ TeV”, JHEP 08 141 (2011)
- [187] T. W. Anderson, “An Introduction to Multivariate Analysis”, New York, Wiley (1958)
- [188] V. W. Berger and Y. Zhou, “Kolmogorov - Smirnov test: Overview”, Wiley Statsref: Statistics Reference Online (2014)
- [189] M. Kearns and L. Valiant (1989). Cryptographic limitations on learning Boolean formulae and finite automata. Symposium on Theory of Computing. 21. ACM. 433 - 444. (1989)
- [190] J. Therhaag, “TMVA: Toolkit for multivariate data analysis”, AIP Conf. Proc. 1504, 1013-1016 (2012)
- [191] CMS Collaboration “Measurement of the B^+ hadron production cross section in pp collisions at 13 TeV”, CMS Physics Analysis Summary, CMS-PAS-BPH-15-004 (2015)
- [192] W. Verkerke and D. P. Kirkby, “The RooFit toolkit for data modeling”, eConf. C0303241, MOLT007 (2003)

- [193] CMS Collaboration, “B meson production in PbPb data: signal extraction and MC validation”, Technical Report CMS-AN-19-219, CERN, Geneva (2019)
- [194] CMS Collaboration, “Upsilon production cross-section in pp collisions at $\sqrt{s} = 7$ TeV”, Phys. Rev. D 83, 112004 (2011)
- [195] M. Tanabashi et al. (Particle Data Group), “Review of Particle Physics”, Phys. Rev. D 98, 030001 (2018)
- [196] CMS Collaboration, “Charged-particle nuclear modification factors in PbPb and pPb collisions at $\sqrt{s_{NN}} = 5.02$ TeV”, JHEP 04, 039 (2017)
- [197] ATLAS Collaboration, “Determination of the Ratio of b-quark Fragmentation Fractions f_s/f_d in pp Collisions at $\sqrt{s} = 7$ TeV with the ATLAS Detector”, Phys. Rev. Lett. 115, 262001 (2015)
- [198] J. N. Butler and T. T de Fatis “A MIP Timing Detector for the CMS Phase-2 Upgrade”, CMS-TDR-020